Bangor University

DOCTOR OF PHILOSOPHY

Design and analysis of adaptively modulated optical orthogonal frequency division multiple access multiband passive optical networks

Groenewald, Jakobus

Award date:
2014

Awarding institution:
Bangor University

[Link to publication](#)

Design and Analysis of Adaptively Modulated Optical Orthogonal Frequency Division Multiple Access Multiband Passive Optical Networks

PRIFYSGOL

BANGOR

UNIVERSITY

JT Groenewald

A thesis submitted for the degree of

Doctor of Philosophy

School of Electronic Engineering

Bangor University

November 2014

Abstract

The aim of this thesis is to explore innovative technical solutions of utilising Optical Orthogonal Frequency Division Multiplexing (OOFDM) in intensity modulation and direct detection (IMDD) based future access networks to provide multi-service capability with a minimum 1 Gb/s per user. This thesis extensively investigates and analyses the feasibility and performance of adaptively modulated optical orthogonal frequency division multiplexing multiple access passive optical networks (AMOOFDMA PONs) upstream transmission systems by numerically simulating AMOOFDMA PONs using experimentally determined parameters. OOFDM transceivers incorporating reflective semiconductor optical amplifiers (RSOAs) and distributed feedback (DFB) lasers are utilised in the transceivers and intensity modulation and direct detection (IMDD) transmission systems are also employed to achieve a low complexity, high speed and large bandwidth PON as a solution for next generation access networks. Numerical simulations has also being undertaken to improve overall AMOOFDMA PON performance and power budget by incorporating optical band-pass filters (OBPFs) at the output of optical network units (ONUs). A major challenge of making PONs spectrally efficient has been addressed in this thesis by investigating the AMOOFDMA PON with ONUs on a single upstream wavelength. The performance of the single upstream wavelength AMOOFDMA PON is compared to the multiple wavelength AMOOFDMA PON. Another major challenge in AMOOFDMA PONs namely improving system capacity has also been addressed by implementing multiband transmission in an AMOOFDMA PON. Results show that for a multiple upstream OOFDMA IMDD PON system over 25 km single mode fibre (SMF) can achieve an aggregated data rate of 11.25 Gb/s and the minimum wavelength spacing between ONUs are independent of the number of ONUs. Results also show that a single upstream wavelength AMOOFDMA IMDD PON with multiband incorporated at the ONUs can achieve a aggregated line rate of 21.25 Gb/s over 25 km SMF.

Acknowledgements

Abbreviations

A

ADC Analogue to Digital Converter

AMOOFDM Adaptively Modulated Optical OFDM

APD Avalanche Photodiode

ASK Amplitude Shift Keying

AMOOFDM Adaptively Modulated OOFDM

B

BER Bit Error Rate

BPSK Binary Phase-Shift Keying

BTB Back-to-Back

C

CD Chromatic Dispersion

CO-OFDM Coherent Optical Orthogonal Frequency Division Multiplexing

CO Central Office

CP Cyclic Prefix

CR Clipping Ratio

CSPR Carrier Signal Power Ratio

D

DAB Digital Audio Broadcast

DAC Digital to Analogue Converter

DBA Dynamic Bandwidth Allocation

DC Direct Current

DFB Distributed Feedback

DFT Discrete Fourier Transform

DML Directly Modulated Laser

DSB Double Sideband

DSL Digital Subscriber Line

DSP Digital Signal Processing

E

EPON Ethernet Passive Optical Network

10G-EPON 10 Gigabit-Ethernet Passive Optical Network

EVM Error Vector Magnitude

E/O Electrical-to-Optical

ER Extinction Ratio

ESSB Electric SSB

F

FDM Frequency Division Multiplexing

FEC Forward Error Correction

FFT Fast Fourier Transform

FPGA Field-Programmable Gate Array

FTTH/B/C/P Fibre-To-The-Home/Building/Curb/Premises

FWM Four-Wave Mixing

G

Gb/s Gigabits per Second

GPON Gigabit-capable Passive Optical Network

10G-PON 10 Gigabit- Passive Optical Network

GS/s Giga Samples per Second

GVD Group-Velocity Dispersion

H

HD High-Definition

I

ICI Inter-Carrier Interference

IDFT Inverse Discrete Fourier Transform

IFFT Inverse Fast Fourier Transform

IMDD Intensity Modulation and Direct Detection

ISI Inter-Symbol Interference

L

LPF Low-Pass Filter

LSSB Lower SSB

M

MAI Multiple Access Interference

MCM Multi-Carrier Modulation

MIMO Multiple-Input- Multiple-Output

MMF Multi-Mode Fibre

MZM Mach-Zehnder Modulator

N

NG-PON Next Generation Passive Optical Network

NM Nanometre

NRZ Non-Return-To-Zero

O

OBI Optical Beating Interference

OBPF Optical Band Pass Filter

ODN Optical Distribution Network

O/E Optical-to-Electrical

OFDM Orthogonal Frequency Division Multiplexing

OLT Optical Line Terminal

ONU Optical Network Unit

OOFDM Optical Orthogonal Frequency Division Multiplexing

OOFDMA OOFDM Multiple Access

OOK On-Off Keying

P

PAM Pulse Amplitude Modulation

PAPR Peak-to-Average Power Ratio

PON Passive Optical Network

PRK Phase-Reversal Keying

P/S Parallel-to-Serial

PSK Phase Shift Keying

PTP Point-to-Point

Q

QAM Quadrature Amplitude Modulation

QB Quantization Bits

QoS Quality of Service

QPSK Quadrature Phase Shift Keying

R

REAM Reflective Electro-Absorption Modulator

RF Radio Frequency

RSOA Reflective Semiconductor Optical Amplifier

S

SMF Single Mode Fibre

SNR Signal-to-Noise Ratio

S/P Serial-to-Parallel

SPM Self-Phase Modulation

SOA Semiconductor Optical Amplifier

STO Symbol Timing Offset

SPM Self-Phase Modulation

SSB Single Sideband

T

TDM Time Division Multiplexing

TDMA Time Division Multiple Access

V

VDSL Very-High-Speed DSL

W

WDM Wavelength Division Multiplexing

X

XPM Cross-Phase Modulation

Contents

1 Chapter 1: Introduction

1.1 Optical networks and challenges

The exponentially increasing demand for more bandwidth and higher speeds due to the present day's fast paced digital lifestyle, creates a need for upgrading existing communication systems. Driven by various emerging bandwidth-hungry services such as social websites, on-line gaming, video sharing and high definition (HD) video on demand, the end-users' need for transmission bandwidth increases more than 70% year on year [1].

Because the current copper wire access technique - namely very-high-speed digital subscriber line (VDSL) - cannot satisfy the ever-increasing bandwidth requirements, the need for passive optical networks (PONs) are ever increasing and needs to be adopted and practically implemented as a promising "future-proof" high-speed technical strategy for broadband access [2].

The communications industry has become very dependent on optical fibre systems for backbone infrastructure. The bandwidth bottle neck that the copper based access networks create is addressed by operators replacing the copper systems with fibre systems. The fast increasing demand for more bandwidth and higher speeds created a need for improving existing systems leading to more integration between the core networks, metro networks and access networks with increased reach, low cost and high capacity.

Currently the PON standards are ITU-T G.984 Gigabit PON (GPON) with a maximum line rate of 2.5 Gb/s [3] and IEEE 802.3ah Ethernet PON (EPON) with a line rate of 1.25 Gb/s [4]. Both these Gigabit-PONs standards specify a reach of up to 20 km. These standards are being replaced with 10 Gigabit-PON technologies to support aggregate data rates of 10 Gb/s. There are two 10 Gigabit-PON standards: ITU-T G987 10 Gigabit PON (10G-PON) [5] and IEEE 802.3av 10 Gigabit EPON (10G-EPON) [6]. 10G PON technologies are still considered as the next generation PON (NG-PON) technologies but development and prototyping of 40 G PONs (NG-PON2) capable of delivering 40 Gb/s downstream line rates is already underway [7].

In a practical system, there are many aspects which need to be considered with regards to the performance of the system. These aspects include modulator choice in the transmitter, fibre type (single mode or multimode), transmission link loss and type of detection at the receiver.

It has been found that the main limiting factors in transmitters and receivers are the resolution and sampling speed of the analogue to digital converter (ADC) [8]. The ideal situation will be the use of an ADC with a high sampling speed and high resolution. However, for commercially available ADCs, there is a trade-off between sampling speed and resolution. Therefore, for a given transmission system, the use of optimum ADCs are important for maximising the system performance.

PONs are point-to-multipoint networks consisting of passive optical components to connect multiple users and/or premises to a single optical line terminal (OLT) as shown in Figure 1. The number of users supported by a PON is typically, 16, 32, or 64 due to a limited power budget [9]. PON systems comes in different varieties such as fibre to the home (FTTH), fibre to the kerb (FTTC), fibre to the premises (FTTP) and fibre to the node (FTTN). For simplicity we refer to optical point-to-multipoint systems as FFTX where X represents the termination point. The backbone fibre is typically 20-60 km in length with short distribution fibres of a few kilometres in length from the power splitter to the optical network unit (ONU).
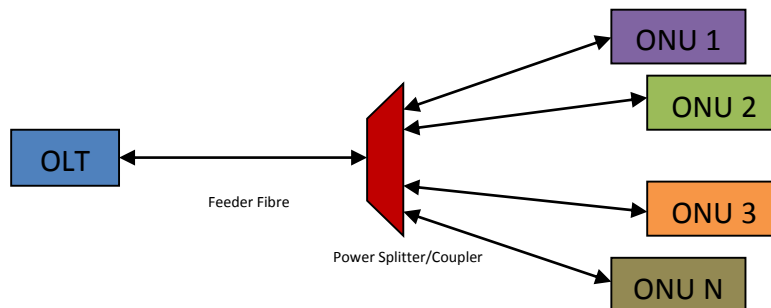
Figure 1: Generic PON system representation.

The main problem with PONs in the optical distribution network (ODN) is the upstream transmission for multiple optical network units (ONUs) to a single OLT. There are three principal methods used to transmit multiple signals through optical fibres namely time division multiplexing (TDM) [10], wavelength division multiplexing (WDM) [11] and hybrid TDM/WDM [11].

PON systems have traditionally been time division multiplexing (TDM) PONs [12]. To utilise TDM in a PON system the downstream signal from the OLT to the ONUs are broadcast to all ONUs and the ONU will only access the data packets allocated to it. The downstream and upstream signals are allocated on different frequency bands at different central wavelengths. A

time division multiple access (TDMA) PON is a point-to-multipoint system between multiple ONUs and one OLT. For upstream transmission TDMA can be used to multiplex upstream signals. TDMA will be very difficult to implement for upstream transmission due to timing differences because of link characteristics for each ONU being different, causing different time delays for different ONUs, thus TDMA is very sensitive to packet latency. This will make the managing of timeslots very difficult making complex scheduling algorithms a necessity for TDMA.
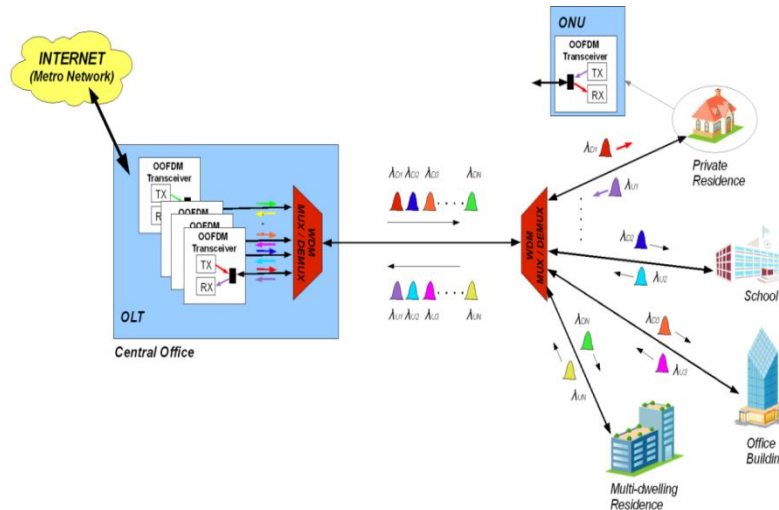
Figure 2: WDM PON system [13].

After TDM PON wavelength division multiplexing (WDM) PONs were developed. In WDM PON systems the upstream and downstream communication between the OLT and ONU is achieved by assigning a specific frequency to each ONU. Thus each ONU will be assigned two wavelengths as shown in Figure 2. For the upstream transmission the wavelengths from different ONUs is multiplexed together and sent to the OLT via the feeder fibre. The OLT receiver de-multiplexes the received WDM signal using filters and an array of photo- detectors. The main challenges is flexibility in WDM PON systems [12].

The hybrid WDM/TDM-PON is where each frequency is also divided up into time slots giving WDM/TDM-PON sub wavelength granularity. Thus multiple ONUs can be assigned to one wavelength and shared by using TDM. ONUs with the need for higher capacity can be assigned multiple wavelengths giving WDM/TDM-PON great flexibility to manage dynamic resource allocation fluctuations making the system more efficient. WDM/TDM-PON can also decrease the number of OLTs needed.

Orthogonal Frequency Division Multiplexing (OFDM) is utilised in PON systems due to its great resistance to fibre dispersion, high spectral efficiency, and extreme flexibility on both multiple services access and dynamic bandwidth allocation [14-16]. The idea of OFDM in optical communications can be extended to PONs with multiple ONUs to a single OLT where each ONU is composed of one or more subcarriers of the OFDM band. This results in optical orthogonal frequency division multiple access (OOFDMA) PONs with dedicated sub-channels for each ONU consisting of one or more OFDM subcarriers and/or time slots, to become fine-grained transparent pipes for the delivery of arbitrary signals [17]. Thus for upstream transmission a novel idea of OOFDMA is used to overcome the problems of normal TDMA by combining frequency division multiplexing (FDM) and TDM.
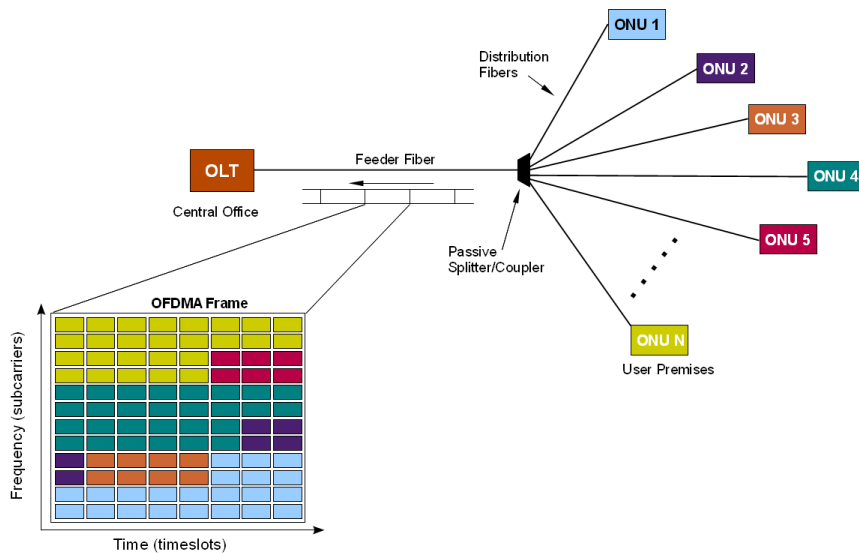
Figure 3: OOFDMA PON system [13].

The frequency and time domain partitioning of an OOFDMA frame is controlled by the optical OLT. As shown in Figure 3 for upstream transmission the subcarriers and timeslots assigned to a specific ONU is colour coded. The assignment of subcarriers and timeslots can be changed dynamically to optimise system throughput. For upstream transmission the ONUs can use the same wavelength if coherent detection is used [18].

A Multi-band system is a system with two or more electrical ONUs with each electrical ONU assigned to a sub-band of frequencies as depicted in Figure 4. For upstream transmission the bands/subcarriers of the ONUs are multiplexed together in the electrical domain before the signal containing all the bands are transmitted to the OLT on the wavelength designated for upstream transmission.
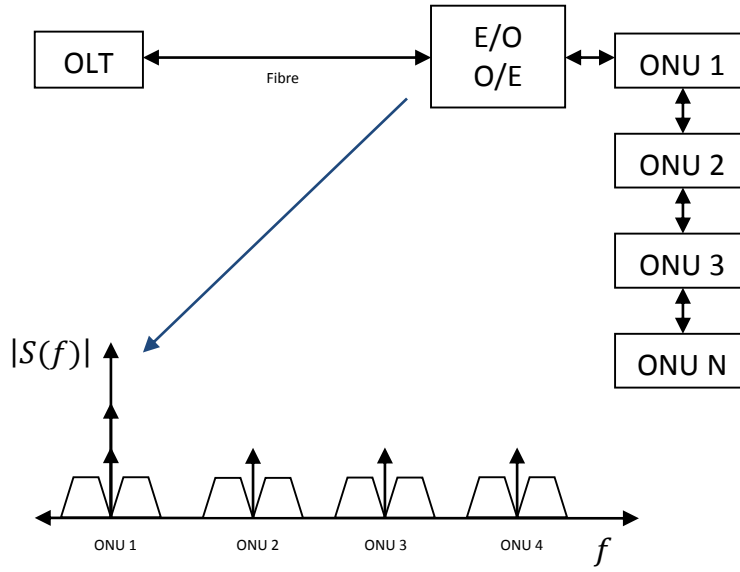
Figure 4: Multiband system representation with upstream optical frequency domain representation.

To achieve maximum capacity, spectral efficiency and flexibility a combination of multiband and OOFDMA PON techniques can be incorporated in one system. Intensity modulation and direct detection (IMDD) can be used to achieve upstream and downstream transmission. In downstream transmission the OLT assigns bands and subcarriers to the ONUs.
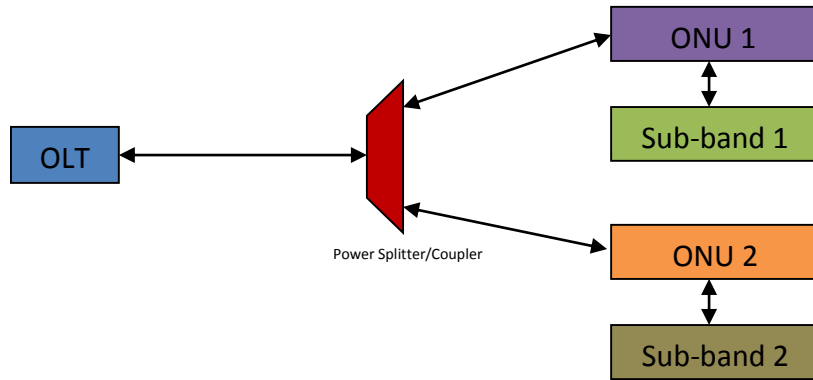
Figure 5: Multi-band OOFDMA PON system.

Different configurations of bands and subcarriers can be considered for example the configuration in Figure 6 the subcarriers of ONU1 are represented by the red, with the green representing sub-band 1 and the blue and orange the subcarriers and sub-band for the second PON.
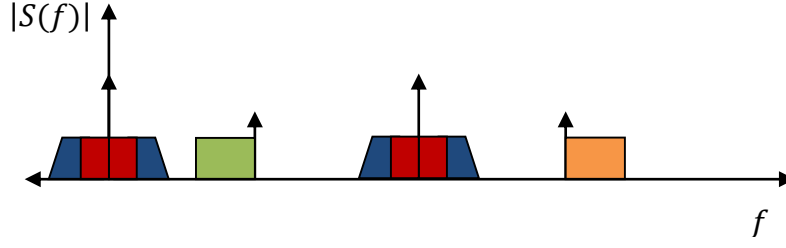
Figure 6: Multi-band OOFDMA upstream optical frequency spectrum.

The electrical received spectrum using direct detection will look like the spectrum in Figure 7 after the direct detection has down mixed the two optical carriers to baseband.
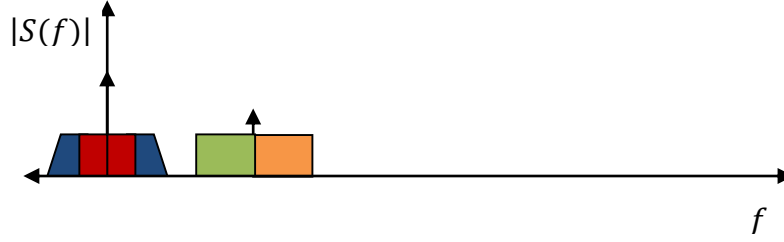
Figure 7: Received Multi-band OOFDMA upstream electrical frequency spectrum.

Upstream transmission of OOFDMA PONs is still a major challenge because of interference between ONUs [19]. Optical beat interference (OBI), which arises due to the direct detection of combined upstream signals of similar wavelengths, generates unwanted frequency products that may fall into the signal spectral region. One way to mitigate the OBI effect is to use different wavelengths for upstream transmission from different ONUs [20]. The drawback of the solution is it considerably increases the optical bandwidth needed to accommodate multiple ONUs and for optimal performance each ONU requires its own optical filter making practical implementation difficult. Another way is the use of coherent detection instead of direct detection at the OLT [21]. The drawback with this is the system considerably increases in complexity in transceivers. To address the issues of practical implementation and overall system complexity a novel technique is proposed where the minimum spacing between ONUs to mitigate the OBI is determined and used for multiple wavelength upstream OOFDMA IMDD PONs.

The advantages of OOFDMA IMDD PONs are:

- Capability of providing an increased number of subscribers with high signal bit rates over extended reach [17].

- Decreased system complexity due to rapid advances in modern digital signal processing (DSP) technology and owing to OOFDMA's unique adaptability, excellent resistance to linear component/system impairments and efficient utilisation of channel spectral characteristics [17, 22-28].

- DSP-based adaptive dynamic bandwidth allocation (DBA) with bandwidth granularity. As mentioned above, the available channel bandwidth is shared between various ONUs using dimensions of frequency, time and signal modulation format. This feature can use limited channel spectral bandwidths to provide end-users with required services [29].

- Backward compatibility. OOFDMA PONs can potentially support multiple TDM PON standards. This coexistence with different standards offers a seamlessly upgrading of installed legacy PONs [25].

- Excellent flexibility. OOFDMA transceivers with adaptive power loading offer the PON systems great adaptability [24].

In this thesis research is reported on the comparison between multiple upstream wavelength OOFDMA PONs and single upstream wavelength OOFDMA PONs. For the single upstream wavelength OOFDMA PON each ONU comprises a OFDM signal being radio frequency (RF) upshifted and reflective semiconductor optical amplifier (RSOA) intensity modulator used to modulate the signal with direct detection at the OLT, with optical single sideband (SSB) achieved by implementing an optical band-pass filter (OBPF) at the OLT. The total number of data carrying subcarriers can be dynamically assigned to different ONUs by the OLT. To further improve the overall system performance, a multiband system is introduced where for a two ONU case, an electrical SSB band is added to each ONU. In this thesis the single upstream wavelength OOFDMA PON with multiband model is verified through numerical simulations and numerical data is analysed and compared to multiple wavelength upstream OOFDMA PON transmission.

1.2 Major Contributions of the Research

- Optimum parameters for a 40 km point-to-point directly modulated distributed feedback laser system are determined. The optimum OOFDM transceiver parameters are 8 quantization bits, a clipping ratio of 13 dB, a directly modulated laser (DML) driving current of 15 mA, a DML bias current of 30 mA at an ADC/DAC sampling speed of 25 GS/s with PIN receiver sensitivity of -19 dBm. With optimised parameters for OFDM transceivers and the DML, simulations of 38.75 Gb/s over 40 km SMF IMDD OOFDM is achieved using adaptive bit loading.

- Numerical simulations have shown that, in IMDD OOFDMA PONs, the minimum ONU wavelength spacing required for eliminating the OBI effect is 8 GHz for RSOA-IM based ONUs and 18 GHz for DML-IM based ONUs and is independent of the number of ONUs. Simulations have also shown that the doubling of the number of ONUs simultaneously accommodated gives a 1.9 dB reduction in upstream power budget.

- The utilisation of an optimum frequency-offset 5th order super-Gaussian optical filter immediately after the RSOA intensity modulator in each ONU can significantly improve the upstream power budget by > 5.3 dB. The filter also reduces the minimum wavelength spacing between RSOA-IM based ONUs from 8 GHz to 4 GHz further increasing the spectral efficiency of the OOFDMA PON system.

- In an adaptively modulated (AM) OOFDMA multiband PON system with frequencies of 2.125 GHz and 6.125 GHz the system can achieve a net rate of 21.25 Gb/s upstream transmission for 2 ONUs over 25 km using RSOA modulators corresponding to a BER of 1×10^{-3} at a received optical power of 0.75 dBm. Only one optical band-pass filter is needed at the optical line terminal to ensure optical single sideband before direct detection due to all ONUs transmitting on the same wavelength.

1.3   Thesis Structure

The thesis comprises of 6 chapters. Chapter 2 presents review work and chapter 3 to 5 details research results. Chapter 6 concludes and discusses future work. The chapter outlines are:

Chapter 1: This chapter provides a brief introduction to the research and presents the challenges facing future optical networks and shows the motivation for researching OOFDMA transmission work and its major achievements.

Chapter 2: To aid understanding of the work presented in this thesis, chapter 2 presents the basic principles incorporated in a OOFDMA system, starting with bit encoding and decoding and moving on to the FFT and IFFT that enables the implementing of OFDM. Focus is placed on the IMDD transmission and compared with coherent OOFDM (CO-OFDM). The basic working principles for intensity modulation are discussed with a focus on DFB lasers and RSOA based intensity modulators. The fundamentals of key components involved in a general OFDM system are described such as error vector magnitude (EVM) and bit error rate (BER). Single mode fibre (SMF) together with its linear and nonlinear effects is also presented.

Chapter 3: Multiple wavelength upstream OOFDMA PON transmission: In this chapter the impact of the number of ONUs involved in a single OOFDMA PON on a practically achievable upstream optical power budget for various PON architectures incorporating intensity modulators such as DFB lasers and RSOAs is investigated. The peak-to-average power ratio (PAPR) and extinction ratio (ER) of the OOFDMA PON system are also investigated through simulation. Finally an investigation is made of the effects of dispersion and chirp on the optical bandwidth and wavelength spacing of OFDMA IMDD PONs with ONUs in upstream transmission.

Chapter 4: Investigation of efficient techniques for improving the multiple wavelength OOFDMA IMDD PON in upstream transmission: Efficient techniques for further improving the capacity versus reach performance of OOFDMA PONs with adequate optical power budgets are investigated including: optical filter-induced single side-band transmission. The effect of the optical filtering on the ONU wavelength spacing is also investigated.

Chapter 5: Single wavelength upstream OOFDMA IMDD PON transmission: Electric single sideband (ESSB) and modulated multi-band transmission with optical SSB (OSSB) and OBPF for single upstream wavelength ONUs is investigated.

Finally, *Chapter 6* summarises the thesis and suggests future research work.

1.4 References

[1]   J. Tang, R. Giddings, X. Jin, J. Wei, X. Zheng, E. Giacoumidis, et al., "Real-Time Optical OFDM Transceivers for PON Applications", in Optical Fiber Communication Conference/National Fiber Optic Engineers Conference 2011, Los Angeles, California, 2011.

[2]   I. Cano, M. C. Santos, X. Escayola, V. Polo, E. Giacoumidis, C. Kachris, et al., "An OFDMA-PON with non-preselected independent ONU sources and centralized feedback wavelength control: Dimensioning and experimental results", in 14th International Conference on Transparent Optical Networks (ICTON), pp. 1-4, 2012.

[3]   ITU-T Recommendation G.984: Gigabit-capable passive optical networks (GPON): General characteristics [Online], http://www.itu.int/rec/T-REC-G.984.1/en.

[4]   802.3ah - IEEE Standard for Information technology-- Local and metropolitan area networks [Online], http://standards.ieee.org/findstds/standard/802.3ah-2004.html.

[5]   G.987.1 : 10-Gigabit-capable passive optical networks (XG-PON): General requirements [Online], http://www.itu.int/rec/T-REC-G.987.1/en.

[6]   802.3av - IEEE Standard for Information technology-- Local and metropolitan area networks- Specific requirements- Carrier Sense Multiple Access with Collision Detection (CSMA/CD) Access Method and Physical Layer Specifications Amendment 1: Physical Layer Specifications and Management Parameters for 10 Gb/s Passive Optical Networks [Online], http://standards.ieee.org/findstds/standard/802.3av-2009.html.

[7]   New FTTH-based Technologies and Applications [Online], http://www.ftthcouncil.eu/resources?category_id=30&location=&topic=Technology.

[8]   J. M. Tang and K. A. Shore, "Maximizing the transmission performance of adaptively modulated optical OFDM signals in multimode-fiber links by optimizing analog-to-digital converters", Journal of Lightwave Technology, vol. 25, pp. 787-798, Mar 2007.

[9]   L. G. Kazovsky, N. Cheng, W. T. Shaw, D. Gutierrez, and S. W. Wong, "Broadband Optical Access Networks", Wiley, 2011.

[10]   G. P. Agrawal, "Fiber-Optic Communication Systems", Wiley, 2002.

[11]   J. L. Wei, X. L. Yang, R. P. Giddings, J. M. Tang and K. A. Shore, "SOA Intensity Modulator-Enabled Colourless Transmission of Adaptively Modulated Optical OFDM Signals for WDM-PONs", in 14th OptoElectronics and Communications Conference (OECC), Hong Kong, China, pp. 1-2, 2009.

[12]   N. Suzuki, K. Nakura, T. Suehiro, M. Nogami, S. Kosaki, and J. Nakagawa, "Over-sampling based burst-mode CDR technology for high-speed TDM-PON systems", in Optical Fiber Communication Conference and Exposition (OFC/NFOEC) and the National Fiber Optic Engineers Conference, 2011, pp. 1-3.

[13]   R. Giddings, "Design, Implementation and Analysis of Real-Time Optical OFDM Transceivers", Electronic Engineering, Bangor University, 2011.

[14]   B. Lin, J. Li, H. Yang, Y. Wan, Y. He, and Z. Chen, "Comparison of DSB and SSB Transmission for OFDM-PON [Invited]", Journal of Optical Communications and Networking, vol. 4, pp. B94-B100, 2012.

[15]   W. Shieh, H. Bao, and Y. Tang, "Coherent optical OFDM: theory and design", Optics Express, vol. 16, pp. 841-859, 2008.

[16]   B. Liu, L. Zhang, X. Xin, and J. Yu, "None pilot-tones and training sequence assisted OFDM technology based on multiple-differential amplitude phase shift keying", Optics Express, vol. 20, pp. 22878-22885, 2012.

[17] N. Cvijetic, D. Y. Qian, and J. Q. Hu, "100 Gb/s Optical Access Based on Optical Orthogonal Frequency-Division Multiplexing", IEEE Communications Magazine, vol. 48, pp. 70-77, Jul 2010.

[18] D. Qian, N. Cvijetic, Junqiang Hu, and Ting Wang, "Orthogonal Frequency Division Multiple Access PON (OFDMA-PON) for Colorless Upstream Transmission Beyond 10 Gb/s", IEEE journal on Selected Areas in Communications, vol. 28, pp. 781-790, Aug. 2010.

[19] L. Chen, J. Zhou, Y. Qiao, Z. Huang, and Y. Ji, "Novel Modulation Scheme Based on Asymmetrically Clipped Optical Orthogonal Frequency Division Multiplexing for Next-Generation Passive Optical Networks", Journal of Optical Communications and Networking, vol. 5, pp. 881-887, 2013.

[20] X. Q. Jin, J. Groenewald, E. Hugues-Salas, R. P. Giddings, and J. M. Tang, "Upstream Power Budgets of IMDD Optical OFDMA PONs Incorporating RSOA Intensity Modulator-Based Colorless ONUs", Journal of Lightwave Technology, vol. 31, pp. 1914-1920, 2013.

[21] D. Qian, Neda Cvijetic, Junqiang Hu, and Ting Wang, "Orthogonal Frequency Division Multiple Access PON (OFDMA-PON) for Colorless Upstream Transmission Beyond 10 Gb/s", IEEE journal on Selected Areas in Communications, vol. 28, pp. 781-790, Aug. 2010..

[22] D. Qian, J. Hu, J. Yu, P. N. Ji, L. Xu, T. Wang, et al., "Experimental Demonstration of a Novel OFDM-A Based 10Gb/s PON Architecture", 33rd European Conference and Exibitiojn of Optical Communication (ECOC), pp. 1-2, 2007.

[23] Q. Dayou, N. Cvijetic, H. Junqiang, and W. Ting, "A Novel OFDMA-PON Architecture With Source-Free ONUs for Next-Generation Optical Access Networks", Photonics Technology Letters, IEEE, vol. 21, pp. 1265-1267, 2009.

[24] X. Q. Jin, J. L. Wei, R. P. Giddings, T. Quinlan, S. Walker, and J. M. Tang, "Experimental Demonstrations and Extensive Comparisons of End-to-End Real-Time Optical OFDM Transceivers With Adaptive Bit and/or Power Loading", Photonics Journal, IEEE, vol. 3, pp. 500-511, 2011.

[25] R. P. Giddings and J. M. Tang, "World-first experimental demonstration of synchronous clock recovery in an 11.25Gb/s real-time end-to-end optical OFDM system using directly modulated DFBs," in Optical Fiber Communication Conference and Exposition (OFC/NFOEC) and the National Fiber Optic Engineers Conference, 2011, pp. 1-3.

[26] R. P. Giddings, X. Q. Jin, E. Hugues-Salas, E. Giacoumidis, J. L. Wei, and J. M. Tang, "Experimental demonstration of a record high 11.25Gb/s real-time optical OFDM transceiver supporting 25km SMF end-to-end transmission in simple IMDD systems", Opt. Express, vol. 18, pp. 5541-5555, 2010.

[27] E. Hugues-Salas, R. P. Giddings, X. Q. Jin, J. L. Wei, X. Zheng, Y. Hong, et al., "Real-time experimental demonstration of low-cost VCSEL intensity-modulated 11.25Gb/s optical OFDM signal transmission over 25km PON systems", Optics Express, vol. 19, pp. 2979-2988, 2011.

[28] X. Q. Jin and J. M. Tang, "Optical OFDM Synchronization With Symbol Timing Offset and Sampling Clock Offset Compensation in Real-Time IMDD Systems", Photonics Journal, IEEE, vol. 3, pp. 187-196, 2011.

[29] X. Q. Jin, E. Hugues-Salas, R. P. Giddings, J. L. Wei, J. Groenewald, and J. M. Tang, "First real-time experimental demonstrations of 11.25Gb/s optical OFDMA PONs with adaptive dynamic bandwidth allocation", Optics Express, vol. 19, pp. 20557-20570, 2011.

2 Chapter 2: Principles of OFDM, OOFDM and OOFDMA

2.1 Introduction

In this chapter the basic building block for orthogonal frequency division multiplexing (OFDM) is discussed. The chapter continues by including a discussion of the elements included in optical OFDM (OOFDM) focusing on intensity modulation and direct detection (IMDD) and moving on to optical orthogonal frequency division multiple access (OOFDMA). Other definitions used in the thesis such as error vector magnitude (EVM), bit error rate (BER), signal to noise ratio (SNR), extinction ratio (ER), carrier signal power ratio (CSPR) and peak to average power ratio (PAPR) will also be introduced in this chapter.

2.2 What is OFDM?

To achieve spectral efficiency and high data throughput in a modern digital transmission system, multicarrier modulation (MCM) is used, where the data is carried over many lower rate subcarriers. Orthogonal frequency division multiplexing (OFDM) is an example of multicarrier modulation where data is allocated to subcarriers and each subcarrier is modulated on a different frequency. Thus OFDM can also be seen as a special type of Frequency Division Multiplexing (FDM) due to the different subcarriers being equally spaced close to one another in the frequency domain. The advantages of OFDM include being robust against dispersive channels and increased immunity against delays in the transmission system.

OFDM was first introduced in a paper by RW Chang in 1966 [1]. Due to a lack of powerful integrated circuits, OFDM was initially mainly developed for military applications and not for mainstream communication applications. However, in 1969, generation of OFDM using a Discrete Fourier Transform (DFT) was proposed and made OFDM communication a real possibility for use in everyday communication systems [2]. The arrival of broadband digital applications and the maturing of CMOS chip technology in the early 1990s sparked a renewed interest in using OFDM in MCM systems due to OFDM being spectrally efficient and could be easily implemented using digital signal processing and CMOS chip technology. In 1995 a Multi-Input-Multiple-Output (MIMO) OFDM system was reported for the first time [3] and was adopted as the European DAB standard. In 1996 the first paper was published for OFDM fibre-based cable TV [3] but it is only since 2005 that research in optical OFDM came to the forefront of research.

The basic idea of OFDM is to transmit multiple signals simultaneously over a fading channel by modulating the signals onto several subcarriers. A channel is described as fading if over

large distances the signal quality degrades due to mechanisms such as multiple signals destructively interfering with each other. In normal FDM signals are spaced in the frequency domain and the spacing between subcarriers will ensure channels do not overlap. What makes OFDM special as a MCM scheme is that the multiplexing of the subcarriers is done in such a way that the neighbouring subcarriers are ninety degrees out of phase (orthogonal) to each other. From a frequency perspective an OFDM signal compared to a normal FDM signal can be represented by Figure 8 and Figure 9 below.
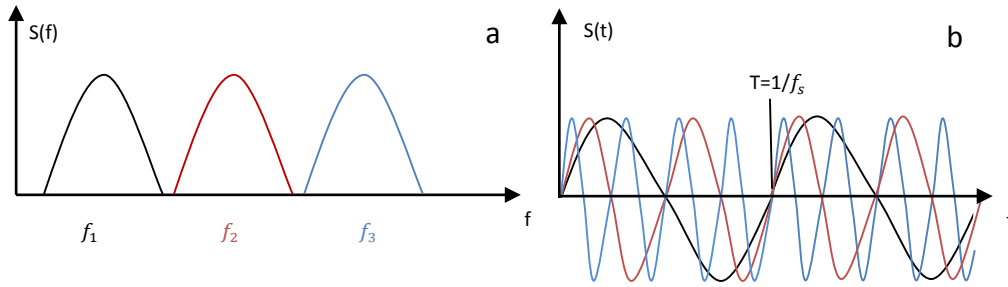
Figure 8: FDM time and frequency representation.
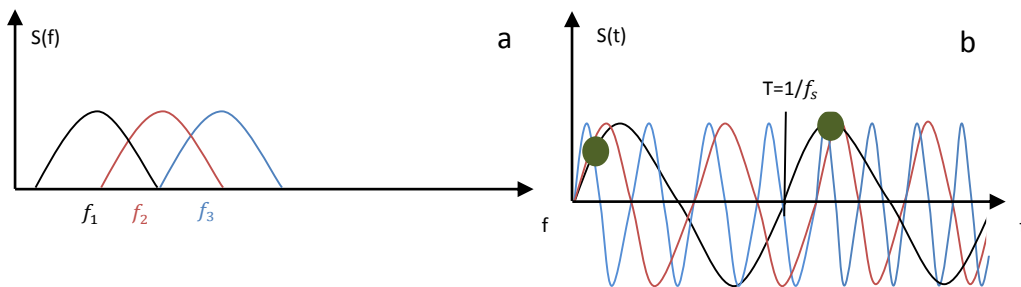
Figure 9: OFDM modulation time and frequency representation.

Comparing Figure 8a and Figure 9a having the same frequency scale, it can be seen that OFDM can offer a 50% or more reduction in the bandwidth of the FDM signal compared to normal FDM in the frequency domain representation. The fact that the neighbouring subcarriers have almost zero amplitude in the frequency domain at the point that intersects with a specific subcarrier's peak, as seen in Figure 9a, makes it possible to retrieve the data from that specific subcarrier even though the subcarrier spectra overlap. This also highlights the drawback of OFDM when considering the time domain representation. As illustrated by the green points in Figure 9b, due to the multiple carriers, there exist points in each symbol interval where the different signals from subcarriers will combine constructively. The constructive addition of the subcarrier amplitudes leads to a high peak that leads to a high power compared to the average power. This high peak to average power of OFDM will be discussed in further detail later in

section 2.10. To show how orthogonally spaced subcarriers or OFDM can be generated, a generic MCM system is presented in Figure 10.
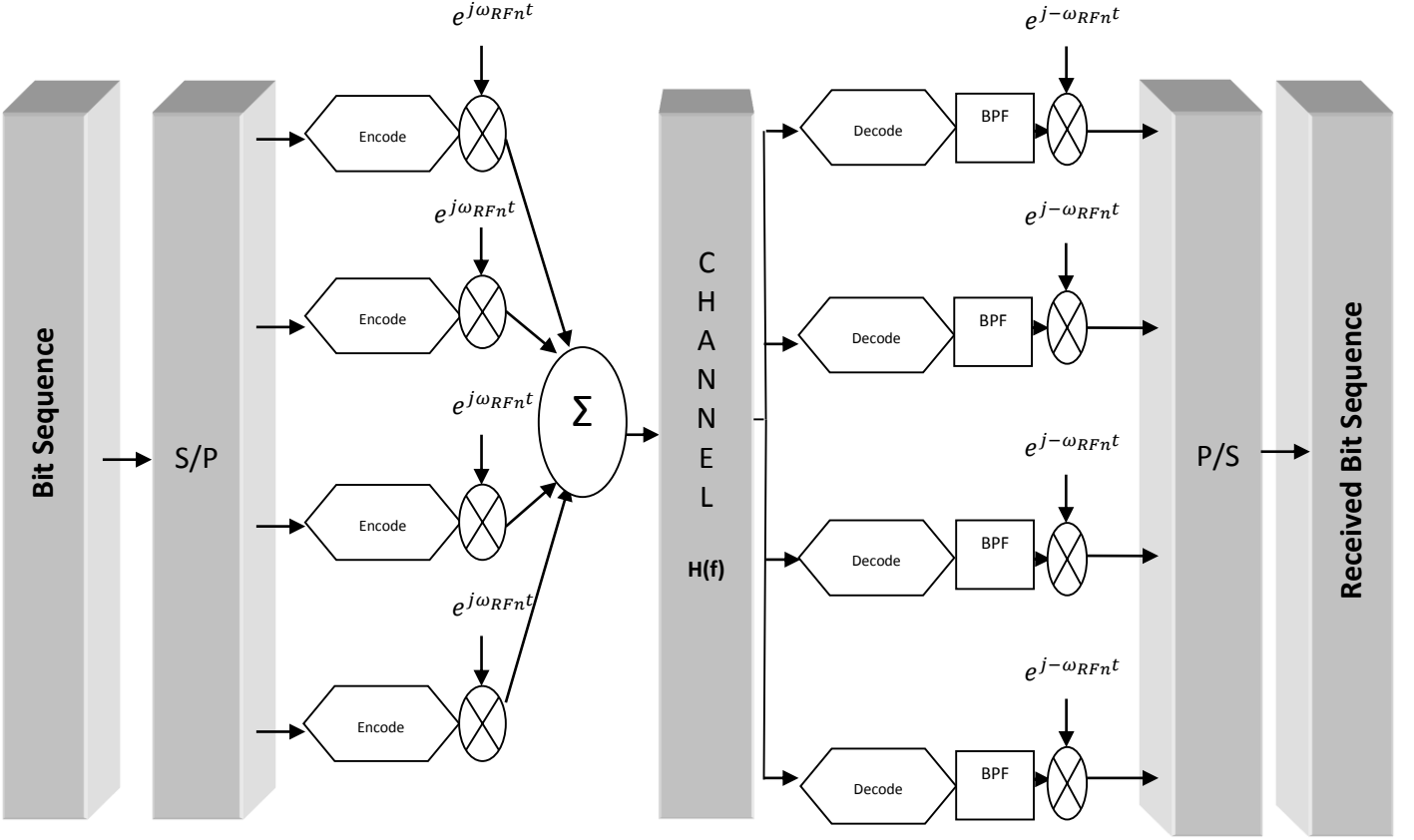
Figure 10: Generic MCM transmission system with n= 1,2,....N

To achieve a MCM scheme, encoded complex numbers needs to be up-converted to a radio frequency (RF) subcarrier frequency and then multiplexed with other subcarriers. When a generic MCM is considered the transmitted signal, $s(t)$, is represented by [4]

$$s(t) = \sum_{i=-\infty}^{\infty} \sum_{k=0}^{Nsc-1} c_{ki} s_k(t - iT_s) \ with \ s_k(t) = \Pi(t)e^{j\omega_k t}$$

$$s(t) = \sum_{i=-\infty}^{\infty} \sum_{k=0}^{Nsc-1} c_{ki} \Pi(t - iT_s)e^{j\omega_k t} \qquad (1)$$

$$\Pi(t) = \begin{cases} 1, (0 < t \le T_s) \\ 0, (t \le 0, t > T_s) \end{cases}$$

where c_{ki} is the ith information symbol at the kth subcarrier, s_k is the waveform for the kth subcarrier, N_{SC} is the number of subcarriers, f_k is the frequency of the subcarrier, T_s is the symbol period and $\Pi(t)$ is the pulse shaping function shown in Figure 11 [4].

17
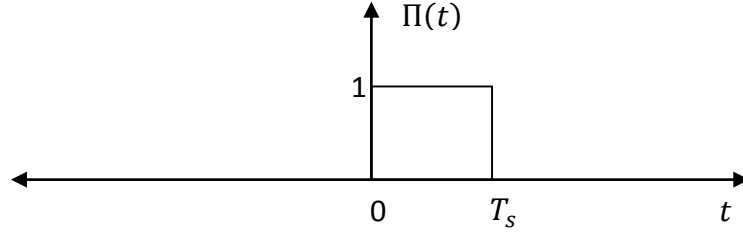
Figure 11: Pulse shaping function.

To ensure a high symbol rate the data bits are encoded using M-ary coding. For real valued QAM c_{ki} is a complex number representing the in-phase (I) and quadrature (Q) components of the information symbol. To ensure real valued transmission c_{ki}, the complex number, is multiplied by its complex conjugate to ensure that the quadrature components of the complex signal cancel each other out. The detected information symbol is represented by [4]

$$c'_{ki} = \frac{1}{T_s}\int_0^{T_s} r(t - iT_s)s_k^* \, dt = \frac{1}{T_s}\int_0^{T_s} r(t - iT_s)e^{-j\omega_k t} \, dt \quad (2)$$

with $r(t)$ the time domain received signal. To improve spectral efficiency of a MCM system the channel spacing can be multiples of the symbol rate with the symbol rate $r = \frac{1}{d}$ and d the duration of the rectangular shaping pulse as shown in Figure 12 . With $d = T_s$ the spacing is $\Delta f = 1/T_s$.
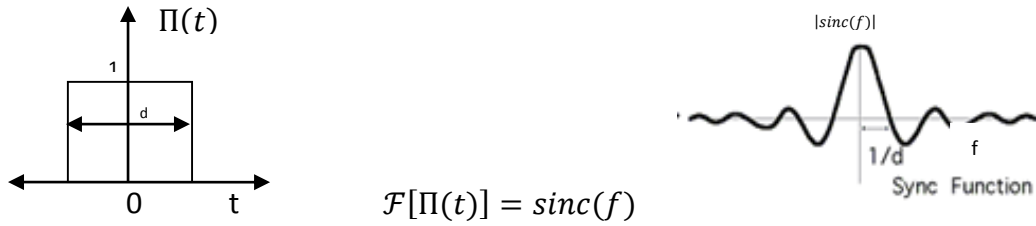
Figure 12: Time and frequency of rectangular pulse.

OFDM employs signals that form orthogonal sets. For the orthogonality condition between two subcarriers to be examined in more detail the correlation, δ_{kl}, between them needs to be shown and is

$$\delta_{kl} = \frac{1}{T_s}\int_0^{T_s} s_k s_l^* \, dt = \frac{1}{T_s}\int_0^{T_s} e^{j2\pi\omega_k t}e^{-j2\pi\omega_l t} \, dt = \frac{1}{T_s}\int_0^{T_s} e^{j2\pi(\omega_k - \omega_l)t} \, dt$$

$$= \frac{1}{T_s}\left[\frac{1}{j(\omega_k - \omega_l)}e^{j(\omega_k - \omega_l)t}\right]_0^{T_s}$$

$$= \frac{1}{T_s} \left[\frac{1}{j(\omega_k - \omega_l)} e^{j(\omega_k - \omega_l)T_s} - \frac{1}{j(\omega_k - \omega_l)} e^{j(\omega_k - \omega_l)0} \right]$$

$$= \frac{1}{j(\omega_k - \omega_l)T_s} \left[e^{j(\omega_k - \omega_l)T_s} - 1 \right] \qquad (3)$$

The correlation can be simplified as shown in appendix A giving:

$$\delta_{kl} = e^{\frac{j}{2}(\omega_k - \omega_l)T_s} (\mathrm{sinc}(\omega_k - \omega_l)\frac{T_s}{2}) \qquad (4)$$

If the condition $(\omega_k - \omega_l) = \pi m \frac{1}{T_s}$ is satisfied with $m = 1,2,3 \dots N_{sc} - 1$ the subcarriers are orthogonal to each other. For equation 1 considering only one OFDM symbol that is made up of one sample from each subcarrier sampling at intervals of $\frac{T_s}{N}$ the nth sample can be represented as

$$s_n(t) = \sum_{k=0}^{N-1} c_k \Pi(t - T_s) e^{j\omega_k t} = \frac{1}{N} \sum_{k=0}^{N-1} c_k e^{j\omega_k \frac{nT_s}{N}} \qquad (5)$$

If we replace ω_k with $\omega_k = \frac{k}{T_s}$, which meets the orthogonality condition, we can rewrite equation 5 as

$$s_n(t) = \frac{1}{N} \sum_{k=0}^{N-1} c_k e^{j\frac{k}{T_s}\frac{nT_s}{N}} = \frac{1}{N} \sum_{k=0}^{N-1} c_k e^{j\frac{kn}{N}} \quad (6) \text{ and}$$

$$x(n) = \frac{1}{N} \sum_{k=0}^{N-1} X_d(k) e^{j\frac{k}{N}n} \qquad (6b)$$

and show that the OFDM waveform can be created using a IDFT when comparing equation 6a and the definition of the inverse discrete Fourier transform (IDFT) in equation 6b. Equation (6a, 6b) demonstrates that the modulation and multiplexing of a large number of OFDM subcarriers can be achieved using an IDFT.

2.3 Bit Encoding/Decoding

2.3.1 Bit Encoding

To improve information throughput in an OFDM system, bit encoding as illustrated in Figure 13 is used. For digital message representation at baseband an amplitude-modulated pulse train is used and may be expressed as [5]

$$x(t) = \sum_i a_i p(t - id) \quad (7)$$

with a_i a set of M discrete amplitudes representing the ith symbol for an infinite number of i.
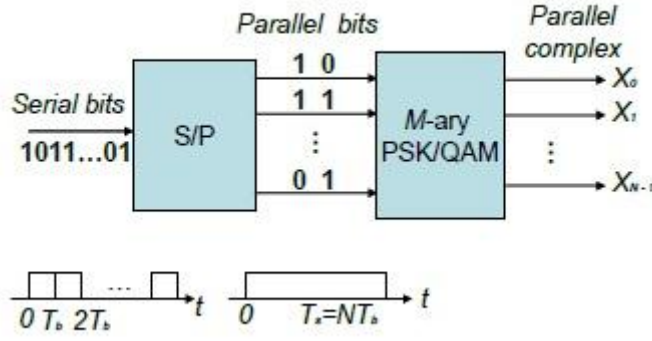
Figure 13: Bit encoding process.

When the pulse $p(t)$ is represented by a rectangular pulse as shown in Figure 12 with a pulse duration equal to d, the message can be recovered by sampling at intervals of d. The signalling rate or symbol rate is $r = \frac{1}{d}$ measured in symbols per second or baud. With M=2 the bit rate is $r_b = \frac{1}{T_b}$ usually measured in bits per second (bps). For quaternary coding 4 amplitude levels are used to code two bits, d = $2\times T_b$ and r = $r_b/2$. When message bits are grouped together it is advantageous to use a grey code scheme where only one bit changes from one level to the next and thus reduces the probability of an error due to noise. When blocks of n message bits are represented by an M-level waveform with $M = 2^n$ it is called M-ary coding. For each pulse corresponding to $n = log_2 M$ bits the signalling rate is r=$r_b/log_2 M$ as indicated in section 14.1 of [4].

The I component of the M-ary digital signal is represented as [5]

$$x_i(t) = \sum_k a_k p(t - kd) \ for \ a_k = 0,1, \dots , M - 1 \quad (8)$$

For amplitude shift keying (ASK) also known as on-off keying (OOK) the Q component is set to zero. The bandwidth is $B_T \approx r$ with r the signalling rate. The pulse is a rectangular shape and the frequency spectrum a sinc function with a bell curve shape as shown in Figure 12 from $f_c - r$ to $f_c + r$ and we assume most of the power is contained within $f_c = \pm r/2$ [4]. For M-ary ASK $B_T=r_b/log_2 M$. The modulation speed or spectral efficiency is defined as $r_b/B_T=log_2 M$ bps/Hz. Quadrature Amplitude (QAM) can be described as a form of quadrature carrier multiplexing where 2 messages $m_1(t)$ and $m_2(t)$ are transmitted on the same carrier frequency using two quadrature carriers $A_c(t)cos\omega_c t$ and $A_c(t)sin\omega_c t$. If $x_c(t) =$

$A_c[x_i(t)\cos(\omega_c t + \theta) - x_q(t)\sin(\omega_c t + \theta)]$ is modified with the phase θ set to zero, the transmitted signal is represented by [5]

$$u(t) = A_c m_1(t)cos\omega_c t + A_c m_2(t)sin\omega_c t$$
$$u(t) = A_{mc} g_T(t)cos\omega_c t + A_{ms} g_T(t)sin\omega_c t \quad for \; m = 1,2,\ldots.,M \qquad (9)$$

If each carrier is amplitude modulating with M= 4 PAM the output constellation will be 16-QAM. QAM can be viewed as a combined digital amplitude and digital phase modulation with [5]

$$u_{mn}(t) = A_m g_T(t)cos(\omega_c t + \theta_n) \; for \; m = 1,2,\ldots,M_1 \; and \; n = 1,2,\ldots,M_2 \; (10)$$

The digital message signal representation is [5]

$$m_1(t) = x_i(t) = \sum_k a_{2k} p(t - kd) \; and \; m_2(t) = x_q(t) = \sum_k a_{2k+1} p(t - kd)$$
$$with \; d = \frac{1}{r} = 2 \times T_b \quad (11)$$

The spectral efficiency for binary QAM is $r_b/B_T = log_2 M$ bps/Hz with M = 4 is 2 bps/Hz compared with 1 bps/Hz for ASK, thus QAM achieves twice the modulation speed of ASK. Digital phase modulation methods where a zero and one are represented by different phases are referred to as binary phase-shift keying (BPSK) or phase-reversal keying (PRK). An M-ary PSK signal is [5]

$$x_c(t) = A_c \sum_k \cos(\omega_c t + \theta + \varphi_k) P_D(t - kd) \qquad (12)$$

With the quadrature form [5]

$$x_i(t) = \sum_k I_k P_D(t - kd) \quad x_q(t) = \sum_k Q_k P_D(t - kd)$$
$$with \; I_k = cos\varphi_k \; and \; Q_k = sin\varphi_k \qquad (13)$$

To ensure the largest possible phase modulation $\varphi_k = \frac{\pi(2a_k + N)}{M}$ with $a_k = 0,1,\ldots\ldots,M-1$
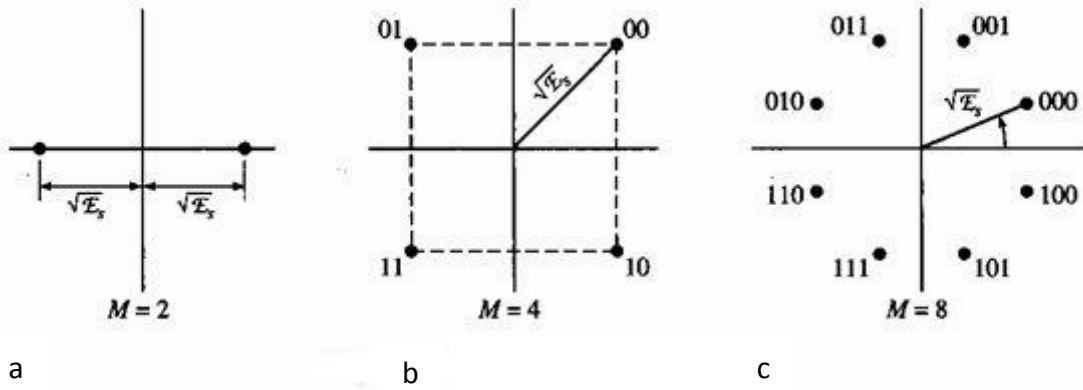
Figure 14: Constellation diagrams for PSK [5].

PSK with M= 4 - also known as quaternary PSK (QPSK) - shown in Figure 14b, is equivalent to binary QAM if N=1. Binary QAM can be considered to be two BPSK signals (in Figure 14a) on quadrature carriers. M-ary PSK has a constant amplitude envelope compared with M-ary ASK because all the information is modulated in the phase. PSK has better power efficiency due to a lack of discrete carrier component but spectral efficiency is the same as that of ASK [4]. When QAM is viewed as a combined amplitude and phase modulation as in equation 10 the symbol rate is [5]

$$r = r_b/log_2 M_1 M_2 \qquad (14)$$

For the 16-QAM described in equation 10 the spectral efficiency is 4 bps/Hz.

2.3.2   Bit Decoding

To demodulate and detect the transmitted QAM signal the input to the detector is correlated with the two basic functions corresponding to each of the quadrature carriers. The basic functions are represented by [5]

$$\psi_1(t) = \sqrt{\frac{2}{E_g}} g_T(t)\cos(\omega_c t + \widehat{\Phi})$$

$$\psi_2(t) = \sqrt{\frac{2}{E_g}} g_T(t)\sin(\omega_c t + \widehat{\Phi}) \quad (15)$$

When a signal is transmitted over a channel and demodulated using a correlation or matched filter demodulator a vector $r = (r_1, r_2, \ldots, r_N)$ contains the signal information. The output of the correlators is sampled and passed to a detector that is optimised by adhering to the decision criterion of maximum a posteriori probability (MAP) criterion as mentioned in section 7.5.3 in [5].

First we look at carrier amplitude demodulation. The received signal is expressed as [5]

$$r(t) = A_m g_T(t)\cos(\omega_c t) + n(t) \quad (16)$$

By cross-correlating the signal with the basic function we obtain [5]

$$r = \int_{-\infty}^{\infty} A_m g_T(t)\cos(\omega_c t)d(t)\sqrt{\frac{2}{E_g}}g_T(t)\cos(\omega_c t) + \int_{-\infty}^{\infty} n(t)\psi(t)dt$$

$$= A_m\sqrt{\frac{2}{E_g}} + n \quad (17)$$

The input to the detector consists of two sampled components with the energy of each of the sampled components half the energy of the pulse $g_T(t)$. The correlation over one time period is [5]

$$r_1 = \int_0^T r(t)\psi_1(t)dt$$
$$r_2 = \int_0^T r(t)\psi_2(t)dt \quad (18)$$

By using the same method of carrier amplitude demodulation to cross-correlate the input of the QAM signal we represent the estimated carrier phase as $\widehat{\Phi}$ and the two sampled cross correlated signals as [5]

$$r_1 = A_{mc}\sqrt{E_s}\cos(\varphi - \widehat{\Phi}) + A_{ms}\sqrt{E_s}\sin(\varphi - \widehat{\Phi}) + n_c\sin\widehat{\Phi} - n_s\cos\widehat{\Phi}$$
$$r_2 = A_{mc}\sqrt{E_s}\sin(\varphi - \widehat{\Phi}) + A_{ms}\sqrt{E_s}\cos(\varphi - \widehat{\Phi}) + n_c\sin\widehat{\Phi} - n_s\cos\widehat{\Phi} \quad (19)$$

The phase difference between the signal phase φ and the estimated carrier phase $\widehat{\Phi}$ causes the desired $A_{ms}\sqrt{E_s}$ and $A_{mc}\sqrt{E_s}$ components to reduce by a factor of $\cos(\varphi - \widehat{\Phi})$. It also causes unwanted components in the baseband signal due to leakage of the quadrature signal components into the signal spectrum. The reduction in signal components can be avoided by estimating the phase in such a way that $(\varphi - \widehat{\Phi})$ is either zero or very small as mentioned in section 7.5.6 in [5]. Then the signal is detected with the optimum detector that computes the distance metric defined as the smallest distance between two points to ensure maximum likelihood of detecting the correct symbol and is represented as [5]

$$D(r, s_m) = |r - s_m|^2 \quad (20)$$

Depending on the modulation format (16, 32, 64, 128 or 256 quadrature amplitude modulation (QAM)) used to encode n blocks of x bits a specific block of x bits can be retrieved by matching the detected symbol to the bit sequence of length x.

2.4 DTFT/IDFT

The discrete-time Fourier transform (DTFT) is defined as [6]

$$X(\Delta\omega) = \Delta t \sum_{n=0}^{N-1} x(n\Delta t) \, e^{-j\Delta\omega n\Delta t} \quad (21)$$

and transforms a discrete time signal into a frequency domain signal. For digital Fourier analysis the time signal is sampled at discrete intervals so the angular frequency difference between frequency components is $\Delta\omega$ and with k the index of discrete frequency components the angular frequency is $\Delta\omega = k\Delta\omega$. The n is the time sample index with $n = 0,1,2,....,N-1$. N is the number of samples considered and Δt is the time between samples (sampling interval or period). The inverse of the sampling period yields the sampling frequency ($\omega_s = \frac{1}{\Delta t}$). $N\Delta t$ corresponds to the window length [6]. The $\Delta\omega$ refers to the sample interval (frequency resolution) in frequency domain and is equal to $\frac{1}{N\Delta t}$. The DFT has the form [6]

$$X_d(k\Delta\omega) = \Delta t \sum_{n=0}^{N-1} x(n\Delta t) \, e^{-jk\Delta\omega n\Delta t} \quad (22)$$

And the inverse DFT is [6]

$$x(n\Delta t) = \Delta\omega \sum_{k=0}^{N-1} X_d(k\Delta\omega) \, e^{jk\Delta\omega n\Delta t} \quad (23)$$

If we set $\Delta t = 1$ and $\Delta f = \frac{1}{N}$ the DFT becomes [6]

$$X_d(k) = \sum_{n=0}^{N-1} x(n) \, e^{-j\frac{2\pi k}{N}n} \quad (24)$$

And the IDFT with $\Delta\omega = \frac{2\pi}{N}$ becomes

$$x(n) = \frac{2\pi}{N} \sum_{k=0}^{N-1} X_d(k) \, e^{j\frac{2\pi k}{N}n} \quad (25)$$

2.5 FFT/IFFT

In practice the IDFT is implemented using the IFFT. The FFT is a powerful tool to transform physically realisable time domain waveforms to the frequency domain. The FFT is an efficient algorithm that calculates the DFT of a signal by reducing the number of calculations from N^2 to $\frac{N}{2}\log_2 N$ with N being the number of elements in the DFT. The number of elements is constrained to $N = 2^r$ with r an integer to ensure it is divisible by two. Thus we ensure N to be even to ensure an even number of pairs of DFTs. The basic idea of a FFT is to factorise an N-point DFT into 2N-point DFTs until the DFT consists of 2 points. The DFT can be described in terms of being a matrix-vector product of a vector space with complex n-vectors [7]. We rewrite the DFT as [7]

$$X_d(k) = \sum_{n=0}^{N-1} x_n \, \omega_N^{kn}$$

$$\text{With } \omega_N = e^{\frac{-j2\pi}{N}} = \cos\left(\frac{2\pi}{N}\right) - j\sin\left(\frac{2\pi}{N}\right) \text{ and } \omega_N{}^2 = e^{\frac{-2j2\pi}{N}} = e^{\frac{-j2\pi}{\frac{N}{2}}} \qquad (26)$$

The DFT in matrix-vector terms is [7]

$$X_d = F_N x \qquad (27)$$

Where $F_N = (f_{pq})$ and $(f_{pq}) = \omega_N^{pq} = e^{-j\frac{2\pi pq}{N}}$ with p the row position and q the column position. For a N=4 DFT matrix F_4 is [7]

$$F_4 = \begin{bmatrix} 1 & 1 & 1 & 1 \\ 1 & -j & -1 & j \\ 1 & -1 & 1 & -1 \\ 1 & j & -1 & -j \end{bmatrix} \qquad (28)$$

The 4-by-4 permutation matrix is obtained by permuting the columns of the identity matrix. The matrix is permuted in such a way that it groups even indexed columns first and then the odd index columns. The permutation is represented by [7]

$$\Pi_4 = \begin{bmatrix} 1 & 0 & 0 & 0 \\ 0 & 0 & 1 & 0 \\ 0 & 1 & 0 & 0 \\ 0 & 0 & 0 & 1 \end{bmatrix} \qquad (29)$$

Then

$$F_4\Pi_4 = \begin{bmatrix} 1 & 1 & 1 & 1 \\ 1 & -1 & -j & j \\ 1 & 1 & -1 & -1 \\ 1 & -1 & j & -j \end{bmatrix} \qquad (30)$$

The permutation of F_4 is a 2-by-2 block matrix and define it as [7]

$$\Omega_2 = \begin{bmatrix} 1 & 0 \\ 0 & -j \end{bmatrix} \text{ and } F_2 = \begin{bmatrix} 1 & 1 \\ 1 & -1 \end{bmatrix} \text{ then } F_4\Pi_4 = \begin{bmatrix} F_2 & \Omega_2 F_2 \\ F_2 & -\Omega_2 F_2 \end{bmatrix} \quad (31)$$

The definition shows that an N-point DFT can be represented by m $\frac{N}{2}$-point DFTs. Mathematically m $\frac{N}{2}$-point DFTs represented as

$$X_d[k] = \sum_{n=0}^{N-1} x(n) e^{-j\frac{2\pi k}{N}n} = \sum_{n=0}^{N-1} x[n] \omega_N^{kn}$$

$$= \sum_{m=0}^{\frac{N}{2}-1} x[2m] \omega_{\frac{N}{2}}^{km} + \omega_N^k \sum_{m=0}^{\frac{N}{2}-1} x[2m+1] \omega_{\frac{N}{2}}^{km} \qquad (32)$$

Thus $X_d[k]$ has been expressed in terms of two $\frac{N}{2}$-point DFTs that is

$$X[k] = X_{even}[k] + \omega_N^k X_{odd}[k] \quad (33)$$

The equation above is graphically represented in Figure 15 with a radix-2 FFT with N=8 structure as derived in appendix B.
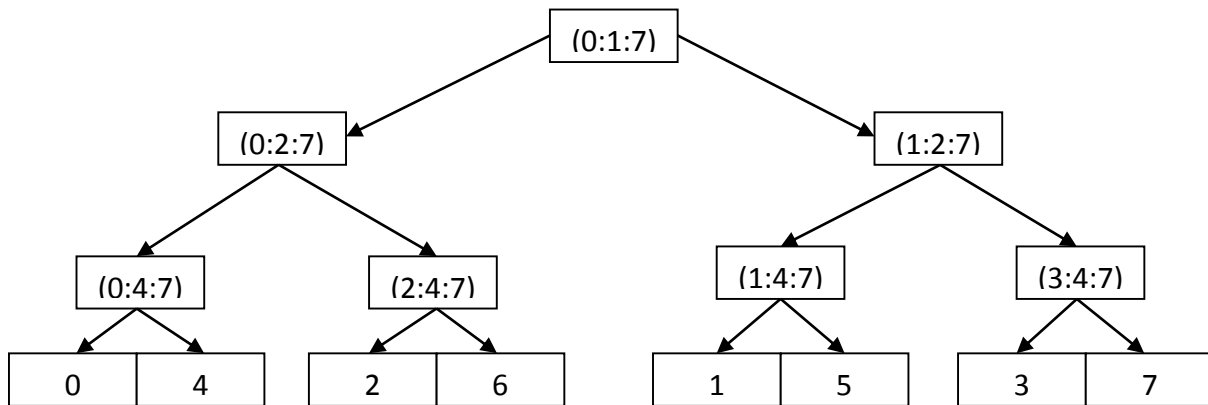
Figure 15: Radix-2 FFT with N=8 structure.

2.6 Generation of complex and real-valued OFDM signals

To generate real-valued OFDM signals the IFFT arrangement is shown in Figure 16. N_s is the total number of IFFT sample points. By using Hermitian symmetry the number of data carrying subcarriers is reduced to $N_{sc} = (N_s/2) - 1$ and the output of the IFFT will be real-valued. This reduces the complexity of transmission because there is no need for I-Q modulation. In I-Q modulation the complex valued output of the IFFT is converted into a real-valued signal using an RF circuit and separate modulation of the I and Q components of the signal is performed. C_k is the complex transmitted information symbol representing x number of bits with x dependent on the specified modulation format for the kth subcarrier and f_k the frequency for the kth subcarrier which for orthogonality between subcarriers needs to correspond to $\Delta f = f_k - f_{k-1} = \frac{1}{T_s}$ with T_s the sampling period. Thus a real valued signal at baseband can be represented as

$$s_B(t) = \sum_{k=-\frac{1}{2}N_{sc}}^{\frac{1}{2}N_{sc}} C_k e^{j2\pi\frac{k}{T_s}t} \quad (34)$$

with the first subcarrier and its complex conjugate pair at $k = N_s/2$ set to zero to ensure no DC component in the baseband OFDM signal. To relate the input of the IFFT to positive and negative parts of the signal the zero frequency needs to be shifted to the centre of the spectrum by relating the input of the IFFT and the subcarrier frequency index k from $-N/2$ to $(N/2)$-1.
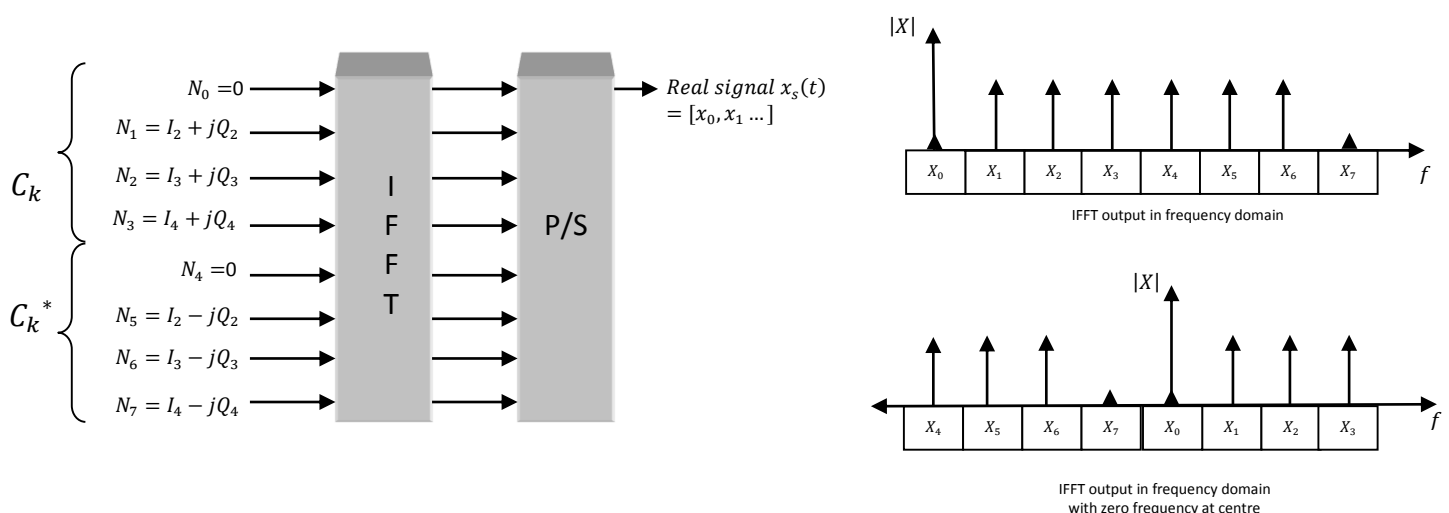
Figure 16: Generation of Real-valued OFDM.

To generate complex-valued signals the input to the IFFT is as shown in Figure 17. For complex OFDM Hermitian symmetry is not needed and the number of data carrying subcarriers is $N_{sc} = (N_s) - 1$ and only the first input to the IFFT needs to be set to zero to ensure no DC component in the output time domain signal. The input paired with the first input of the IFFT does not need to be zero but can be used to carry data as the output signal is complex in nature.
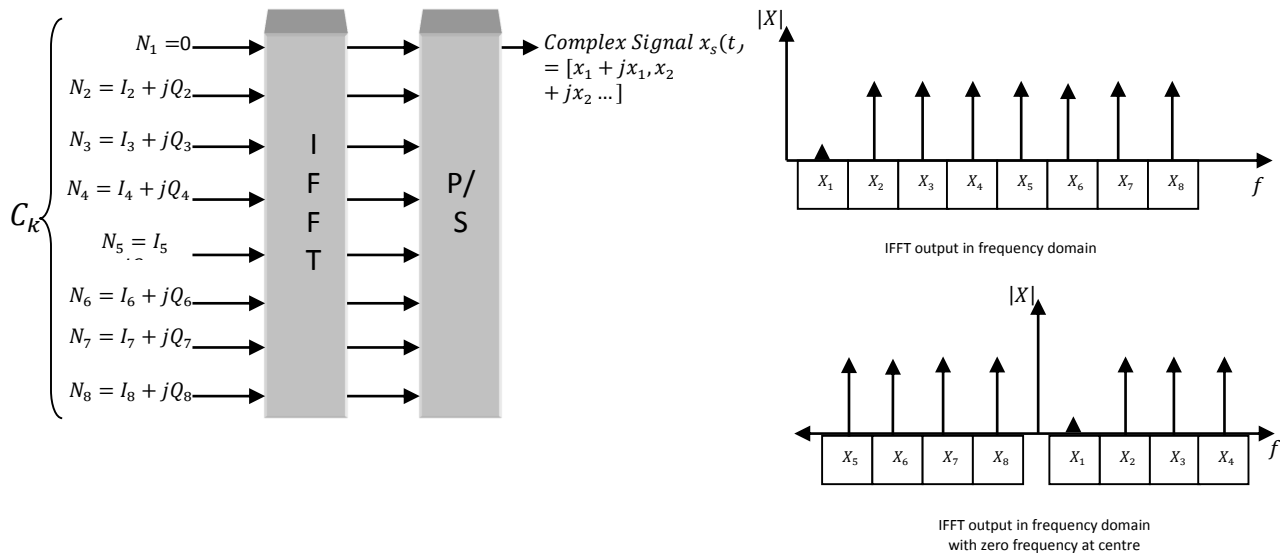
Figure 17: Generation of Complex OFDM

2.7 Cyclic prefix
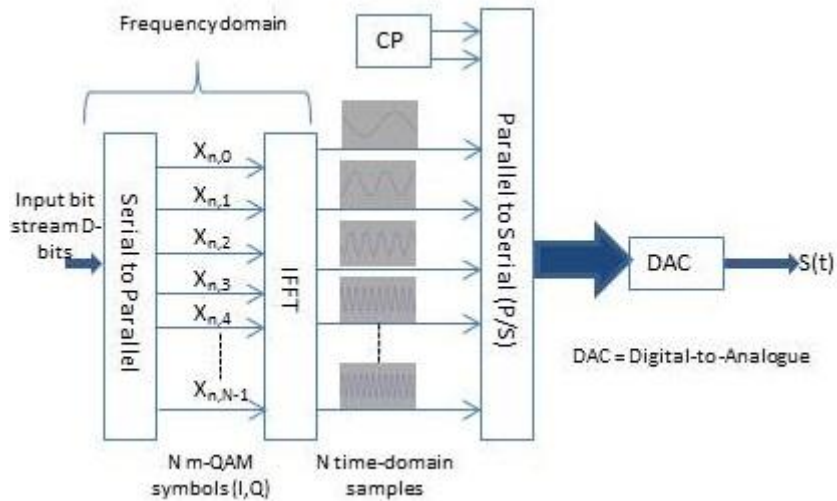
Figure 18: Cyclic Prefix (CP) insertion in OFDM system.
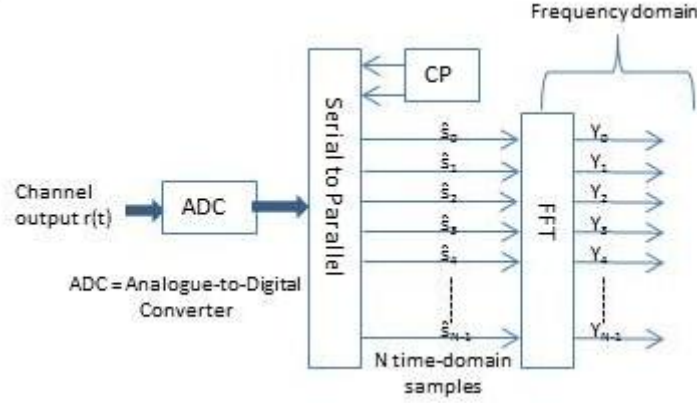
Figure 19: Cyclic Prefix (CP) removal in OFDM system.

The group velocity associated with the fundamental mode is frequency dependent, causing group-velocity dispersion (GVD). To avoid inter-symbol interference (ISI) between OFDM symbols due to the GVD broadening of the propagating light pulses in an OFDM system, a cyclic prefix (CP) is inserted to mitigate the delay introduced by a dispersive channel as shown in Figure 18 above. When the DFT operation is performed on the OFDM symbols after the cyclic prefix have been removed, as shown in Figure 19, the time shift in the symbol translates into a phase shift. It is important to note that the CP is always a copy of the original OFDM symbol to ensure that there is no abrupt change in the phase between the CP and symbol that would cause the signal to get distorted. To correct this phase shift, channel equalization is performed after the DFT operation in the receiver. This not only compensates for the dispersion-induced phase shift but also for any other phase shift which arises in the channel. Thus for a large enough CP and proper equalisation, ISI and inter-carrier interference (ICI) can be successfully compensated. The extent of the pulse broadening i.t.o. time delay that leads to ISI is [20]

$$\Delta T = DL\Delta\lambda \quad (35)$$

with D is the dispersion parameter in nm/(ps.km) and L the length of transmission link in km and $\Delta\lambda$ the bandwidth of the signal in nm. For a point-to-point (PTP) system the subcarriers are orthogonally placed and experience a delay of ΔT, calculated in equation 35, after the subcarriers propagated through the fibre. Assume a scenario with 4 subcarriers in the PTP system. We show the simple system representation for upstream transmission in Figure 20:
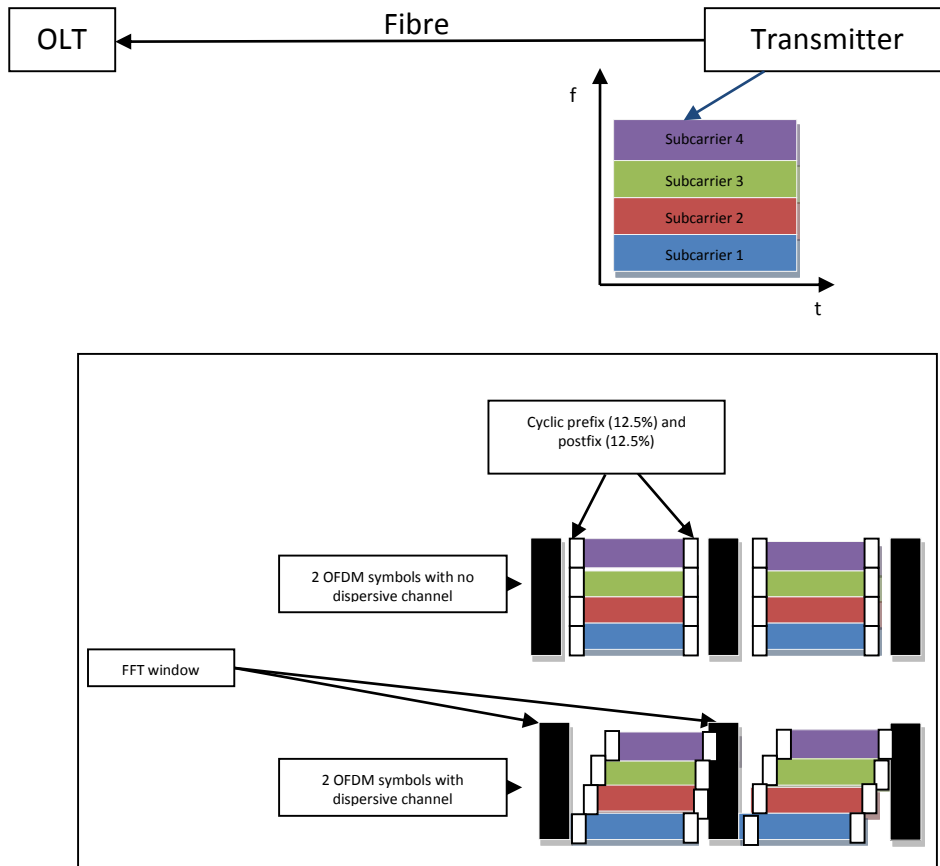
Figure 20: System with Cyclic Prefix (CP) with and without a dispersive channel.

with the insert representing 2 OFDM symbols with 4 subcarriers with CP before and after transmission through the fibre. Each colour represents a subcarrier. The black blocks represent the beginning and the end of the FFT windows. The subcarrier data of symbol one represented by the purple will start to interfere with the blue of symbol two representing the data on the first subcarrier. When the dispersive effect on the channel becomes too severe ISI will occur. The time delay between subcarriers is shown in Figure 21.
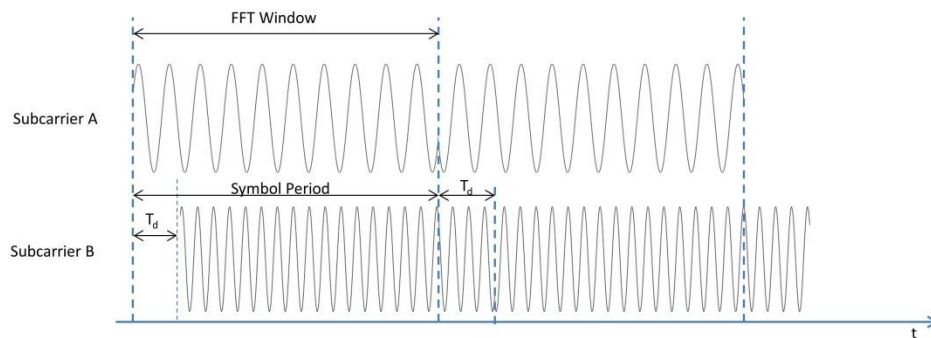
Figure 21: Fast and slow subcarriers.

It is can be seen from Figure 21 that subcarrier B suffers from a time delay compared to subcarrier A and if the time delay is bigger than the CP the symbols in that slow subcarrier will suffer from ISI. This delay will cause subcarrier B to have incomplete data in the FFT window which will cause the subcarrier orthogonality to be destroyed when the FFT operation is applied to the subcarriers to demodulate and recover the data of each subcarrier. The ISI leads to the destruction of orthogonality between subcarriers. The ISI is caused by delays between subcarriers due to the frequency dependence of the refractive index of the fibre and multipath effects. Thus if ISI can be prevented ICI can be prevented and subcarrier orthogonality can be maintained. To combat ISI the CP length can be increased but this will cause a high overhead of data that cannot be used.

2.8   Serialisation

After inserting the CP into each OFDM symbol, the OFDM signal is serialised through a parallel to serial converter and a number of low-speed parallel subcarrier signals are converted into a high-speed serial signal. This process is the inverse of the serial to parallel conversion in the OFDM receiver as shown in Figure 22.
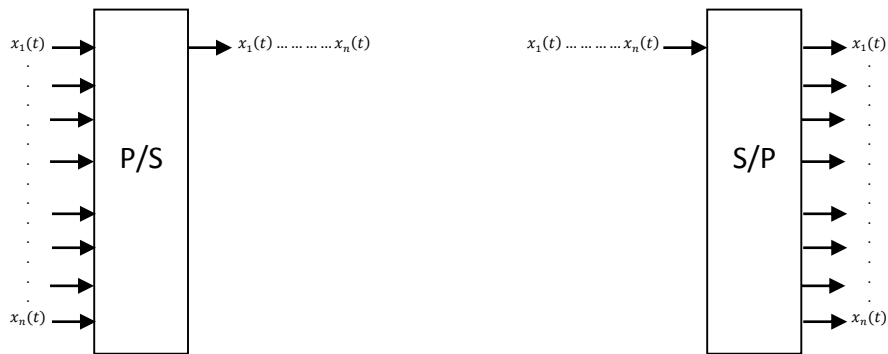
Figure 22: S/P and P/S conversion.

2.9   D/A and A/D conversion, quantisation and clipping

The Digital to Analogue Converter (DAC) and Analogue to Digital Converter (ADC) are important components in modern digital transmission systems. They are limiting factors with regards to overall system performance due to limited sampling speed, quantization noise and clipping noise. The DAC converts the output OFDM signal from the IFFT to an analogue signal that can be modulated unto a carrier for transmission. OFDM signals suffer from high Peak-to-Average Power Ratio (PAPR) as discussed in section 2.2 and this poses a problem for

the DAC conversion due to the limited resolution. The first step of DAC conversion is to clip the signal levels to a specified clipping ratio (CR). The maximum amplitude of the signal is defined as $\Lambda = \sqrt{\xi P_m}$ with ξ the clipping ratio and P_m the average signal power [8]. The clipping ratio can be represented by [8]

$$\xi = \frac{\Lambda^2}{P_m} \ and \ \xi_{dB} = 10 \log_{10} \frac{\Lambda^2}{P_m} \ then \ \Lambda = \sqrt{10^{\frac{\xi_{dB}}{10}} P_m} \quad (36)$$

And the clipping process described mathematically by [8]

$$A_{clipped}(t) = \begin{cases} A_E(t) & |A_E(t)| \leq \Lambda \\ \Lambda e^{j \ arg|A_E(t)|} & |A_E(t)| > \Lambda \end{cases} \quad (37)$$

Clipping helps to improve utilisation of the limited resolution of the DAC by reducing the OFDM signal's PAPR. This reduction in PAPR allows for higher average powers to be transmitted thus improving the SNR at the receiver. If the clipping ratio is too small then the maximum amplitude will be small and will cut into the signal causing degradation of performance. If the clipping ratio is too large the quantization noise will increase and degrade the performance due to the number of quantization steps being too low for the range of signal. Thus the more quantization steps there are for a given range the more the quantization noise will reduce. Mathematically quantization can be described as [8]

$$Q(A_s) = \sum_{i=\frac{L}{2}+1}^{\frac{L}{2}} \frac{\hat{A}_i + \hat{A}_{i-1}}{2} g(A_s, \hat{A}_i, \hat{A}_{i-1}) \ with \ g(x, x_1, x_2) = \begin{cases} 1, x_1 \leq x < x_2 \\ 0, otherwise \end{cases} \quad (38)$$

with A_s the sampled input at the sampling rate r_s and $\hat{A}_i$ and $\hat{A}_{i-1}$ representing the ith and $(i-1)$th threshold levels. L is the number of quantization levels and related to quantization bits by $L = 2^b$ with b the quantization bits. The step size is $\frac{2\Lambda}{L}$ in the dynamic signal range of $[-\Lambda, \Lambda]$.

2.10 PAPR, ER and CSPR

OFDM signals suffer from a high peak to average power ratio (PAPR). In the time domain, a multicarrier signal is the sum of many narrowband signals. At some time instances, this sum is large and at other times it is small, which means that the peak value of the signal is substantially

larger than the average value. The superposition of subcarriers that cause the high PAPR is a problem in systems with a high number of subcarriers. Mathematically the PAPR is represented as [9]

$$PAPR = \frac{max[x(t).x^*(t)]}{E[x(t).x^*(t)]} \ with \ PAPR_{dB} = 10log_{10}(PAPR) \ (39)$$

with $E[x(t).x^*(t)]$ being the mean or expected value of the power of $x(t)$. As shown in appendix C, the PAPR for an OFDM signal is equal the number of subcarriers, N [9]. Thus for a system with 32 subcarriers assuming equal modulation formats on all subcarriers the PAPR for OFDM is calculated in appendix C and shows the tendency for OFDM to have high PAPR. The maximum of the signal amplitude after the DAC will be equal to the maximum amplitude determined by the clipping ratio as defined in equation 36. Thus the PAPR for a OFDM signal after the DAC can be written as

$$PAPR = \frac{\Lambda^2}{E[s(t).s^*(t)]} \ with \ E[s(t).s^*(t)] = mean(|s(t)|^2) \quad (40)$$

The extinction ratio ER can be defined as

$$ER = \frac{mean(P1)}{mean(P2)} \ with \ \begin{cases} P1 = \sum_{i=0}^{K1} s(i\Delta T)^2 \geq \bar{P} \\ P2 = \sum_{J=0}^{K2} s(J\Delta T)^2 < \bar{P} \end{cases} \quad (41)$$

with $\bar{P}$ the average optical power and the sampling duration [10] . When comparing a PTP system compared with a multi ONU system there are a few things that are needed to be considered:

The first ONU of the multi ONU system compared to a PTP system with 15 data-carrying subcarriers will have less data on its 15 subcarriers. The mean power and peak power for the one ONU of the multi ONU system will be reduced compared to a PTP system due to the reduced number of time domain narrowband signals considered. The PAPR is reduced for a smaller peak-to-peak range of the signal entering the DAC. Thus for a multi ONU system we can expect a smaller DAC time step due to the smaller peak-to-peak range. This argues the case for reduced DAC/ADC parameters in multi ONU systems.

For an ideal case we look at the ER. The ER for the first ONU for a 15 ONU system will be increased compared to the PTP system due to a lower average optical power for the one ONU in the 15 ONU case. For an ideal modulator the signal $s(t)$ becomes $\sqrt{(s(t) + min(s(t)))}$ with

the addition of $\min(s(t))$ representing the biasing of the signal. The signal $s(t)$ will have a minimum of $-\Lambda$ due to the clipping on the signal in the DAC. Thus we can rewrite the ER as

$$ER = \frac{mean(P1)}{mean(P2)} \quad with \begin{cases} P1 = \sum_{i=0}^{K1} s(i\Delta T)^2 \geq \bar{P} \\ \overline{} \\ P2 = \sum_{j=0}^{K2} s(j\Delta T)^2 < \bar{P} \end{cases}$$

$$with \ \bar{P} = mean\left[|s_{optical}(t)|^2\right]$$

$$and \ s_{optical}(t) = \sqrt{s_{electrical}(t) + min(s_{electrical}(t))} = \sqrt{s_{electrical}(t) + (-\Lambda)} \quad (42)$$

From equation 41 we get

$$\Lambda^2 = PAPR.\,mean(|s_{electrical}(t)|^2) \ and \ \Lambda = \sqrt{PAPR.\,mean(|s_{electrical}(t)|^2)} \quad (43)$$

resulting in the relationship between ER and PAPR to be

$$ER = \frac{mean\left(\sum_{i=0}^{K1} s(i\Delta T)^2 \geq mean\left[\left|\sqrt{s_{electrical}(t) - (\sqrt{PAPR.mean(|s_{electrical}(t)|^2)})}\right|^2\right]\right)}{mean\left(\sum_{j=0}^{K2} s(j\Delta T)^2 < mean\left[\left|\sqrt{s_{electrical}(t) - (\sqrt{PAPR.mean(|s_{electrical}(t)|^2)})}\right|^2\right]\right)} \quad (44)$$

The carrier to signal power ratio (CSPR) is defined as the ratio between the main optical carrier and total power of OFDM subcarriers. The CSPR can be calculated as [10]

$$CSPR = |A_0|^2 / \sum_{k=-\frac{1}{2}N_{sc}}^{\frac{1}{2}N_{sc}} |C_k|^2 \quad (45)$$

where A_0 and $|C_k|$ are the amplitudes of the carrier and the data on the kth subcarrier, respectively [10]. The CSPR will increase for a ONU transmitter with data only on one subcarrier, for example in the multi ONU system, compared to a PTP system's CSPR due to having more subcarriers. For the received electrical signal the CSPR of a multi ONU OOFDMA PON system will increase with the number of ONUs increasing due to the carrier power being the addition of all the carrier powers from the different ONUs, thus $|A_0|^2$ becomes $|NA_0|^2$ with N the number of ONUs. Thus the CSPR for a multi ONU system is [10]

$$CSPR = |NA_0|^2 / \sum_{l=1}^{N} \sum_{k=-\frac{1}{2}N_{sc}}^{\frac{1}{2}N_{sc}} |C_k|^2 \quad (46)$$

2.11 Coherent OOFDM and IMDD OOFDM

To investigate optical orthogonal frequency division multiplexing (OOFDM) in detail the first step is to look at the basic operation of nonlinearly mapped direct detection OFDM (NM-DD-OFDM) [11]. The mapping between the baseband OFDM electric field and the optical field at the transmitter is nonlinear due to intensity modulation instead of a coherent signal generation resulting in the optical spectrum not being an exact replica of the baseband OFDM signal. The electrical baseband signal can be represented as shown in equation 34. If we assume a directly modulated distributed feedback (DFB) laser the output optical field is [11]

$$E(t) = A(t)e^{j(\omega_0 + \varphi)t} \quad (47)$$

with $A(t)$ the amplitude, φ the phase of the DFB laser emission and ω_0 the carrier frequency. $A(t)$ is represented by [12]

$$A(t) = \sqrt{P(t)} = \sqrt{I_{DC} + \alpha_{scaling}Re(e^{j\omega_{IF}t}.S_B(t))} \quad (48)$$

where $P(t)$ is the output optical intensity or power. For an ideal intensity modulator the optical power is $P(t) = i(t)$ making the output modulated power proportional to the baseband electrical signal because $i(t) = I_{DC} + s_B(t)$. Thus a linear mapping between the baseband OFDM signal and the optical intensity rather than the optical field is achieved. The $\alpha_{scaling}$ is the scaling constant to set a modulation index m to obtain a certain peak current value to minimise the clipping noise and ω_{IF} is the intermediate frequency for the electrical baseband OFDM signal for modulation. The optical signal is now detected with a square law device as derived in appendix D.

The frequency domain representation of the received signal and the beating components from appendix D are represented in Figure 23 and the terms are colour coded to clearly show where the wanted (blue) and unwanted (orange) beating products will be with the carrier represented by the red. From Figure 23 is can be seen that the beating products fall in the baseband region and will cause interference with the wanted beating products between carrier and subcarriers.
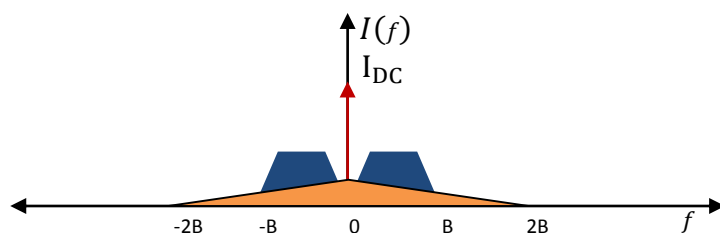
Figure 23: Frequency representation of the received signal in an IMDD system.

For Coherent Optical Orthogonal Frequency Division Multiplexing (CO-OFDM) the signal from the IFFT is complex as described in section 2.4. Thus the I and Q components needs to be converted from digital to analogue using separate DAC's. Then the I and Q components are converted to the optical domain using an optical I-Q modulator, for example utilising two Mach-Zehnder Modulators (MZM) as shown in Figure 24.
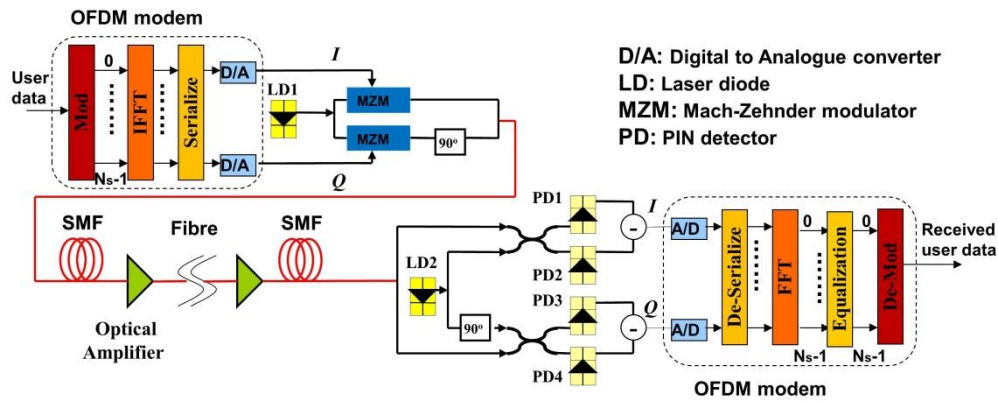
Figure 24: CO-OFDM system [13].

When semiconductor lasers are directly modulated they suffer from frequency chirp. A pulse is chirped if its carrier frequency changes with time [12]. The chirp is related to the derivative of the phase of the initial optical field. Thus a chirped pulse will increase or decrease in frequency as it propagates down the fibre. A pulse that is chirped is wider than that of an un-chirped pulse. The envelope of an optical pulse moves at the group velocity, thus the dispersion of the group velocity causes pulse broadening. The pulse broadening when a pulse is transmitted through a fibre due to the group velocity dispersion (GVD) is enhanced due to chirp.

High-speed, low-chirp modulators are needed to take advantage of the wide bandwidth of optical fibres. Modulators are a critical component both in high-speed time-domain-multiplexing (TDM) and wavelength-division-multiplexing systems (WDM). To avoid the problem of chirp, external modulators are used on a continuous laser beam. To implement CO-OFDM the Mach-Zehnder-Modulator is utilised as shown in Figure 24 and the MZM is based on the electro-optic effect is commonly used as an external modulator. The electro-optic effect also known as the Pockels effect is where the refractive index of a medium depends on the strength of the applied electric field.

The MZM is a planar waveguide structure deposited on the substrate, with two pairs of electrodes. One pair of electrodes is for the high-speed ac voltage representing the modulation data (RF) signal and the other pair for dc bias voltage. In the MZM the phase change is due to a voltage applied to each arm. The operation of the MZM is discussed further in appendix E. Thus in the detection process for CO-OFDM the detected complex signal is a linear down converted replica of the input OFDM signal. This linearity in the detection process is highly advantageous due to assumed linearity throughout the OFDM modulated system.

2.12 AOOFDM

Adaptive OOFDM (AOOFDM) can be implemented by either bit loading, power loading or both. With bit loading, the modulation format on each subcarrier is adapted to combat the roll-off in the system's frequency response. Subcarriers at a lower frequency will have a high SNR because the subcarrier's SNR are not affected by the frequency roll-off and a large modulation format for example 128-QAM can be utilised to maximise performance. Subcarriers at higher frequencies will suffer more due to frequency roll-off and a smaller modulation format, for example 16-QAM, can be used to increase the SNR but still have maximum data throughput. With power loading the power of the individual subcarriers are adjusted such that the subcarriers that suffer a high loss due to frequency roll-off of the system are given more power to combat the fading in power due to the roll-off. Power loading will lead to equal power of subcarriers at the receiver side. When both power and bit loading are implemented in an OOFDM system AOOFDM gives great flexibility to optimise the system's performance but also leads to an increase in system complexity.

2.13 Modulation

As discussed earlier in section 2.13, modulators in optical systems play a vital role in designing a good optical communication system. The role of the intensity modulator is to convert an electrical OFDM signal into an optical signal but this does not produce a linear replica optical field from the baseband OFDM signal. The intensity modulator maps the electrical baseband OFDM signal linearly to the optical intensity, causing the optical field to be nonlinear. The low complexity of this nonlinear modulation coupled with direct detection using a single photo detector makes IMDD systems very attractive for use in short-reach SMF transmission. Due to the nonlinear nature of the system any type of dispersion in the link will add to the nonlinearity of the signal making it unsuitable for long reach systems [13]. To illustrate the advantages and

trade-offs of intensity modulation for use in future PON's the two main types of modulators namely direct modulators and external modulators is discussed.

2.13.1 Direct modulation

In a directly modulated laser (DML), the optical output power is modulated by an electrical driving current applied directly to the laser device. The laser has to be biased in such a way that the DML is operating above the threshold current and that there is enough scope to ensure the positive and negative swing of the modulating signal is in a highly linear region of operation without distorting due to saturation or operating too close to the threshold current. Compared to external intensity modulators, DMLs are compact with a relatively small driving voltage and high output power [14].

2.13.1.1 DFB based DML

The dynamics of a single mode semiconductor laser are described by rate equations described in [20] forms the basis of the model used in simulations for the DML. The model will be further discussed in section 3.2.1.

In order to ensure single longitudinal mode emission a distributed feedback (DFB) laser incorporating a Bragg grating is used. This single mode can be selected in a DFB at a wavelength λ_B by satisfying the following condition

$$\Lambda = m(\lambda_B/2\bar{n}) \qquad (49)$$

with Λ the grating period, $\bar{n}$ the average mode index and m the order of Bragg diffraction. The coupling is the strongest for first-order Bragg diffraction with $m = 1$.

2.13.2 External modulation

High-speed, low-chirp modulators are needed to take advantage of the wide bandwidth of optical fibres. Modulators have become a critical component both in the high-speed time-domain-multiplexing (TDM) and wavelength-division-multiplexing systems (WDM). To reduce the problem of chirp, external modulators are used to modulate the laser emission.

In an external intensity modulator, the laser is biased at a constant current to provide a continuous wave light output and an optical modulator is placed at the output of the laser to convert the continuous wave light into a modulated optical intensity. Thus the external modulator uses an electrical signal to modulate the light output from the laser source. The external modulators that will be discussed are: Semiconductor Optical Amplifier (SOA) and Reflective Semiconductor Optical Amplifier (RSOA).

2.13.2.1 Semiconductor optical amplifier (SOA)

An SOA is an optoelectronic device that can amplify an input light signal. The basic structure is shown in Figure 25.
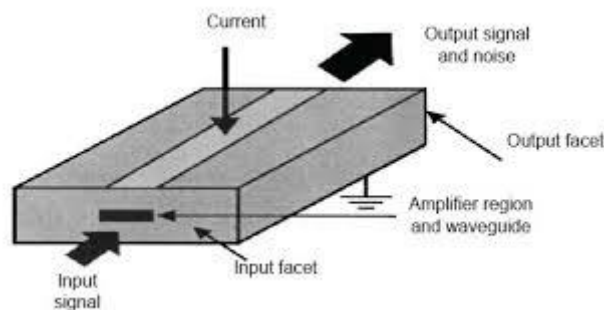
Figure 25: Basic SOA structure [15].

The external current provides the energy to amplify the input signal. To use the semiconductor device to amplify optical signals the cavity's facets have anti-reflective coatings which reduce the facet reflectivities to the order of 10^{-4} and thus supress laser action. The input signal is confined to the active region by an embedded waveguide where the signal is amplified.

2.13.2.2 Reflective semiconductor optical amplifier (RSOA)

If only one facet of the SOA has an anti-reflective coating the signal will transverse the cavity twice. The propagating signal will experience a high optical gain and will amplify the input signal even more. This is called a Reflective Semiconductor Optical Amplifier (RSOA). SOA/RSOA's are excellent candidates for use in colourless ONUs in OOFDM PON systems due to their ability to amplify a range of different frequencies enabling their use in colourless systems. A colourless ONU can be realised in three ways:

1. A tuneable laser located in each ONU to provide the light source for colourless RSOAs/SOAs intensity modulation [16].

2. A centrally supplied wavelength for remote modulation. This means two wavelengths are transmitted to an ONU, one carries downstream data and the other is reserved for upstream modulation [17].

3. Re-modulation of the downstream signal so that a single wavelength can be used by both downstream and upstream signals. Typically, this scheme uses the

RSOA/SOA gain saturation to erase the downstream signal waveform, which is

then re-modulated to transmit signal upstream [18] .

RSOAs generally have small 3-dB bandwidths of approximately 1GHz, which are much smaller than the OFDM bandwidth. For an RSOA/SOA the effective carrier lifetime is defined by [19]

$$\tau_e = \frac{1}{1/\tau_c + P_{out}/E_{sat}} \quad (50)$$

with P_{out} the output power, E_{sat} the saturation energy and τ_c the carrier lifetime. The output power can be changed by adjusting the SOA/RSOA parameters. The main limitation for a SOA/RSOA is the slow temporal response governed by the carrier lifetime, thus a reduction in the carrier lifetime through optimisation of parameters will allow larger modulation bandwidths and higher signal data rates.

To enable the use of RSOA's as an external modulator in the transmission system, the RSOA needs an unmodulated input from a laser source on which to modulate the signal data. The RSOA's external current source is the input of the biased data signal and the changes in the current source due to the changing data signal will change the gain in the RSOA. This gain change will change the intensity of the input laser ensuring the output light signal is intensity modulated with the fundamental carrier frequency dependant on the input light source frequency.

2.14 Optical fibre transmission

The two main categories of fibre in general optical transmission systems are multi-mode fibre (MMF) and single-mode fibre (SMF). Generally MMF has large core diameters to support multiple modes being sent down the fibre simultaneously and SMF have a small core diameter

to ensure that only one mode propagates. SMF is more suited for long-haul transmission and MMF is mostly used for LAN applications.

2.14.1 Chromatic dispersion

Chromatic dispersion (CD) is the frequency dependence of the refractive index of the fibre. Different frequencies of an optical OFDM signal will travel through the fibre at different speeds due to the frequencies experiencing a different refractive index and thus a different delay for each frequency. In MMF the different modes will propagate down the fibre using different paths causing the modes to arrive at the end of the fibre at different times. In SMF the individual spectral components of a pulse will travel down the fibre at different velocities causing the pulse to broaden. This is called group velocity dispersion (GVD). The delay ΔT experienced by the leading and trailing edges of the pulse will govern the amount of pulse broadening and can be calculated as [20]

$$\Delta T = DL\Delta\lambda \; with \; D = \frac{2\pi c}{\lambda^2}\beta_2 \quad (51)$$

D is the dispersion parameter characterising the GVD parameter with the unit of ps/(km-nm) and is defined as [20]

$$\beta_2 = \frac{d^2\beta}{d(2\pi f)^2} \; with \; \beta = \bar{n}. \frac{(2\pi f)}{c} \quad (52)$$

β it the propagation constant. To show the effects of fibre dispersion on a propagating pulse the propagation constant is expanded using a Taylor series around frequency f_0 as [20]

$$\beta(2\pi f) = \beta_0 + \beta_1(2\pi f - 2\pi f_0) + \frac{1}{2}\beta_2(2\pi f - 2\pi f_0)^2 \dots$$
$$with \; \beta_1 = \frac{1}{v_g} = \frac{n_g}{c} \quad (53)$$

with v_g the group velocity, c the speed of light in a vacuum and n_g the group index. The group velocity of light in a medium is the inverse of the group delay per unit length [21]. The group delay is defined as [20]

$$T_g = \frac{d\vartheta}{d(2\pi f)} \quad (54)$$

and is the derivative of the spectral phase of the electrical field of the optical signal with respect to the angular frequency. The dispersion relates to β_1 as [20]

41

$$D = \frac{d(\beta_1)}{d\lambda} = \frac{d}{d\lambda}\left(\frac{1}{v_g}\right) = \frac{d}{d\lambda}\left(\frac{1}{1/T_g}\right) = \frac{d(T_g)}{d\lambda} \quad (55)$$

The above equation shows that an increase in group delay will lead to an increase in dispersion. Figure 26 illustrates the group velocity's dependence on the refractive index.

Non DSF: Non dispersion shifted fiber, which is also called
standard single-mode fiber or ITU-T G.652 fiber.
(-D) NZ-DSF: negative non-zero dispersion shifted fiber
(+D) NZ-DSF: positive non-zero dispersion shifted fiber
DSF: dispersion shifted fiber with nearly zero dispersion in C-band
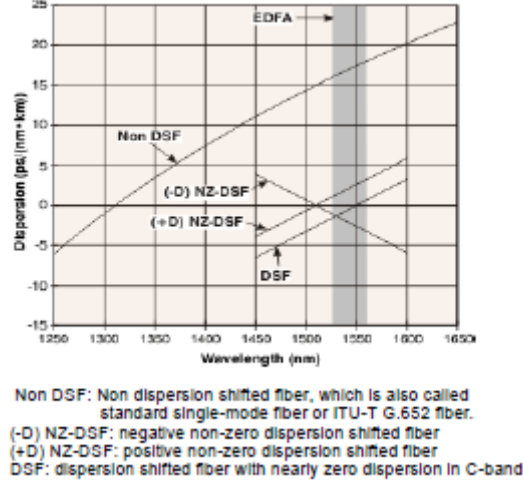
Figure 26: Dispersion parameter versus wavelength for various fibres [13].

Another phenomenon contributing to the pulse broadening due to GVD is the chirp of a pulse. A transmitted field of a chirped Gaussian pulse is [12]

$$E(L,T) = \frac{T_0}{[T_0^2 - j\beta_2 L(1+jC)]^{1/2}} \exp\left(\frac{(1+jC)T^2}{2[T_0^2 - j\beta_2 L(1+jC)]}\right) \quad (56)$$

with T_0 the initial width of the pulse and β_2 the GVD parameter. To show the pulse broadening due to the combined effects of the GVD and chirp we relate the width T_1 after propagating length L down the fibre to the initial pulse width T_0 and get [12]

$$\frac{T_1}{T_0} = \left[\left(1 + \frac{C\beta_2 L}{T_0^2}\right)^2 + \left(\frac{\beta_2 L}{T_0^2}\right)^2\right]^{1/2} \quad (57)$$

If the pulse is unchirped with C=0 the pulse broadens with factor $\frac{T_1}{T_0} = \left(1 + \left(\frac{\beta_2 z}{T_0^2}\right)^2\right)^{1/2}$. When $C\beta_2 > 0$, a chirped pulse broadens at a significant faster rate than an unchirped pulse. If $C\beta_2 < 0$ the pulse will compress [20].

2.14.2 Fibre loss
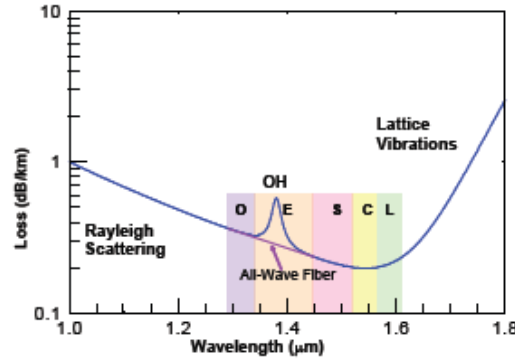
Figure 27: Loss in optical fibre versus wavelength [13].

A pulse propagating down a fibre will experience losses of the signal power. The fibre induced power loss is dependent on the wavelength as shown in Figure 27 of the transmitted light. This fibre-loss parameter is [20]

$$\alpha = -\frac{10}{L} log_{10} \left(\frac{P_{out}}{P_{in}} \right) \quad dB/km \quad (58)$$

with P_{out} and P_{in} the input and output power of the fibre and L the length of the fibre.

2.14.3 Fibre nonlinearity

For high input intensities fibre nonlinearities such as the Kerr nonlinearity becomes significant [11]. Other nonlinear effects considered in this thesis caused by the dependence of refractive index on the intensity of the propagating signal are Self-phase Modulation (SPM), Cross-phase Modulation (XPM), and Four Wave-mixing (FWM).

2.14.4 Nonlinear phase modulation

High optical powers causes increase in the refractive index of optical fibres giving rise to a nonlinear phase shift.

2.14.4.1 Self-phase modulation

Self-Phase Modulation (SPM) is the nonlinear phase shift imposed on a propagating pulse. SPM leads to frequency chirping that is proportional to the derivative of the input power. The SPM-caused frequency chirp is calculated by [12]

$$\delta\omega(T) = -\frac{d\varphi_{NL}}{dT} \; with \; \varphi_{NL} = n_2 \, {}^{2\pi}/_{\lambda} \, L|E|^2 \quad (59)$$

and will increase the pulse-broadening through fibre CD, with φ_{NL} is the nonlinear phase shift that is intensity dependent, L is the length of the fiber, λ is the carrier wavelength, $|E|^2$ is the optical intensity in the fibre and n_2 the nonlinear-index coefficient also known as the Kerr coefficient.

2.14.4.2 Cross-phase modulation

Cross-Phase Modulation (XPM) is the phase shift induced on an optical field by another optical field at a different frequency. The total phase shift depends on all the powers of the fields in the channel. SPM is always present when XPM is present in a channel.

2.14.4.3 Four-wave mixing

For multiple signals at different wavelengths propagating in the fibre, the intensity dependence of refractive index not only induces SPM and XPM on each signal but also causes Four-Wave Mixing (FWM). FWM is when three optical fields at different frequencies propagating in a medium simultaneously they interact causing a new optical field at a new optical frequency. When FWM occurs energy transfers efficiently from one frequency to another when phase matching between the propagating signals is achieved. Since the signals at different wavelengths travel at different speeds due to GVD, the FWM is dependent on fibre dispersion due to the destruction of the phase matching condition due to the GVD induced phase change.

2.14.5 SMF fibre transfer function

In designing a communication system the transfer functions of different elements of the system needs to be considered. The transfer function of the SMF is no exception. In order to optimise the system throughput the signal needs to be placed in the frequency spectrum where it will be affected the least by roll-off of the SMF transfer function.

The transfer function defined in [22] for a communication link considering a DSB signal with an ideal modulator with direct detection becomes [22]

$$H_{RF}(2\pi f_{RF}) =$$

$$(\Re\, Z_L).\frac{P_0}{2\pi}.\mathrm{I_{DC}}.\,e^{j\frac{1}{6}\beta_3 L(2\pi f_{RF})^3}\, P_0\big(\big(e^{j2\pi f_{RF}t}\sum_{k=-\frac{1}{2}N_{sc}+1}^{\frac{1}{2}N_{sc}}C_k e^{j2\pi f_k t}\big)e^{j\frac{1}{2}\beta_2 L(2\pi f_{RF})^2} +$$

$$\big(e^{-j2\pi f_{RF}t}\sum_{k=-\frac{1}{2}N_{sc}+1}^{\frac{1}{2}N_{sc}}C_k e^{j2\pi f_k t}\big)e^{-j\frac{1}{2}\beta_2 L(2\pi f_{RF})^2}\big) \quad (60)$$

with $\Re$ the responsivity of the photo-detector, Z_L impedance of fibre as seen by receiver, P_0 the power of the optical carrier and $\mathrm{I_{DC}}$ is the detected DC current due to the carrier in OFDM DSB signal. β_2 is the GVD parameter as shown in equation 52, β_3 is related to the slope of the dispersion and f_{RF} the radio frequency (RF) that the DSB signal is upshifted with in the transmitter. The length of the fibre is L and f_k is the kth subcarrier frequency. The frequency response for 50 km SMF is plotted in Figure 28.
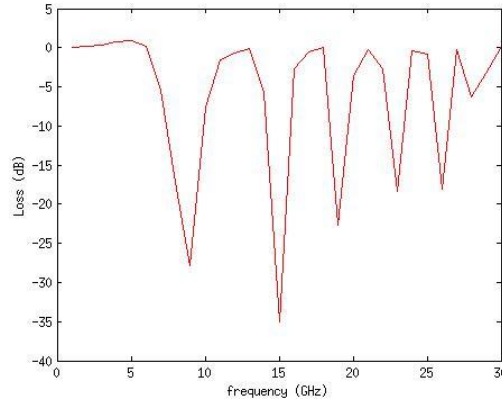
Figure 28: Ideal modulator frequency response for 50 km transmission with DSB signal.

For certain frequencies destructive interference occurs between the upper and lower sidebands of the DSB signal, causing dips as seen in Figure 28. This can cause problems for the transmission if a signal falls within the band where these dips occur. The frequencies where these dips will occur is governed by $e^{j\frac{1}{2}\beta_2 L(2\pi f_{RF})^2}$ and $e^{-j\frac{1}{2}\beta_2 L(2\pi f_{RF})^2}$ from equation 60. For a DSB signal the complex exponentials become $e^{j\frac{1}{2}\beta_2 L(2\pi f_{RF})^2} + e^{-j\frac{1}{2}\beta_2 L(2\pi f_{RF})^2} = 2.\cos(\frac{1}{2}\beta_2 L(2\pi f_{RF})^2)$ resulting in cyclic occurrence of the dips in Figure 28. Thus the position of the dips is dependent on β_2, L and f_{RF}. To mitigate the destructive interaction, an optical filter at the output of the modulator can be used to achieve a single sideband in the optical domain. To implement this an optical bandpass super Gaussian filter can be used and the transfer function is [23]

$$|H(f)|^2 = e^{[\ln(\frac{1}{2}).(\frac{f-f_0}{f_{BW}/2})^{2k}]} \quad (61)$$

with f_0 the frequency-offset between the centre frequency of the optical filter and the optical carrier, f_{BW} is the 3dB bandwidth of the optical filter and k the order of the optical filter. The frequency response for the SSB signal is
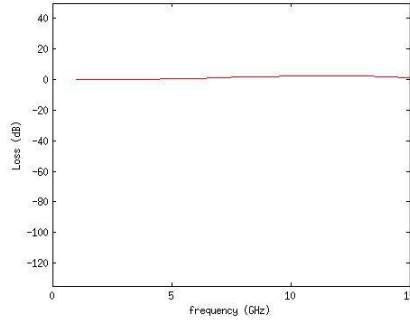
Figure 29: Ideal modulator frequency response with optical filter for single sideband signal.

An issue with the optical filter is the group delay (defined in equation 54) introduced to the signal. This is due to the optical filter adding different delays to different frequencies of the signal passing through the filter. This will cause distortions in the OOFDM signal [23] and the group delay will cause the system dispersion to increase but dips in the frequency response will disappear as shown in Figure 29 and overall performance will increase.

2.15 Photo-detector

The key role of the Photo-detector or photodiode is to absorb photons of the incoming optical signal and thereby generate an electrical current.

2.15.1 PIN and APD

Common photodiodes include the PN photodiode, the PIN photodiode and the avalanche photodiode (APD). The photo detectors of interest here are the PIN and APD. The PIN photodiode is a PN photodiode with a wider depletion region. By adding an intrinsic layer between the PN junction the depletion region width is increased. More of the incident power is absorbed in the enlarged depletion region and the responsivity is thus increased. The photocurrent $I_p(t)$ is proportional to the power of incident light P_{in} so [20]

$$I_p = RP_{in} \qquad (62)$$

46

With R the photodiode responsivity in A/W. Responsitvity can be in terms of the fundamental quantity called quantum efficiency as [20]

$$\eta = \frac{electron\ generation\ rate}{photon\ generation\ rate} = \frac{\frac{I_p}{q}}{\frac{P_{in}}{hv}} = \frac{hv}{q}R \quad (63)$$

All detectors require a minimum current to operate that is defined as [20]

$$P_{in} = \frac{I_p}{R} \quad (64)$$

Detectors with a large responsitivity are preferred since they require less optical power to be able to detect a signal. Avalanche diodes can provide much larger values of R than a PIN diode due to having internal current gain. For an APD I_p is shown below with M the multiplication factor due to the internal current gain of the APD [20].

$$I_p = MRP_{in} \quad (65)$$

 The receiver sensitivity is defined as the minimum average received power by the receiver to operate at a given BER level. For a PIN with M=1 the minimum required power is [20]

$$(P_{rec})_{PIN} = \frac{Q\sigma_T}{R} \quad (66)$$

with σ_T the thermal noise that dominates in this type of receivers [11]. Random thermal motion of electrons in a resistor causes the current to fluctuate. This is called thermal noise. Shot noise and thermal noise are two fundamental noise mechanisms responsible for current fluctuations in all optical receivers even with a constant incident power. Shot noise for a PIN can be calculated with [20]

$$\sigma_s^2 = i_s^2(t) = 2qI_p\Delta f \quad (67)$$

with Δf the effective noise bandwidth and the total current $I(t) = I_p + i_s(t)$. For an APD the shot noise is [20]

$$\sigma_s^2 = 2q\text{M}^2\text{F}_\text{A}(RP_{in} + I_d)\Delta f \quad (68)$$

with F_A the excess noise factor of the APD and I_d the current fluctuation due to dark current. Dark current is the current generated when there is no optical signal present.

2.16 OBI

In OOFDMA PON system using direct detection the square law nature of the detection of multiple ONU (Optical Network Unit) signals will cause optical beating interference (OBI) that is the beating between ONUs and will cause unwanted products that can interfere with the desired data. During the photo-detection process quantum noise and thermal noise will also be generated.

To show the effects of OBI analysis of the beating between 2 ONUs working at the same wavelength is done. The optical field at the output of each ONU can be represented by [11]

$$E_{out_n} = E_n e^{j\omega_n t} \quad (69)$$

where E_n is the field magnitude and $e^{j\omega_n t}$ represents the phase of the field of the nth ONU. The subcarriers is assigned to specific ONUs as shown in Figure 30 where the first half of the subcarriers shown in red is assigned to ONU1 and the second half of the subcarriers shown in blue is assigned to ONU 2.
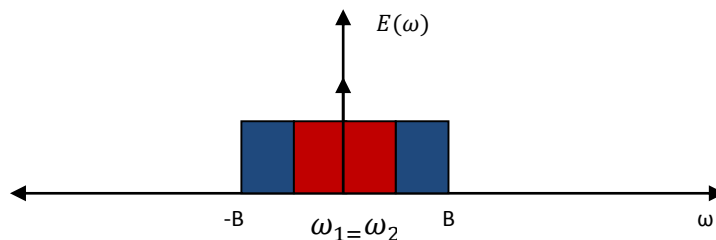
Figure 30: Frequency spectrum of two ONUs on the same optical wavelength after optical modulators.

After detection the electrical signal $i_{out}(t)$ will be represented by

$$
\begin{aligned}
i_{out}(t) &= \left| E_1 e^{j\omega_1 t} + E_2 e^{j\omega_2 t} \right|^2 \\
i_{out}(t) &= \left(E_1 e^{j\omega_1 t} + E_2 e^{j\omega_2 t} \right)\left(E_1 e^{-j\omega_1 t} + E_2 e^{-j\omega_2 t} \right) \\
i_{out}(t) &= E_1{}^2 + E_2{}^2 + E_1 E_2 e^{-j\omega_1 t} e^{j\omega_2 t} + E_1 E_2 e^{j\omega_1 t} e^{-j\omega_2 t} \\
i_{out}(t) &= E_1{}^2 + E_2{}^2 + E_1 E_2 e^{j(\omega_2 - \omega_1)t} + E_1 E_2 e^{j(\omega_1 - \omega_2)t} \quad (70)
\end{aligned}
$$

Because ω_1 and ω_2 are the same $i_{out}(t)$ becomes

$$i_{out}(t) = E_1{}^2 + E_2{}^2 + E_1E_2e^{j(0)t} + E_1E_2e^{j(0)t}$$
$$i_{out}(t) = E_1{}^2 + E_2{}^2 + E_1E_2 + E_1E_2$$
$$I(\omega) = E_1 * E_1 + E_2 * E_2 + E_1 * E_2 + E_1 * E_2 \quad (71)$$
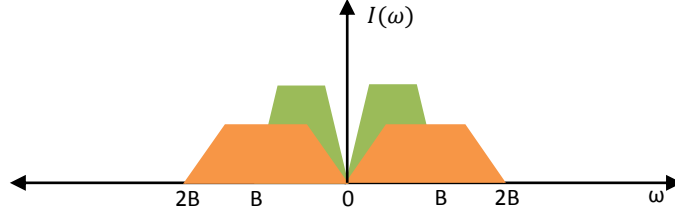
Figure 31: Frequency spectrum of two ONUs at same wavelengths in electrical domain after detection.

In Figure 31 the frequency spectrum of the detected signal is shown. The wanted data is shown in red and the OBI components due to beating between signals from different ONUs is shown in orange. The OBI beating falls in the same region as the wanted data and will interfere causing a decrease in the system performance.

2.17 Subcarrier-subcarrier and sub-band intermixing

In OOFDMA PON systems multiband can be utilised in each ONU to increase the system capacity. Multiband is where more bands are added electrically in the ONU before the signal is converted to the optical domain. In a direct detection system the added bands will give rise to additional beating products.

There are two types of beating components in multiband systems. The first is the beating between subcarriers in each separate band. The second type of beating is the beating occurring between the subcarriers of the different bands. The position of the beating components in direct detection will be determined by the RF up-shift of the bands. The RF up-shift is the shift relative to baseband of the signal in the frequency domain in the ONU before electrical to optical conversion.

In Figure 23 the beating between subcarriers is represented by the orange blocks and falls in the baseband region. In section 2.6 the baseband OFDM signal with no RF up-shift is defined. For the case with a RF upshift in the electric domain the baseband signal becomes

$$s_B(t) = e^{j2\pi f_{RF}t} \cdot \sum_{k=-\frac{1}{2}N_{sc}}^{\frac{1}{2}N_{sc}} C_k e^{j2\pi \frac{k}{T_s}t} \quad (72)$$

49

The frequency representation for a RF up-shifted signal as derived in appendix F is

$$I(f) = \delta(f).I_{DC} + \frac{1}{2}\sum_{k=-\frac{1}{2}N_{sc}}^{\frac{1}{2}N_{sc}} C_k.\delta\left(f - \frac{k}{T_s} + f_{RF}\right) + \frac{1}{2}\sum_{k=-\frac{1}{2}N_{sc}}^{\frac{1}{2}N_{sc}} C_k.\delta\left(f - \frac{k}{T_s} - f_{RF}\right)$$

$$+ \frac{1}{8I_{DC}}\left(\sum_{k_1=-\frac{1}{2}N_{sc}}^{\frac{1}{2}N_{sc}}\sum_{k_2=-\frac{1}{2}N_{sc}}^{\frac{1}{2}N_{sc}} C_{k_1}.C_{k_2}.\delta(f - (\frac{k_1}{T_s} + \frac{k_2}{T_s} + 2\pi - 2f_{RF})))\right) +$$

$$\frac{1}{4I_{DC}}\left(\sum_{k_1=-\frac{1}{2}N_{sc}}^{\frac{1}{2}N_{sc}}\sum_{k_2=-\frac{1}{2}N_{sc}}^{\frac{1}{2}N_{sc}} C_{k_1}.C_{k_2}.\delta(f - (\frac{k_1}{T_s} + \frac{k_2}{T_s})))\right) +$$

$$\frac{1}{4I_{DC}}\left(\sum_{k_1=-\frac{1}{2}N_{sc}}^{\frac{1}{2}N_{sc}}\sum_{k_2=-\frac{1}{2}N_{sc}}^{\frac{1}{2}N_{sc}} C_{k_1}.C_{k_2}.\delta(f - (\frac{k_1}{T_s} + \frac{k_2}{T_s} + 2f_{RF} + 2\pi)))\right) \dots (73)$$

Figure 32: Frequency representation of signal with subcarrier-subcarrier intermixing for baseband with RF upshift.

For the RF upshift case the wanted components fall outside of the baseband where beating components will dominate if the RF upshift is large enough. For a multiband system with two bands we have

$$s_B(t) = \sum_{k=-\frac{1}{2}N_{sc}}^{\frac{1}{2}N_{sc}} C_k e^{j2\pi\frac{k}{T_s}t} + e^{j2\pi f_{RF}t}.\sum_{k=-\frac{1}{2}N_{sc}}^{\frac{1}{2}N_{sc}} C_k e^{j2\pi\frac{k}{T_s}t} \quad (74)$$

with one band in baseband and one band RF upshifted. Both bands are DSB. Substituting $s_B(t)$ into the equation for the detected signal the frequency representation as derived in appendix G is shown in Figure 33.
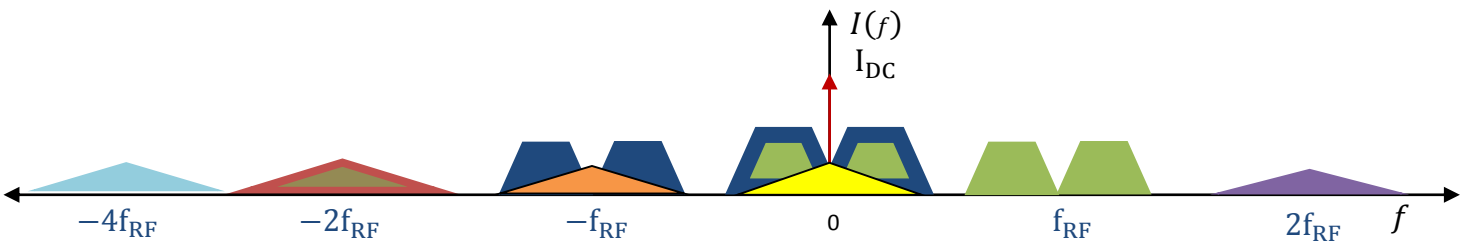
Figure 33: Frequency representation of signal with subcarrier-subcarrier intermixing for DSB Multiband.

In the multiband system's electrical frequency representation the components marked in a yellow colour represent the beating between the subcarriers. The remaining components are due to the subcarriers of the different bands mixing together. To limit the number of component that can mix in the detection process electrical SSB can be applied to the signal before it is transmitted.

To achieve SSB in the electrical domain the Hilbert transform is used to take the real valued output of the IFFT and convert it into a real valued single sideband signal, also called the Hartley modulator.

The Hartley method used for SSB generation uses phasing to suppress the unwanted sideband. The Hartley modulator is illustrated in Figure 34 and the output frequency representation of the SSB signal is shown in Figure 35.
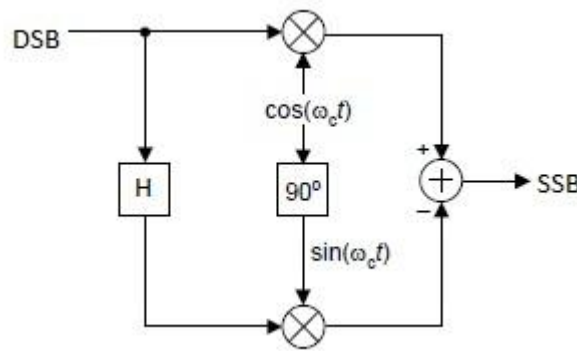
Figure 34: Hartley Modulator.

This derivation of the SSB signal is done using the Hilbert transform as shown in equation [75]. The sign determines if the left or right sideband is generated. For USSB a minus is used and for LSSB a plus [4].

$$S_{SSB}(t) = A_{DSB}(t)cos(\omega_{RF}t) \pm H[A_{DSB}(t)]sin(\omega_{RF}t) \quad (75)$$
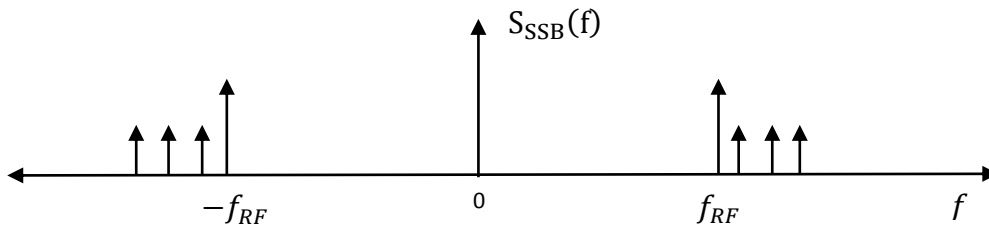
Figure 35: Output of Hartley Modulator with real valued input and upper SSB output.

2.18 MAI

Multiple access is defined as the idea of allowing several transmitters to share communication resources. Multiple access interference (MAI) always occurs when a system consists of two or more ONUs in an OOFDMA IMDD system. MAI arises in OFDMA channels due to effects such as multipath [24]. The different ONUs suffer different delays due to dispersion. If there is a delay between subcarriers of the different ONUs that causes a change in the phase the subcarriers are not orthogonal to each other anymore. Thus the MAI arises due to these imperfections in subcarrier orthogonality between ONU subcarriers.

2.19 Pilot-assisted channel estimation and equalisation
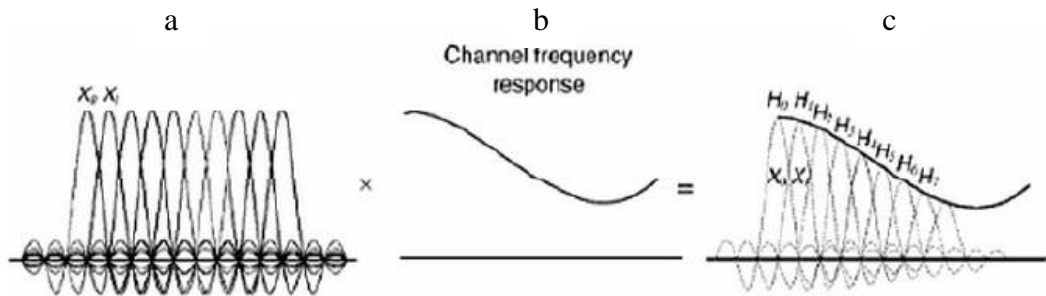
Figure 36: Channel frequency response [13].

To combat the roll-off in the channel frequency response shown in Figure 36b the channel response is estimated by using a pilot tone inserted into the signal before transmission. The channel transfer function can be estimated by dividing the received signal by the known pilot as follows [25]:

$$\hat{C}(k) = \frac{Y(k)}{X(k)} \qquad (76)$$

with the received signal described by

$$Y(k) = C(k)X(k) + Z(k) \quad (77)$$

with k the kth subcarrier, C the channel transfer function, X the transmitted pilot data and Z the noise in the channel. To equalise the received signal the received signal is multiplied with the inverse of the estimated channel response resulting in the equalised signal of

$$\hat{X}(k) = Y(k).\hat{C}(k)^{-1} \quad (78)$$

2.20 Synchronisation

Synchronisation between the transmitter and receiver is vital in communication systems to ensure data is decoded correctly. The delay caused by the channel is known as symbol timing offset (STO). The STO is calculated by sweeping the FFT window over a few samples of the symbol observing at which sample the BER is the lowest. This sample point is then used as the new FFT window start point in the receiver and by using the new FFT window start point the STO is compensated for. If the STO is not compensated for it can cause the FFT window to fall over parts of 2 adjacent OFDM symbols leading to ISI which will lead to ICI after the FFT operation in the receiver.

2.21 EVM, BER and SNR

In this thesis Error Vector Magnitude (EVM), bit error rate (BER) for a specific line rate and signal to noise ratio (SNR) are used in performance measurements. EVM is defined for results in this thesis as the difference between a collection of measured symbols in the constellation of mapped data points in the receiver and ideal symbols in the constellation of mapped data points in the transmitter. These differences are averaged over a given, typically large, number of symbols. EVM can be mathematically represented as

$$EVM_{db} = 10log_{10}\left[\frac{\frac{1}{N}\sum_{i=1}^{N}|S_{reference}-S_{\text{received}}|^2}{\frac{1}{N}\sum_{i=1}^{N}|S_{reference}|^2}\right] \quad (79)$$

where S_{received} is the measured symbols and $S_{reference}$ is the ideal symbols in the constellation. The EVM defined in equation 79 is used in [27] and [28], so in order to ensure a fair comparison between results the above EVM definition is used throughout the thesis.

The total channel BER and line rate is defined as

$$BER = \sum_{k=2}^{N_{SC}} E_k / \sum_{k=2}^{N_{SC}} b_k \quad (80a)$$

$$Line\ rate = \sum_{k=2}^{N_{SC}} S_k = \frac{\sum_{k=2}^{N_{SC}} n_k}{T_s} = \frac{r_s \sum_{k=2}^{N_{SC}} n_k}{2N_{SC}(1 + \eta_{CP})} \quad (80b)$$

with N_{SC} the number of data carrying subcarriers, E_k the total number of detected error bits for the kth subcarrier, b_k the total number of transmitted bits for the kth subcarrier. For the line rate the S_k is the signal bit rate for the kth subcarrier, n_k the total number of bits for the kth

subcarrier within one symbol period T_s. The ADC/DAC sampling speed r_s is related to the line rate by $T_s = 2N_{SC}(1 + (\frac{\eta_{CP}}{100}))$ with η_{CP} the percentage of cyclic prefix for the system.

Another important parameter in optical communications is the SNR defined as

$$SNR = \frac{Signal\ Power}{Noise\ Power} = \frac{\frac{1}{T}\sum_{t=1}^{T}[(I_t)^2 + (Q_t)^2]}{\frac{1}{T}\sum_{t=1}^{T}|n_{I,t}|^2 + |n_{Q,t}|^2} \qquad (81)$$

with I_t and Q_t the in-phase and quadrature signal amplitudes of the M-ary modulations. $n_{I,t}$ and $n_{Q,t}$ are the in-phase and quadrature noise amplitudes of the complex noise being considered. The relationship between SNR and EVM is [29]

$$SNR \approx \frac{1}{EVM^2} \qquad (82)$$

2.22 References

[1] R.W. Chang, "Synthesis of band-limited orthogonal signals for multichannel data transmission", Bell System Technical Journal, vol. 45, pp. 1775-1796, Dec. 1966.

[2] J. Salz and S. B. Weinstein, "Fourier transform communication system", presented at the Proceedings of the first ACM symposium on Problems in the optimization of data communications systems, Pine Mountain, Georgia, USA, 1969.

[3] Q. Pan and R. Green, "Bit-Error-Rate Performance of Lighwave Hybrid AM/OFDM Systems with Comparison with AM/QAM Systems in the Presence of Clipping", IEEE Photonics Technology Letters, vol. 8, pp. 278-280, Feb. 1996.

[4] A. Carlson, "Communication Systems," ed: McGrawHill, 2002.

[5] J. Proakis, "Communication Systems Engineering", ed: Prentice Hall, 1994.

[6] R. W. Ramirez, "The FFT: fundamentals and Concepts", 1975.

[7] C. V. Loan, "Computational Frameworks for the Fast Fourier Transform", ed: SIAM, 1992.

[8] J. M. Tang and K. A. Shore, "Maximizing the Transmission Performance of Adaptively Modulated Optical OFDM Signals in Multimode-Fiber Links by Optimizing Analog-to-Digital Converters", Journal of Lightwave Technology, vol. 25, pp. 787-798, March 2007.

[9] Jean-Benoit Larouche, "Understanding PAPR in OFDM systems", http://nutaq.com/en/blog/understanding-papr-ofdm-systems, Jan. 2014.

[10] J. L. Wei, C. Sánchez, R. P. Giddings, E. Hugues-Salas and J. M. Tang, "Significant improvements in optical power budgets of real-time optical OFDM PON systems", Opt. Express, vol. 18, pp. 20732-20745, 2010.

[11] W. Shieh and D. Ivan, "OFDM for Optical Communications", Elsevier, 2010.

[12] G. P. Agrawal, "Nonlinear Fiber Optics", 2007.

[13] J. Wei, "Intensity Modulation of Optical OFDM Signals Using Low-Cost Semiconductor Laser Devices for Next-Generation PONs", Electronic Engineering, Bangor University, 2010.

[14] J. J. Yu, Z. S. Jia, M. F. Huang, M. Haris, P. N. Ji, T. Wang and G. K. Chang, "Applications of 40-Gb/s chirp managed laser in access and metro networks", Journal of Lightwave Technology, vol. 27, pp. 253-265,Feb 2009.

[15] M. Connelly, "Semiconductor Optical Amplifiers", Springer, 2002.

[16] J. L. Wei, X. L. Yang, R. P. Giddings, J. M. Tang and K. A. Shore, "SOA Intensity Modulator-Enabled Colourless Transmission of Adaptively Modulated Optical OFDM Signals for WDM-PONs", in 14th OptoElectronics and Communications Conference (OECC), Hong Kong, China, pp. 1-2, 2009.

[17] K. H. Han and Y. C. Chung, "Spectrum-sliced bidirectional passive optical network for simultaneous transmission of WDM and digital broadcast video signals", Electronics Letters, vol. 37, pp. 308-309, Mar. 2001.

[18] C.W. Chow, C. H. Wang, F. Y. Shih and S. Chi, "Demonstration of signal remodulation long reach carrier distributed passive optical network using OFDM QAM signal", in 35th European Conference on Optical Communication (ECOC) Vienna, Austria, pp. 1-2, Sept. 2009.

[19] R. Gutiérrez-Castrejón, L. Occhi, and G. Guekos,", "Modeling and measurement of longitudinal gain dynamics in saturated semiconductor optical amplifiers of different length", IEEE Journal of Quantum Electronics, vol. 36,pp. 1476-1484, Dec 2000.

[20] G. P. Agrawal, "Fiber-Optic Communication Systems", Wiley, 2002.

[21] G. J. Peatross, S. A. Glasgow and M. Ware, "Average Energy Flow of Optical Pulses in Dispersive Media", Physical Review Letters, vol. 84, pp. 2370-2373, 2000.

[22]   J. Mora, B. Ortega, A. Diez, J. L. Cruz, M. V. Andres, J. Capmany, et al., "Photonic microwave tunable single-bandpass filter based on a Mach-Zehnder interferometer", Journal of Lightwave Technology, vol. 24, pp. 2500-2509, 2006.

[23]   J. L. Wei, C. Sanchez, E. Hugues-Salas, P. S. Spencer, and J. M. Tang, "Wavelength Offset Filtering in Optical OFDM IMDD Systems Using Directly Modulated DFB Lasers", Journal of Lightwave Technology, vol. 29, pp. 2861-2870, 2011.

[24]   L. Cohen and M. O. Scully,"Classical, Semi-classical and Quantum Noise", Springer, 2012.

[25]   L. Hanzo, "Quadrature amplitude modulation", Wiley, 1952.

[26]   T. N. Duong, "Study of Technical Multicarrier Modulation OFDM", De Rennes University 2010.

[27]   J. Tang, X. Jin, J. Groenewald, E. Hugues-Salas and R. P. Giddings, "Dependence of Upstream Power Budget on the Number of ONUs in IMDD Optical OFDMA PONs", in Optical Fiber Communication Conference/National Fiber Optic Engineers Conference, Anaheim, California, 2013, p. JW2A.73.

[28]   X. Q. Jin, J. Groenewald, E. Hugues-Salas, R. P. Giddings, and J. M. Tang, "Upstream Power Budgets of IMDD Optical OFDMA PONs Incorporating RSOA Intensity Modulator-Based Colorless ONUs", Journal of Lightwave Technology, vol. 31, pp. 1914-1920,2013

[29]   R. A. Shafik, S. Rahman, and M. R. Islam, "On the Extended Relationships Among EVM, BER and SNR as Performance Metrics", in Electrical and Computer Engineering, ICECE '06 International Conference, 2006, pp. 408-411.

3   Chapter 3: Multiple wavelength OOFDMA PON upstream transmission

3.1 Introduction

In this the first of three results chapters, multiple wavelength upstream optical orthogonal frequency division multiple access (OOFDMA) passive optical network (PON) transmission is presented. First a point-to-point (PTP) system over 40 km single mode fibre (SMF) is modelled to investigate the performance of the system to confirm the viability of the technology as a future candidate for short reach passive optical access networks and to determine the optimal orthogonal frequency division multiplexing (OFDM) transceiver parameters. To validate the OOFDMA PON simulations parameters from experimental results are fitted to the numerical model. The dependence of the upstream power budget on the number of optical network units (ONUs) in intensity modulation direct detection (IMDD) OOFDMA PONs is explored to show the viability of the system utilising a different number of ONUs as a solution for next generation PONs. Finally an investigation is undertaken on the effects of dispersion, nonlinear effects and chirp on the optical bandwidth and wavelength spacing of IMDD OOFDMA PONs in upstream transmission.

3.2 Exploring optimal simulation transceiver parameters for PTP OOFDM transmission over 40 km SMF
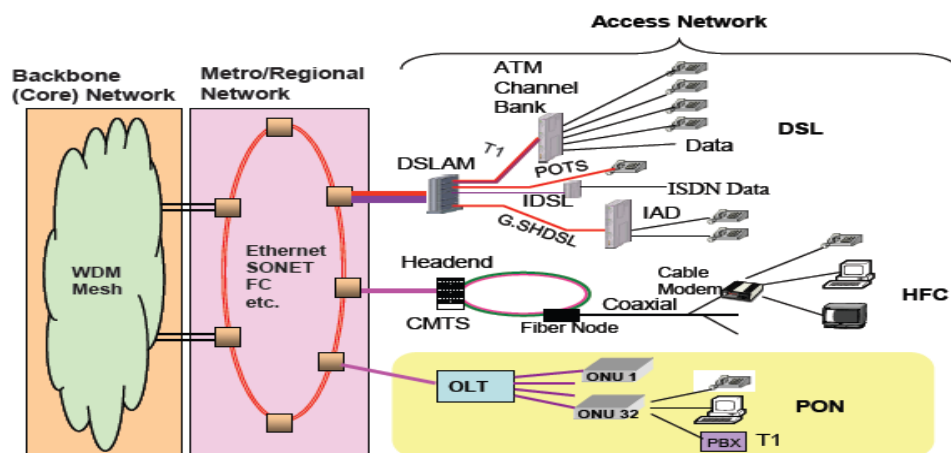
Figure 37: Generic telecommunications system [1].

A generic telecommunications system is shown in Figure 37, and consists of three sub-networks namely core networks, metro/regional networks and access networks. The core networks are the central parts of the telecommunication networks, and interconnect big cities or major communication hubs. A typical core network can commonly support bandwidth on a Tb/s scale over transmission distances of several hundred kilometres [2]. The metro/regional networks are deployed throughout a city or metropolitan area and support signal line rates of

10 Gb/s over transmission distances of up to 320 km [3]. Located at the edge of the telecommunication networks are the access networks. Existing access networks only support signal line rates of < 60 Mb/s per user over a transmission distance of up to 20 km [4]. In this thesis the focus is placed on upstream transmission as simultaneous upstream transmission from ONUs is currently a major constraint in optical access networks due to the beating noise at the optical line terminal (OLT). To verify the suitability of OFDM utilising IMDD in the optical access network an upstream PTP system over 40 km of SSMF is simulated. First the optimum parameters for the OFDM modems such as clipping ratio (CR), number of quantization bits (QB) and sampling speed is determined and analysed to maximise system capacity. Finally the effect of dispersion on the OOFDM IMDD system is investigated and optimal distributed feedback (DFB) based directly modulated laser (DML) modulator parameters are determined with optimised OFDM modem parameters.

3.2.1 Transmission system models
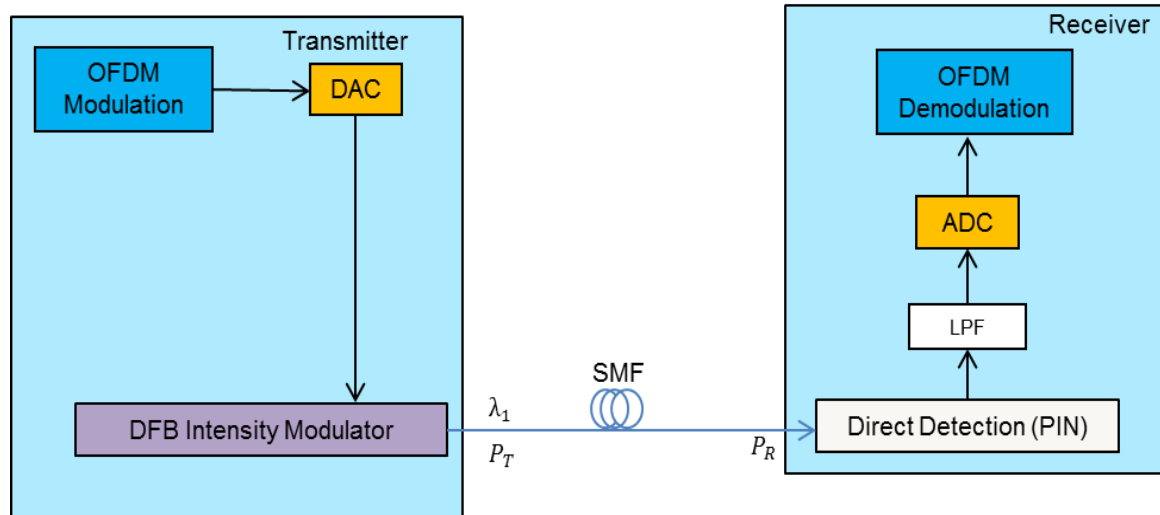
Figure 38 : System setup diagram for OOFDM IMDD upstream transmission.

Figure 38 depicts the OOFDM upstream transmission system considered in this chapter. The model with all major transceiver components was developed in Matlab. The system consists of an OOFDM transmitter SMF link (data file in appendix K) and an OOFDM receiver. The OOFDM transmitter is composed of an electrical OFDM modem (code in appendix K), a digital to analogue converter (DAC) (code in appendix K) and a DFB laser (code in appendix K) as intensity modulator. The OOFDM receiver has a square-law photon detector (code in appendix K), an electrical low-pass filter (LPF) (code in appendix K), an analogue to digital converter (ADC) (code in appendix K) and an electrical OFDM modem. The number of symbols used in

all simulations in the thesis is 500 to enable fair comparison. This number was the minimum number of symbols for the largest system namely 15 ONUs in the PON, that would ensure accurate performance measurements while simulation time is kept to a minimum.

3.2.2 OOFDM transceivers

In the transmitter, the generation of an electrical OFDM signal in the OFDM modem is modelled using the techniques discussed in Section 2.3-2.8. The operation in the modem of the transmitter is as follows:

- Firstly data is mapped using adaptive modulation (BPSK, QPSK, 8-QAM, 16-QAM, 32-QAM, 64-QAM, 128 QAM and 256-QAM).
- A real valued inverse fast Fourier transform (IFFT) is used to modulate all the data on subcarriers that is orthogonally spaced.
- The cyclic prefix (CP) is inserted.
- The OFDM symbols are then serialised.
- The digital signal is the converted to analogue with a DAC.
- An optimum direct current (DC) bias is added to the signal and is used to drive the DFB based DML.

In the receiver the signal from the SMF is detected by the PIN diode followed by a low-pass filter (LPF) where finally the inverse of the procedure of the OFDM transmitter is applied to the signal.

3.2.3 DFB Laser

To simulate the DFB laser a theoretical model developed in [5], with code shown in appendix K, is used. The validity of the laser model has been verified in [5, 11].

3.2.4 SMF, PIN detectors and LPF

A standard theoretical SMF model successfully used in [11] is utilised and the effects of loss, chromatic dispersion and nonlinear effects described in section 2.14 are taken into account. Because the dispersion and nonlinearity act together along the length of the fibre, a split-step method is used and the fibre is divided into equal segments with the two steps of the method

being nonlinearity acting alone and dispersion acting alone [7]. After the OFDM signal is transmitted through the fibre a square-law PIN photon detector is employed in the receiver to detect the optical signals emerging from the SMF with shot noise and thermal noise included as described in section 2.17. An ideal LPF is employed after the PIN photon detector to ensure that any unwanted part of the signal is not part of the electrical signal sent to the OFDM receiver. The signals from individual ONUs are added in optical field and not optical power.

3.2.5   Simulation parameters

The following parameters were used in simulating a 40 km PTP OFDM upstream system:

- For the OOFDM transceivers, the total number of subcarriers is 64, of which 31 subcarriers in the positive frequency bins are used to carry user data and one subcarrier close to the optical carrier frequency is dropped completely.
- The modulation format taken on all the 31 data-carrying subcarriers is adaptively modulated with BPSK, QPSK, 8-QAM, 16-QAM, 32-QAM, 64-QAM, 128-QAM and 256-QAM.
- The sampling rates of the DAC/ADC are varied in the simulations.
- The CP parameter described in section 2.7 is 25 %.
- The number of QB and the signal clipping level is varied for the simulations.
- A PIN detector with a bandwidth of 12.4 GHz and a receiver sensitivity of -19 dBm is adopted.
- The LPF has a 3 dB bandwidth equal to the baseband OFDM signal bandwidth.
- For simulating DFB based DMLs operating at 1550 nm, the parameters identical to those reported in [5] are shown in Table 1.
- The SMF parameters are detailed in Table 1.

DFB DML		SMF		PIN	
Parameter	**Value**	**Parameter**	**Value**	**Parameter**	**Value**
Cavity length	300 μm	Effective area	80 μm^2	Bandwidth	12.4 GHz
Nonlinear gain coefficient	4x10-23 m^3	Dispersion	17.0 ps/nm/km	PIN sensitivity	-19 dBm
Carrier lifetime	10 ns	Dispersion slope	0.07 ps/nm/nm/km	**Other System Parameters**	
Photon lifetime	3.6 ps	Loss	0.2 dB/km	**Parameter**	**Value**
Confinement factor	0.07	Kerr coefficient	2.35×10^{-20} m^2/W	DACs/ADCs Quantization bits	8 bits
Linewidth enhancement factor	2.5			DACs/ADCs Clipping Ratio	13 dB
Optical frequency	1550nm			DACs/ADCs Sampling speed	4 GS/s
Transparency carrier density	1.5×10^{24}m^{-3}			IFFT/FFT size	64 (cyclic prefix: 16)
Active region cross section	0.066 μm^2				
Auger recombination coefficient	6.5×10-41 m^6/s				
Bimolecular recombination coefficient	1.0×10^{-16} m^3/s				
Group refractive index	3.7				
Phase refractive index	3.2203				
Coupling efficiency	38%				
Linear gain coefficient	7.5×10-20 m^2				
Optical width (vertical)	0.47 μm				
Optical width (horizontal)	1.80 μm				

Table 1: Summary of system parameters.

3.2.6 Results

In the beginning of this section the effects of the ADC and DAC parameters, namely the CR and number of QB, on the maximum achievable capacity in an OOFDM upstream system over 40 km SMF transmission are investigated. Similar experiments for shorter transmission distances and multimode fibre was done in [6] and similar results to those presented here were achieved.
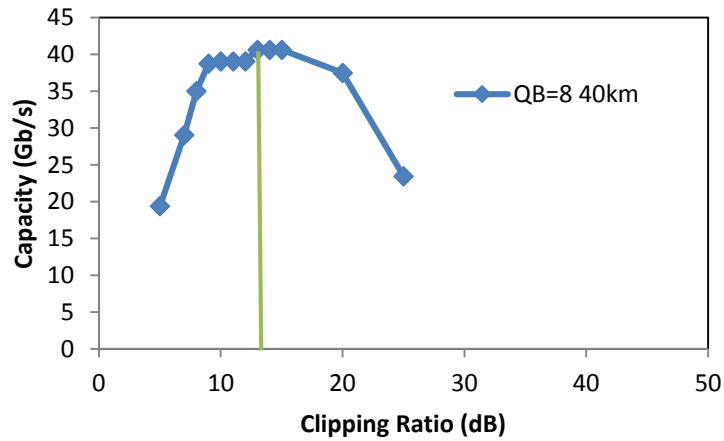
Figure 39: Capacity versus clipping ratio for 40 km SMF transmission with 8 quantization bits.

In Figure 39 the OOFDM system is simulated over 40 km with the QB fixed at 8 with a sweep of the CR with CR defined in section 2.9. The capacity of the system is then maximised through adaptive bit loading on the subcarriers to achieve a maximum capacity at a given CR. The bit loading is done by determining the highest modulation format that each subcarrier can accommodate for a specific system setup and transmission link characteristics. The capacity has reached a maximum if the bit error rate (BER), defined in section 2.21, is at 1×10^{-3}. From Figure 39 it can be seen that if the CR is too low the signal is clipped excessively and this will affect system performance due to important signal information being lost. As the CR increases the signal is not clipped enough to reduce the high peak-to-average power ratio (PAPR) described in section 2.9. If the signal range is to large, due to clipping not being sufficient, the quantization steps will be too large for a given number of quantization bits leading to more quantization noise that will degrade system performance. The optimum CR for an upstream PTP OOFDM system over 40 km SMF is 13 dB to achieve a capacity of 40 Gb/s.
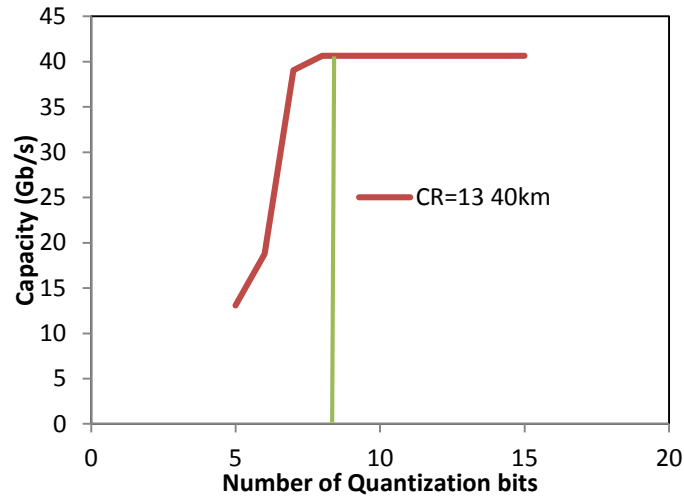
Figure 40: Capacity versus quantization bits for 40 km SMF transmission with a clipping ratio of 13 dB.

In Figure 40 the number of levels for quantization is varied to investigate the minimum number of levels required for maximum capacity in an OOFDM 40 km SMF upstream transmission with an optimised CR of 13 dB. When the QB are too low the range of the signal cannot be sufficiently quantized to achieve good accuracy due to the lack of sufficient number of discrete quantization levels for the given range of the signal. Thus there is a lot of quantization noise present for low number of QB. As the number of bits increase the quantization noise decreases

and reaches a performance ceiling due to other limiting effects in the system becoming dominant. The minimum QB for maximum performance are found to be 8 for an OOFDM 40 km upstream transmission utilising adaptive modulation.
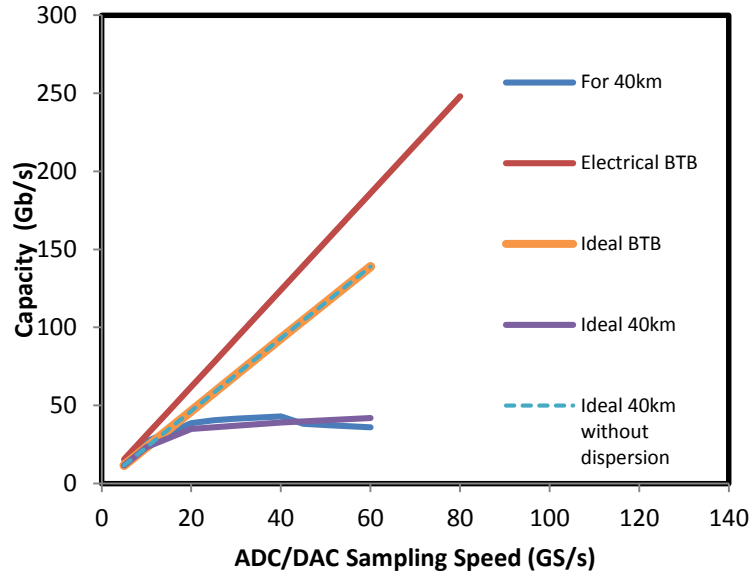
Figure 41: Capacity versus sampling speed.

Armed with the knowledge of the optimum DAC/ADC parameters, the sampling speed limitations of the OOFDM upstream system are investigated. In Figure 41 the DAC/ADC sampling speed is varied with a clipping ratio of 13 dB and 8 QB. To increase the capacity of a system without increasing the number of subcarriers the sampling speed can be increased to increase the bandwidth of the system. By increasing the sampling for an electrical back to back (BTB) system, a linear relationship is seen between capacity and sampling speed. This is due to the increase in system bandwidth due to an increase in the sampling speed even if the number of subcarriers remains constant. This relationship is confirmed in Figure 41 which also shows the optical BTB transmission using an ideal modulator. For the optical BTB transmission the relationship between capacity and sampling speed is still linear but due to the addition of noise sources in the PIN detector the slope of the optical BTB system is less compared to the electrical BTB case. Transmission over 40 km SMF with a DFB based DML is shown in Figure 41 and from 20 GS/s there is a performance ceiling. This ceiling is investigated by plotting the capacity versus sampling speed over 40 km SMF utilising an ideal modulator. From Figure 41 it can be seen that the same performance ceiling occurs. If the dispersion in the fibre is not taken into account the performance is the same as for an optical BTB system. Thus the performance ceiling for 40 km transmission cases with different modulators is purely due to the dispersion and the fact that the cyclic prefix becomes insufficient as ADC/DAC sampling

64

speeds are increased. The maximum sampling speed in the system is governed by the following:

As the sampling speed continues to increase the symbol length will decrease and the time delay compensation introduced by the CP, with the CP a fixed percentage of total symbol length, will decrease. Thus the probability of symbols interfering with each other due to dispersion induces time delays will increase as the sampling speed is increased. The sampling speed is not chosen at the maximum value due to the fact that the ADC/DAC has physical limitations to stop achieving high sampling speeds in practical applications. Keeping practical implementation in mind without compromising on capacity use is made of a sampling speed of 25 GS/s. Figure 41 shows that the chosen value of the sampling speed is in a flat part of the curve.
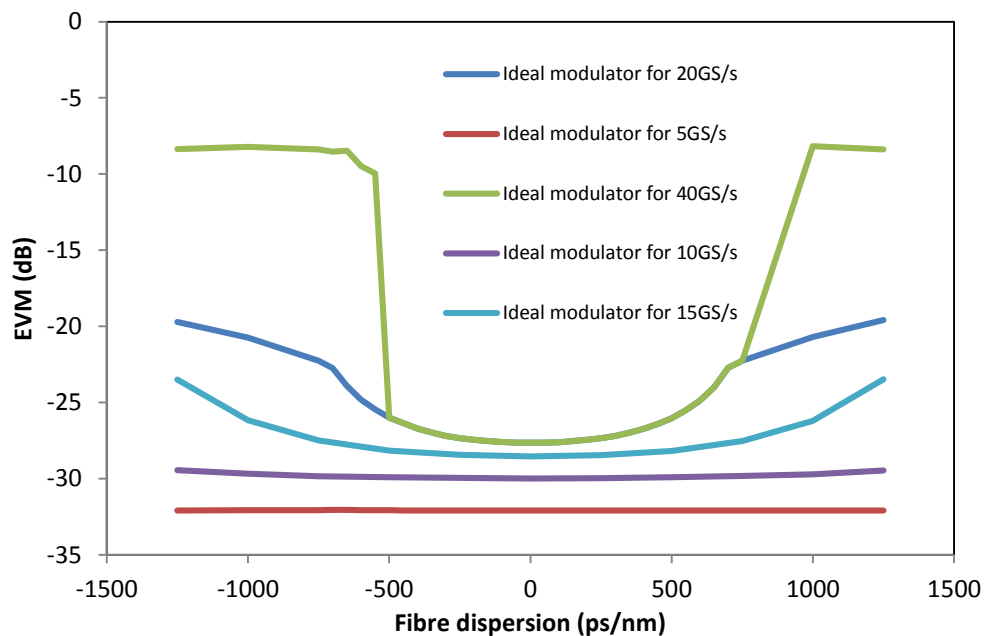
Figure 42: EVM versus fibre dispersion of different sampling speeds.

To show the effect of fibre dispersion on the system as the sampling speed is increased, the fibre dispersion is varied and the resulting error vector magnitude (EVM) is plotted in Figure 42. The EVM (calculated as shown in section 2.21) was chosen rather than BER due to EVM giving a better resolution which enables clearer presentation of the effects of the fibre dispersion. The EVM floor at zero dispersion for different sampling speeds will differ due to the different modulation formats which are used to enable maximum capacity through bit loading. In Figure 42 the increase in dispersion leading to an increased time delay experienced by the transmitted signal starts to affect performance from 15 GS/s onwards and the region

where the delay does not affect the system performance for 40 GS/s is very small. Thus the increase in sampling speed results in the cyclic prefix to become insufficient. The dispersion in the fibre is 17 ps/nm/km. Thus for 40 km the time delay calculated using equation 51 in chapter 2 for a signal with a 12.5 GHz bandwidth is 68 ps. The bandwidth in nanometre (nm) is the optical source bandwidth as described in [8]. A 12.5 GHz bandwidth can be converted to a wavelength difference using the following relation:

$$\Delta\lambda = \Delta f \times \frac{\lambda^2}{c} \quad [40]$$

with $c = 2.997924580 \times 10^8 \ m/s$ the speed of light resulting in $\Delta\lambda = 0.1$nm. The delay compensated for by the prefix is

$$\Delta T_{compentation} = \frac{1}{F_s} \times N_{Prefix} \ [41]$$

with N_{Prefix} the number of samples used for the CP. This gives a total CP length of 4000 ps and is more than sufficient to compensate for the dispersion induced time delay of 68 ps. If the bandwidth were to be increased to, for example 60 GHz, the dispersion induced time delay would be 340 ps and the CP length will be 266 ps which is not sufficient to compensate for the time delay and this will lead to inter-symbol interference (ISI) between the OFDM symbols.

The final parameters that needs to be optimised is the bias current of the DFB based DML and a peak-to-peak driving current. OOFDM upstream transmission with a DFB based DML as modulator over 40 km SMF at a sampling speed of 25 GS/s for different bias and driving current is shown in Figure 43. For bias currents ≤ 30 mA the system capacity decreases sharply as the bias current is decreasing. The smaller bias current reduces the optical output power resulting in inferior performance. For the case of bias currents > 30 mA a capacity ceiling is reached mainly due to frequency chirp. The capacity of the system improves as the drive current is decreased due to the fact that a low drive current can reduce the nonlinearity of the DFB based DML. If for the optimum bias current the drive current is too low the signal will not have sufficient power to be detected properly at receiver and system capacity will reduce.
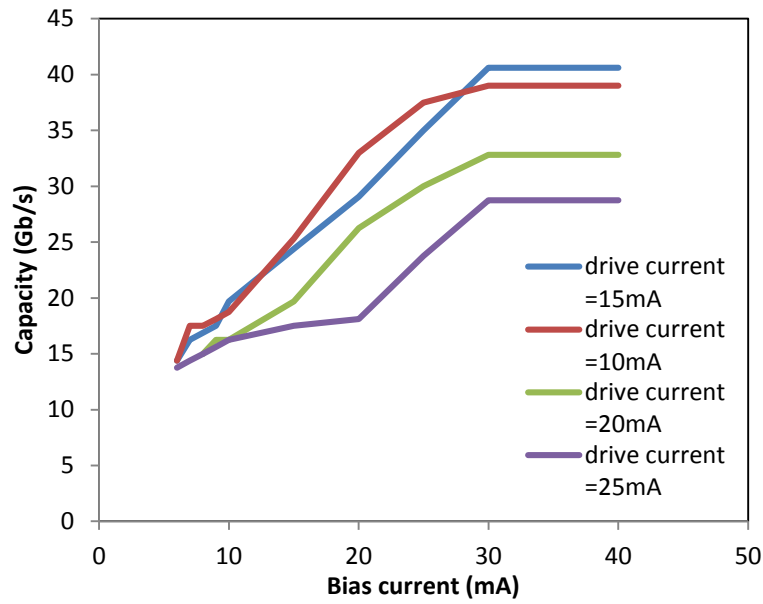
Figure 43: Capacity versus bias current for different DFB drive current.

To conclude, the optimum parameters for an upstream OOFDM 40 km SMF transmission with a DFB-based DML modulator are 8 QB, a CR of 13 dB, a DFB driving current of 15 mA and a DFB bias current of 30 mA at an ADC/DAC sampling speed of 25 GS/s with the PIN having a sensitivity of -19 dBm. Thus an OOFDM upstream system is validated as a good candidate for short reach access networks. The following section describes an investigation of the use of OOFDM in access networks for multiple users in upstream transmission.

3.3 Dependence of the upstream power budget on the number of ONUs in IMDD optical OFDMA PONs

In this section the OOFDMA PON upstream transmission system is validated by comparing simulations results with experimental results. The simulation model is then utilised to investigate the OOFDMA PON and answer two important questions that arise when multiple access is deployed in the optical domain namely:

- Does the number of ONUs affect the minimum wavelength spacing between two adjacent ONUs?
- Does the number of simultaneously accommodated ONUs affect the upstream optical power budget?

To answer these questions, first an upstream OOFDMA PON system is designed and parameters fitted to experimental results. Then the system is scaled up by increasing the number of ONUs and the minimum wavelength spacing between ONUs as well as the overall system power budget will be investigated.

3.3.1 System setup and parameter fitting to numerical model from experimental results
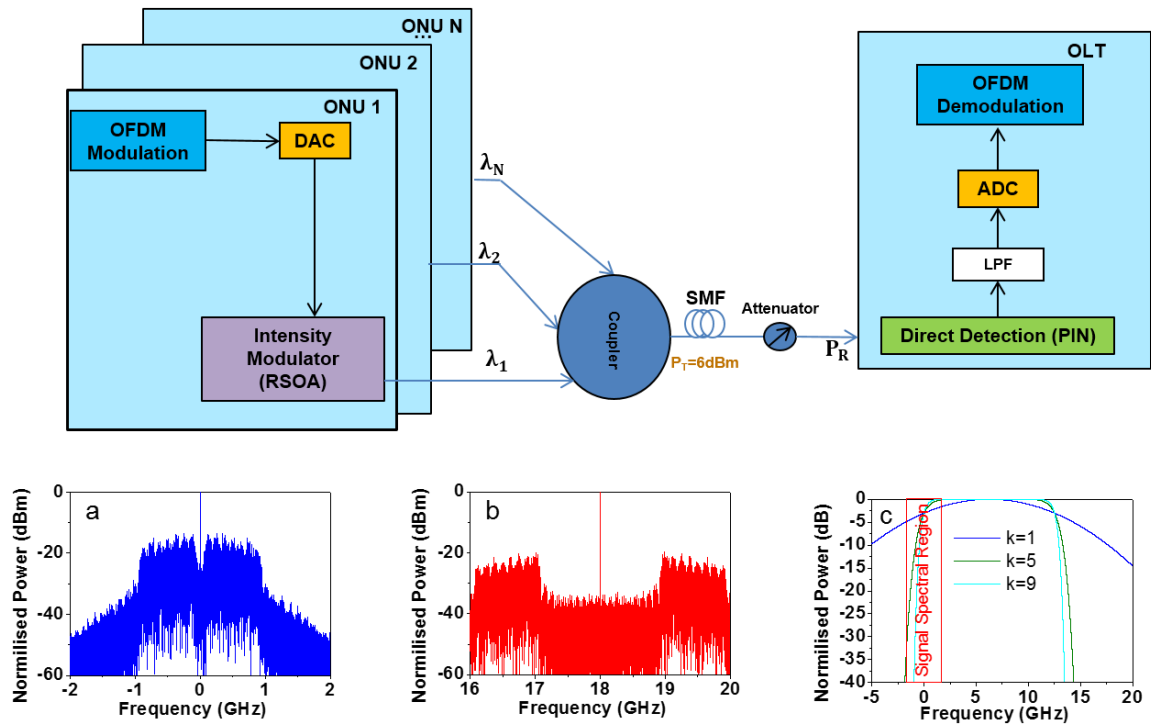
Figure 44: IMDD OOFDMA PON system with frequency spectrums for ONU 1 and ONU2 and the power spectrum of the OBPF for different filter orders.

Figure 44 shows the IMDD OOFDMA PON with RSOA-based colourless ONUs with the number of ONUs ≥ 2. In each of the ONU transmitters, a digital electrical OFDM signal is generated following a digital signal processing (DSP) procedure listed below:

- 64-QAM encoding resulting in an aggregated 11.25 Gb/s upstream signal bit rate.
- 32-point IFFT with 15 data-carrying subcarriers with a 25 % cyclic prefix (CP) insertion and OFDM symbol serialisation.
- A 4 GS/s @8-bit DAC converts the digital OFDM signal into an analogue OFDM signal.

- The output of the DAC is directly modulated with the RSOA-IM operating at a specified wavelength depending on ONU with a bias current of 70 mA and driving current of 4.9 mA.

- After combining all the upstream ONU signals of different wavelengths at a splitter/coupler, the combined OOFDM signal propagates along a 25 km SMF.

In the OLT the following procedure is followed:

- An optical attenuator is applied at the output of fibre to achieve various received optical powers (ROP).

- The signal is detected with a PIN diode in the OLT with a receiver sensitivity of -19 dBm.

- The signal is passed through an ideal LPF with a bandwidth equal to that of the baseband signal.

- A 4 GS/s@8-bit ADC converts the electrical signal from the analogue to digital domain.

- The transmitted data is finally recovered using an inverse procedure of the ONU transmitter and also includes channel estimation as described in section 2.19, synchronisation as described in section 2.20 and BER/EVM as calculated in section 2.21.

To verify and validate the theoretical models used in the upstream transmission system, fittings of experimental results reported in [9] (with all experimental results obtained by Dr X.Q Jin) to numerical simulations is undertaken. Here all experimentally measured component/system parameters adopted can be found in [9] for the RSOA intensity modulator model verified in [10] and DML intensity modulator model verified in [11]. The initial values of all unknown microscopic RSOA-IM/DML-IM parameters are taken from [10, 11] and the parameter values for the RSOA-IM's confinement factor and differential gain and the DML-IM's transparency carrier density are carefully adjusted until excellent agreements between numerical simulations and experimental measurements is achieved. The RSOA-IM's fitted confinement factor is 0.2 from the measured value of 0.45 reported in [9] and the fitted differential gain is 1.5×10^{-20} m^2 from the experimental value of 3×10^{-20} m^2 whilst for the DFB laser, the fitted transparency carrier density is 3.98×10^{24} m^{-3} from the experimentally value of 1.5×10^{24} m^{-3} and the linewidth enhancement factor is 2.5.
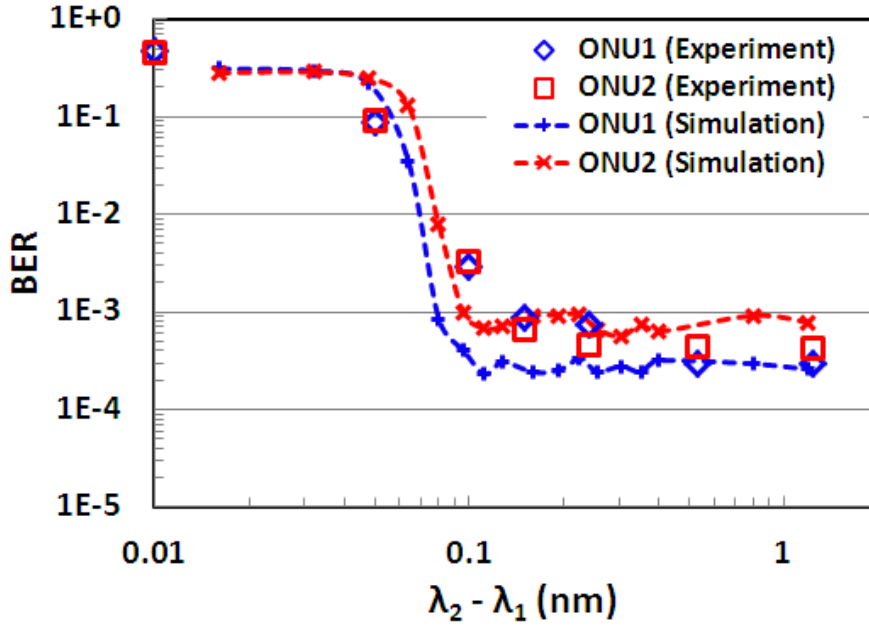
Figure 45: Total channel BER against ONU wavelength spacing at a received optical power of -10 dBm.

In fitting the experimental results, the total number of information-bearing OFDM subcarriers in the simulation is fixed at 15, and owing to the narrow modulation bandwidth of the RSOA-IM, the low frequency subcarriers (1st – 7th) encoded using 32-QAM are assigned to ONU1. The high frequency subcarriers (8th – 15th) encoded using 64-QAM are assigned to ONU2 incorporating the DML-IM. The variation in the upstream optical signal wavelength spacing $\lambda_1 - \lambda_2$, between ONU1 and ONU2 as shown in Figure 45, is achieved by adjusting the wavelength of a 6.5 dBm CW optical beam injected into the RSOA-IM, and the wavelength of the DML-IM is fixed at 1551.18 nm.
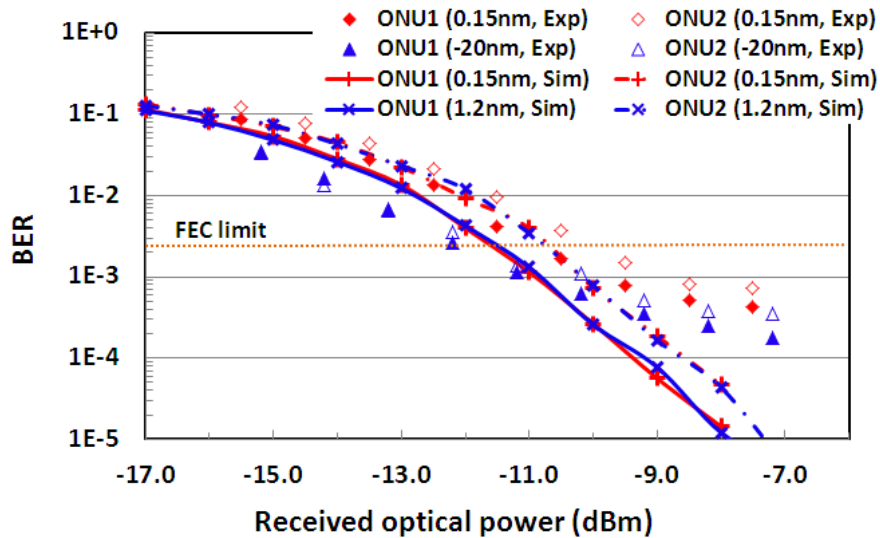
Figure 46: Total channel BER versus received optical power. A RSOA (DFB) intensity modulator is used in ONU 1 (ONU 2). Exp: experiments, Sim: simulations.

In Figure 46 excellent agreement between numerical simulations and experimental measurements is achieved for the received optical power dependent BER for different ONU wavelength spacing. With the parameters thus fitted, simulations for upstream IMDD OOFDMA PONs are performed for a 2, 4, 8, 12 and 15 colorless ONUs. Using Figure 44, the upstream signal transmission process can be briefly described as follows: In the nth ONU transmitter, an electrical digital OFDM signal is generated. The nth ONU conveys data on its pre-assigned subcarriers only, while the ONU sets the amplitudes (powers) of all the remaining subcarriers not assigned to it to be zero. After passing through a 4 GS/s, 8-bit DAC, the digital OFDM signal is converted into an analogue OFDM signal, which is combined with an optimum bias current. The combined electrical signal is employed to directly modulate a RSOA-IM operating at a specified wavelength. The optical power from the RSOA-IM is fixed at P_T/N with P_T being the total optical power launched into the fibre taken to be 6 dBm and N being the total number of accommodated ONUs. After passively combining all the upstream optical signals of different wavelengths at an optical coupler, the combined OOFDM signal propagates along SMF to the OLT. At the OLT receiver, an optical attenuator is used to vary the received optical power. The received optical signal is detected using a PIN diode with a bandwidth of 12.4 GHz and a sensitivity of -19 dBm. After being low-pass filtered, the electrical analogue signal is converted into the digital domain using a 4 GS/s, 8-bit ADC. The received data is finally decoded and the EVM is calculated. The next section presents the results for the minimum wavelength spacing and optical power budget for an upstream OOFDMA PON transmission with RSOA-based intensity modulators.

3.3.2 Results

Based on the verified RSOA-IM model, detailed numerical simulations are first made of the ONU wavelength spacing versus total channel EVM performance as shown in Figure 47. To achieve an aggregated 11.25 Gb/s upstream signal bit rate, 64-QAM is used on all the 15 information-bearing OFDM subcarriers, which are evenly distributed among all the ONUs considered for different cases. When 15/N is not an integer, an extra subcarrier is assigned to one subcarrier is removed from the last ONU. For example, for a 4 ONU PON architecture, the subcarriers assigned to ONU1, ONU2, ONU3 and ONU4 are (1st-4th), (5th-8th), (9th-12th) and (13th-15th), respectively.
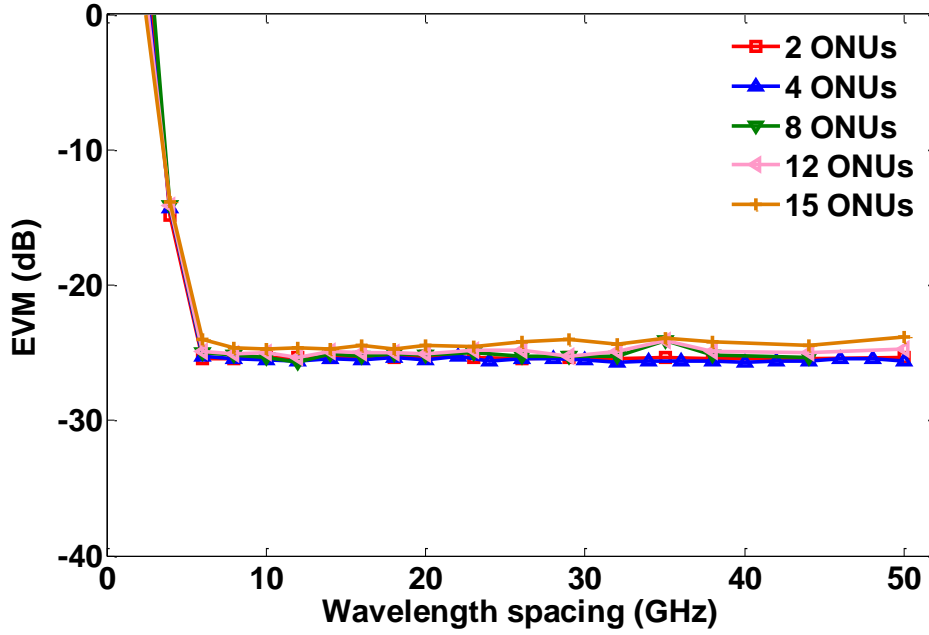
Figure 47: EVM performance versus ONU wavelength spacing, |Δλ|.

In simulating Figure 47 the received optical power is fixed at 0.75 dBm. It can be seen in Figure 47 that, for different numbers of ONUs, almost identical EVM developing trends are observed, which become flat (at values below an EVM of -22 dB corresponding to a FEC limit of 2.3×10^{-3} for 64-QAM) when the ONU wavelength spacing is larger than > 8 GHz. The EVM trend becoming flat at wavelength spacing's larger than > 8 GHz indicates that the minimum ONU wavelength spacing is independent of the number of simultaneously accommodated ONUs, and that the optical beating interference (OBI) (discussed in section 2.16) effect is significant only when wavelength spacing is < 8 GHz.

To better understand the upstream OOFDMA PON system behaviour with multiple ONUs the carrier to signal power ratio (CSPR) as defined in section 2.10 is investigated. Figure 48a shows the received electrical signal spectra for the cases of 2, 4 and 8 ONUs for a fixed received optical power in the OLT receiver and the signal power reduces for an increase in ONUs. Figure 48b shows the CSPR of the received electrical signal for a different number of ONUs with RSOA-IMs and increases as the number of ONUs increase. From the definition in section 2.10 it is clear the CSPR will increase due to the carrier power being the sum of all the powers of the different carriers from the different ONUs.
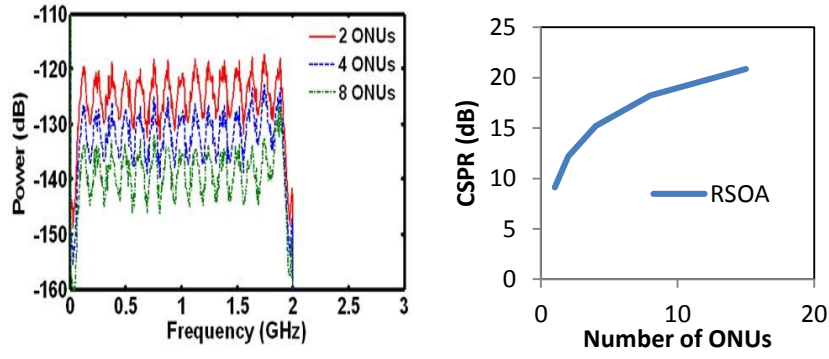
Figure 48: (a) Electrical signal power spectra measured in the OLT for different number of ONUs. (b)Electrical CSPR in OLT versus number of ONUs for a 25 km SMF transmission with a fixed received optical power of 0.75 dBm.

Another factor to consider to enhance understanding of utilising multiple upstream PONs with IMDD is the high PAPR associated with OFDM (discussed in section 2.10) and to establish how that relates to OOFDMA PON systems. The high PAPR is inherently less in OFDM in a PON system utilising dynamic bandwidth allocation (DBA) due to the fact that each ONU will only have a few subcarriers with data, compared to a PTP system with data on all subcarriers. The PAPR reduction is shown in Figure 49a where the average PAPR for all ONUs decreases with an increase in the number of ONUs. Figure 49a also shows the PAPR for the first ONU and confirms the PAPR reduces for that specific ONU. The reduction in PAPR is due to fewer data carrying subcarriers for each ONU as the number of ONUs in the system increases. The relationship between PAPR and ER established in section 2.10 shows that a decrease in the PAPR will lead to an increase in the ER, as can be seen comparing Figure 49a and Figure 49b for and ideal modulator. Figure 49b shows the average ER of ONUs and the ER for the first ONU and both increase with the number of ONUs increasing. In relation to the case at hand, Figure 49c shows the average ER for RSOA based ONU 1 slightly increases. An increase is also observed for the average ER of all ONUs in Figure 49c. The ER for ONU one is also plotted and shows a greater increase in ER as the number of ONUs is increased.
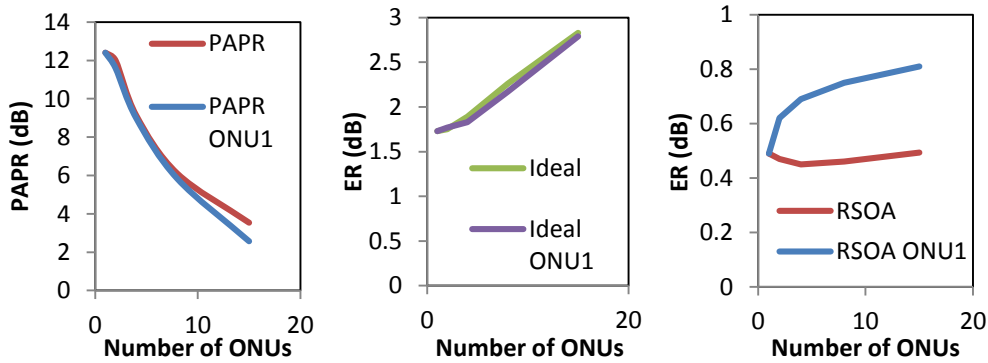
Figure 49: Number of ONUs versus (a) PAPR ;(b) ER for Ideal modulators; (c) ER for RSOA modulators.

For various numbers of colourless ONUs simultaneously accommodated in 25 km SMF IMDD OOFDMA PON systems, the received optical power versus total upstream EVM is shown in Figure 50 with an ONU wavelength spacing fixed at 18 GHz to ensure that the OBI is insignificant in the system. It can be seen in Figure 50 that, for both the 25 km SMF and optical BTB cases, the minimal received optical power required for achieving the FEC limit (2.3×10^{-3}), P_{FEC}, increases with increasing number of ONUs.
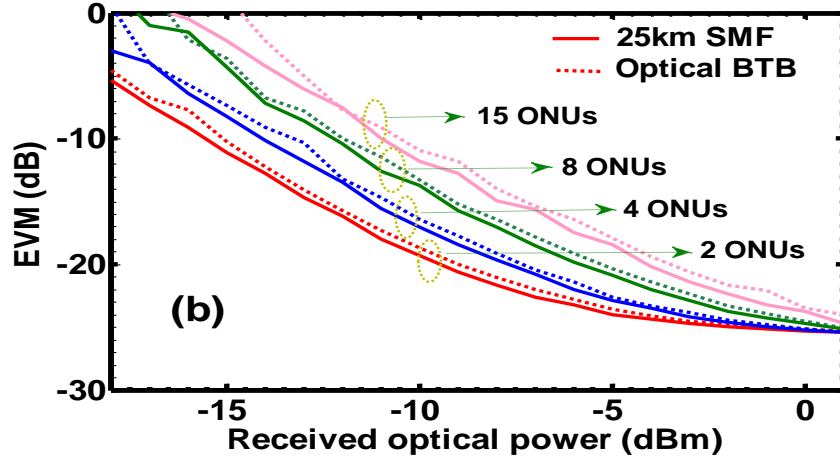
Figure 50: EVM performance versus received optical power at |Δλ| of 18 GHz for optical BTB and 25 km SMF transmission.

In Figure 50, for the 25 km SMF transmission compared to optical BTB systems, a negative power penalty of about -0.5 dB is observed for different cases. This is due to the fact that the negative frequency chirp associated with the RSOA-IM is compensated by the positive chromatic dispersion associated with SMFs [12].
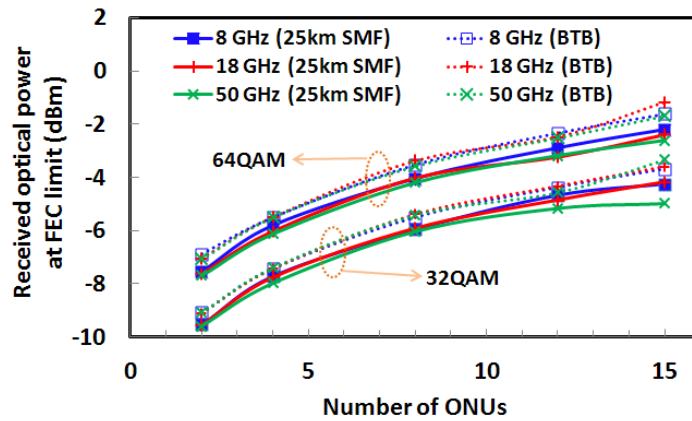
Figure 51: Received optical power at the FEC limit versus the number of ONUs.

To clearly demonstrate such a significant behaviour, Figure 51 is plotted to explicitly show the dependence of P_{FEC} upon the number of ONUs for various ONU wavelength spacing of 8, 18 and 50 GHz and also for 32-QAM modulation. It is very interesting to note in Figure 51 that P_{FEC} increases almost linearly with the number of ONUs, and that P_{FEC} is increased by approximately 1.9 dB when the number of ONUs is doubled. The same trend is observed for 32-QAM modulation except for the P_{FEC} that is lower due to a lower modulation format used on all subcarriers. This implies that, for a specific PON system, doubling the number of ONUs gives rise to a 1.9 dB reduction in upstream power budget.
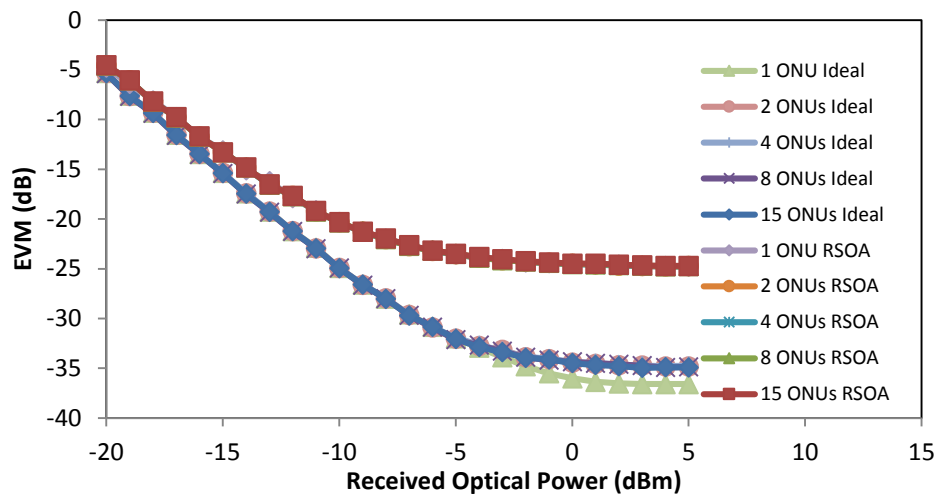
Figure 52: EVM performance for electrically combined OFDM signals from each individual ONU incorporating different types of IMs.

Equation 46 in section 2.10 suggests that a CSPR increase occurs only when individual electrical-to–optical (E/O) conversion takes place in each ONU. When all electrical ONU signals are combined directly in the electrical domain and the combined electrical signal is subsequently used to modulate the RSOA-IM or ideal IM, the total upstream EVM performance is independent of the variation in the number of ONUs, N. This expectation is verified in Figure 52 where almost perfectly overlapped EVM curves are present for different number of ONUs, regardless of the type of the IMs considered. The major physical mechanism underpinning the *N* dependent upstream power budget is the multiple independent E/O conversion induced increase in CSPR of OOFDM signals, rather than any impairments caused by E/O components. Here it is also worth mentioning that, theoretically speaking, when the number of ONUs is doubled, the effective OOFDM signal power from each ONU should be decreased by 1.5 dB (half of 3 dB in the electrical domain) rather than the value of 1.9 dB, as observed in Figure 51. Such a 0.4 dB difference is mainly contributed by the multiple access interference (MAI) effect associated with the nonlinear E/O and O/E conversion, as a 0.7 dB

MAI induced increase in received optical power for upstream transmission is measured experimentally in an 11.25 Gb/s over 25 km SMF IMDD OOFDMA PON [13].
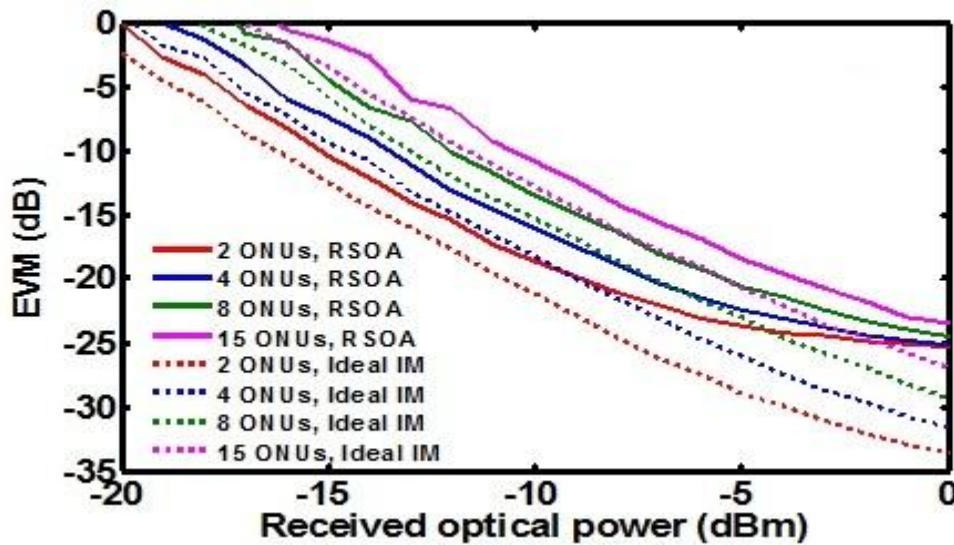
Figure 53: Comparisons of the EVM performance of the RSOA-IM and ideal IM for optical BTB systems.

The observed EVM floor occurring at an EVM of -25 dB for both 25 km SMF and optical BTB in Figure 50 is mainly due to the modulation nonlinearity of the RSOA-IM, as evidenced by the fact that such a floor disappears when the RSOA-IM is replaced by an ideal IM, as shown in Figure 53.

The results presented in this section have shown that in IMDD OOFDMA PONs with RSOA-IM's, the minimum ONU wavelength spacing is independent of the number of simultaneously accommodated ONUs, and that the OBI effect is significant only when wavelength spacing is < 8 GHz. Results also show that doubling the number of ONUs gives an 1.9 dB reduction in upstream power budget, and that the corresponding upstream power budget and the minimum ONU wavelength spacing required for eliminating the OBI effect are independent of the number of ONUs. In the next section further investigations into the effects of dispersion and chirp on the system performance and minimum wavelength spacing are performed.

3.4 Investigation of the effects of dispersion and chirp on the optical bandwidth and wavelength spacing of upstream OFDMA PONs

With Orthogonal Frequency Division Multiple Access (OFDMA) several users can share communication resources such as bandwidth with typical channel spacings of 25 GHz [14].

In section 3.3.2 a minimum channel spacing of 8 GHz was confirmed. In this section, a comparison is made between DFB based DMLs and Reflective Semiconductor Optical Amplifiers (RSOAs) as possible candidates for ONU modulators. An investigation is made into the dispersive effects of the channel by compensating each ONU for the dispersion induced time delay showing that this compensation improves performance for larger optical bandwidths with RSOAs as modulators compared to DFBs. A comparison is made of the limit on the optical bandwidth size imposed by the dispersion and chirp (due to the increase in optical bandwidth) as the number of ONUs are increased for RSOAs and DFB lasers as intensity modulators. The comparison shows the RSOA intensity modulator to be an excellent candidate for modulators in future PON networks [15].

3.4.1 Transmission system model and parameters

In Figure 44 the setup of the simulated upstream OOFDMA PON system is shown using multiple ONUs, each using an RSOA or DFB as intensity modulator. In each ONU data is generated and modulated with a 64-QAM modulation format corresponding to 11.25 Gb/s and pilot data added for channel estimation and equalisation. The data is subject to a 32-point IFFT corresponding to the 32 subcarriers of which the first subcarrier is set to zero to ensure no DC component is present in OFDM signal. The next 15 subcarriers are used for the transmitted data encoded with 64-QAM. The remaining subcarriers carry the complex conjugate of the data subcarriers to ensure Hermitian symmetry for real valued transmission. Then a CP of 25 % (giving a length of 2 ns) or 50 % (giving a length of 4 ns) is inserted, parallel to serial conversion performed and an 8-bit DAC running at 4 GS/s implemented in the transmitter. The RSOA-based intensity modulators, representative for InGaAsP semiconductor materials operating at a wavelength of 1550 nm with a driving current of 70 mA and bias current of 4.9 mA corresponding to experimental results, converts the electrical signal to an optical signal [9]. For the cases where a DFB based DML is used as intensity modulator the driving current is 1.1 mA and the bias current 36 mA corresponding to experimental values in [9]. The total optical power into the coupler is fixed at 6 dBm, with each ONU having equal power. The 25 km SMF was simulated using a split-step method with the same parameters as described in section 3.2.5. The PIN diode at the OLT has a sensitivity of -19 dBm (corresponding to 10 Gb/s NRZ). At the OLT an optical attenuator is used to vary the received optical power (ROP) and is set to 0.75 dBm for simulating the results below. Performance measurements are measured in Error

Vector Magnitude (EVM) due to the limited number of symbols used for simulation and to achieve a higher resolution compared to BER.

3.4.2 Results

First the RSOA based OOFDMA PON system is investigated. Then the RSOA based intensity modulators are replaced with DFB based DML intensity modulators and the effects of chirp and dispersion are studied.
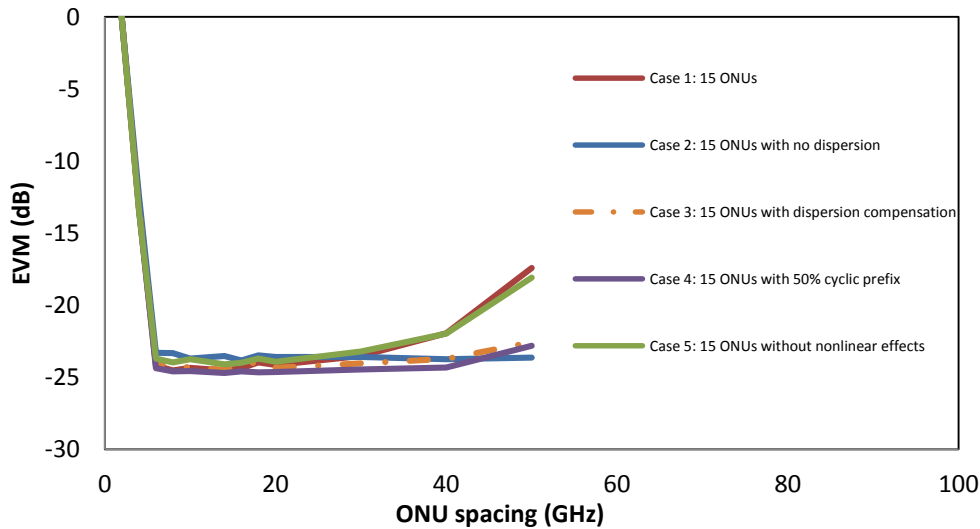
Figure 54: EVM versus ONU spacing for RSOA based OOFDMA PON system with different ONUs for upstream transmission.

Figure 54 shows the EVM performance versus wavelength spacing between the ONUs for five cases utilising the RSOA based OOFDMA PON system for a different number of ONUs for upstream transmission. For case 1 the performance of the system is measured for RSOA-based modulators over 25 km with 15 ONUs with dispersion and nonlinear effects considered in the fibre while increasing the wavelength spacing and the performance improves until 8 GHz spacing between ONUs is reached. For case 1 an EVM ceiling value is reach for wavelength spacing's between 8 GHz and 20 GHz. The EVM performance starts to degrade gradually from 30 GHz to 50 GHz spacing between ONUs below a value of -22.9 dB which for 64-QAM corresponds to a BER of 1×10^{-3}. For a 2 ONU system with 50 GHz spacing the total optical bandwidth is 52 GHz and for the same spacing for 15 ONUs the total optical bandwidth goes up to 702 GHz equivalent to a $\Delta\lambda$ of 5.6 nm. Thus the signal from the 15th ONU will experience a delay due to dispersion of

$$\Delta T_{disp} \approx D \times L \times \Delta\lambda \quad [42]$$

which here is 2380 ps. The CP length can be calculated by multiplying the number of samples used for the CP, in this case 8 samples, with the time between samples Δt calculated as $\Delta t = 1/f_s$ with f_s the sampling frequency. The CP length is 2000 ps for a sampling frequency of 4 GHz. To avoid ISI the following condition needs to be met:

$$\Delta T_{disp} < \Delta T_{cyclic} \ \ [43]$$

where ΔT_{cyclic} is the CP length calculated as 2000 ps which is smaller than 2380 ps. The insufficient CP length leads to ISI between the OFDM symbols for the 15 ONU case with a large optical bandwidth. The ISI will cause the EVM performance to degrade. The fact that the degradation in performance is due to ISI caused by dispersion is confirmed by case 2 in Figure 54 where the system is considered without the effects of dispersion in the fibre and no EVM performance degradation is observed. So due to dispersion, even with a small wavelength spacing but with multiple ONUs the system will have a limit on the size of the total optical bandwidth.

To confirm this effect is mainly due to dispersion, case 5 in Figure 54 shows the performance as a function of the wavelength spacing. Case 5 considers a system without nonlinear effect but with dispersion. Case 5 is seen to be similar to case 1 in Figure 54 which includes nonlinear effects such as self-phase modulation (SPM) due to the Kerr effect. The fact that case 1 and case 5 is similar is proof that the degrading of EVM performance is purely due to dispersion. Case 4 compared case 1 in Figure 54 shows that in the case of a large optical bandwidth doubling the CP from 25 % to 50 % for 15 ONUs over 25 km improves the EVM at a wavelength spacing with 4.8 dB.
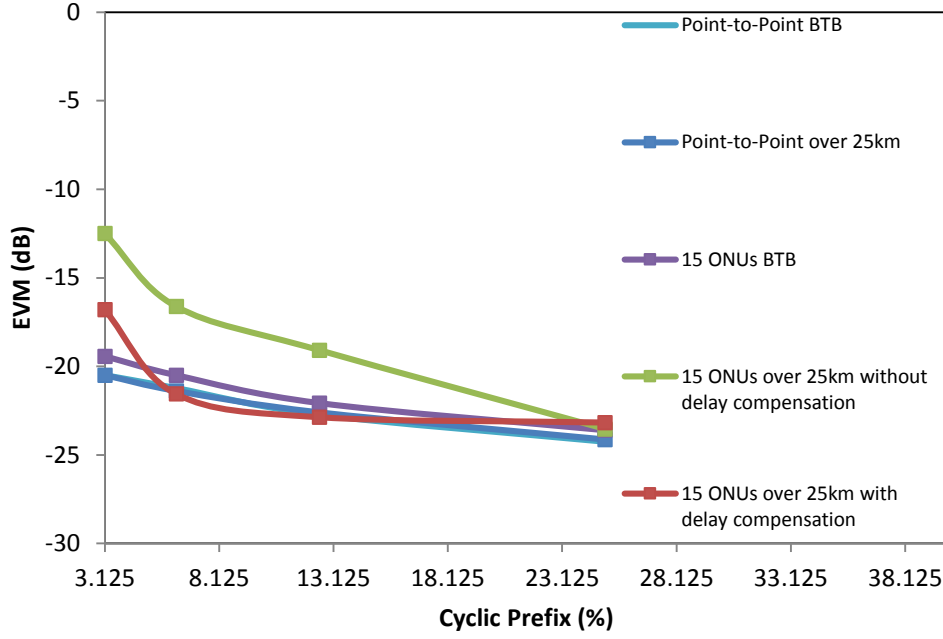
Figure 55: EVM versus percentage cyclic prefix.

To further investigate the effect of ONU wavelength spacing on the efficiency of the CP, the CP length is varied for a PTP case and a multiple wavelength case with 15 ONUs . The relevant EVM performance is plotted in Figure 55. For the PTP case in Figure 55 the EVM varies by 3 dB for both the BTB and 25 km SMF transmission and has almost identical trends as the CP is varied from 3.125 % to 25 % of an OFDM symbol's length. For the BTB case with 15 ONUs only a slight reduction in overall performance is seen with only a 3 dB variation in EVM over the varied CP range. If the multiple wavelength 15 ONUs transmission is sent over 25 km SMF the dispersion causes an EVM variation of 11 dB over the varied cyclic prefix length of 3.125 % to 25 % of the OFDM symbol.

This confirms that if the optical bandwidth is large due to large wavelength spacing the CP length becomes insufficient. The optical bandwidth of the signal will also be large for the case where the ONU wavelength spacing is small but a large number of ONUs are present in the system. For this scenario the same bandwidth limitations will be valid for a system with fewer ONUs but with a larger wavelength spacing. To avoid an increase in the overhead of the system due to an extended CP the the time delay due to dispersion (ΔT_{disp}) is compensated in the individual ONUs by applying a time delay (ΔT_{comp}) in the digital time domain to each ONU signal so that $\Delta T_{comp} = \Delta T_{disp}$. Although the granularity of the compensation can only be as small as the sample interval this compensation still improves the performance of the RSOA based PON system as shown in Figure 55. In Figure 55 the delay compensation decreases the

EVM variation over the CP range of 3.125 % to 25 % from 11 dB to 6 dB. The overall improvement in the system can be seen in Figure 54 between case 2 and case 4.
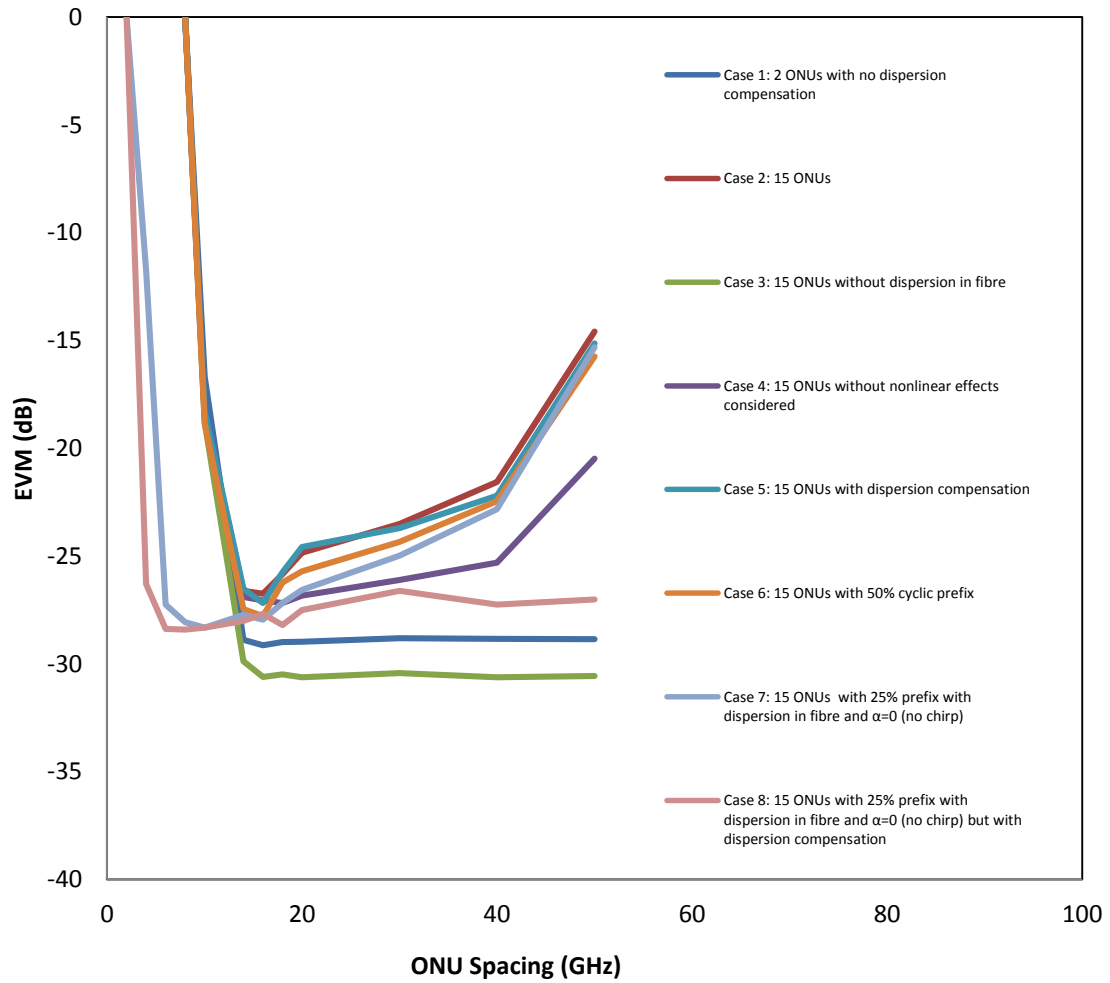
Figure 56: EVM versus ONU spacing for DFB based OOFDMA PON system with different ONUs for upstream transmission over 25 km SMF.

An investigation has also been made into the DFB based DML as modulator in a multiple wavelength upstream transmission. In Figure 56, case 1 is for the ONU spacing versus EVM for 2 ONUs over 25 km SMF. It is seen that the EVM performance approaches a floor value at -29 dB with a minimum wavelength spacing of and 18 GHz. In Figure 56, case 2 reaches an EVM floor at -27 dB at a wavelength spacing of 18 GHz, after which the EVM degrades rapidly from 20 GHz wavelength spacing onwards. To identify the effects which contribute to this degradation in performance case 3 explores the 25 km transmission without dispersion. The EVM floor in case 3 is -30 dB and the minimum wavelength spacing is 18 GHz. If case 3 is compared to case 1 the EVM floor is -3 dB lower and this is mainly due to the improved ER due to the reduced PAPR when the number of ONUs increase from 2 to 15 as shown in Figure 49. The improvement in performance due to an improved ER in an IMDD system utilising a

DFB based DML is confirmed in [16]. Case 4 is for multiple wavelength transmission of 15 ONUs over 25 km SMF without considering the nonlinear effects. It is observed that the degrading of the EVM performance due to the nonlinear effects is relatively small compared to the EVM increasing due to dispersion in the optical link. For case 4 the minimum wavelength spacing is 18 GHz. The time delay compensation in case 4 of Figure 54, is used for case 5 in Figure 56 and is found not to improve the EVM performance for a larger optical bandwidth. The increase in CP from 25 % to 50 % in case 6 in Figure 56 also shows no improvement in performance. When the linewidth enhancement factor α is set to zero to simulate a DFB based DML without chirp effect, case 7 in Figure 56, we still see the degradation in performance for larger optical bandwidths. It is interesting to note that the minimum wavelength spacing for the DFB PON system decreases from 18 GHz to about 8 GHz if no chirp is considered. When dispersion compensation is applied to the system in case 8 in Figure 56, the compensation improves the EVM performance with larger wavelength spacing.

As such, an investigation was made into the possibility of compensating for the dispersion induced time delay. Time delay compensation is suggested instead of increasing the cyclic prefix. The difference in minimum wavelength spacing between the RSOA-based and DFB based optical systems investigated in Figure 54 and Figure 56 showed that the EVM performance approaches a floor value for both the RSOA and the DFB laser for a transmission for the case of 2 ONUs, with 8 subcarriers and 7 subcarriers assigned to each ONU respectively. The minimum wavelength spacing value for the two different modulators is independent of the number of ONUs and is significantly smaller for the RSOA. The minimum wavelength spacing value is determined by the amount of beating between the ONUs in the direct detection process and the values are 8 GHz for the RSOA and 18 GHz for the DFB laser.

3.5 Conclusions

In this chapter the optimum parameters for an upstream OOFDM 40 km SMF transmission with a DFB based DML modulator have been identified. The optimum DFB based system parameters are 8 QB, a CR of 13 dB, a DFB driving current of 15 mA and a DFB bias current of 30 mA. The ADC/DAC sampling speed is fixed at 25 GS/s with the PIN having a sensitivity of -19 dBm. The OOFDM upstream system was validated as a good candidate for short reach access networks and provided a basis to investigate the use of multiple wavelength ONUs in the upstream utilising OOFDM in each ONU and combining the signals from the upstream ONUs in the optical domain passively to achieve multiple access. This resulted in aggregated

11.25 Gb/s over 25 km SSMF IMDD OOFDMA PONs incorporating RSOA-IM based colourless ONUs where excellent agreements have been obtained between real time upstream experimental measurements and numerical simulations in terms of BER performances as functions of both ONU wavelength spacing and received optical power. Making use of experimentally verified theoretical models and component/system parameters, extensive numerical explorations have been undertaken, for the first time, of the impact of the number of ONUs on both upstream optical power budget and minimum ONU wavelength spacing as published in [17] . It has been shown that the minimum ONU wavelength spacing required for eliminating the OBI effect is independent of the number of ONUs, and that doubling the number of ONUs simultaneously accommodated gives a 1.9 dB reduction in upstream power budget. Further investigation into the effects of dispersion, nonlinear effects and chirp in the OOFDMA PON was done with a RSOA and DFB based intensity modulator. For the DFB based DML the dispersion effect enhanced by the chirp in the modulator is too severe to be compensated for and is thus unsuitable for optical OFDMA PONs with large optical bandwidths. Due to not having a limit on the performance because of chirp - as is the case in the DFB based DML system - an RSOA based PON system is more suited for OOFDMA PON system with a high number of ONUs. Although the minimum wavelength spacing is determined by the beating in the system the chirp also causes the minimum wavelength spacing value for a DFB PON system to be much higher than that of a RSOA PON system due to the increased spreading of the noise-like OFDM signals. For the RSOA case the dispersion effects due to increased optical bandwidth for PON systems can be successfully compensated by implementing a delay proportional to the ONU's position in wavelength relative to the first ONU to ensure the CP to be sufficient to combat ISI without increasing the CP at the cost of data throughput of the system. The small wavelength spacing of a RSOA intensity modulator compared with that of a DFB makes the RSOA an excellent candidate for use in spectrally efficient next generation IMDD OOFDMA PON systems.

3.6 References

[1]   *J. Wei, "Intensity Modulation of Optical OFDM Signals Using Low-Cost Semiconductor Laser Devices for Next-Generation PONs", Electronic Engineering, Bangor University, 2010.*

[2]   *E. Sasaoka, "Optical fibres for future high capacity networks", in Optoelectronics and Communications Conference (OECC), 2010, pp. 508-509.*

[3]   *H. S. Chung, Y. G. Jang, and Y. C. Chung, "Directly modulated 10-Gb/s signal transmission over 320 km of negative dispersion fiber for regional metro network", Photonics Technology Letters, IEEE, vol. 15, pp. 1306-1308, 2003.*

[4]   *L. G. Kazovsky, W. T. Shaw, D. Gutierrez, N. Cheng, and S. W. Wong, "Next-Generation Optical Access Networks", Journal of Lightwave Technology, vol. 25, pp. 3428-3442, 2007.*

[5]   *P. M. Lane, K. A. Shore. and J. M. Tang, "Transmission performance of adaptively modulated optical OFDM signals in multimode fibre links", IEEE Photonics Technology Letters, vol. 18, pp. 205-207, Jan. 2006.*

[6]   *P. M. Lane, K. A. Shore. and J. M. Tang, "Maximizing the Transmission performance of adaptively modulated optical OFDM signals in multimode fibre links by Optimizing Analogue-to-Digital Converters", Journal of Lightwave Technology, vol. 18, pp. 787-798, March 2007. [7] G. P. Agrawal, "Nonlinear Fibre Optics", Academic Press, 1995.*

[7]   *G. P. Agrawal, "Nonlinear Fibre Optics ", Academic Press, 1995.*

[8]   *G. P. Agrawal, "Fiber-Optic Communication Systems", Wiley, 2002.*

[9]   *X. Q. Jin and J. M. Tang, "Experimental Investigations of Wavelength Spacing and Colorlessness of RSOA-Based ONUs in Real-Time Optical OFDMA PONs", Journal of Lightwave Technology, vol. 30, pp. 2603-2609, Aug. 2012.*

[10]   *J. L. Wei, A. Hamié, R. P. Gidding, E. Hugues-Salas, X. Zheng, S. Mansoor, et al., "Adaptively modulated optical OFDM modems utilizing RSOAs as intensity modulators in IMDD SMF transmission systems", Optics Express, vol. 18, pp. 8556-8573, 2010.*

[11]   *K. A. Shore and J. M. Tang, "30-Gb/s Signal Transmission Over 40-km Directly Modulated DFB-Laser-Based Single-Mode-Fiber Links Without Optical Amplification and Dispersion Compensation", Journal of Lightwave Technology, vol. 24, pp. 2318-2327, June 2006.*

[12]   *X. Zheng, X. Q. Jin, R. P. Giddings, J. L. Wei, E. Hugues-Salas, Y. H. Hong, et al., "Negative Power Penalties of Optical OFDM Signal Transmissions in Directly Modulated DFB Laser-Based IMDD Systems Incorporating Negative Dispersion Fibres", IEEE Photonics Journal, vol. 2, pp. 532-542, 2010.*

[13]   *X. Q. Jin, E. Hugues-Salas, R. P. Giddings, J. L. Wei, J. Groenewald, and J. M. Tang, "First real-time experimental demonstrations of 11.25Gb/s optical OFDMA PONs with adaptive dynamic bandwidth allocation", Optics Express, vol. 19, pp. 20557-20570, Oct. 2011.*

[14]   J. Y. Kim, S. R. Moon, S. H. Yoo and C. H. Lee, "DWDM-PON at 25 GHz channel spacing based on ASE injection seeding", Optics Express, vol. 20, pp. B45-B51, 2012.

[15]   J. L. Bangjiang Lin, Hui Yang, Yangsha Wan, Yongqi He, Zhangyuan Chen, "Comparison of DSB and SSB transmission for OFDM-PON", Optical Fiber Communication Conference (OFC), pp. 1-3, 2012.

[16]   C. Sanchez, J. L. Wei, R. P. Giddings, E. Hugues-Salas and J. M. Tang, "Significant improvements in optical power budgets of real-time optical OFDM PON systems", Optics Express, vol. 18, pp. 20732-20745, 2010.

[17]   J. Tang, X. Jin, J. Groenewald, E. Hugues-Salas and R. P. Giddings, "Dependence of Upstream Power Budget on the Number of ONUs in IMDD Optical OFDMA PONs", in Optical Fiber Communication Conference/National Fiber Optic Engineers Conference, Anaheim, California, 2013, p. JW2A.73.

4 Chapter 4: Investigation of efficient techniques for improving multiple wavelength OOFDMA PON in upstream transmission

4.1 Introduction

In the previous chapter it was established that the minimum optical network unit (ONU) wavelength spacing required for eliminating the optical beating interference (OBI) effect is independent of the number of ONUs, and that doubling the number of ONUs simultaneously accommodated gives a 1.9 dB reduction in upstream power budget. In this chapter investigations are presented of the effect of optical filtering in upstream multiple wavelength optical orthogonal frequency division multiple access (OOFDMA) passive optical network (PON) with reflective semiconductor optical amplifier (RSOA) based intensity modulators. Optical filtering is an efficient technique in terms of system complexity for further improving the capacity versus reach performance of OOFDMA PONs with adequate optical power budgets. The effect of the optical filtering on the minimum ONU wavelength spacing is thus also investigated to determine if the measure of capacity versus reach can be improved for an OOFDMA upstream system.

4.2 OOFDMA PON multiple wavelength upstream transmission utilising optical filter-induced single sideband transmission.

Here optical band pass filter parameters are calculated to optimise the OOFDMA PON upstream power budget for different numbers of ONUs. The effect of optical filtering on the capacity versus reach performance of a two ONUs and fifteen ONUs system is also investigated. Optical band pass filters (OBPFs) are inserted at the modulated output of each ONU to suppress one of the sidebands of the optical signal in order to reduce subcarrier-subcarrier beating. A second benefit of OBPF is the suppression of the carrier that will lead to a reduced carrier to signal power ratio (CSPR). Thus the OBPF is evaluated as a possible candidate as an effective technique of improving overall upstream OOFDMA system performance.

4.2.1 Transmission system model and parameters
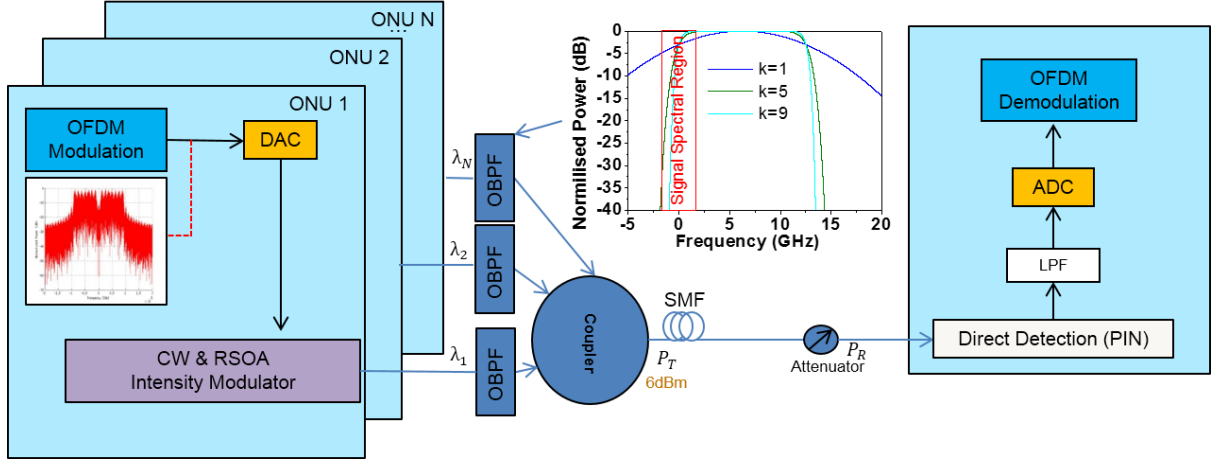
Figure 57: System setup diagram for OOFDMA intensity modulation direct detection (IMDD) upstream transmission with an insert of a super Gaussian optical filter power transfer functions for different filter orders.

The transmission model is shown in Figure 57 and is identical to that presented in Figure 38 in chapter 3.2 except for the OBPFs inserted at the outputs of each ONU. Parameters for the system are also identical to those of the system described in chapter 3.2.1; the electrical bandwidth of the system is 2 GHz. From [1] it is shown that the upstream optical power budget of an IMDD OOFDM can be considerably improved by introducing an optimised frequency-offset optical super-Gaussian filter immediately after the RSOA intensity modulator in each ONU transmitter. As it is possible to compensate for the group delay of the filter by using an all-pass optical filter as shown in [1] that will not attenuate the gain of the frequencies but will change the phase relationship between various frequencies thus changing group delay, only filter power transfer functions are considered in this chapter. The super Gaussian OBPF adopted in this chapter has a power transfer function of the form

$$|H(f)|^2 = e^{[ln\left(\frac{1}{2}\right) \times (\frac{f-f_0}{f_{BW}/2})^{2k}]} \qquad [44]$$

The 3 dB bandwidth is defined by f_{BW} and k represents the order of the filter. When k = 1 equation 1 represents a normal Gaussian optical filter. The f_0 term represents the central frequency of the filter. In the inset of Figure 57 the power transfer functions for different orders of the Gaussian filter are shown. By using optimised parameters for the wavelength offset and filter orders, optical single sideband (SSB) can be achieved at the output of each ONU resulting in optimum carrier and signal sideband suppression. Due to the single sideband the direct detection process has fewer optical frequency components to cause optical beating interference.

4.2.2 Results

Here the effect of the order of the filters for different number of ONUs is investigated. First the impact of the optical filter order on the upstream power budget is explored in Figure 58 with the bandwidth and frequency-offset of the optical super Gaussian filters fixed at 12.5 GHz (0.1 nm at a wavelength of 1550 nm) and 6.25 GHz, respectively. Figure 58 shows that, to achieve the best EVM performance, there exists an optimum filter order of approximately 5-independent of the number of ONUs.
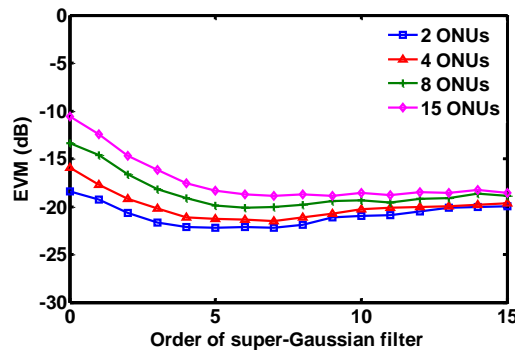
Figure 58: EVM performance versus filter order for different number of ONUs.

The filter frequency-offset effect on the upstream EVM performance is investigated and the optical carrier attenuation α_0 is defined as

$$\alpha_0 = 20 \times log_{10}(|H(f)|^2) \quad [45]$$

with α_0 the attenuation of the carrier at the optical carrier frequency. For a filter with a filter bandwidth of 12.5 GHz and a frequency-offset of 6.25 GHz the α_0 corresponds to -3 dB and a frequency-offset of 7.55 GHz to a α_0 of -20 dB.
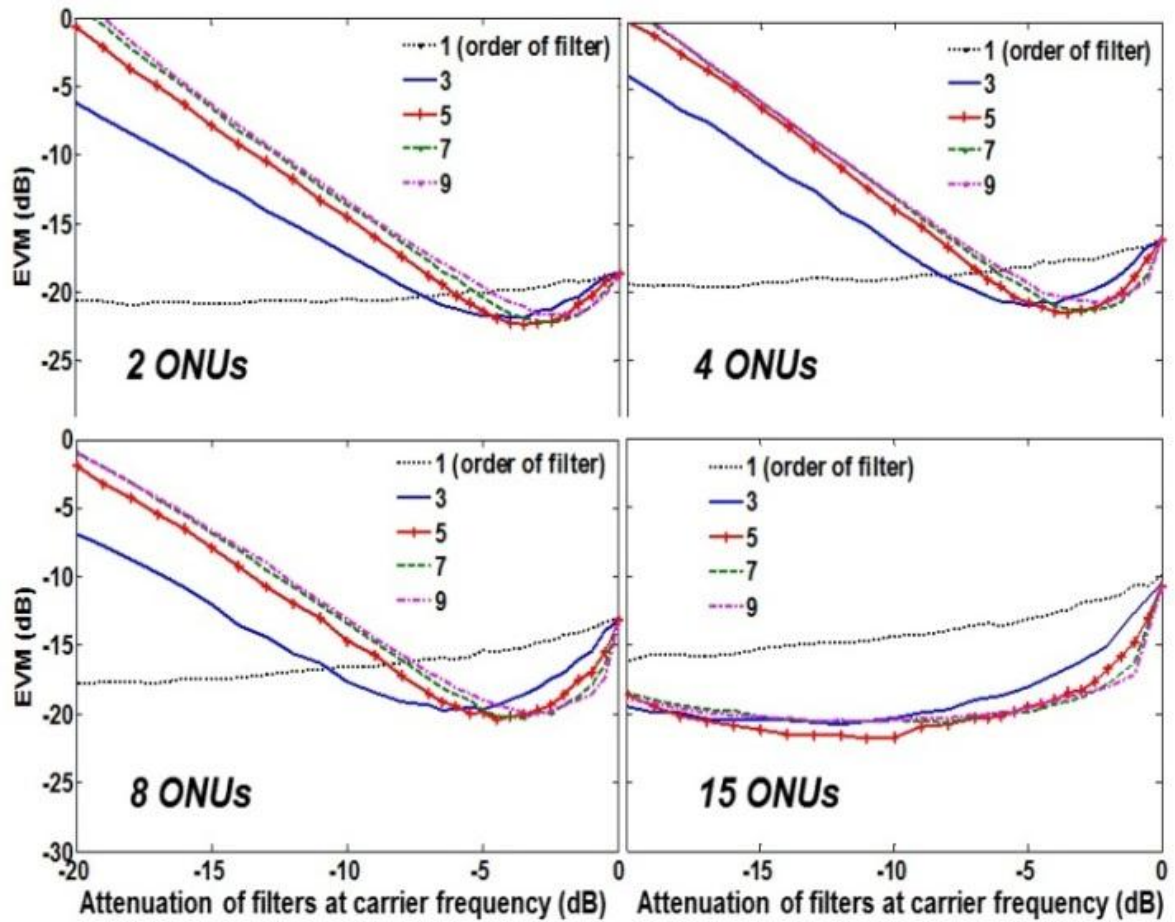
Figure 59: EVM as a function of optical carrier attenuation α0 for different numbers of ONUs utilising optical filters of different orders. Received optical power: -10dBm. ONU wavelength spacing: 18GHz.

In order to gain an in-depth understanding of the overall EVM performance, various EVM versus α_0 curves for different k values and different number of ONUs are presented in Figure 59. It can be seen in Figure 59 that, for a given number of ONUs, an optimum α_0 is observed, above which an increase in EVM is due to a CSPR increase because of the existence of a relatively large optical carrier power. For the α_0 below the optimum value an increase in EVM is mainly caused by excessive attenuation of carrier power thereby inducing a signal clipping effect. From chapter 3.3, it is seen that a large number of ONUs increases the CSPR, thus requiring high optical carrier power attenuation in order to achieve the best EVM performance. This results in a reduction in optimum α_0 with increasing the number of ONU, as shown in Figure 59.
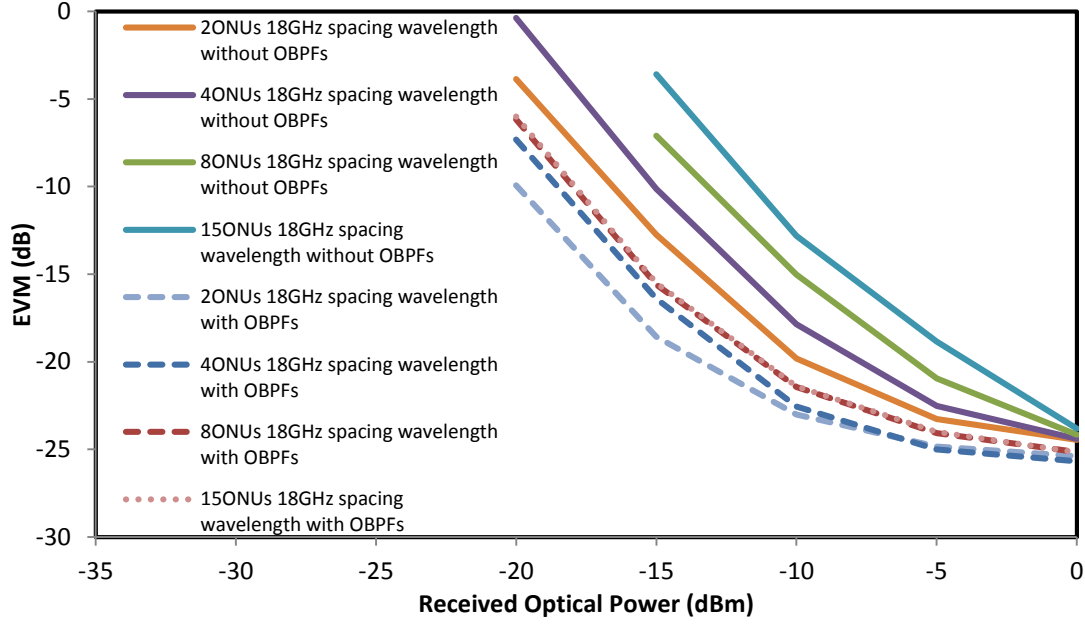
Figure 60: EVM performance versus received optical power for different number of ONUs utilising super-Gaussian optical filters with optimised orders and frequency-offset.

Simulated EVM performance as a function of received optical power is presented in Figure 60 for 25 km SMF IMDD multiple wavelengths upstream OOFDMA PONs. Optimum k and α_0 values of the 12.5 GHz bandwidth super-Gaussian optical filters for different number of ONUs is used for simulations shown in Figure 60. As seen in Figure 60 in comparison with the optical filter-free cases, the utilisation of optimum super-Gaussian optical filters not only improves considerably the EVM and decreases the minimum received optical power required for achieving the FEC limit for a different number of ONUs, but also minimises the EVM performance differences between the different number of ONUs .
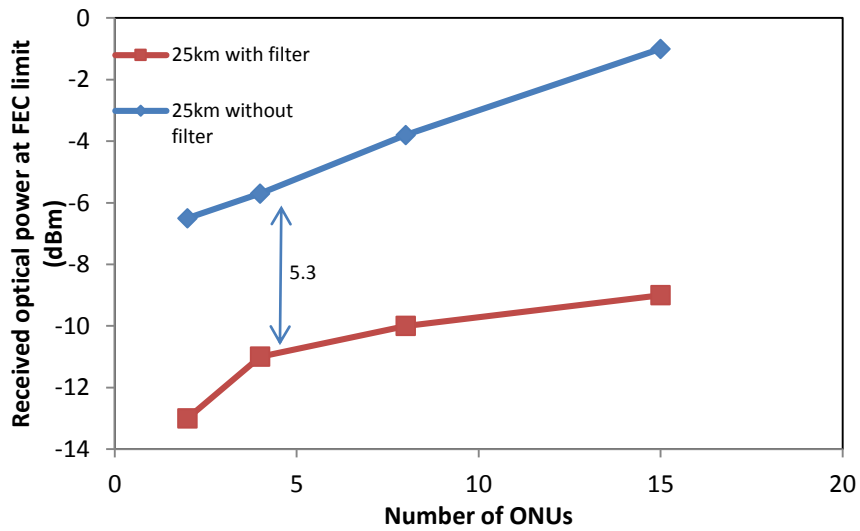
Figure 61: Minimum received optical power at the FEC limit versus the number of ONUs.

To explicitly demonstrate the optimum optical filter-induced improvement on the upstream optical power budget, the minimum received optical power for different numbers of ONUs is given in Figure 61, for the cases of including and excluding the optical filters. The minimum received optical power corresponds to the forward error correction (FEC) limit that is the BER limit at which codes can detect and correct a number of errors without retransmitting the data stream [2]. It is interesting to note in Figure 61 that, compared with the optical filter free cases, the utilisation of optimum super Gaussian optical filters can enhance the upstream optical power budget by at least 5.3 dB for up to 15 ONUs.
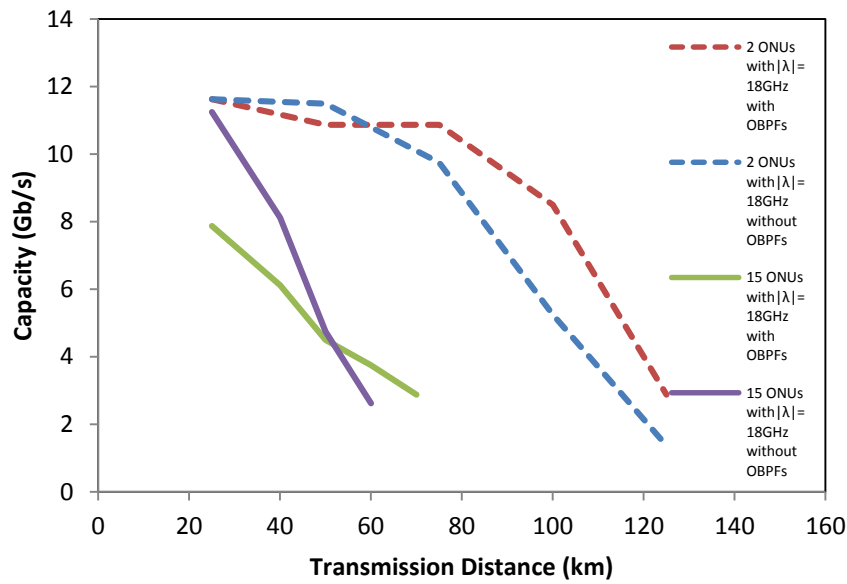
Figure 62: Capacity versus reach for 2 and 15 ONUs with and without OBPFs. ONU wavelength spacing is 18GHz.

The effect of the filtering on the capacity versus reach performance is investigated. The capacity of the system is the signal line rate that is defined as the sum of the signal bit rates corresponding to each data-carrying subcarrier with the condition that the total channel BER (as described in section 2.21) is less than 1×10^{-3} [3]. The transmission distance is varied from 25 km to 125 km. From Figure 62 for the case of 2 ONUs the effect of the filtering can be seen to improve the capacity of the system for distances greater than 75 km. For the case of 15 ONUs optical filtering does not improve the system capacity for distances smaller than 50 km due to the CSPR increasing due to an increase in ONUs and the carrier then being suppressed by the optical filter but can only be seen to improve the capacity of the system for distances greater than 50 km.

The optical power budget is improved by at least 5.3 dB for the upstream multiple wavelengths OOFDMA PON system. In the next section investigations are described of the effect of the

optical filtering on the minimum wavelength spacing of the upstream multiple wavelength OOFDMA PON system to ascertain whether spectral efficiency can be increased by utilising optical filters in the upstream transmission.

4.3 Effect of optical filtering on the minimum ONU wavelength spacing in an OOFDMA PON multiple wavelength upstream transmission.

To ensure that the OOFDMA PON system is suitable for use in access networks the system must have a high spectral efficiency. The system introduced in chapter 3 of multiple wavelengths upstream OOFDMA PON with RSOA based intensity modulators has a minimum wavelength spacing of 8 GHz as shown in chapter 3.3.2, and is independent of the number of ONUs. The wavelength spacing is mainly determined by subcarrier-subcarrier beating in the detection process. Optical filtering will suppress one sideband in the optical domain reducing the number of subcarrier-subcarrier beating components and could offer a reduction in the minimum wavelength spacing as will be discussed in more detail in chapter 5. In this section the wavelength spacing will be varied for cases with and without OBPFs for the cases of 2 and 15 ONUs. The new minimum wavelength spacing is then used to determine whether capacity versus reach performance can be improved for a system with a large number of ONUs.

4.3.1 Transmission system model and parameters

The system model and all system parameters that are not explicitly mentioned here are the same as those in section 4.2.1 of this chapter. By using optimised parameters for the wavelength offset and filter orders, optical SSB can be achieved at the output of each ONU [4] for the following system.

4.3.2 Results

First the EVM versus ONU wavelength spacing is discussed for different cases of filter order and wavelength offset. In Figure 63 case 1 shows the EVM versus ONU wavelength spacing for 2 ONUs with no OBPFs at the outputs of the ONUs. For case 1 the minimum wavelength spacing of 8 GHz at the EVM floor of -24 dB is reached. The error floor is due to the RSOA intensity modulators limited 3 dB bandwidth of 1.25 GHz. Cases 2 to 6 in Figure 63 show the 2 ONUs upstream transmission with OBPFs for different order filters with k= 1,3,5,7 and 9 with the attenuation coefficient α_0 = -3 dB. For the optimum filter parameters of k = 5 and α_0 = -3 dB the minimum wavelength spacing for a OOFDMA PON system utilising RSOA

modulators is 4 GHz, resulting in a further 4 GHz improvement from relative to the case without OBPFs with a minimum wavelength spacing of 8 GHz. Due to the single sideband the direct detection process has fewer optical subcarrier-subcarrier components that can beat to cause a wider beating bandwidth. Thus the optical bandwidth can be better utilised with the incorporation of RSOA based modulators and optical bandpass filters due to the frequency spacing of ONUs being reduced. The beating components will fall outside of the baseband at the OLT in the electrical domain and the wanted data will be located at baseband.
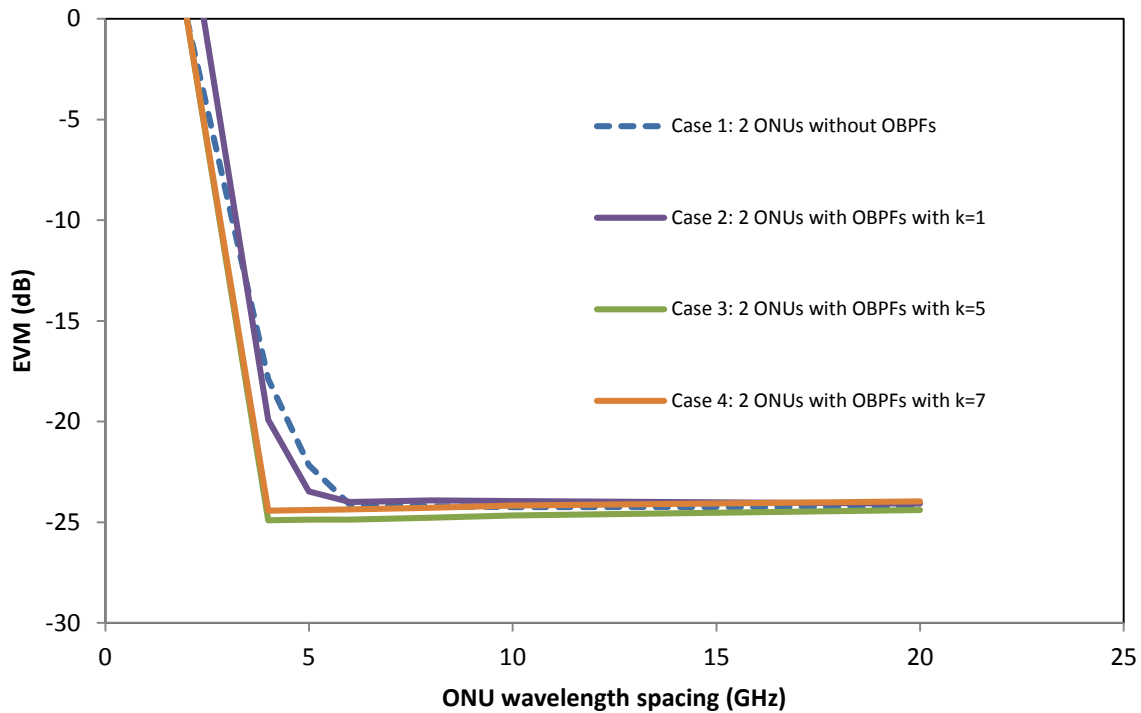
Figure 63: EVM versus ONU wavelength spacing for 2 ONUs over 25 km with received optical power fixed at 0.75 dBm.

To investigate whether the OBPF improvement is independent of the number of ONUs the EVM versus ONU wavelength spacing for 15 ONUs is plotted in Figure 64. For this simulation the number of symbols was also 500 to make comparison to other cases fair. For case 1 in Figure 64 the minimum wavelength spacing is 8 GHz at an EVM value of -24 dB for 15 ONUs without OBPFs at the outputs of the ONUs. Cases 2 to 5 in Figure 64 show the 15 ONUs upstream transmission with OBPFs for different order filters with k= 1,3,5 and 7 with the attenuation coefficient α_0 = -11 dB. For the optimum filter parameters of k = 5 and α_0 = -11 dB the minimum wavelength spacing for a OOFDMA PON system utilising RSOA modulators is 4 GHz, resulting in a further 4 GHz improvement from the case without OBPFs with a minimum wavelength spacing of 8 GHz.
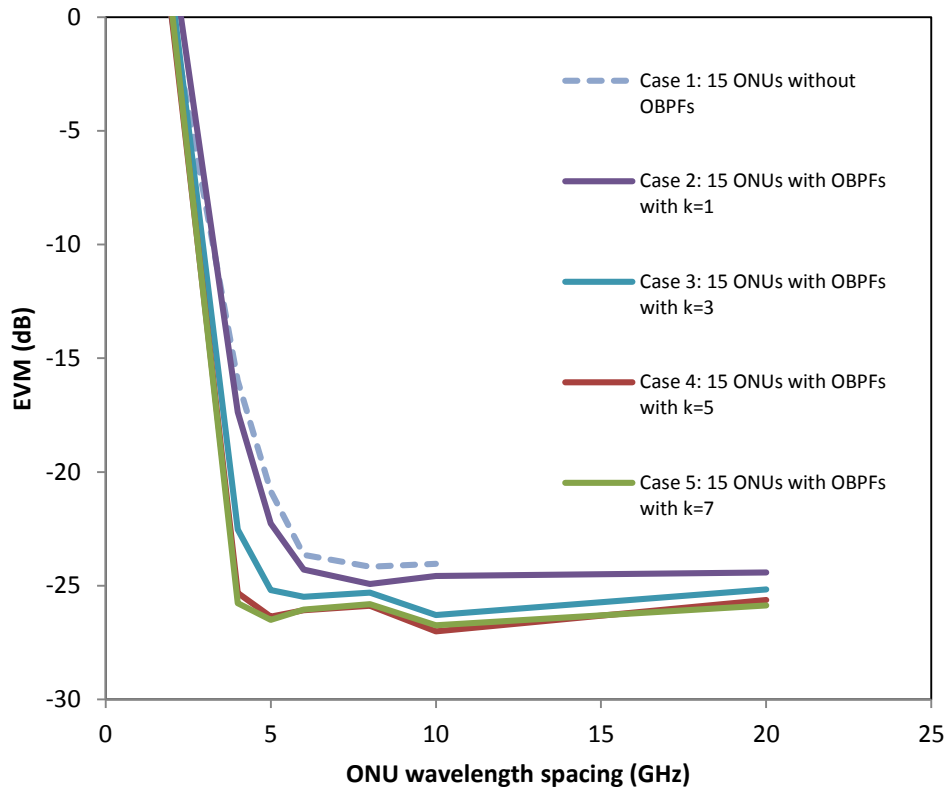
Figure 64: EVM versus ONU wavelength spacing for 15 ONUs over 25 km with received optical power fixed at 0.75 dBm.

To fully investigate the benefits of the OBPFs utilised in upstream OOFDMA transmission over 25 km SMF, the capacity versus reach is investigated for 2 and 15 ONUs with and without OBPFs for different wavelength spacings and the results are presented in Figure 65. For case 1 in Figure 65 the 4 GHz wavelength spacing for 2 ONUs over 25 km with OBPFs is shown. For case 2 in Figure 65, transmission for 2 ONUs with 18 GHz spacing with OBPFs is shown and compared to case 1 in Figure 65, showing that the capacity for case 2 is less than the capacity for case 1 for transmission distances up to 60 km. Due to the increased spectral efficiency the system in case 1 Figure 65 is more tolerant to dispersion induced effects in the fibre link compared to case 2. Thus case 1 will have better capacity for smaller distances but as the transmission distances increase the system becomes loss limited and the closer spaced ONUs in case 1 will be less tolerant to beating components and noise than case 2.
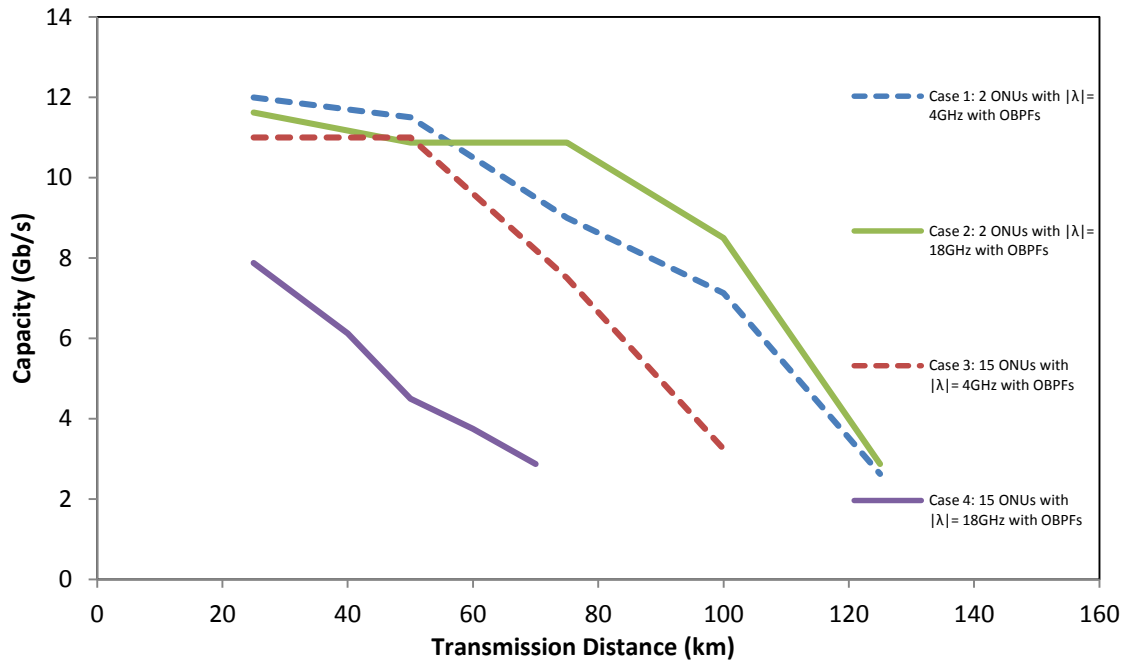
Figure 65: Capacity versus reach for 2 and 15 ONUs with different wavelength spacing's for cases with and without OBPF's.

In Figure 65 the 15 ONU cases for 4 and 8 GHz spacing are represented by case 3 and case 4. Comparing these cases in Figure 65 it is clear that the closer-spaced ONUs of case 3 have a much greater capacity over short and long transmission distances compared to case 4. Due to the increase in ONUs the RSOA based 15 ONU transmission system will experience an increase in the CSPR compared to 2 ONUs. This causes case 3 in Figure 65 to be more tolerant to dispersion when the system transmission distances increase because the capacity remains larger compared to case 4.

To conclude, in has been shown in Figure 63 and Figure 64 that with the filters the minimum wavelength spacing is still independent of the number of ONUs and optimised filtering leads to a reduction in minimum wavelength spacing. It has also been shown that the capacity versus reach performance of a 15 ONUs OOFDMA upstream transmission can be significantly improved over distances varying from 25 km to 100 km by utilising optimal OBPFs that enables closer spaced ONUs.

4.4   Conclusions

Numerical simulations results, published in [4], have shown that the utilisation of an optimum frequency-offset super-Gaussian optical filter at an order of 5 immediately after the RSOA intensity modulator in each ONU can significantly improve the upstream power budget by > 5.3dB, and simultaneously enhance the upstream power budget robustness to variations in the number of ONUs. Optical beating interference in RSOA-based IMDD OOFDMA PON systems can be reduced by implementing Gaussian optical bandpass filters to achieve optical single sideband leading to less frequency components of the signal present at detection. The reduced number of components at detection that can beat with each other will allow the ONUs to be spaced closer together improving the minimum wavelength spacing from 8 GHz to 4 GHz resulting in a more efficient use of the optical bandwidth of the signal. Investigations also have shown that the use of OBPFs to decrease the minimum wavelength spacing leads to an improved capacity versus reach performances for 15 ONUs enabling the OOFDMA PON with RSOA based intensity modulators in the upstream transmission system utilising OBPFs to be an excellent high capacity and spectrally efficient solution for next generation PON networks.

4.5   References

[1]   J. L. Wei, C. Sanchez, E. Hugues-Salas, P. S. Spencer, and J. M. Tang, "Wavelength-Offset Filtering in Optical OFDM IMDD Systems Using Directly Modulated DFB Lasers", Journal of Lightwave Technology, vol. 29, pp. 2861-2870, 2011.

[2]   A. Carlson, "Communication Systems", McGrawHill, 2002.

[3]   K. A. Shore and J. M. Tang, "30-Gb/s Signal Transmission Over 40-km Directly Modulated DFB-Laser-Based Single-Mode-Fiber Links Without Optical Amplification and Dispersion Compensation", Journal of Lightwave Technology, vol. 24, pp. 2318-2327, June 2006.

[4]   X. Q. Jin, J. Groenewald, E. Hugues-Salas, R. P. Giddings, and J. M. Tang, "Upstream Power Budgets of IMDD Optical OFDMA PONs Incorporating RSOA Intensity Modulator-Based Colorless ONUs", Journal of Lightwave Technology, vol. 31, pp. 1914-1920,2013.

5   Chapter 5: Single wavelength upstream OOFDMA PON transmission

5.1 Introduction

Upstream transmission of optical orthogonal frequency division multiple access passive optical networks (OOFDMA PONs) remains a major challenge because of interference between optical network units (ONUs) [1]. Optical beat interference (OBI), which arises due to the direct detection of combined upstream signals of similar wavelengths, generates unwanted frequency products that falls into the useful signal spectral region. One way to mitigate the OBI effect is to use different wavelengths for upstream transmission from different ONUs as discussed in chapter 3 [2]. The drawbacks of the solution are that it considerably increases the optical spectrum needed to accommodate multiple ONUs and for optimal performance each ONU requires its own optical filter making practical implementation difficult. An alternative approach is the use of coherent detection instead of direct detection at the optical line terminal (OLT) [3]. The drawback with this is that the approach considerably increases the complexity of transceivers.

To address the issues of practical implementation and overall system complexity a novel technique is proposed where only a single upstream wavelength is assigned to all ONUs. Each ONU would consist of a

- OFDM signal being radio frequency (RF) upshifted.
- A reflective semiconductor optical amplifier (RSOA) intensity modulator used to modulate the signal.
- Optical single sideband (SSB) achieved by implementing an optical band-pass filter (OBPF) at the OLT.

The total number of data-carrying subcarriers can be dynamically assigned to different ONUs by the OLT. To further improve the overall system performance, a multiband system is introduced where for a two ONU case, an electrical SSB band is added to each ONU. In this chapter the model of a single upstream wavelength OOFDMA PON with multiple bands is verified through numerical simulations. Numerical data is analysed and compared to multiple wavelengths upstream OOFDMA PON transmission.

The remainder of this chapter is divided into three parts. The first part is section 5.2 where the novel single wavelength upstream transmission OOFDMA PON model is verified and optimum parameters calculated. The second part in section 5.3 of the chapter investigates the

optical power budget and the measure of capacity versus reach for a single upstream wavelength OOFDMA system and compares performance to the multiple wavelengths OOFDMA upstream transmission system. The third part in section 5.4 of the chapter consists of an in-depth investigation of a single wavelength upstream transmission with multiband.

5.2 Investigation into single wavelength upstream OOFDMA PON transmission with and without OBPF for different numbers of ONUs

To introduce single wavelength upstream transmission, first the transmission system model and beating in the direct detection process are discussed. The following sub-section is a detailed discussion of the single upstream wavelength OOFDMA intensity modulation direct detection (IMDD) PON setup. An investigation into the beating in the direct detection process for such a system is performed in order to better understand the requirement of the optimum system parameters and model evaluation is also described.

5.2.1 Transmission system model and parameters
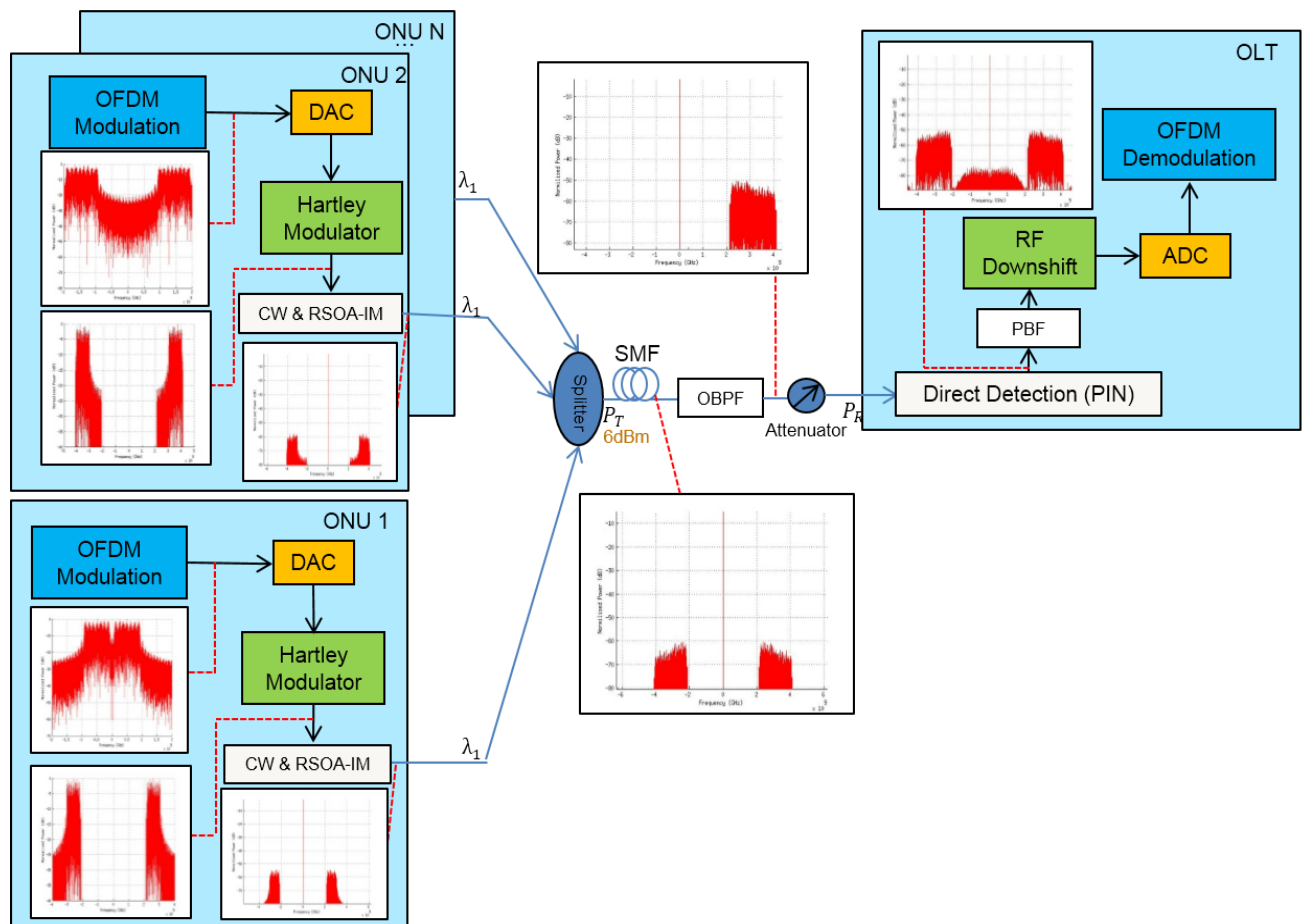
Figure 66: System setup and frequency spectrums for a single wavelength OOFDMA PON system.

RSOA		SMF		PIN	
Parameter	**Value**	**Parameter**	**Value**	**Parameter**	**Value**
Cavity length	300 μm	Effective area	80 μm²	Quantum efficiency	0.8
Width of active region	1.5 μm	Dispersion	17.0 ps/nm/km	Noise current density	8pA/√Hz
Depth of active region	0.27μm	Dispersion slope	0.07 ps/nm/nm/km	PIN sensitivity	-19dBm
Carrier lifetime	0.3ns	Dispersion wavelength	1550 nm	**Other System Parameters**	
Confinement factor	0.45	Loss	0.2 dB/km	**Parameter**	**Value**
Linewidth enhancement factor	5	Kerr coefficient	2.35×10^{-20} m²/W	DACs/ADCs Quantization bits	8-bits
Group velocity	8.43×10^7 m/s			DACs/ADCs Clipping Ratio	13dB
Optical frequency	1550 nm			DACs/ADCs Sampling speed	4 GS/s
Differential gain	3×10^{-20} m²			IFFT/FFT size	32 (cyclic prefix: 8)
Carrier density at transparency	1.2×10^{24} m⁻³				
Noise Figure	8dB				

Table 1: Summary of system parameters.

In Figure 66 a single wavelength upstream IMDD OOFDMA PON with reflective semiconductor optical amplifier (RSOA) intensity modulators at the ONUs is illustrated. The system was simulated including different numbers of ONUs, each using an RSOA as intensity modulator. The 25 km fibre was simulated using a split-step method as described in chapter 2.11. The total number of subcarriers for the system was 32. The OFDM baseband signal is generated using the same method described in [4] with parameters as listed in Table 1. The signal modulation format for all subcarriers are 64 Quadrature Amplitude Modulation (QAM) corresponding to line rate of 11.25 Gb/s, except for the capacity versus reach cases where adaptive modulation was used. The cyclic prefix parameter is taken to be 25 %, which gives a cyclic prefix length of 1.28 ns within each OFDM symbol having total time duration of 6.4 ns. The parameters used in simulating RSOA based intensity modulators are representative for InGaAsP semiconductor materials operating at a wavelength of 1550 nm and are summarised in Table 1 below. Single mode fibre (SMF), PIN and other system parameters are also listed in Table 1. The optical power into the coupler is fixed at 6 dBm. Simulation results for the RSOA have been verified through comparison with experimental results in [4]. The RSOA's driving current is 70 mA and bias current is 4.9 mA (optimal values obtained from experimental results). Up to 15 ONUs are simulated as this is the maximum number of ONUs for 15 data carrying subcarriers. Performance is measured in EVM due to a smaller number of symbols used to shorten simulation time and to achieve a higher resolution. The minimum number of symbols is 500 to optimise simulation times without losing accuracy of the EVM.

The baseband signal of each ONU is upshifted in the RF domain and converted to an electrical SSB (ESSB) signal by means of a Hartley modulator discussed in chapter 2.19. Before the direct detection at the OLT, a single OBPF is used to effect carrier suppression and achieve an optical SSB signal. The parameters used for the super-Gaussian optical filter is the same as in

[2]. The super-Gaussian filter has been shown to improve system performance in an IMDD system [5, 6]. After direct detection the combined signal is band-pass filtered and down-shifted by f_{RF} to baseband followed by normal baseband demodulation.

To verify the model the basic principle of beating between the ONUs in the direct detection (DD) process needs to be studied and verified with simulations. The single wavelength upstream OOFDMA PON simulations are then compared to previously published results of a multiple upstream wavelength OOFDMA PON system. In all the following discussions the proposed new technique with a single upstream wavelength OOFDMA PON will be referred to as case 1 and the OOFDMA PON utilising multiple upstream wavelengths for each ONU as described in [2] will be referred to as case 2.
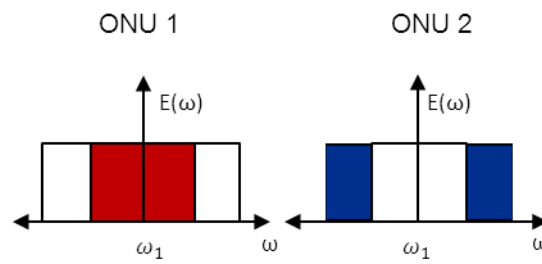
Figure 67: Frequency spectrum representation of two ONUs at same wavelength in electrical domain before addition in optical domain

Figure 67 shows the assignment of subcarriers to ONUs for two ONUs assigned to the same wavelength. For the simulation the first subcarrier carries no data to ensure a guard band between the data band and the carrier and to ensure that there is no DC component in the baseband signal. The next seven subcarriers are assigned to ONU 1 and the last 8 subcarriers of the 15 subcarriers available for data transmission is assigned to ONU 2. The complex conjugate of the data band is the lower sideband to the left of the carrier resulting in a 32- point FFT in the system.
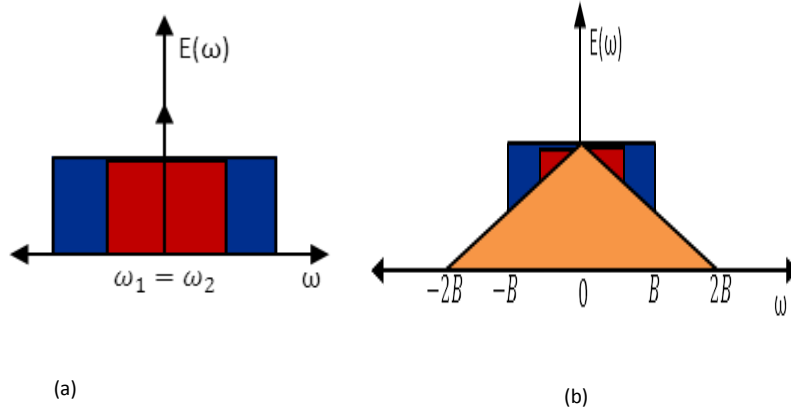
Figure 68: (a) Frequency spectrum of two ONUs on the same optical wavelength after the optical modulator signals are added together. (b) Frequency spectrum of two ONUs at same wavelength in electrical domain after detection with the orange block representing the subcarrier-subcarrier beating products.

Figure 68a shows the optical signal representation when two ONUs are combined in the optical domain. The unwanted beating products of subcarrier-subcarrier and carrier-carrier beating (two optical carriers from the different ONUs) fall within the baseband region after detection, as shown in Figure 68b. The blue and red bands in Figure 68b represent the wanted beating products between the carrier and the subcarriers. From appendix D it can be seen that the size of the band that the beating occupies is directly related to the bandwidth (B) of the data signal, yielding a subcarrier-subcarrier beating bandwidth of 2B.
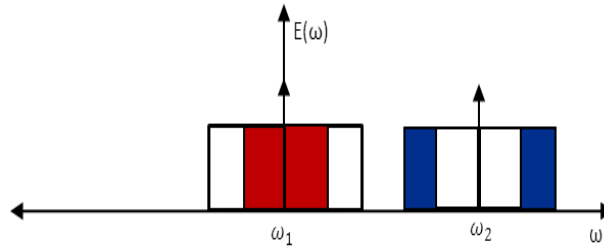
Figure 69: Frequency spectrum of two ONUs at different wavelengths in optical domain after addition.
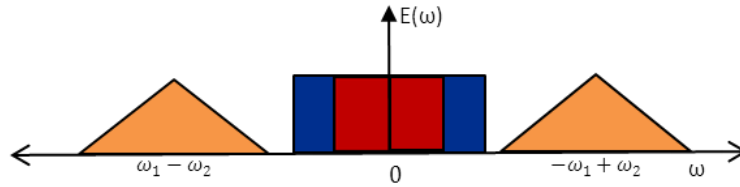
Figure 70: Frequency spectrum of two ONUs at different wavelengths in electrical domain after direct detection with the orange block representing the subcarrier-subcarrier beating products.

Figure 69 represents case 2 for two ONUs at different wavelengths after addition of signals from ONUs in the optical domain. To ensure the OBI between the two signals fall out of baseband after direct detection as shown in Figure 70, the optical spacing between ONUs needs to be sufficiently large as shown in [4] . If the wavelength difference is large enough the

unwanted beating components will fall outside the baseband area and data recovery will be possible. This however is not spectrally efficient.
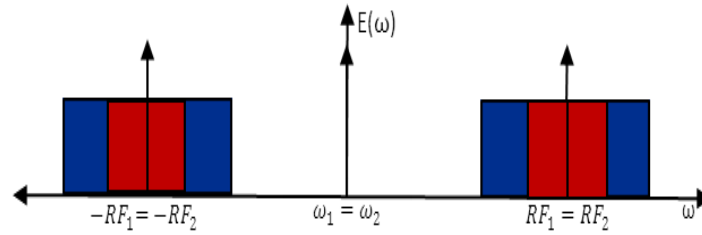
Figure 71: Frequency spectrum of two ONUs at same wavelength in optical domain with an equal RF upshift after addition.

Figure 71 represents case 1 in the optical domain and both ONUs are assigned to the same upstream wavelength. If the following condition is met for dual sideband signals (DSB) signals:

$$f_{RF} > 4B \quad [46]$$

the wanted data will fall out of baseband occupied by the beating products.
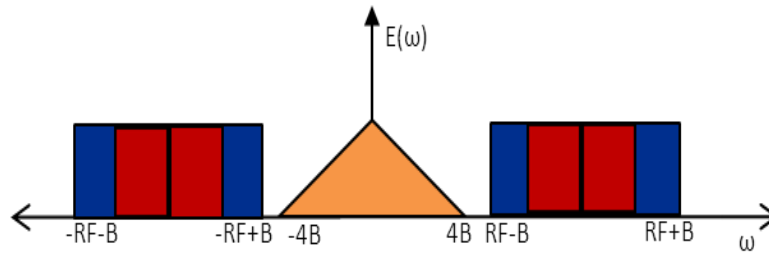
Figure 72: Frequency spectrum of two ONUs at different wavelengths in electrical domain after direct detection with RF upshift with the orange block representing the subcarrier-subcarrier beating products.

In Figure 72 the DSB case 1 detected signal is represented showing the beating band in orange. In case 1 the signal is SSB generated using equation 1, as shown in Figure 73. Due to SSB less subcarrier-subcarrier beating will occur [7]. The detected signal representation for SSB case 1 is shown in Figure 74 where it is seen that due to SSB data signals the minimum value for f_{RF} needs to conform to the following requirement to ensure the successful recovery of data at the OLT:

$$f_{RF} > 2B \quad [47]$$
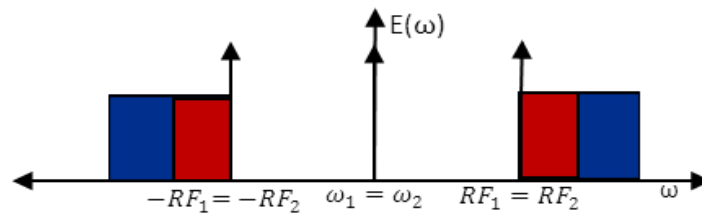
Figure 73: Frequency spectrum of two ONUs at same wavelength in optical domain with an equal RF upshift after addition and SSB baseband data signals.
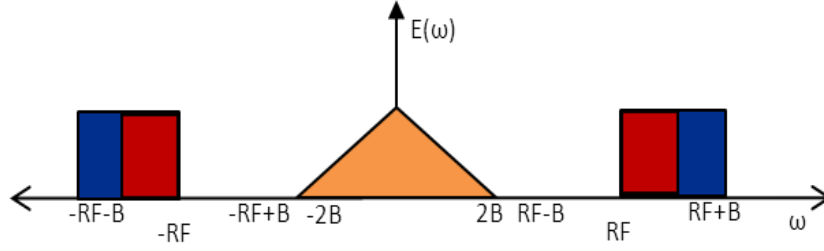
Figure 74: Frequency spectrum of two ONUs at different wavelengths in electrical domain after direct detection with RF upshift with SSB data signal with the orange block representing the subcarrier-subcarrier beating products.

To verify the model the minimum f_{RF} spacing needs to be calculated for case 1 with SSB data signals from ONUs. To see the effect of subcarrier-subcarrier beating more clearly with regards to the minimum wavelength spacing, a point-to-point upstream system with an ideal modulator is demonstrated in Figure 75.

.
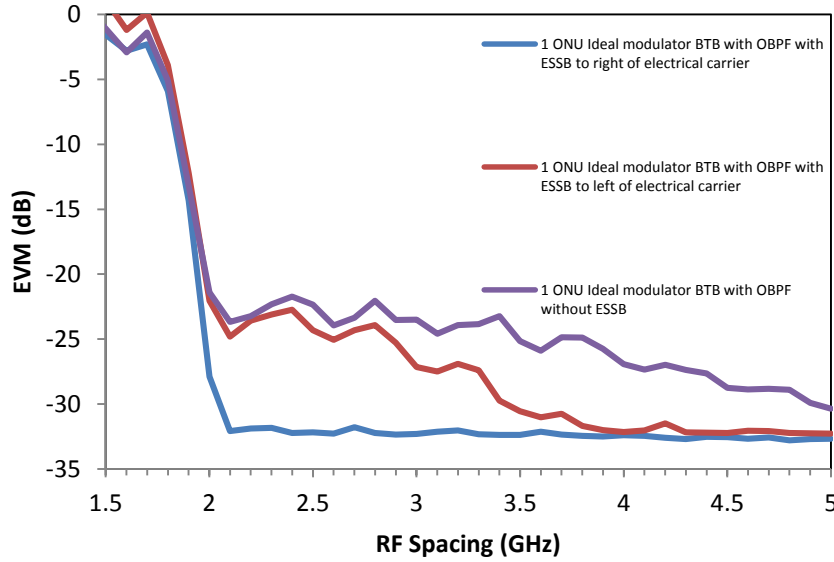
Figure 75: EVM vs. RF spacing of electrical baseband OFDM signal with/without ESSB back-to-back (BTB) transmission.

From Figure 75 it can be seen that for a signal with a 2 GHz bandwidth, with the baseband signal being DSB in the electrical domain, the beating band size will follow the requirement in equation 2 on page 109, giving a minimum RF spacing of f_{RF} larger than 4 GHz. If the baseband signal is converted to SSB using equation 1 with the sign of the equation a minus to ensure the band of data carrying subcarriers is to the right of the RF tone, the requirement for the RF spacing follows equation 3 on the previous page yielding a minimum RF spacing of f_{RF} larger than 2 GHz. This is due to fewer subcarriers beating with each other in the direct detection process. If the data-carrying subcarriers are to the left of the RF tone, the minimum RF spacing will be larger due to the wanted data falling into the beating band even at f_{RF}

slightly larger than 2 GHz, as shown in Figure 75. The sharp increase in performance for all three cases in Figure 75 is due to three contributing factors. The first is the beating between ONUs have two main components namely beating between the optical carriers that will dominate around baseband and beating between the subcarriers [3]. As soon as f_{RF} is large enough for the beating effect between the optical carriers not to be the major contributing factor to system performance, the system performance will improve. The second contributing factor is the OBPF that will only be able to successfully filter out the negative bins if f_{RF} is large enough but not necessarily large enough to satisfy the conditions of equations 2 and 3. The third and dominant factor to consider is the point at which the f_{RF} upshift will be large enough so that the RF tone's power of the RF up shifted signal is notably larger than the power of the beating components, to enable the OLT to retrieve the wanted data. Due to the decreasing nature of the beating the point where the signal can be 'seen' by the OLT will be where the f_{RF} is roughly equal to the bandwidth of the signal, rather than the conditions to mitigate the beating band as set out in equations 2 and 3.
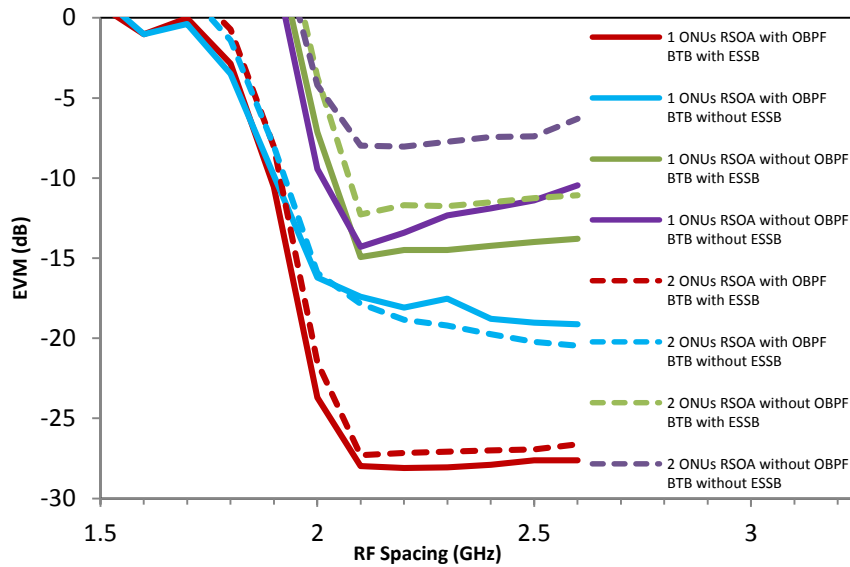
Figure 76: EVM versus RF spacing for 1 ONU and 2 ONUs back-to-back (BTB) transmissions with and without ESSB and OBPF.

In Figure 76 the minimum RF spacing is determined for case 1. The solid lines in Figure 76 represent a point-to-point (PTP) system with a RSOA based intensity modulator. To study the effect of how the ESSB affects the minimum f_{RF} value, the red and blue solid line curves in Figure 76 are presented and clearly show how, with ESSB, the minimum f_{RF} is 2.125 GHz. This is also true for the case with 2 ONUs. A super Gaussian OBPF, as described in [2], is used at the input of the OLT to ensure an optical SSB signal in the direct detection. If the ESSB is utilised with an OBPF (dotted red curve), the system reaches a lower EVM floor faster. The

lower EVM floor is due to the reduced carrier signal power ratio (CSPR) due to the optical filter.

The optical filter cannot isolate and filter out one sideband if the RF upshift is smaller than the bandwidth of the signal. It can be seen from Figure 76 that for the cases where the optical filter is implemented the error ceiling is lower and the performance starts to approach the performance floor faster due to fewer beating components due to the filtering.
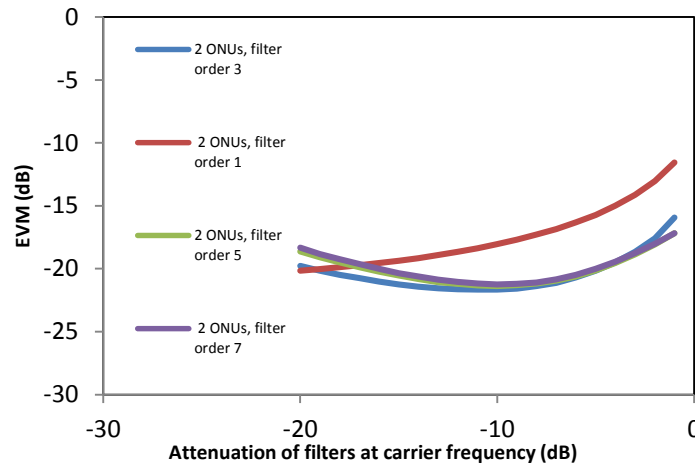
Figure 77: EVM as a function of optical carrier attenuation for 2 ONUs utilising optical filters of different orders.

The optimisation of the OBPF parameters for case 1 with ESSB is shown in Figure 77 and the optimum value for the filter attenuation at the optical carrier frequency is $\alpha_0 = -11\ dB$ ensuring optimum carrier suppression and optical single sideband with a filter order of 3.

5.2.2 Results

To further verify the model a comparison is made between the results for case 2 without utilising OPBF's at the ONUs and case 1 without an OBPF at the OLT and without a RF upshift at the ONUs. In Figure 78 case 1 experiences an error floor at -7 dBm due to the strong beating caused by optical beating interference (OBI) and subcarrier-subcarrier beating. The OBI is mainly caused by beating between the optical carriers and subcarriers of the signals from different ONUs. If an optical filter is introduced to case 1 it will only slightly improve due to a reduction in the CSPR but will still reach an error floor at -18 dB. The filter is not ideal and some residue of the filtered band will still be present at detection in the OLT. The error floor at -18 dB is due to double sideband signals containing more frequency components that can beat with each other to create beating products with direct detection at baseband.

The subcarrier-subcarrier beating is also strong at baseband where wanted data carrying subcarriers will be if the optical signal is direct detected. After the RF shift and ESSB is introduced with a value of 2.125 GHz (optimisation of RF value shown in Figure 76), the error floor at -7 dBm disappears and the received optical power at an EVM value of -22 dB (corresponding to a FEC limit with BER of 2.3×10^{-3} for 64-QAM) is -4 dBm (shown by the green curve in Figure 78). To be able to make a fair comparison between case 1 and case 2 the optimised cases using OBPFs to improve system performance need to be considered. For case 2, the use of OBPFs at the output of the ONUs to achieve optical SSB improves the received optical power at a EVM value of -22 dB (corresponding to a FEC limit with BER of 2.3×10^{-3} for 64-QAM) with 5.3 dB (shown by the red dotted curve and the orange dotted curve in Figure 78).

Implementing a RF upshift in case 1 enables the possibility of generating electrical single sideband (ESSB) signals in the ONUs. Utilising an optimised OBPF at the OLT in case 1 if ESSB is implemented with the use of a Hartley modulator, results in an EVM of -22 dB at a received optical power of -14 dBm (shown by the solid orange curve in Figure 78). From Figure 78 it is observed for case 1 with ESSB that the received optical power at an EVM value of -22 dB is improved by 3 dBm compared to the best case scenario for case 2.

This shows that the major factors governing the performance of case 2 is the OBI and subcarrier-subcarrier beating that falls in the baseband region when using direct detection. Case 1 mitigates the OBI and subcarrier-subcarrier beating problem by introducing a RF shift to move the data bands out of baseband to enable single upstream wavelength allocation to all ONUs.
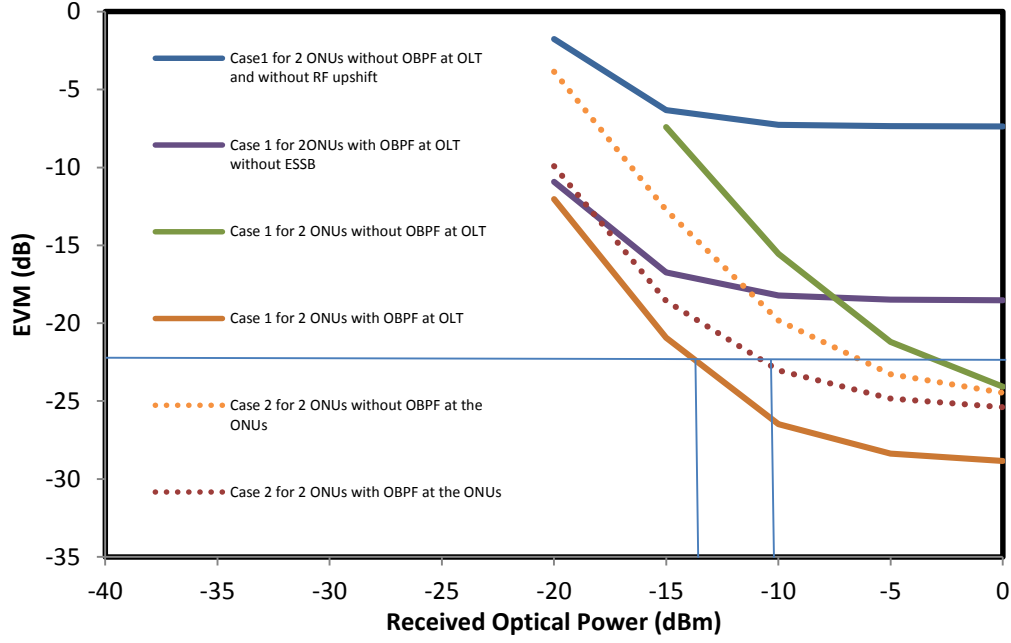
Figure 78: EVM versus received optical power for Case 1 with 2 ONUs with and without OBPF at the OLT and for Case 2 with 2 ONUs with and without OBPF's at each ONU for 25km SMF transmission.
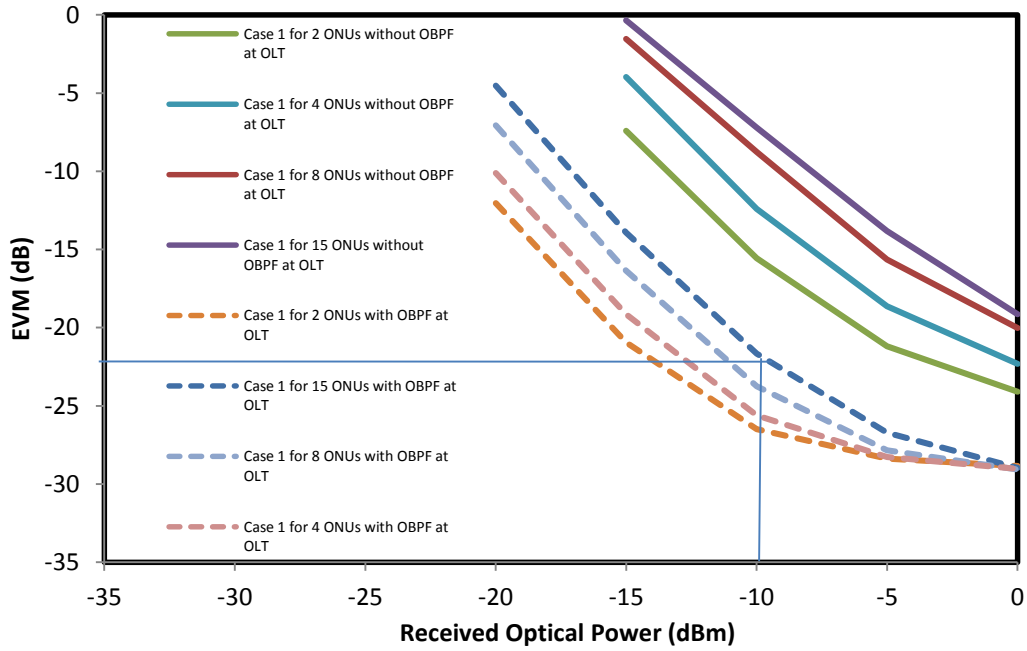
Figure 79: EVM versus received optical power for different number of ONUs at single upstream wavelength with and without OBPF at OLT for a net rate of 9 Gb/s (64-QAM modulation).

For single upstream wavelength OOFDMA PONs to be a viable solution in access networks, they will need to be able to work with multiple ONUs while still ensuring a high capacity at small received optical powers. To determine the impact of the number of ONUs on the received optical power the received optical power is swept for a different number of ONUs, as shown

in Figure 79. Utilising an RF upshift of 2.125 GHz with a OBPF enables a aggregated data rate of 11.25 Gb/s for 15 ONUs corresponding to a EVM value of -22 dB at -10 dBm of received optical power. The EVM floor at -29 dBm in not due to the intermixing between subcarriers but due to the nonlinearity of the RSOA intensity modulator. For case 2 in [2] the error floor is at -25 dBm, and disappears if the RSOA intensity modulator is replaced with an ideal modulator. The 4 dBm difference in the error floor between case 1 and case 2 is due to the extra beating components between the sidebands of the DSB signal in case 2. Due to ESSB in case 1 there is no beating between the lower sidebands. The power penalty observed when the number of ONUs is increased is due to the multiple electrical to optical conversions increasing the CSPR and the multiple access interference (MAI). The MAI leads to the destruction of orthogonality between subcarriers due to the subcarriers being generated by different ONUs. Figure 79 clearly shows that even if the number of ONUs is increased, case 1 still exhibits excellent system performance.

5.3   OOFDMA IMDD PONs with single wavelength upstream compared to multiple wavelength upstream transmission

This section investigates the optical power budget and capacity versus reach performance for a single upstream wavelength OOFDMA system and compares performance to the multiple wavelengths OOFDMA upstream system to show the advantages of the single wavelength upstream OOFDMA IMDD system proposed in this chapter.

5.3.1   Transmission system model and parameters

The model for the single wavelength upstream OOFDMA IMDD transmission is described in section 5.2 with optimised parameters for the RF upshift 2.125 GHz as determined in section 5.2.3. The parameters for the single upstream wavelength are the same as in section 5.2, with the optimum parameters for the OBPF at the OLT with the filter attenuation $\alpha_0 = -11\ dB$ and a filter order of 3. For the multiple upstream wavelengths OOFDMA IMDD, the model is the same as described in section 4.2 with optimised parameter for the OBPFs used as calculated in section 5.2.2.

5.3.2 Results

In Figure 80 the received optical power versus EVM for case 1 compared to case 2 is plotted. For the multiple upstream wavelengths case 2 in Figure 80, the different number of ONUs all converge to an EVM floor as the received optical power is increased due to the subcarrier-subcarrier beating products that fall in the baseband region. The wavelength spaced ONUs will mitigate the subcarrier-subcarrier beating between the subcarriers of different ONUs, but the beating of subcarriers of a single ONU will still fall in baseband leading to the EVM ceiling at -25 dB as shown in Figure 80.
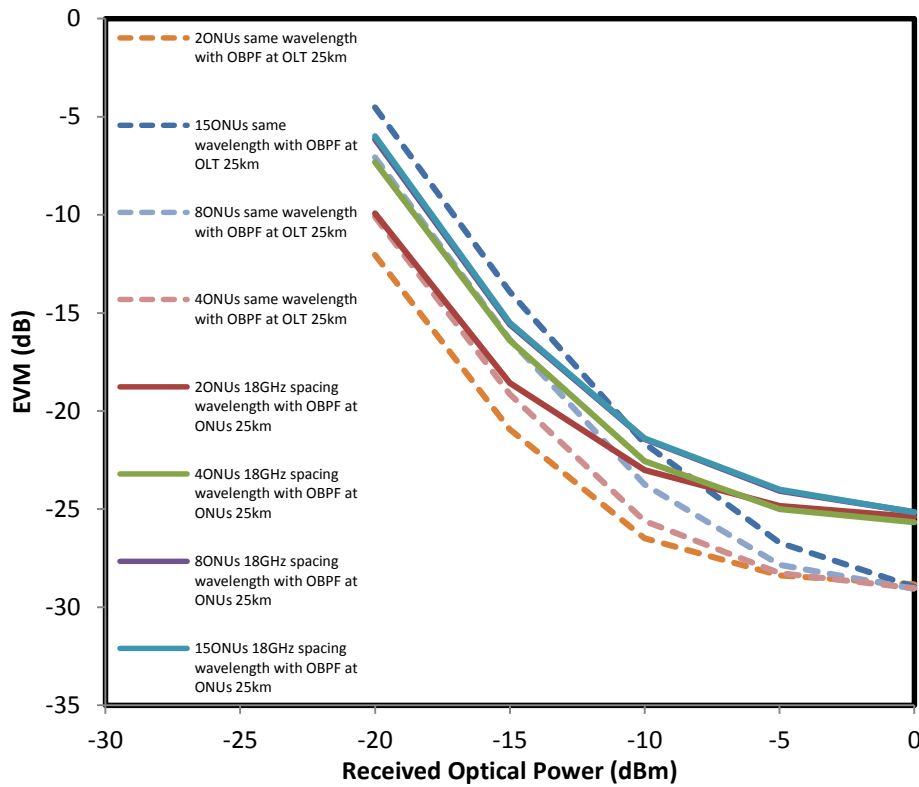
Figure 80: Received optical power versus EVM for cases with optical filters for ONUs on same wavelength (case 1) and 18 GHz spacing (case 2) for different number of ONUs.

The received optical power versus EVM performance for case 1 with an optimised OBPF at the OLT for single wavelength upstream transmission shown in Figure 80 has an error floor at -29 dB due to nonlinear behaviour of RSOA intensity modulators.
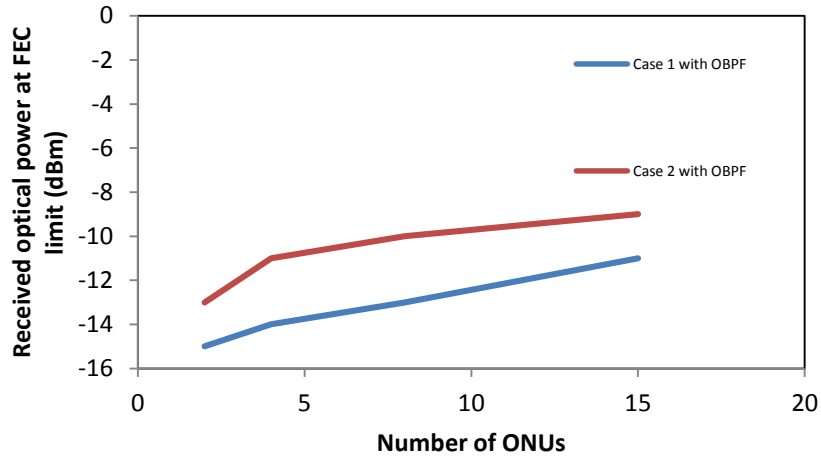
Figure 81: Minimum received optical power at the FEC limit versus the number of ONUs for cases with and without wavelength spacing over 25km SMF transmission with OBPFs at an aggregated line rate of 11.25 Gb/s.

The received optical power at FEC limit for case 1 compared to case 2 shows a power budget improvement of at least 2 dB for case 1 as shown in Figure 81. This is very significant as case 1 only uses a single upstream wavelength. An increase in the number of ONUs results in almost linear increase in the received optical power required at FEC limit for both cases. This is due to the fact that MAI and an increased CSPR due to multiple electrical to optical conversions is still dependent on the number of ONUs.

Figure 81 shows that case 1 has an improved power budget which is due to the fact that subcarrier-subcarrier beating is always a contributing factor to overall system performance degradation if the signal is in baseband. Although wavelength spacing between ONUs can decrease the strength of OBI in the baseband region, the beating between ONUs optical signals with direct detection will always have subcarrier-subcarrier beating components at baseband. This confirms the superior performance of case 1 with the salient advantage of being highly spectrally efficient due to a single upstream wavelength and with no penalty on capacity.
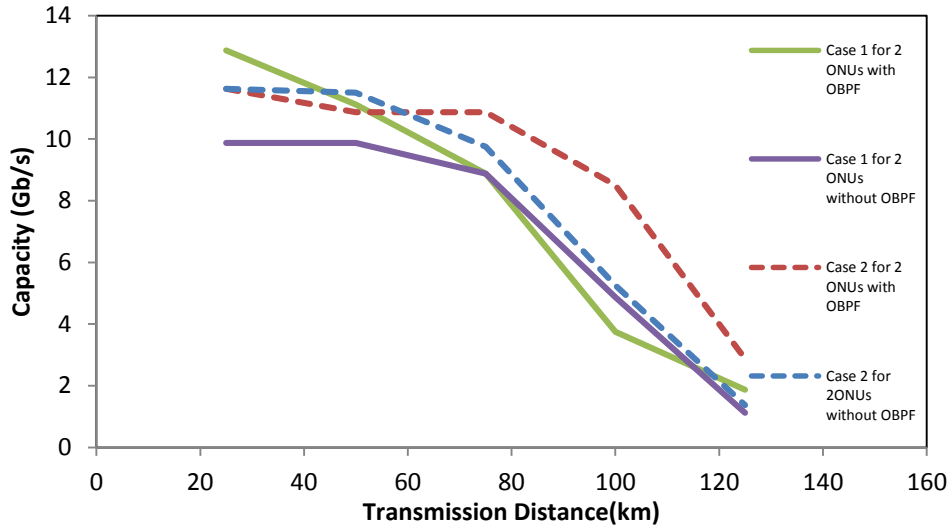
Figure 82: Signal aggregated line rate capacity versus reach performance comparison for Case 1 and Case 2 with 2 ONUs and with adaptive modulation (AM).

To demonstrate the advantages of using case 1 for next generation access networks, an investigation is made both of the improvement in the received optical power and also the capacity versus reach for case 1 with 2 ONUs and case 2 with 2 ONUs as shown in Figure 82. By using adaptive modulation the capacity can be maximised for different cases due to the change in length in the transmission link. For case 1 in Figure 82 a capacity improvement of 3.1 Gb/s over 25 km SMF is observed using 2 ONUs using optimised OBPF at the OLT compared to case 1 without a OBPF at the OLT. The capacity is increased for case 1 with an OBPF for distances smaller than 80 km. For case 2 in Figure 82 the OBPFs at the ONUs improve capacity for transmission distances greater than 60 km but for smaller distances no significant improvement is achieved with the use of OBPFs. For case 1 with an OBPF at the OLT the capacity improves with 1.5 Gb/s over a 25 km distance compared to case 2 with optical filters at the ONUs.
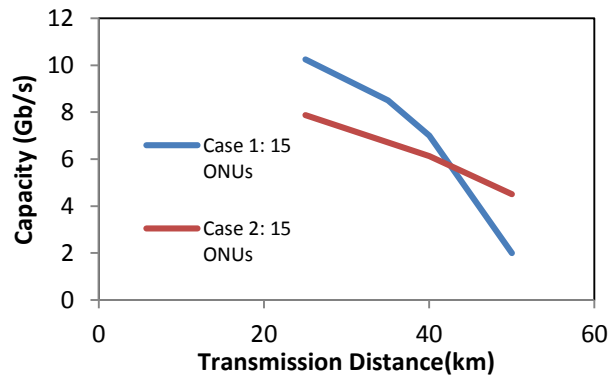
Figure 83: Capacity versus reach for case 1 and case 2 with 15 ONUs and with adaptive modulation (AM).

To confirm the advantages of case 1 the number of ONUs is increased to 15 and compared to the equivalent case 2. In Figure 83 the capacity versus reach for case 1 and case 2 is plotted and a capacity improvement of 2.5 Gb/s over 25 km SMF is observed for case 1 using 2 ONUs using an optimised OBPF compared to case 2.

For distances greater than 40 km overall capacity is worse for case 1 compared to case 2. This is due to the proposed scheme being less tolerant to link dispersion due to the wider optical band at each ONU due to the RF upshift.

For transmission distances smaller than 40 km it is better to utilise case 1 with a OBPF at the OLT to achieve optimum capacity in the system. Case 1 performs better due to the different signals from different ONUs experiencing the same nominal dispersion, reducing the need for complex synchronisation algorithms for each individual ONU. Case 1 is also not performance limited due to any subcarrier-subcarrier beating components present in the baseband.

5.4 Multiband OOFDMA PONs

For a single wavelength upstream OOFDMA IMDD PON the power budget and capacity can be improved utilising an OBPF at the OLT. However, to increase the system capacity even more, a second band of subcarriers can be introduced in the electrical domain of each ONU. This is known as multiband OOFDMA and allows for a spectrally efficient and high capacity OOFDMA IMDD PON system with low complexity for easy implementation. In this section the single upstream with multiband OOFDMA PON is investigated and capacity performance compared to a single wavelength OOFDMA PON system.

5.4.1 Transmission system model and parameters
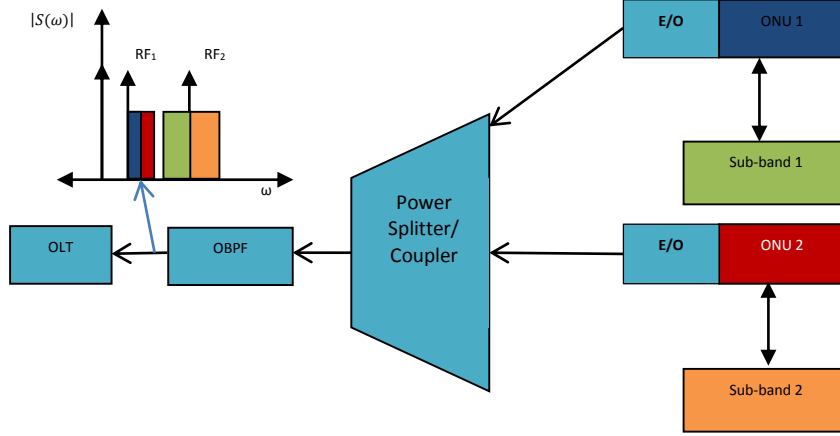
Figure 84: General layout of multiband OOFDMA PON system with 2 ONUs with an insert of the optical frequency spectrum representation.

To achieve maximum capacity, spectral efficiency and flexibility a combination of multiband and OOFDMA PON techniques can be incorporated in one system. IMDD can be used to achieve upstream and downstream transmission to reduce system complexity. For upstream transmission, OOFDMA is used to overcome the problems of normal time division multiple access (TDMA) by combining the best of frequency division multiplexing (FDM) and TDM. Each ONU for upstream transmission can be assigned to the same wavelength. The problem is that with direct detection the optical beating between the ONUs will cause severe beating products mainly in the baseband and it will not be possible to recover the signal properly if ONUs are all assigned to the same nominal wavelength. To overcome this problem the ONU spectra can be shifted out of the baseband by upshifting each ONU spectrum in the transmitter with a RF shift bigger than the bandwidth of the signal. For the system setup in this section the SSB bandwidth of the signal is 2 GHz, thus the upshift in the RF domain is 2.125 GHz as calculated in section 5.2. As discussed in section 2.16.5, fading of the signal in the link due to destructive interference, when direct detection is used with DSB signals at certain frequencies, is governed by β_2 the general velocity dispersion parameter, L the length of the fibre and f_{RF} the frequency of the RF upshift. Optical SSB is implemented by using a single filter at the receiver before direct detection.

115

Compared to previous IMDD OOFDMA systems in [1], the capacity of the system incorporating RSOA based modulators is increased by incorporating a dual band transmission at each ONU. The RSOA has a limited 3 dB bandwidth but lower modulation formats can be transmitted on the bands in the frequency domain falling out of the 3 dB bandwidth spectrum of the RSOA modulator. To improve the spectral efficiency even more each ONU spectrum is electrical single sideband (ESSB) and is generated using the Hartley method in the RF domain in the transmitter as discussed in section 2.17. This enables the system to use the multiband spectrum more efficiently by assigning the data from one ONU to the sideband below the second band's RF tone and the data from another ONU to the subcarriers corresponding to above the second band's RF tone. This results in a multiband spectrum where 30 data carrying subcarriers are utilising the same bandwidth as a conventional DSB OFDM signal. In the conventional DSB OFDM signal only 15 subcarriers are used for data and 15 subcarriers is used for Hermitian symmetry to achieve real valued signals. Due to the ESSB generation the sub-band signal is still real-valued and direct detection can still be used to detect the multiband signal from the combined optical signal. In the second band of the multiband signal, 1 subcarrier is set to zero to act as a guard band between the sub-bands, resulting in only 30 data-carrying subcarriers in the combined second band. Figure 84 shows a typical multiband OOFDMA PON system for 2 ONUs. In Figure 84 the insert showing the optical spectrum shows the data from ONU 1 represented by the blue and green blocks. The insert also shows data from ONU 2 represented by the red and the orange blocks. The first subcarrier (from the left) of the green block is set to zero for a guard band. Due to the fact that there are only a few sub-band and subcarrier beating products that fall between the first and second bands, the frequency difference between RF 1 and RF 2 can be equal to the baseband bandwidth. The close spacing of the bands will result in excellent spectral efficiency as will be shown in the next section.

5.4.2 Results
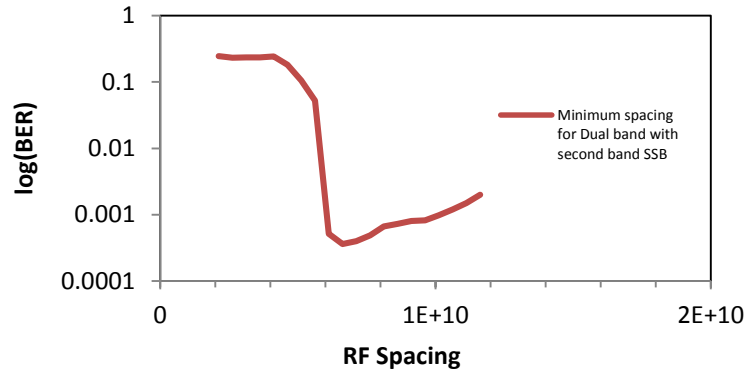
Figure 85: BER performance of system utilising dual-band with a sweep of the RF spacing of the second band while the first band is fixed at 2.125GHz.

In Figure 85 the RF spacing is calculated as $RF_2 - RF_1$. The second band is swept from 2.125 GHz to 11.625 GHz but RF_1 is fixed at 2.125 GHz. It can be seen that as soon as the second band RF upshift is larger than the RF upshift of the first sub-band (fixed at 2.125 Hz) plus the bandwidth of the first band of 2 GHz the performance improves dramatically. Optimum performance at 6.125 GHz is achieved with a sub-band arrangement as seen in the insert in Figure 84. The RF upshift spacing of 6.125 GHz for the second band corresponds to the RF upshift of the first band plus bandwidth of first RF band. If the RF upshift spacing is increased from 6.125 GHz the performance starts to degrade again due to beating components of sub-band mixing increasing in the spectrum of the wanted data. The equations for describing the beating in direct detection for the dual-band OFDMA PON system are shown in Appendix H.
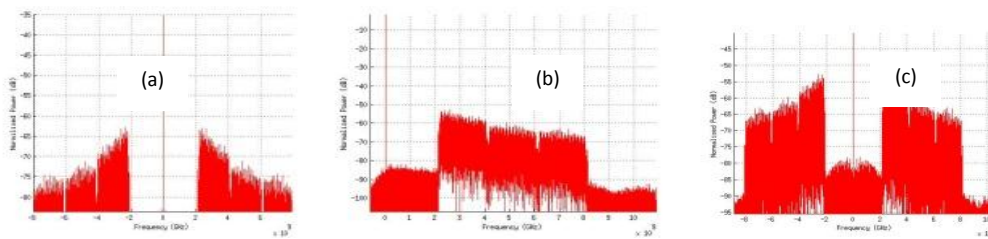
Figure 86: (a) Frequency spectrum of optical signal combined from ONUs before transmission through fibre. The zero on the graph corresponds to 1550 nm. (b) Frequency spectrum of optical signal combined from ONUs after 25 km transmission before detection and after OBPF. The zero on the graph corresponds to 1550 nm. (c) Frequency spectrum of signal after direct detection. The zero on the graph corresponds to 1550 nm.

Figure 86a shows the measured frequency spectrum after the optical combination of the signals from 2 ONUs with a dual-band at each ONU. The first band from 2.125 GHz to 4.125 GHz has 15 data carrying subcarriers of which the first 7 are assigned to ONU 1 and the remaining 8 to

117

ONU 2. The second sub-band has 15 subcarriers from ONU 1 and the third sub-band another 15 data carrying subcarriers from ONU 2. In Figure 86b the optical SSB is shown for the signal after transmission through 25 km of SMF at the output of the OBPF at the OLT. Figure 86c is the electrical spectrum of the signal after direct detection and the beating components in baseband can clearly be seen. Thus the multiband OOFDMA PON is an excellent candidate as a spectrally efficient, high capacity next generation FFTX optical network employing IMDD without increased system complexity compared to [1]. To further investigate the advantages of the single upstream wavelength multiband OOFDMA PON the improvement in capacity versus reach is investigated.
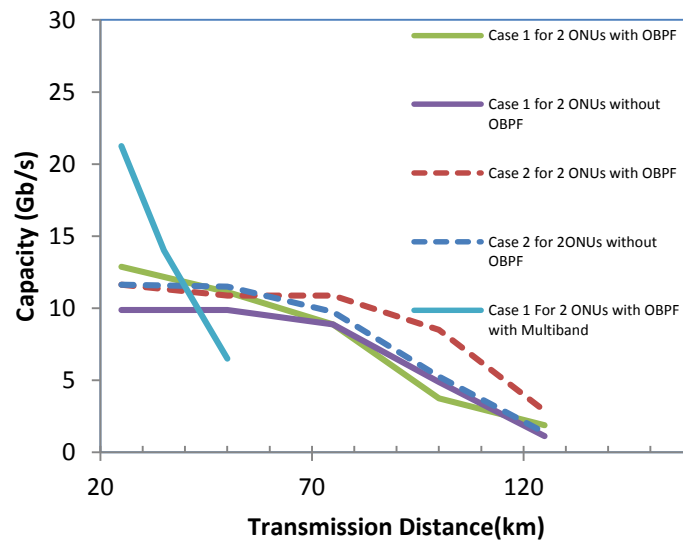
Figure 87: Capacity versus reach for Case 1 and Case 2 with and without OBPFs and for a 2 ONUs multiband system with AM.

In Figure 87 the capacity versus reach performance of the aforementioned system is displayed and compared to case 2 presented in [1]. In all cases adaptive modulation was used to optimise throughput by using bit loading to utilise the channel's frequency characteristics to their maximum potential. For the proposed single wavelength upstream multiband OOFDMA IMDD system, the performance for a transmission distance of 25 km is 8.3 Gb/s more than case 1 with a OBPF at the OLT. For distances over 40 km the multiband system capacity advantage is lost due to a wider total optical signal and performs worse than the other cases due to the scheme being less tolerant to link dispersion due to the wider optical band. By incorporating the multiband scheme introduced previously, the capacity increases with 8.35 Gb/s with a total positive optical bandwidth of 8.125 GHz compared to the capacity of case 1 and the optical bandwidth of 20 GHz of case 2 for 2 ONUs by using RSOAs as modulators and direct detection and only utilising one OBPF at the OLT.

Thus with RF1 = 2.125 GHz and RF2 = 6.125 GHz and using adaptive modulation the system can achieve a net rate of 21.25 Gb/s upstream transmission for 2 ONUs over 25 km using RSOA modulators corresponding to a BER of $1\text{x}10^{-3}$. Only one optical band-pass filter (OBPF) is needed at the OLT to ensure optical SSB before direct detection due to all ONUs transmitting on the same wavelength. Thus a reduction in system complexity is achieved due to fewer optical filters being required compared to the system in [1].

5.5 Conclusions

A novel technique enabling single upstream wavelength sharing among ONUs using OFDMA over 25 km and a RF upshift has been demonstrated. With optimised parameters for OFDM transceivers and a RSOA intensity modulator, aggregated 11.25 Gb/s over 25 km is achieved with only one OBPF at the OLT for single wavelength upstream transmission with a EVM of -22 dB at a received optical power of -14 dBm.

The novel single upstream transmission is achieved by using a combination of an equal RF upshift at each ONU, ESSB using the Hilbert transform and optical single sideband with an optical filter at the OLT.

Numerical simulations have shown that, in IMDD OOFDMA PONs, the use of a RF upshift and a single upstream wavelength enables an aggregated data rate of 11.25 Gb/s for 15 ONUs corresponding to a EVM value of -22 dB at -10 dBm of received optical power with a RF spacing of only 2.125 GHz resulting in a total optical signal bandwidth of only 4.125 GHz.

A power budget improvement of at least 2 dB for single wavelength upstream transmission is achieved compared to wavelength spaced upstream transmission.

Capacity improvement of 9.6 Gb/s is observed for 25 km transmission of single upstream wavelength multiband OOFDMA IMDD PON transmission for 2 ONUs using optimised OBPF compared to wavelength spaced ONUs utilising optimised OBPFs at the 2 ONUs outputs.

5.6 References

[1] L. Chen, J. Zhou, Y. Qiao, Z. Huang, and Y. Ji, "Novel Modulation Scheme Based on Asymmetrically Clipped Optical Orthogonal Frequency Division Multiplexing for Next-Generation Passive Optical Networks", Journal of Optical Communications and Networking, vol. 5, pp. 881-887, 2013.

[2] X. Q. Jin, J. Groenewald, E. Hugues-Salas, R. P. Giddings, and J. M. Tang, "Upstream Power Budgets of IMDD Optical OFDMA PONs Incorporating RSOA Intensity Modulator-Based Colorless ONUs", Journal of Lightwave Technology, vol. 31, pp. 1914-1920, 2013.

[3] D. Q. Neda Cvijetic, Junqiang Hu, and Ting Wang, "Orthogonal Frequency Division Multiple Access PON (OFDMA-PON) for Colorless Upstream Transmission Beyond 10 Gb/s", IEEE Journal on Selected Areas in Communications, vol. 28, pp. 781-790, Aug. 2010.

[4] J. Tang, X. Jin, J. Groenewald, E. Hugues-Salas and R. P. Giddings, "Dependence of Upstream Power Budget on the Number of ONUs in IMDD Optical OFDMA PONs", in Optical Fiber Communication Conference/National Fiber Optic Engineers Conference, Anaheim, California, 2013, p. JW2A.73.

[5] J. L. Wei, C. Sánchez, R. P. Giddings, E. Hugues-Salas and J. M. Tang, "Significant improvements in optical power budgets of real-time optical OFDM PON systems", Opt. Express, vol. 18, pp. 20732-20745, 2010.

[6] J. L. Wei, C. Sanchez, E. Hugues-Salas, P. S. Spencer, and J. M. Tang, "Wavelength-Offset Filtering in Optical OFDM IMDD Systems Using Directly Modulated DFB Lasers", Journal of Lightwave Technology, vol. 29, pp. 2861-2870, 2011.

[7] X. Zheng, J. L. Wei, and J. M. Tang, "Transmission performance of adaptively modulated optical OFDM modems using subcarrier modulation over SMF IMDD links for access and metropolitan area networks", Optics Express, vol. 16, pp. 20427-20440, 2008.

6 Chapter 6: Conclusions and Future work

6.1 Conclusions

At the start of this thesis, a need for a next generation access network technology to address the fast growing and maturing optical telecommunications network was identified. The next generation network needs to be low maintenance, spectrally efficient, high capacity, flexible and have the ability to integrate into the existing infrastructure.

The passive optical network (PON) is identified as a candidate for next generation access networks. To verify this investigations had to be made and the following new knowledge about PONs was discovered:

The optimum parameters for an upstream optical orthogonal frequency division multiplexing (OOFDM) 40 km single mode fibre (SMF) transmission with a distributed feedback (DFB) based directly modulated laser (DML) modulator were investigated. The optimum DFB based system parameters are 8 quantization bits (QB), a clipping ratio (CR) of 13 dB, a DFB driving current of 15 mA and a DFB bias current of 30 mA. The ADC/DAC sampling speed is fixed at 25 GS/s with the PIN having a sensitivity of -19 dBm. The OOFDM upstream system was validated as a good candidate for short reach access networks and provided a basis to investigate the use of multiple wavelength optical network units (ONUs) in the upstream utilising OOFDM in each ONU and combining the signals from the upstream ONUs in the optical domain to achieve multiple access. This resulted in aggregated 11.25 Gb/s over 25 km SSMF IMDD OOFDMA PONs incorporating reflective semiconductor optical amplifier (RSOA) intensity modulator based colourless ONUs where excellent agreements have been obtained between real time upstream experimental measurements and numerical simulations in terms of BER performances as functions of both ONU wavelength spacing and received optical power. Making use of experimentally verified theoretical models and component/system parameters, extensive numerical explorations have been undertaken, for the first time, of the impact of the number of ONUs on both upstream optical power budget and minimum ONU wavelength spacing as published in [1] . It has been shown that the minimum ONU wavelength spacing required for eliminating the optical beating interference (OBI) effect is independent of the number of ONUs, and that doubling the number of ONUs simultaneously accommodated gives a 1.9 dB reduction in upstream power budget. Further investigation into the effects of dispersion, nonlinear effects and chirp in the OOFDMA PON was done with a RSOA and DFB based intensity modulator at the ONUs. For the DFB based DML the dispersion effect enhanced by the chirp in the modulator is too severe to be compensated for and is thus unsuitable for optical OFDMA PONs with large optical bandwidths'. Due to not

having a limit on the performance because of chirp as is the case in the DFB based DML system an RSOA based PON system is more suited for OOFDMA PON system with a high number of ONUs. Although the minimum wavelength spacing is determined by the beating in the system the chirp also causes the minimum wavelength spacing value for a DFB PON system to be much higher than that of a RSOA PON system due to the increased spreading of the noise-like OFDM signals. For the RSOA case the dispersion effects due to increased optical bandwidth for PON systems can be successfully compensated for by implementing a delay proportional to the ONU's position in wavelength relative to the first ONU to ensure the cyclic prefix (CP) to be sufficient to combat inter-symbol interference (ISI) without increasing the CP at the cost of data throughput of the system. The small wavelength spacing of a RSOA intensity modulator compared with that of a DFB makes the RSOA an excellent candidate for use in spectrally efficient next generation IMDD OOFDMA PON systems.

Further numerical simulations results, published in [2], have shown that the utilisation of an optimum frequency-offset super-Gaussian optical filter at an order of 5 immediately after the RSOA intensity modulator in each ONU can significantly improve the upstream power budget by > 5.3dB, and simultaneously enhance the upstream power budget robustness to variations in the number of ONUs. OBI in RSOA-based IMDD OOFDMA PON systems can be reduced by implementing Gaussian optical band-pass filters to achieve optical single sideband leading to less frequency components of the signal present at detection. The reduced components at detection that can beat with each other will allow the ONUs to be spaced closer together improving the minimum wavelength spacing by another 4 GHz resulting in a more efficient use of the optical bandwidth of the signal. Investigations also show that the use of OBPFs to decrease the minimum wavelength spacing leads to an improved capacity versus reach performances for 15 ONUs enabling the OOFDMA PON with RSOA based intensity modulators in the upstream transmission system utilising OBPFs to be an excellent high capacity and spectrally efficient solution for next generation PON networks.

Also a novel technique enabling single upstream wavelength sharing among ONUs using OFDMA over 25 km and a RF upshift have been demonstrated. With optimised parameters for OFDM transceivers and a RSOA intensity modulator, aggregated 11.25 Gb/s over 25 km is achieved with only one OBPF at the optical line terminal (OLT) for single wavelength upstream transmission with a EVM of -22 dB at a received optical power of -14 dBm.

The novel single upstream transmission simulations have shown that, in OOFDMA IMDD PONs, the use of a RF upshift and a single upstream wavelength enables an aggregated data rate of 11.25 Gb/s for 15 ONUs corresponding to a EVM value of -22 dB at -10 dBm of

received optical power with a RF spacing of only 2.125 GHz resulting in a total optical signal bandwidth of only 4.125 GHz. A power budget improvement of at least 2 dB for single wavelength upstream transmission is achieved compared to wavelength spaced upstream transmission. Capacity improvement of 9.6 Gb/s is observed for 25 km transmission of single upstream wavelength multiband OOFDMA IMDD PON transmission for 2 ONUs using optimised OBPF compared to wavelength spaced ONUs utilising optimised OBPFs at the 2 ONUs outputs. This confirms that OOFDMA IMDD PONs is suitable for next generation access networks.

6.2 Future Work

The work that has been done in this thesis answers questions in regard to the suitability of implementing PONs in next generation access networks. However the research also raises additional questions on how to improve the technology even more to enable PONs to be become "future proof". After identifying the single upstream wavelength AMOOFDMA PON as an excellent candidate for next generation access networks the system capacity needs to be improved even more to ensure it will comply with NG-PON2 specifications. The main challenges for the system are:

- Limited bandwidth dictated by the modulator.
- Increased overall signal bandwidth due to a large bandgap between optical carrier and subcarriers due to beating in direct detection.
- Multiband implementation for increased number of ONUs.

To address these challenges the first task would be to investigate other possible candidates for modulators in an AMOOFDMA IMDD PON with a larger bandwidth than a RSOA but with low chirp characteristics for example reflective electro-absorption modulators (REAMs) [3]. The next task will be to address the large bandgap by investigating the use of a beat interference cancellation receiver to reduce the bandgap needed to enable the use of direct detection in upstream PONs [4]. The combination of a decreased bandgap between the optical carrier and subcarriers and a larger modulation bandwidth at the ONUs will also give better scope to utilise multiband in the system for a larger number of ONUs. The increased modulation bandwidth will allow for increased data throughput by enabling higher modulation formats to be used on subcarriers in a multiband system and allow for more bands to be introduced in the system. A

decrease in the bandgap will free up more bandwidth to use for additional bands. Addressing these challenges will ensure a place for AMOOFDMA IMDD PON in the future of optical networking.

6.3   References

[1]   J. Tang, X. Jin, J. Groenewald, E. Hugues-Salas and R. P. Giddings, "Dependence of Upstream Power Budget on the Number of ONUs in IMDD Optical OFDMA PONs", in Optical Fiber Communication Conference/National Fiber Optic Engineers Conference 2013, Anaheim, California, 2013, p. JW2A.73.

[2]   X. Q. Jin, J. Groenewald, E. Hugues-Salas, R. P. Giddings and J. M. Tang, "Upstream Power Budgets of IMDD Optical OFDMA PONs Incorporating RSOA Intensity Modulator-Based Colorless ONUs", Journal of Lightwave Technology, vol. 31, pp. 1914-1920, 2013.

[3]   E. Hugues-Salas, Q. W. Zhang, R. P. Giddings, M. Wang, and J. M. Tang, "Experimental demonstrations of record high REAM intensity modulator-enabled 19.25Gb/s real-time end-to-end dual-band optical OFDM colorless transmissions over 25km SSMF IMDD systems", vol. 21, pp. 9167-9179, 2013.

[4]   Alireza Nezamalhosseini, Qunbi Zhuge, Mahdi Malekiha, Farokh Marvasti, and David V. Plant, "Theoretical and experimental investigation of direct detection optical OFDM transmission using beat interference cancellation receiver", vol. 21, pp. 15237-15246, 2013.

Appendices

Appendix A: Simplifying the correlation between orthogonal subcarriers

The correlation between two subcarriers is:

$$\delta_{kl} = \frac{1}{T_s}\int_0^{T_s} s_k s_l^* \, dt = \frac{1}{T_s}\int_0^{T_s} e^{j2\pi\omega_k t} e^{-j2\pi\omega_l t} \, dt = \frac{1}{T_s}\int_0^{T_s} e^{j2\pi(\omega_k-\omega_l)t} \, dt$$

$$= \frac{1}{T_s}\left[\frac{1}{j(\omega_k-\omega_l)} e^{j(\omega_k-\omega_l)t}\right]_0^{T_s}$$

$$= \frac{1}{T_s}\left[\frac{1}{j(\omega_k-\omega_l)} e^{j(\omega_k-\omega_l)T_s} - \frac{1}{j(\omega_k-\omega_l)} e^{j(\omega_k-\omega_l)0}\right]$$

$$= \frac{1}{j(\omega_k-\omega_l)T_s}\left[e^{j(\omega_k-\omega_l)T_s} - 1\right]$$

We can rewrite $\left[e^{j(\omega_k-\omega_l)T_s} - 1\right]$ as $e^{\frac{j}{2}(\omega_k-\omega_l)T_s}\left[e^{\frac{j}{2}(\omega_k-\omega_l)T_s} - e^{-\frac{j}{2}(\omega_k-\omega_l)T_s}\right]$ with δ_{kl} then

$$\delta_{kl} = \frac{e^{\frac{j}{2}(\omega_k-\omega_l)T_s}}{j(\omega_k-\omega_l)T_s}\left[e^{\frac{j}{2}(\omega_k-\omega_l)T_s} - e^{-\frac{j}{2}(\omega_k-\omega_l)T_s}\right]$$

$$= e^{\frac{j}{2}(\omega_k-\omega_l)T_s}\left[\frac{e^{\frac{j}{2}(\omega_k-\omega_l)T_s} - e^{-\frac{j}{2}(\omega_k-\omega_l)T_s}}{j(\omega_k-\omega_l)T_s}\right]$$

$$= e^{\frac{j}{2}(\omega_k-\omega_l)T_s}\left[\frac{\sin(\omega_k-\omega_l)\frac{T_s}{2}}{(\omega_k-\omega_l)T_s}\right]$$

$$= e^{\frac{j}{2}(\omega_k-\omega_l)T_s}\left(\text{sinc}(\omega_k-\omega_l)\frac{T_s}{2}\right)$$

Appendix B: DFT Breakdown

Splitting two $\frac{N}{2}$-point DFTs is

$$X[k] = X_{even}[k] + \omega_{\frac{N}{2}}^k X_{odd}[k]$$

$$X_{even}[k] = \sum_{p=0}^{\frac{N}{4}-1} x[4p]\,\omega_{\frac{N}{4}}^{4kp} + \omega_{\frac{N}{2}}^{2k}\sum_{p=0}^{\frac{N}{4}-1} x[4p+2]\,\omega_{\frac{N}{4}}^{4kp}$$

$$X_{even}[k] = X_{eveneven}[k] + \omega_{\frac{N}{2}}^{2k} X_{evenodd}[k]$$

$$X_{odd}[k] = \sum_{m=0}^{\frac{N}{2}-1} x[2m+1]\,\omega_{\frac{N}{2}}^{2km} = \sum_{p=0}^{\frac{N}{4}-1} x[4p+1]\,\omega_{\frac{N}{4}}^{4kp} + \omega_{\frac{N}{4}}^{2k}\sum_{p=0}^{\frac{N}{4}-1} x[4p+3]\,\omega_{\frac{N}{4}}^{4kp}$$

$$X_{odd}[k] = X_{oddeven}[k] + \omega_{\frac{N}{4}}^{2k} X_{oddodd}[k]$$

$$X_d[k] = X_{eveneven}[k] + \omega_{\frac{N}{2}}^{2k} X_{evenodd}[k] + \omega_{\frac{N}{2}}^{k}(X_{oddeven}[k] + \omega_{\frac{N}{4}}^{2k} X_{oddodd}[k])$$

Appendix C: PAPR comparison between single tone, complex sinusoid and OFDM signal

Mathematically the PAPR is represented as [2]

$$PAPR = \frac{max[x(t).x^*(t)]}{E[x(t).x^*(t)]} \ with \ PAPR_{dB} = 10log_{10}(PAPR)$$

with $E[x(t).x^*(t)]$ being the mean or expected value of the power of $x(t)$. For a **single sine tone** we have [2]

$$x(t) = \cos(\omega t) \ with \ max[x(t).x^*(t)] = 1 \ and \ E[x(t).x^*(t)] = \frac{1}{T}\int_0^T sin^2(\omega t) = \frac{1}{2}$$

$$with \ PAPR = \frac{1}{1/2} = 2$$

For a **complex sinusoid** we have [2]

$$x(t) = e^{j\omega t} with \ max[x(t).x^*(t)] = 1 \ and \ E[x(t).x^*(t)] = \frac{1}{T}\int_0^T e^{j\omega t}e^{-j\omega t} = 1$$

$$with \ PAPR = \frac{1}{1} = 1$$

For an **OFDM signal** we have [2]

$$s_n = \sum_{k=0}^{N-1} c_k e^{j\frac{kn}{N}} \ and \ s_n^* = \sum_{k=0}^{N-1} c_k^* e^{-j\frac{kn}{N}}$$

$$with \ max[s_n.s_n^*] = max[\sum_{k=0}^{N-1} c_k e^{j\frac{kn}{N}} . \sum_{k=0}^{N-1} c_k^* e^{-j\frac{kn}{N}}]$$

$$= max[c_k c_k^* \sum_{k=0}^{N-1}\sum_{k=0}^{N-1} e^{j\frac{kn}{N}}e^{-j\frac{kn}{N}}]$$

$$= N^2 \ if \ we \ assume \ a \ phase \ shift \ keying \ scheme \ with \ a \ fixed \ amplitude \ with \ c_k = 1$$

$$and \ E[s_n.s_n^*] = \frac{1}{T}\int_0^T \sum_{k=0}^{N-1} c_k e^{j\frac{kn}{N}} . \sum_{k=0}^{N-1} c_k^* e^{-j\frac{kn}{N}} = \frac{1}{T}\int_0^T c_k c_k^* \sum_{k=0}^{N-1}\sum_{k=0}^{N-1} e^{j\frac{kn}{N}}e^{-j\frac{kn}{N}}$$

$$with \ T = \frac{1}{\Delta f} \ with \ \Delta f = \frac{1}{N\Delta t}$$

$$E[s_n.s_n^*] = N \ with \ PAPR = \frac{N^2}{N} = N$$

Appendix D: Square Law detection representation

The optical signal is detected with a square law device yielding the following output:

$$I(t) = |E(t)|^2 = \left| A(t)e^{j\omega_0 t} \right|^2 = \left| \sqrt{I_{DC} + \alpha_{scaling}Re(e^{j\omega_{IF}t}.S_B(t))}\; e^{j(\omega_0+\varphi)t} \right|^2$$

$$= \sqrt{I_{DC} + \alpha_{scaling}Re(e^{j\omega_{IF}t}.S_B(t))}e^{j(\omega_0+\varphi)t}.\sqrt{I_{DC} + \alpha_{scaling}Re(e^{j\omega_{IF}t}.S_B(t))}e^{j(\omega_0+\varphi)t^*}\quad [48]$$

The received signal and beating components can be represented in the frequency domain as:

$$I(f) = \delta(f).I_{DC} + \sum_{k=-\frac{1}{2}N_{sc}}^{\frac{1}{2}N_{sc}} C_k.\delta\left(f - \frac{k}{T_s}\right) + \frac{1}{4I_{DC}}\left(\sum_{k_1=-\frac{1}{2}N_{sc}}^{\frac{1}{2}N_{sc}} \sum_{k_2=-\frac{1}{2}N_{sc}}^{\frac{1}{2}N_{sc}} C_{k_1}.C_{k_2}.\delta(f-(\frac{k_1}{T_s}+\frac{k_2}{T_s}+2\pi)) \right)$$

$$+ \frac{1}{4I_{DC}}\left(\sum_{k_1=-\frac{1}{2}N_{sc}}^{\frac{1}{2}N_{sc}} \sum_{k_2=-\frac{1}{2}N_{sc}}^{\frac{1}{2}N_{sc}} C_{k_1}.C_{k_2}.\delta(f-(\frac{k_1}{T_s}+\frac{k_2}{T_s})) \right) ...$$

The frequency domain representation of the received signal and the beating components are represented in the figure below and the terms are colour coded to clearly show where the wanted an unwanted beating products will fall.
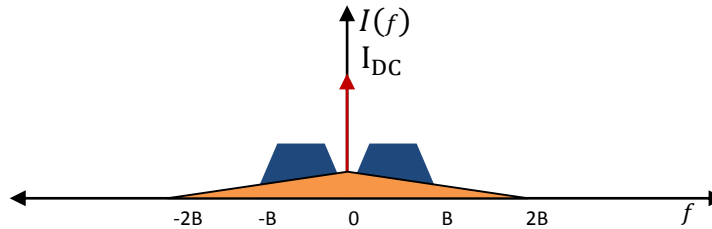
Figure 88: Frequency representation of direct detection beating products.

Appendix E: MZM operation

By combining the two paths with different phase modulations, this phase modulation is turned into an intensity modulation. The output intensity is controlled by changing the delay through one or both of the optical paths by means of the electro-optic effect. This effect occurs in some materials such as lithium niobate (LiNbO3), some semiconductors, as well as some polymers and causes the refractive index to change in the presence of an electric field.

The MZM is a planar waveguide structure deposited on the substrate, with two pairs of electrodes. One pair of electrodes is for the high-speed ac voltage representing the modulation

data (RF) signal and the other pair for dc bias voltage. In the MZM the phase change is due to a voltage applied to each arm. To phase-modulate the light propagating into that arm which is the incoming light from laser split into the two waveguides according to the electric voltage applied to each electrode we relate the input field to the output field as follows:

$$E_{out} = E_{in}((1 - \alpha)e^{-j\theta_1} + \alpha e^{-j\theta_2})$$

With α the splitting ratio of incoming beam and is 0.5 ideally. The transfer function of the Push Pull MZM is

$$\frac{E_{out}}{E_{in}} = \cos\left(\frac{\pi}{V_{\pi 1}} V_1\right) \textit{ but the value for } V_1 = V_{RF} + V_{DCBIAS} \textit{ and } E_{in} = \sqrt{P}e^{j\omega_{LD}t + \varphi_{LD}}$$

with P the power of the continuous wave. The Push-Pull configuration will ensure a chirp-free amplitude modulation. The coherent system is highly linear in the E/O and O/E conversion and the output of an optical I-Q modulator consisting of 2 MZM's and a phase modulator in one of the branches is [1]

$$\text{E(t)} = \frac{1}{2} \cdot \cos\left(\frac{\pi}{V_{\pi 1}} V_1\right) \cdot \sqrt{P}e^{j\omega_{LD}t + \varphi_{LD}} + j \cdot \frac{1}{2} \cdot \cos\left(\frac{\pi}{V_{\pi 1}} V_2\right) \cdot \sqrt{P}e^{j\omega_{LD}t + \varphi_{LD}}$$

$$\textit{with } V_1 = V_I + V_{DCBIAS} \textit{ and } V_2 = V_Q + V_{DCBIAS}$$

$$\text{E(t)} = \frac{1}{2}\cos\left(\frac{\pi}{V_{\pi 1}} V_I + \frac{\pi}{V_{\pi 1}} V_{DCBIAS}\right) \cdot \sqrt{P}e^{j\omega_{LD}t + \varphi_{LD}}$$

$$+ j\frac{1}{2}\cos\left(\frac{\pi}{V_{\pi 1}} V_Q + \frac{\pi}{V_{\pi 1}} V_{DCBIAS}\right) \cdot \sqrt{P}e^{j\omega_{LD}t + \varphi_{LD}}$$

$$\textit{for simplicity we set } \sqrt{P} = 1$$

$$\text{E(t)} = E_B(t)e^{j\omega_{LD}t + \varphi_{LD}}$$

$$\textit{with } E_B(t) = \frac{1}{2}\cos\left(\frac{\pi}{V_{\pi 1}} V_I + \frac{\pi}{V_{\pi 1}} V_{DCBIAS}\right) + j\frac{1}{2}\cos\left(\frac{\pi}{V_{\pi 1}} V_Q + \frac{\pi}{V_{\pi 1}} V_{DCBIAS}\right)$$

Appendix F: Derivation of the frequency representation for a DSB RF up-shifted signal

Following the steps in Appendix D with the baseband OFDM signal replaced with a RF upshifted signal the detected current at the square law detector becomes

$$I(t) =$$

$$I_{DC} + \frac{1}{2}.Re\left(e^{-j2\pi f_{RF}t}.\sum_{k=-\frac{1}{2}N_{sc}}^{\frac{1}{2}N_{sc}} C_k e^{j2\pi\frac{k}{T_s}t}\right) + \frac{1}{8I_{DC}}.Re\left(e^{-j2\pi f_{RF}t}.\sum_{k=-\frac{1}{2}N_{sc}}^{\frac{1}{2}N_{sc}} C_k e^{j\left(2\pi\frac{k}{T_s}+\pi\right)t}\right)^2$$

$$+\frac{1}{2}.Re\left(e^{j2\pi f_{RF}t}.\sum_{k=-\frac{1}{2}N_{sc}}^{\frac{1}{2}N_{sc}} C_k e^{j2\pi\frac{k}{T_s}t}\right) + \frac{1}{4I_{DC}}\left(Re\left(e^{-j2\pi f_{RF}t}e^{j2\pi f_{RF}t}.\sum_{k=-\frac{1}{2}N_{sc}}^{\frac{1}{2}N_{sc}} C_k e^{j2\pi\frac{k}{T_s}t}\right)\right)^2$$

$$+\frac{1}{16I_{DC}{}^2}.Re\left(e^{j2\pi f_{RF}t}e^{-j2\pi f_{RF}t}e^{-j2\pi f_{RF}t}.\sum_{k=-\frac{1}{2}N_{sc}}^{\frac{1}{2}N_{sc}} C_k e^{j\left(2\pi\frac{k}{T_s}+\pi\right)t}\right)^3 + \frac{1}{8I_{DC}}.Re\left(e^{j2\pi f_{RF}t}e^{j2\pi f_{RF}t}.\sum_{k=-\frac{1}{2}N_{sc}}^{\frac{1}{2}N_{sc}} C_k e^{j\left(2\pi\frac{k}{T_s}+\pi\right)t}\right)^2$$

$$+\frac{1}{16I_{DC}{}^2}.Re\left(e^{-j2\pi f_{RF}t}e^{j2\pi f_{RF}t}e^{j2\pi f_{RF}t}.\sum_{k=-\frac{1}{2}N_{sc}}^{\frac{1}{2}N_{sc}} C_k e^{j(2\pi\frac{k}{T_s}+\pi)t}\right)^3 + \frac{1}{64I_{DC}{}^3}.Re\left(e^{-j2\pi f_{RF}t}e^{-j2\pi f_{RF}t}e^{j2\pi f_{RF}t}e^{j2\pi f_{RF}t}.\sum_{k=-\frac{1}{2}N_{sc}}^{\frac{1}{2}N_{sc}} C_k e^{j2\pi\frac{k}{T_s}t}\right)^4$$

Considering only the first and second order terms of the signal to illustrate the subcarrier-subcarrier beating with the result:

$$= \delta(f).I_{DC} + \frac{1}{2}\sum_{k=-\frac{1}{2}N_{sc}}^{\frac{1}{2}N_{sc}} C_k.\delta\left(f - \frac{k}{T_s} + f_{RF}\right)$$

$$+\frac{1}{2}\sum_{k=-\frac{1}{2}N_{sc}}^{\frac{1}{2}N_{sc}} C_k.\delta\left(f - \frac{k}{T_s} - f_{RF}\right) + \frac{1}{8I_{DC}}\left(\sum_{k_1=-\frac{1}{2}N_{sc}}^{\frac{1}{2}N_{sc}}\sum_{k_2=-\frac{1}{2}N_{sc}}^{\frac{1}{2}N_{sc}} C_{k_1}.C_{k_2}.\delta\left(f - \left(\frac{k_1}{T_s} + \frac{k_2}{T_s} + 2\pi - 2f_{RF}\right)\right)\right)$$

$$+\frac{1}{4I_{DC}}\left(\sum_{k_1=-\frac{1}{2}N_{sc}}^{\frac{1}{2}N_{sc}}\sum_{k_2=-\frac{1}{2}N_{sc}}^{\frac{1}{2}N_{sc}} C_{k_1}.C_{k_2}.\delta(f - (\frac{k_1}{T_s} + \frac{k_2}{T_s}))\right) + \frac{1}{4I_{DC}}\left(\sum_{k_1=-\frac{1}{2}N_{sc}}^{\frac{1}{2}N_{sc}}\sum_{k_2=-\frac{1}{2}N_{sc}}^{\frac{1}{2}N_{sc}} C_{k_1}.C_{k_2}.\delta(f - (\frac{k_1}{T_s} + \frac{k_2}{T_s} + 2f_{RF} + 2\pi))\right) \dots$$

Appendix G: Derivation of DSB multiband beating components

Following the procedure from appendix D and appendix F to illustrate the beating between subcarriers and sub-bands in the square law detected OFDM signal with one band at baseband and a second band RF upshifted the result is:

$$I(t) = \left[I_{DC} + \frac{1}{2}\left(Re\left(\sum_{k=-\frac{1}{2}N_{sc}}^{\frac{1}{2}N_{sc}} C_k e^{j2\pi\frac{k}{T_s}t} + e^{-j2\pi f_{RF}t}.\sum_{k=-\frac{1}{2}N_{sc}}^{\frac{1}{2}N_{sc}} C_k e^{j2\pi\frac{k}{T_s}t}\right)\right)\right.$$

$$\left. -\frac{1}{8I_{DC}}.Re\left(\sum_{k=-\frac{1}{2}N_{sc}}^{\frac{1}{2}N_{sc}} C_k e^{j2\pi\frac{k}{T_s}t} + e^{-j2\pi f_{RF}t}.\sum_{k=-\frac{1}{2}N_{sc}}^{\frac{1}{2}N_{sc}} C_k e^{j2\pi\frac{k}{T_s}t}\right)^2\right]$$

$$+\left[\frac{1}{2}\left(Re\left(\sum_{k=-\frac{1}{2}N_{sc}}^{\frac{1}{2}N_{sc}}C_k e^{j2\pi\frac{k}{T_s}t}+e^{j2\pi f_{RF}t}.\sum_{k=-\frac{1}{2}N_{sc}}^{\frac{1}{2}N_{sc}}C_k e^{j2\pi\frac{k}{T_s}t}\right)\right)+\frac{1}{4}\left(Re\left(\sum_{k=-\frac{1}{2}N_{sc}}^{\frac{1}{2}N_{sc}}C_k e^{j2\pi\frac{k}{T_s}t}+e^{-j2\pi f_{RF}t}e^{j2\pi f_{RF}t}.\sum_{k=-\frac{1}{2}N_{sc}}^{\frac{1}{2}N_{sc}}C_k e^{j2\pi\frac{k}{T_s}t}\right)\right)^2/I_{DC}\right.$$

$$-\frac{1}{16}.Re\left(\sum_{k=-\frac{1}{2}N_{sc}}^{\frac{1}{2}N_{sc}}C_k e^{j2\pi\frac{k}{T_s}t}+e^{j2\pi f_{RF}t}e^{-j2\pi f_{RF}t}e^{-j2\pi f_{RF}t}.\sum_{k=-\frac{1}{2}N_{sc}}^{\frac{1}{2}N_{sc}}C_k e^{j2\pi\frac{k}{T_s}t}\right)^3/I_{DC}{}^2\right]$$

$$+\left[-\frac{1}{8}.Re\left(\sum_{k=-\frac{1}{2}N_{sc}}^{\frac{1}{2}N_{sc}}C_k e^{j2\pi\frac{k}{T_s}t}+e^{j2\pi f_{RF}t}e^{j2\pi f_{RF}t}.\sum_{k=-\frac{1}{2}N_{sc}}^{\frac{1}{2}N_{sc}}C_k e^{j2\pi\frac{k}{T_s}t}\right)^2/I_{DC}\right.$$

$$-\frac{1}{16}.Re\left(\sum_{k=-\frac{1}{2}N_{sc}}^{\frac{1}{2}N_{sc}}C_k e^{j2\pi\frac{k}{T_s}t}+e^{-j2\pi f_{RF}t}e^{j2\pi f_{RF}t}e^{j2\pi f_{RF}t}.\sum_{k=-\frac{1}{2}N_{sc}}^{\frac{1}{2}N_{sc}}C_k e^{j2\pi\frac{k}{T_s}t}\right)^3/I_{DC}$$

$$+\frac{1}{64}.Re\left(\sum_{k=-\frac{1}{2}N_{sc}}^{\frac{1}{2}N_{sc}}C_k e^{j2\pi\frac{k}{T_s}t}+e^{j2\pi f_{RF}t}e^{j2\pi f_{RF}t}e^{-j2\pi f_{RF}t}e^{-j2\pi f_{RF}t}.\sum_{k=-\frac{1}{2}N_{sc}}^{\frac{1}{2}N_{sc}}C_k e^{j2\pi\frac{k}{T_s}t}\right)^4/I_{DC}{}^3\right]$$

Considering only first and second order terms the frequency domain signal becomes:

$$=\delta(f).I_{DC}+\frac{1}{2}\sum_{k=-\frac{1}{2}N_{sc}}^{\frac{1}{2}N_{sc}}C_k.\delta\left(f-\frac{k}{T_s}\right)+\frac{1}{2}\sum_{k=-\frac{1}{2}N_{sc}}^{\frac{1}{2}N_{sc}}C_k.\delta\left(f-\frac{k}{T_s}+f_{RF}\right)$$

$$+\frac{1}{2}\sum_{k=-\frac{1}{2}N_{sc}}^{\frac{1}{2}N_{sc}}C_k.\delta\left(f-\frac{k}{T_s}\right)+\frac{1}{2}\sum_{k=-\frac{1}{2}N_{sc}}^{\frac{1}{2}N_{sc}}C_k.\delta\left(f-\frac{k}{T_s}-f_{RF}\right)$$

$$+\frac{1}{8I_{DC}}\left(\sum_{k_1=-\frac{1}{2}N_{sc}}^{\frac{1}{2}N_{sc}}\sum_{k_2=-\frac{1}{2}N_{sc}}^{\frac{1}{2}N_{sc}}C_{k_1}.C_{k_2}.\delta\left(f-\left(\frac{k_1}{T_s}+\frac{k_2}{T_s}\right)\right)\sum_{k_1=-\frac{1}{2}N_{sc}}^{\frac{1}{2}N_{sc}}\sum_{k_2=-\frac{1}{2}N_{sc}}^{\frac{1}{2}N_{sc}}C_{k_1}.C_{k_2}.\delta(f-(\frac{k_1}{T_s}+\frac{k_2}{T_s}+\pi-f_{RF}))\right.$$

$$+\sum_{k_1=-\frac{1}{2}N_{sc}}^{\frac{1}{2}N_{sc}}\sum_{k_2=-\frac{1}{2}N_{sc}}^{\frac{1}{2}N_{sc}}C_{k_1}.C_{k_2}.\delta(f-(\frac{k_1}{T_s}+\frac{k_2}{T_s}+\pi-f_{RF}))$$

$$\left.+\sum_{k_1=-\frac{1}{2}N_{sc}}^{\frac{1}{2}N_{sc}}\sum_{k_2=-\frac{1}{2}N_{sc}}^{\frac{1}{2}N_{sc}}C_{k_1}.C_{k_2}.\delta(f-(\frac{k_1}{T_s}+\frac{k_2}{T_s}+2\pi-2f_{RF}))\right)$$

$$+\frac{1}{4I_{DC}}\left(\sum_{k_1=-\frac{1}{2}N_{sc}}^{\frac{1}{2}N_{sc}}\sum_{k_2=-\frac{1}{2}N_{sc}}^{\frac{1}{2}N_{sc}}C_{k_1}.C_{k_2}.\delta\left(f-\left(\frac{k_1}{T_s}+\frac{k_2}{T_s}\right)\right)+\sum_{k_1=-\frac{1}{2}N_{sc}}^{\frac{1}{2}N_{sc}}\sum_{k_2=-\frac{1}{2}N_{sc}}^{\frac{1}{2}N_{sc}}C_{k_1}.C_{k_2}.\delta(f-(\frac{k_1}{T_s}+\frac{k_2}{T_s}))\right.$$

$$\left.+\sum_{k_1=-\frac{1}{2}N_{sc}}^{\frac{1}{2}N_{sc}}\sum_{k_2=-\frac{1}{2}N_{sc}}^{\frac{1}{2}N_{sc}}C_{k_1}.C_{k_2}.\delta(f-(\frac{k_1}{T_s}+\frac{k_2}{T_s}))+\sum_{k_1=-\frac{1}{2}N_{sc}}^{\frac{1}{2}N_{sc}}\sum_{k_2=-\frac{1}{2}N_{sc}}^{\frac{1}{2}N_{sc}}C_{k_1}.C_{k_2}.\delta(f-(\frac{k_1}{T_s}+\frac{k_2}{T_s}))\right)$$

$$+\frac{1}{8I_{DC}}\left(\sum_{k_1=-\frac{1}{2}N_{sc}}^{\frac{1}{2}N_{sc}}\sum_{k_2=-\frac{1}{2}N_{sc}}^{\frac{1}{2}N_{sc}}C_{k_1}.C_{k_2}.\delta\left(f-\left(\frac{k_1}{T_s}+\frac{k_2}{T_s}\right)\right)+\sum_{k_1=-\frac{1}{2}N_{sc}}^{\frac{1}{2}N_{sc}}\sum_{k_2=-\frac{1}{2}N_{sc}}^{\frac{1}{2}N_{sc}}C_{k_1}.C_{k_2}.\delta(f-(\frac{k_1}{T_s}+\frac{k_2}{T_s}+2\pi-2f_{RF}))\right.$$

$$+\sum_{k_1=-\frac{1}{2}N_{sc}}^{\frac{1}{2}N_{sc}}\sum_{k_2=-\frac{1}{2}N_{sc}}^{\frac{1}{2}N_{sc}}C_{k_1}.C_{k_2}.\delta(f-(\frac{k_1}{T_s}+\frac{k_2}{T_s}+2\pi-2f_{RF}))$$

$$\left.+\sum_{k_1=-\frac{1}{2}N_{sc}}^{\frac{1}{2}N_{sc}}\sum_{k_2=-\frac{1}{2}N_{sc}}^{\frac{1}{2}N_{sc}}C_{k_1}.C_{k_2}.\delta(f-(\frac{k_1}{T_s}+\frac{k_2}{T_s}+4\pi-4f_{RF}))\right)$$

Appendix H: Beating products in direct detection process of a single wavelength upstream OOFDMA PON multiband system

For the proposed single wavelength upstream OOFDMA PON multiband system the signal representing the optical field before detection can be presented as

$$E(t) = \sqrt{I_{DC} + \alpha Re(S_{B1}(t))}\, e^{j(\omega_0 + \varphi)t} + \sqrt{I_{DC} + \alpha Re(S_{B2}(t))}\, e^{j(\omega_0 + \varphi)t}$$

with $E(t)$ the output optical field, φ the phase of the modulator , ω_0 the carrier frequency and $S_{B1}(t)$ and $S_{B2}(t)$

$$s_{B1}(t) = e^{j2\pi f_{RF}t} \cdot \sum_{k=0}^{\frac{1}{2}N_{sc}} C_{k1} e^{j2\pi \frac{k}{T_s}t} + e^{j2\pi f_{RF2}t} \cdot \sum_{k=-\frac{1}{2}N_{sc}}^{-1} C_{k1MB} e^{j2\pi \frac{k}{T_s}t}$$

$$s_{B2}(t) = e^{j2\pi f_{RF}t} \cdot \sum_{k=0}^{\frac{1}{2}N_{sc}} C_{k2} e^{j2\pi \frac{k}{T_s}t} + e^{j2\pi f_{RF2}t} \cdot \sum_{k=0}^{\frac{1}{2}N_{sc}} C_{k1MB} e^{j2\pi \frac{k}{T_s}t}$$

$$s_{B1*}(t) = e^{-j2\pi f_{RF}t} \cdot \sum_{k=0}^{\frac{1}{2}N_{sc}} C_{k1*} e^{-j2\pi \frac{k}{T_s}t} + e^{-j2\pi f_{RF2}t} \cdot \sum_{k=-\frac{1}{2}N_{sc}}^{-1} C_{k1*MB} e^{-j2\pi \frac{k}{T_s}t}$$

$$s_{B2*}(t) = e^{-j2\pi f_{RF}t} \cdot \sum_{k=0}^{\frac{1}{2}N_{sc}} C_{k2*} e^{-j2\pi \frac{k}{T_s}t} + e^{-j2\pi f_{RF2}t} \cdot \sum_{k=0}^{\frac{1}{2}N_{sc}} C_{k2*MB} e^{-j2\pi \frac{k}{T_s}t}$$

The direct detection of the optical field is

$$i_{out}(t) = \left| \sqrt{I_{DC} + \alpha Re(.S_{B1}(t))}\, e^{j(\omega_0+\varphi)t} + \sqrt{I_{DC} + \alpha Re(S_{B2}(t))}\, e^{j(\omega_0+\varphi)t} \right|^2$$

$$= \sqrt{I_{DC} + \alpha Re(S_{B1}(t))}\, e^{j(\omega_0+\varphi)t} + \sqrt{I_{DC} + \alpha Re(S_{B2}(t))}\, e^{j(\omega_0+\varphi)t}$$

$$\cdot \left(\sqrt{I_{DC} + \alpha Re(S_{B1}(t))}\, e^{j(\omega_0+\varphi)t} + \sqrt{I_{DC} + \alpha Re(S_{B2}(t))}\, e^{j(\omega_0+\varphi)t} \right)^*$$

Multiplying the expression above yields

$$= \sqrt{I_{DC} + \alpha Re(.S_{B1}(t))} \cdot \sqrt{I_{DC} + \alpha Re(.S_{B1}(t))}^* +$$
$$\sqrt{I_{DC} + \alpha Re(S_{B2}(t))} \cdot \sqrt{I_{DC} + \alpha Re(S_{B2}(t))}^* +$$
$$\sqrt{I_{DC} + \alpha Re(S_{B2}(t))} \cdot \sqrt{I_{DC} + \alpha Re(S_{B1}(t))}^* +$$
$$\sqrt{I_{DC} + \alpha Re(S_{B1}(t))} \cdot \sqrt{I_{DC} + \alpha Re(S_{B2}(t))}^*$$

After expanding the equation above using a Taylor series and substituting $S_{B1}(t)$ and $S_{B2}(t)$ and setting $\alpha = 1$ for simplicity and simplifying the equation we end up with an expression that will show the wanted and subcarrier-subcarrier beating products including beating of the subcarriers of sub-bands in the frequency domain. The expression and frequency spectrum representation for the wanted products is

$$I(f) = 4\mathrm{I_{DC}} + \left(\left(e^{-j2\pi f_{RF}t} \cdot \sum_{k=0}^{\frac{1}{2}N_{sc}} C_{k1*} e^{-j2\pi\frac{k}{T_s}t} + e^{-j2\pi f_{RF2}t} \cdot \sum_{k=-\frac{1}{2}N_{sc}}^{-1} C_{k1*MB} e^{-j2\pi\frac{k}{T_s}t} \right) \right)$$

$$+ \left(\left(e^{-j2\pi f_{RF}t} \cdot \sum_{k=0}^{\frac{1}{2}N_{sc}} C_{k2*} e^{-j2\pi\frac{k}{T_s}t} + e^{-j2\pi f_{RF2}t} \cdot \sum_{k=0}^{\frac{1}{2}N_{sc}} C_{k2*MB} e^{-j2\pi\frac{k}{T_s}t} \right) \right)$$

$$+ e^{j2\pi f_{RF}t} \cdot \sum_{k=0}^{\frac{1}{2}N_{sc}} C_{k1} e^{j2\pi\frac{k}{T_s}t} + e^{j2\pi f_{RF2}t} \cdot \sum_{k=-\frac{1}{2}N_{sc}}^{-1} C_{k1MB} e^{j2\pi\frac{k}{T_s}t}$$

$$+ \left(\left(e^{j2\pi f_{RF}t} \cdot \sum_{k=0}^{\frac{1}{2}N_{sc}} C_{k2} e^{j2\pi\frac{k}{T_s}t} + e^{j2\pi f_{RF2}t} \cdot \sum_{k=0}^{\frac{1}{2}N_{sc}} C_{k2MB} e^{j2\pi\frac{k}{T_s}t} \right) \right)$$

$$= 4\delta(f)\mathrm{I_{DC}} + \left(\left(\sum_{k=0}^{\frac{1}{2}N_{sc}} C_{k1*}\delta\left(f + \frac{k}{T_s} + f_{RF}\right) + \sum_{k=-\frac{1}{2}N_{sc}}^{-1} C_{k1*MB}\delta\left(f + \frac{k}{T_s} + f_{RF2}\right) \right) \right)$$

$$+ \left(\left(\sum_{k=0}^{\frac{1}{2}N_{sc}} C_{k2*}\delta\left(f + \frac{k}{T_s} + f_{RF}\right) + \sum_{k=0}^{\frac{1}{2}N_{sc}} C_{k2*MB}\delta\left(f + \frac{k}{T_s} + f_{RF2}\right) \right) \right)$$

$$+ \sum_{k=0}^{\frac{1}{2}N_{sc}} C_{k1}\delta\left(f - \frac{k}{T_s} - f_{RF}\right) + \sum_{k=-\frac{1}{2}N_{sc}}^{-1} C_{k1MB}\delta\left(f - \frac{k}{T_s} - f_{RF2}\right)$$

$$+ \left(\left(\sum_{k=0}^{\frac{1}{2}N_{sc}} C_{k2}\delta\left(f - \frac{k}{T_s} - f_{RF}\right) + \sum_{k=0}^{\frac{1}{2}N_{sc}} C_{k2MB}\delta\left(f - \frac{k}{T_s} - f_{RF2}\right) \right) \right)$$
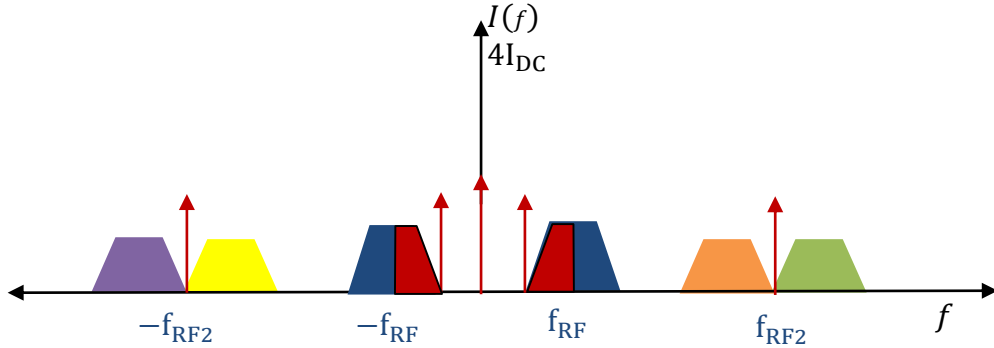
Figure 89: Frequency representation of OOFDMA PON multiband received signal spectrum.

The expression and frequency domain representation for the unwanted products is shown below. For simplicity the products are broken up into 6 groups. The first group is

$$
-\frac{1}{4I_{DC}}\left(\left(\sum_{k1=0}^{\frac{1}{2}N_{sc}}\sum_{k2=0}^{\frac{1}{2}N_{sc}}C_{k1*}C_{k1*}\delta\left(f+\frac{k1}{T_s}+\frac{k2}{T_s}+f_{RF}\right)+2.\sum_{k1=-\frac{1}{2}N_{sc}}^{-1}\sum_{k2=0}^{\frac{1}{2}N_{sc}}C_{k1*}C_{k1*MB}\delta\left(f+\frac{k1}{T_s}+\frac{k2}{T_s}+f_{RF}+f_{RF2}\right)\right.\right.
$$

$$
\left.\left.+\sum_{k1=-\frac{1}{2}N_{sc}}^{-1}\sum_{k2=-\frac{1}{2}N_{sc}}^{-1}C_{k1*MB}C_{k1*MB}\delta\left(f+\frac{k1}{T_s}+\frac{k2}{T_s}+2f_{RF2}\right)\right)\right)
$$

$$
-\frac{1}{4I_{DC}}\left(\left(\sum_{k1=0}^{\frac{1}{2}N_{sc}}\sum_{k2=0}^{\frac{1}{2}N_{sc}}C_{k2*}C_{k2*}\delta\left(f+\frac{k1}{T_s}+\frac{k2}{T_s}+2f_{RF}\right)+2.\sum_{k1=0}^{\frac{1}{2}N_{sc}}\sum_{k2=0}^{\frac{1}{2}N_{sc}}C_{k2*}C_{k2*MB}\delta\left(f+\frac{k1}{T_s}+\frac{k2}{T_s}+f_{RF}+f_{RF2}\right)\right.\right.
$$

$$
\left.\left.+\sum_{k1=0}^{\frac{1}{2}N_{sc}}\sum_{k2=0}^{\frac{1}{2}N_{sc}}C_{k2*MB}C_{k2*MB}\delta\left(f+\frac{k1}{T_s}+\frac{k2}{T_s}+2f_{RF2}\right)\right)\right)
$$

$$
+\frac{1}{4I_{DC}}\left(.\sum_{k1=0}^{\frac{1}{2}N_{sc}}\sum_{k2=0}^{\frac{1}{2}N_{sc}}C_{k1*}C_{k1*}\delta\left(f-\frac{k1}{T_s}+\frac{k2}{T_s}\right)+\sum_{k1=-\frac{1}{2}N_{sc}}^{-1}\sum_{k2=0}^{\frac{1}{2}N_{sc}}C_{k1*}C_{k1MB}\delta\left(f-(\frac{k1}{T_s}+\frac{k2}{T_s}+f_{RF}-f_{RF2})\right)\right.
$$

$$
\left.+\sum_{k1=0}^{\frac{1}{2}N_{sc}}\sum_{k2=-\frac{1}{2}N_{sc}}^{-1}C_{k1}C_{k1*MB}\delta\left(f-(\frac{k1}{T_s}-\frac{k2}{T_s}+f_{RF}-f_{RF2})\right)+\sum_{k1=-\frac{1}{2}N_{sc}}^{-1}\sum_{k2=-\frac{1}{2}N_{sc}}^{-1}C_{k1MB}C_{k1*MB}\delta\left(f-\frac{k1}{T_s}+\frac{k2}{T_s}\right)\right)
$$

$$
+\frac{1}{4I_{DC}}\left(.\sum_{k1=0}^{\frac{1}{2}N_{sc}}\sum_{k2=0}^{\frac{1}{2}N_{sc}}C_{k2}C_{k2*}\delta\left(f-\frac{k1}{T_s}+\frac{k2}{T_s}\right)+\sum_{k1=0}^{\frac{1}{2}N_{sc}}\sum_{k2=0}^{\frac{1}{2}N_{sc}}C_{k2*}C_{k2MB}\delta\left(f-(\frac{k1}{T_s}-\frac{k2}{T_s}-f_{RF}+f_{RF2})\right)\right.
$$

$$
\left.+\sum_{k1=0}^{\frac{1}{2}N_{sc}}\sum_{k=20}^{\frac{1}{2}N_{sc}}C_{k2}C_{k2*MB}\delta\left(f-\frac{k1}{T_s}-\frac{k2}{T_s}+f_{RF}-f_{RF2})\right)+\sum_{k1=0}^{1\frac{1}{2}N_{sc}-}\sum_{k2=0}^{\frac{1}{2}N_{sc}}C_{k2*}C_{k2MB}\delta\left(f-(\frac{k1}{T_s}-\frac{k2}{T_s})\right)\right)
$$

135

Figure 90: Frequency representation of group one beating products.

The second group is

$$+\frac{1}{4I_{DC}}\left(\left(\sum_{k1=0}^{\frac{1}{2}N_{sc}}\sum_{k2=0}^{\frac{1}{2}N_{sc}}C_{k1*}C_{k2}\delta\left(f-(-\frac{k1}{T_s}-\frac{k2}{T_s})\right)+\sum_{k1=0}^{\frac{1}{2}N_{sc}}\sum_{k2=0}^{\frac{1}{2}N_{sc}}C_{k1*}C_{k2MB}\delta\left(f-(-\frac{k1}{T_s}-\frac{k2}{T_s}-f_{RF}+f_{RF2})\right)\right.\right.$$

$$\left.\left.+\sum_{k1=-\frac{1}{2}N_{sc}}^{-1}\sum_{k2=0}^{\frac{1}{2}N_{sc}}C_{k2}C_{k1*MB}\delta\left(f-(-\frac{k1}{T_s}-\frac{k2}{T_s}-f_{RF}-f_{RF2})\right)+\sum_{k1=-\frac{1}{2}N_{sc}}^{-1}\sum_{k2=0}^{\frac{1}{2}N_{sc}}C_{k2MB}C_{k1*MB}\delta\left(f-(\frac{k1}{T_s}-\frac{k2}{T_s})\right)\right)\right)$$

$$+\frac{1}{4I_{DC}}\left(\left(\sum_{k1=0}^{\frac{1}{2}N_{sc}}\sum_{k2=0}^{\frac{1}{2}N_{sc}}C_{k1}C_{k2*}\delta\left(f-(\frac{k1}{T_s}-\frac{k2}{T_s})\right)+\sum_{k1=0}^{\frac{1}{2}N_{sc}}\sum_{k2=-\frac{1}{2}N_{sc}}^{-1}C_{k2*}C_{k1MB}\delta\left(f-(-\frac{k1}{T_s}+\frac{k2}{T_s}-f_{RF}+f_{RF2})\right)\right.\right.$$

$$\left.\left.+\sum_{k1=0}^{\frac{1}{2}N_{sc}}\sum_{k2=0}^{\frac{1}{2}N_{sc}}C_{k1}C_{k1*MB}\delta\left(f-(+\frac{k1}{T_s}-\frac{k2}{T_s}+f_{RF}-f_{RF2})\right)+\sum_{k1=0}^{\frac{1}{2}N_{sc}}\sum_{k2=-\frac{1}{2}N_{sc}}^{-1}C_{k1MB}C_{k2*MB}\delta\left(f-(\frac{k1}{T_s}-\frac{k2}{T_s})\right)\right)\right)$$

$$-\frac{1}{4I_{DC}}\left(\cdot\sum_{k1=0}^{\frac{1}{2}N_{sc}}\sum_{k2=0}^{\frac{1}{2}N_{sc}}C_{k1}C_{k1}\delta\left(f-(\frac{k1}{T_s}+\frac{k2}{T_s}+2f_{RF})\right)+\sum_{k1=-\frac{1}{2}N_{sc}}^{-1}\sum_{k2=0}^{\frac{1}{2}N_{sc}}C_{k1}C_{k1MB}\delta\left(f-(\frac{k1}{T_s}+\frac{k2}{T_s}+f_{RF}+f_{RF2})\right)\right.$$

$$+\sum_{k1=0}^{\frac{1}{2}N_{sc}}\sum_{k2=-\frac{1}{2}N_{sc}}^{-1}C_{k1}C_{k1*MB}\delta\left(f-(\frac{k1}{T_s}-\frac{k2}{T_s}+f_{RF}-f_{RF2})\right)$$

$$\left.+\sum_{k1=-\frac{1}{2}N_{sc}}^{-1}\sum_{k2=-\frac{1}{2}N_{sc}}^{-1}C_{k1MB}C_{k1MB}\delta\left(f-(\frac{k1}{T_s}+\frac{k2}{T_s}-2f_{RF})\right)\right)$$

$$-\frac{1}{4I_{DC}}\left(\cdot\sum_{k1=0}^{\frac{1}{2}N_{sc}}\sum_{k2=0}^{\frac{1}{2}N_{sc}}C_{k2}C_{k2}\delta\left(f-(\frac{k1}{T_s}+\frac{k2}{T_s})\right)+\sum_{k1=0}^{\frac{1}{2}N_{sc}}\sum_{k2=0}^{\frac{1}{2}N_{sc}}C_{k2}C_{k2MB}\delta\left(f-(\frac{k1}{T_s}+\frac{k2}{T_s}+f_{RF}+f_{RF2})\right)\right.$$

$$\left.+\sum_{k1=0}^{\frac{1}{2}N_{sc}}\sum_{k=20}^{\frac{1}{2}N_{sc}}C_{k2}C_{k2MB}\delta\left(f-(\frac{k1}{T_s}+\frac{k2}{T_s}+f_{RF}+f_{RF2})\right)+\sum_{k1=0}^{\frac{1}{2}N_{sc}}\sum_{k2=0}^{\frac{1}{2}N_{sc}}C_{k2MB}C_{k2MB}\delta\left(f-(\frac{k1}{T_s}+\frac{k2}{T_s}+2f_{RF2})\right)\right)$$

Figure 91: Frequency representation of group two beating products.

The third group is

$$+\frac{1}{16{I_{DC}}^2}\left(\left(\sum_{k1=0}^{\frac{1}{2}N_{sc}}\sum_{k2=0}^{\frac{1}{2}N_{sc}}\sum_{k3=0}^{\frac{1}{2}N_{sc}}C_{k1}C_{k1*}C_{k1}\delta\left(f-(\frac{k1}{T_s}-\frac{k2}{T_s}+\frac{k3}{T_s}+f_{RF})\right)+\sum_{k1=0}^{\frac{1}{2}N_{sc}}\sum_{k2=-\frac{1}{2}N_{sc}}^{-1}\sum_{k3=0}^{\frac{1}{2}N_{sc}}C_{k1}C_{k1*}C_{k1*MB}\delta\left(f-(\frac{k1}{T_s}-\frac{k2}{T_s}-\frac{k3}{T_s}+f_{RF2})\right)\right.\right.$$

$$+\sum_{k1=-\frac{1}{2}N_{sc}}^{-1}\sum_{k2=0}^{\frac{1}{2}N_{sc}}\sum_{k3=0}^{\frac{1}{2}N_{sc}}C_{k1}C_{k1}C_{k1*MB}\delta\left(f-(\frac{k1}{T_s}+\frac{k2}{T_s}-\frac{k3}{T_s}-f_{RF2}+2f_{RF})\right)$$

$$\left.\left.+\sum_{k1=-\frac{1}{2}N_{sc}}^{-1}\sum_{k2=-\frac{1}{2}N_{sc}}^{-1}\sum_{k3=0}^{\frac{1}{2}N_{sc}}C_{k1}C_{k1MB}C_{k1*MB}\delta\left(f-(\frac{k1}{T_s}+\frac{k2}{T_s}-\frac{k3}{T_s}+f_{RF})\right)\right)\right)$$

$$+\frac{1}{16{I_{DC}}^2}\left(\left(\sum_{k1=0}^{\frac{1}{2}N_{sc}}\sum_{k2=0}^{\frac{1}{2}N_{sc}}\sum_{k3=-\frac{1}{2}N_{sc}}^{-1}C_{k1MB}C_{k1*}C_{k1}\delta\left(f-(\frac{k1}{T_s}-\frac{k2}{T_s}+\frac{k3}{T_s}+f_{RF2})\right)\right.\right.$$

$$+\sum_{k1=0}^{\frac{1}{2}N_{sc}}\sum_{k2=-\frac{1}{2}N_{sc}}^{-1}\sum_{k3=-\frac{1}{2}N_{sc}}^{-1}C_{k1MB}C_{k1*}C_{k1*MB}\delta\left(f-(\frac{k1}{T_s}-\frac{k2}{T_s}-\frac{k3}{T_s}+2f_{RF2}-f_{RF})\right)$$

$$+\sum_{k1=-\frac{1}{2}N_{sc}}^{-1}\sum_{k2=0}^{\frac{1}{2}N_{sc}}\sum_{k3=-\frac{1}{2}N_{sc}}^{-1}C_{k1MB}C_{k1}C_{k1*MB}\delta\left(f-(\frac{k1}{T_s}+\frac{k2}{T_s}-\frac{k3}{T_s}+f_{RF})\right)$$

$$\left.\left.+\sum_{k1=-\frac{1}{2}N_{sc}}^{-1}\sum_{k2=-\frac{1}{2}N_{sc}}^{-1}\sum_{k3=-\frac{1}{2}N_{sc}}^{-1}C_{k1MB}C_{k1MB}C_{k1*MB}\delta\left(f-(\frac{k1}{T_s}+\frac{k2}{T_s}-\frac{k3}{T_s}+f_{RF2})\right)\right)\right)$$
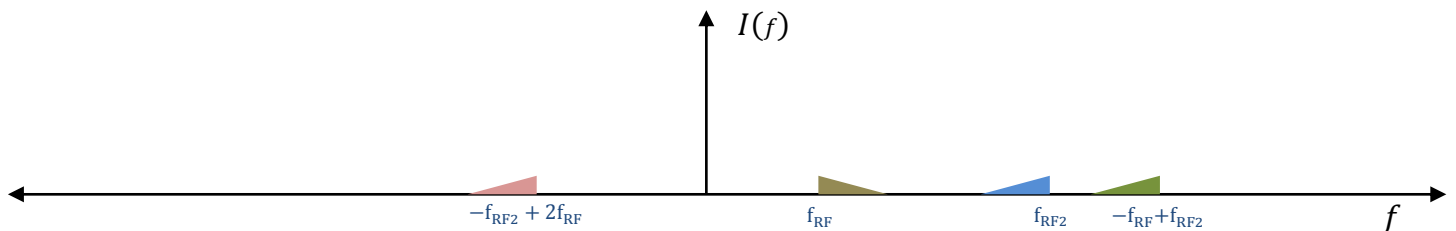
Figure 92: Frequency representation of group three beating products.

The fourth group is

$$-\frac{1}{16{I_{DC}}^2}\left(\left(\sum_{k1=0}^{\frac{1}{2}N_{sc}}\sum_{k2=0}^{\frac{1}{2}N_{sc}}\sum_{k3=0}^{\frac{1}{2}N_{sc}}C_{k1}C_{k1}C_{k1}\delta\left(f-(\frac{k1}{T_s}-\frac{k2}{T_s}-\frac{k3}{T_s}-f_{RF})\right)+\sum_{k1=0}^{\frac{1}{2}N_{sc}}\sum_{k2=-\frac{1}{2}N_{sc}}^{-1}\sum_{k3=0}^{\frac{1}{2}N_{sc}}C_{k1}C_{k1*}C_{k1*MB}\delta\left(f-(\frac{k1}{T_s}-\frac{k2}{T_s}-\frac{k3}{T_s}+f_{RF2})\right)\right.\right.$$

$$+\sum_{k1=-\frac{1}{2}N_{sc}}^{-1}\sum_{k2=0}^{\frac{1}{2}N_{sc}}\sum_{k3=0}^{\frac{1}{2}N_{sc}}C_{k1}C_{k1}C_{k1*MB}\delta\left(f-(\frac{k1}{T_s}-\frac{k2}{T_s}-\frac{k3}{T_s}-f_{RF2})\right)$$

$$\left.\left.+\sum_{k1=-\frac{1}{2}N_{sc}}^{-1}\sum_{k2=-\frac{1}{2}N_{sc}}^{-1}\sum_{k3=0}^{\frac{1}{2}N_{sc}}C_{k1}C_{k1MB}C_{k1*MB}\delta\left(f-(\frac{k1}{T_s}-\frac{k2}{T_s}-\frac{k3}{T_s}+f_{RF}-2f_{RF2})\right)\right)\right)$$

$$-\frac{1}{16I_{DC}{}^2}\left(\left(\sum_{k1=0}^{\frac{1}{2}N_{sc}}\sum_{k2=0}^{\frac{1}{2}N_{sc}}\sum_{k3=-\frac{1}{2}N_{sc}}^{-1}C_{k1MB}C_{k1}C_{k1}\delta\left(f-(\frac{k1}{T_s}-\frac{k2}{T_s}-\frac{k3}{T_s}+f_{RF2}-f_{RF})\right)\right.\right.$$

$$+\sum_{k1=0}^{\frac{1}{2}N_{sc}}\sum_{k2=-\frac{1}{2}N_{sc}}^{-1}\sum_{k3=-\frac{1}{2}N_{sc}}^{-1}C_{k1MB}C_{k1*}C_{k1*MB}\delta\left(f-(\frac{k1}{T_s}-\frac{k2}{T_s}-\frac{k3}{T_s}+f_{RF2}-f_{RF})\right)$$

$$+\sum_{k1=0}^{\frac{1}{2}N_{sc}}\sum_{k2=-\frac{1}{2}N_{sc}}^{-1}\sum_{k3=-\frac{1}{2}N_{sc}}^{-1}C_{k1MB}C_{k1}C_{k1*MB}\delta\left(f-(\frac{k1}{T_s}-\frac{k2}{T_s}-\frac{k3}{T_s}-f_{RF}+f_{RF2})\right)$$

$$\left.\left.+\sum_{k1=-\frac{1}{2}N_{sc}}^{-1}\sum_{k2=-\frac{1}{2}N_{sc}}^{-1}\sum_{k3=-\frac{1}{2}N_{sc}}^{-1}C_{k1MB}C_{k1*MB}C_{k1*MB}\delta\left(f-(\frac{k1}{T_s}-\frac{k2}{T_s}-\frac{k3}{T_s})\right)\right)\right)$$
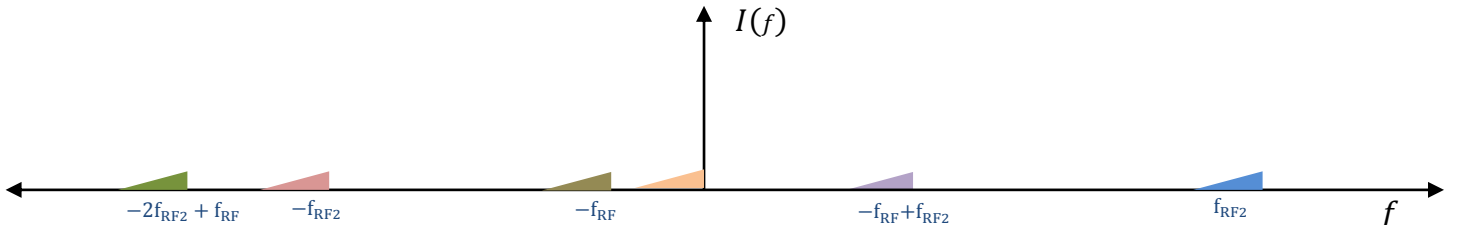
Figure 93: Frequency representation of fourth group beating products.

The fifth group is

$$-\frac{1}{16I_{DC}{}^2}\left(\left(\sum_{k1=0}^{\frac{1}{2}N_{sc}}\sum_{k2=0}^{\frac{1}{2}N_{sc}}\sum_{k3=0}^{\frac{1}{2}N_{sc}}C_{k2}C_{k1*}C_{k2*}\delta\left(f-(\frac{k1}{T_s}-\frac{k2}{T_s}-\frac{k3}{T_s}-f_{RF})\right)+\sum_{k1=0}^{\frac{1}{2}N_{sc}}\sum_{k2=-\frac{1}{2}N_{sc}}^{-1}\sum_{k3=0}^{\frac{1}{2}N_{sc}}C_{k2}C_{k2*}C_{k1*MB}\delta\left(f-(\frac{k1}{T_s}-\frac{k2}{T_s}-\frac{k3}{T_s}-f_{RF2})\right)\right.\right.$$

$$+\sum_{k1=0}^{\frac{1}{2}N_{sc}}\sum_{k2=0}^{\frac{1}{2}N_{sc}}\sum_{k3=0}^{\frac{1}{2}N_{sc}}C_{k2}C_{k1*}C_{k2*MB}\delta\left(f-(\frac{k1}{T_s}-\frac{k2}{T_s}-\frac{k3}{T_s}-f_{RF})\right)$$

$$\left.\left.+\sum_{k1=-\frac{1}{2}N_{sc}}^{-1}\sum_{k2=0}^{\frac{1}{2}N_{sc}}\sum_{k3=0}^{\frac{1}{2}N_{sc}}C_{k2}C_{k1*MB}C_{k2*MB}\delta\left(f-(\frac{k1}{T_s}-\frac{k2}{T_s}-\frac{k3}{T_s}-f_{RF2})\right)\right)\right)$$

$$-\frac{1}{16I_{DC}{}^2}\left(\left(\sum_{k1=0}^{\frac{1}{2}N_{sc}}\sum_{k2=0}^{\frac{1}{2}N_{sc}}\sum_{k3=0}^{\frac{1}{2}N_{sc}}C_{k2MB}C_{k1*}C_{k2*}\delta\left(f-(\frac{k1}{T_s}-\frac{k2}{T_s}-\frac{k3}{T_s}+f_{RF2}-2f_{RF})\right)\right.\right.$$

$$+\sum_{k1=0}^{\frac{1}{2}N_{sc}}\sum_{k2=0}^{\frac{1}{2}N_{sc}}\sum_{k3=-\frac{1}{2}N_{sc}}^{-1}C_{k2MB}C_{k2*}C_{k1*MB}\delta\left(f-(\frac{k1}{T_s}-\frac{k2}{T_s}-\frac{k3}{T_s}-f_{RF})\right)$$

$$+\sum_{k1=0}^{\frac{1}{2}N_{sc}}\sum_{k2=0}^{\frac{1}{2}N_{sc}}\sum_{k3=0}^{\frac{1}{2}N_{sc}}C_{k2MB}C_{k1*}C_{k2*MB}\delta\left(f-(\frac{k1}{T_s}-\frac{k2}{T_s}-\frac{k3}{T_s}+f_{RF2}-2f_{RF})\right)$$

$$\left.\left.+\sum_{k1=-\frac{1}{2}N_{sc}}^{-1}\sum_{k2=0}^{\frac{1}{2}N_{sc}}\sum_{k3=0}^{\frac{1}{2}N_{sc}}C_{k2MB}C_{k1*MB}C_{k2*MB}\delta\left(f-(\frac{k1}{T_s}-\frac{k2}{T_s}-\frac{k3}{T_s}-f_{RF})\right)\right)\right)$$
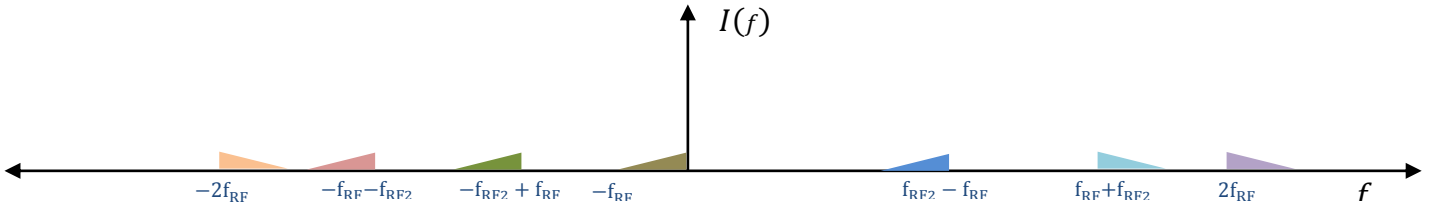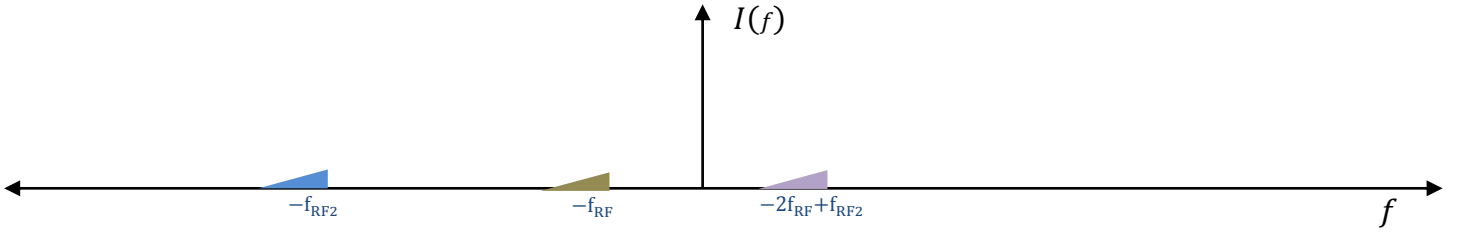
Figure 94: Frequency representation of group five beating products.

The sixth group is

$$
-\frac{1}{16 I_{DC}{}^2}\left(\left(\sum_{k1=0}^{\frac{1}{2}N_{sc}}\sum_{k2=0}^{\frac{1}{2}N_{sc}}\sum_{k3=0}^{\frac{1}{2}N_{sc}} C_{k2}C_{k1*}C_{k1*}\delta\left(f-(\frac{k1}{T_s}-\frac{k2}{T_s}-\frac{k3}{T_s}-f_{RF})\right)+\sum_{k1=0}^{\frac{1}{2}N_{sc}}\sum_{k2=-\frac{1}{2}N_{sc}}^{-1}\sum_{k3=0}^{\frac{1}{2}N_{sc}} C_{k2}C_{k1*}C_{k1*MB}\delta\left(f-(\frac{k1}{T_s}-\frac{k2}{T_s}-\frac{k3}{T_s}-f_{RF2})\right)\right.\right.
$$

$$
+\sum_{k1=0}^{\frac{1}{2}N_{sc}}\sum_{k2=-\frac{1}{2}N_{sc}}^{-1}\sum_{k3=0}^{\frac{1}{2}N_{sc}} C_{k2}C_{k1*MB}C_{k1*}\delta\left(f-(\frac{k1}{T_s}-\frac{k2}{T_s}-\frac{k3}{T_s}-f_{RF2})\right)
$$

$$
\left.\left.+\sum_{k1=-\frac{1}{2}N_{sc}}^{-1}\sum_{k2=-\frac{1}{2}N_{sc}}^{-1}\sum_{k3=0}^{\frac{1}{2}N_{sc}} C_{k2}C_{k1*MB}C_{k1*MB}\delta\left(f-(\frac{k1}{T_s}-\frac{k2}{T_s}-\frac{k3}{T_s}-2f_{RF2}+f_{RF})\right)\right)\right)
$$

$$
-\frac{1}{16 I_{DC}{}^2}\left(\left(\sum_{k1=0}^{\frac{1}{2}N_{sc}}\sum_{k2=0}^{\frac{1}{2}N_{sc}}\sum_{k3=0}^{\frac{1}{2}N_{sc}} C_{k2MB}C_{k1*}C_{k1*}\delta\left(f-(\frac{k1}{T_s}-\frac{k2}{T_s}-\frac{k3}{T_s}-2f_{RF})\right)\right.\right.
$$

$$
+\sum_{k1=0}^{\frac{1}{2}N_{sc}}\sum_{k2=0}^{\frac{1}{2}N_{sc}}\sum_{k3=-\frac{1}{2}N_{sc}}^{-1} C_{k2MB}C_{k1*}C_{k1*MB}\delta\left(f-(\frac{k1}{T_s}-\frac{k2}{T_s}-\frac{k3}{T_s}-f_{RF})\right)
$$

$$
+\sum_{k1=0}^{\frac{1}{2}N_{sc}}\sum_{k2=-\frac{1}{2}N_{sc}}^{-1}\sum_{k3=0}^{\frac{1}{2}N_{sc}} C_{k2MB}C_{k1*}C_{k1*MB}\delta\left(f-(\frac{k1}{T_s}-\frac{k2}{T_s}-\frac{k3}{T_s}-f_{RF})\right)
$$

$$
\left.\left.+\sum_{k1=-\frac{1}{2}N_{sc}}^{-1}\sum_{k2=-\frac{1}{2}N_{sc}}^{-1}\sum_{k3=0}^{\frac{1}{2}N_{sc}} C_{k2MB}C_{k1*MB}C_{k1*MB}\delta\left(f-(\frac{k1}{T_s}-\frac{k2}{T_s}-\frac{k3}{T_s}-f_{RF2})\right)\right)\right)
$$
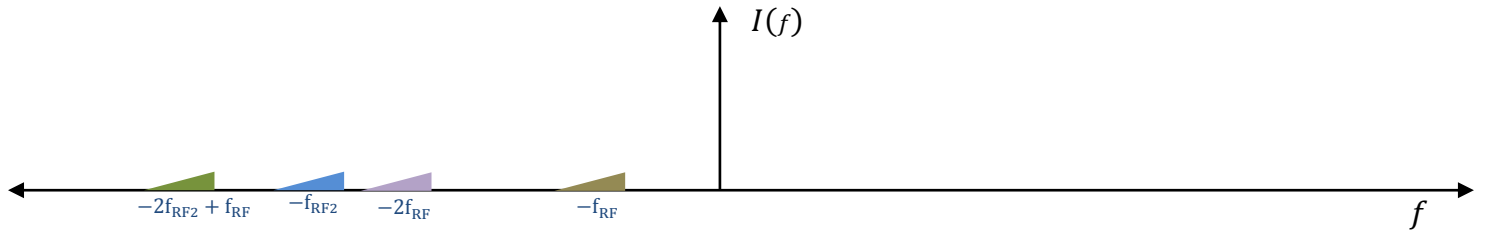
Figure 95: Frequency representation of group six beating products.

We are only interested in the components in the positive spectrum due to low pass filtering after direct detection. The combined unwanted products for positive part will be assuming $f_{RF} < f_{RF2}$:
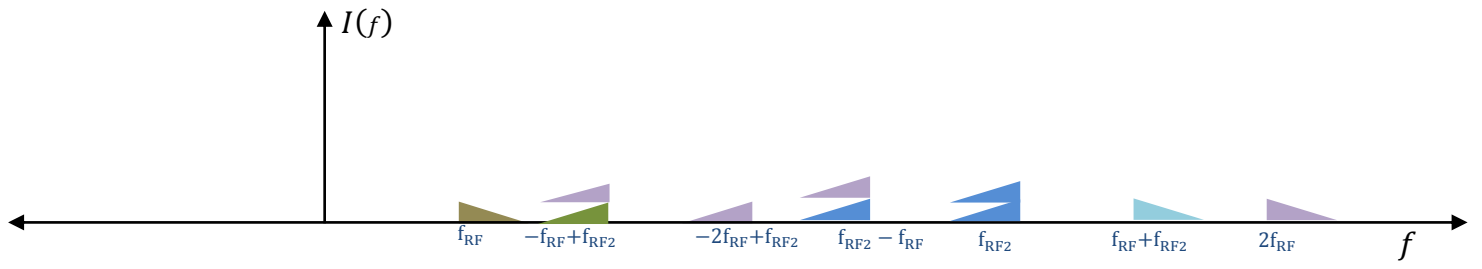
Figure 96: Frequency representation of combined beating products.

Appendix I: Publications in Conferences

Real-Time Optical OFDM Transceivers for PON Applications

J.M. Tang, R.P. Giddings, X.Q. Jin, J.L. Wei, X. Zheng, E. Giacoumidis, E. Hugues-Salas, Y. Hong, C. Shu, J. Groenewald and K. Muthusamy
School of Electronic Engineering, Bangor University, BANGOR, GWYNEDD LL57 1UT, UK
Tel:0044-1248-382697;Fax: 0044-1248-361429; Email: j.tang@bangor.ac.uk

Abstract: Recent real-time optical OFDM (OOFDM) research progress is reviewed extensively in terms of adaptive transceiver design, intensity modulators, synchronisation techniques and network architectures. Results indicate that OOFDM is feasible for mass deployment in PONs.
@2011 Optical Society of America
OCIS codes: (060.2330) Fibre Optical Communications, (060.4080) Modulation, (060.2430) Fibres, single mode.

1. Introduction

Driven by various emerging bandwidth-hungry services such as 3D-TV, HDTV, social websites, on-line gaming, video sharing, video on demand and e-Health, the end-users' demand for transmission bandwidth increases more than 70% year on year. As a direct result of such a rapid traffic growth, according to Infonetics, the global telecommunication equipment sales in the access network sector sequentially grow by 71% per year and are expected to reach $2.4 billion in 2010, with Europe, South and East Asia, North America and Asia Pacific representing 30.6%, 25.2%, 20.4% and 14% of the global market share, respectively. It is also estimated that by 2014 the access equipment market in APAC alone will exceed $2 billion with China dominating at approximately 90% of the market size.

The existing copper cable-based "last-mile" access networks are, however, only capable of sustaining at most 50Mb/s per subscriber and have become the main obstacles to providing the ultra-wide bandwidth services required in the near future. Passive optical networks (PONs) have been widely considered to be a promising strategy to enable each individual end-user to enjoy >1Gb/s everywhere. Cost effectiveness and flexibility are the key challenges for future mass deployment of PONs. To solve the challenges, great research and development effort has been expanded on exploring cost-effective, "future-proof", flexible technical solutions to satisfy future end-users' requirements.

As one of the strongest contenders for practical applications in PONs, optical OFDM (OOFDM) has been extensively investigated world-wide because of its unique advantages including: a) potential for cost-effective implementation by fully exploiting the advances in high-speed DSP technology; b) ability of exploiting high signal transmission capacity versus reach performance; c) resistance to various linear system impairments; d) tolerance to transmission system imperfections due to efficient utilization of channel spectrum; e) system flexibility and performance robustness due to its adaptive subcarrier manipulation capability, and f) dynamic provision of hybrid bandwidth allocation in both the frequency and time domains. The experimental demonstration of end-to-end real-time OOFDM transceivers is critical for rigorously evaluating the OOFDM technique and exploring the feasibility of the technique for practical implementation. The implementation of highly complex, computationally intense and high-speed DSP algorithms with sufficient precision, and the availability of high-speed DACs/ADCs with sufficiently large resolution are the major challenges in experimentally demonstrating real-time OOFDM transceivers. As far as we are aware, Bangor University is the first and only institute in the world that has experimentally demonstrated a series of ground-breaking end-to-end real-time OOFDM transceivers at record-high speeds of up to 11.25Gb/s with essential functionalities for adaptive operation such as on-line performance monitoring and live parameter optimization [1,2]. Very recently, our experimental investigations of real-time dual-band OOFDM transceivers have also indicated that >20Gb/s real-time OOFDM transceivers are also feasible using off-the-shelf, low-cost electrical/optical components in simple intensity modulation and direct detection (IMDD) transmission systems.

In this paper, our major OOFDM research achievements made within 2010 are extensively reviewed with special attention being given to evaluating its feasibility for use in cost-sensitive PON application scenarios.

2. Real-time OOFDM transceivers with adaptability for varying transmission system characteristics

For a specific IMDD OOFDM system, to maximize its transmission performance and simultaneously improve the system flexibility and performance robustness, adaptive loading can be adopted by optimising bit and/or power distribution over all subcarriers according to the transmission channel's state. Adaptive loading is highly effective

in not only efficiently utilizing the available spectral characteristics determined by system/network elements, but also combating component/system impairments. The widely adopted adaptive loading algorithms include bit-loading (BL), power-loading (PL) and bit-and-power-loading (BPL). Of these three algorithms, BPL has the ability of achieving the largest signal bit rate/optical power budget, but it suffers from the highest level of functional complexity and requires sophisticated OOFDM transceiver designs to accommodate variations in both the number of bits per symbol and the selective modulation formats. On the other hand, as a direct result of the lowest functional complexity and the simplest OOFDM transceiver architecture, PL has been first experimentally implemented in real-time OOFDM transceivers [1,2]. Very recently, adaptive bit and/or power loading-enabled, end-to-end real-time OOFDM transceivers at 11.75Gb/s utilizing 4GS/s ADCs/DACs have also been experimentally demonstrated successfully over directly modulated DFB laser (DML)-based IMDD 25km systems [3]. Performance comparisons between these three algorithms indicate that BPL-enabled highest signal bit rates are always approximately 7% higher than PL-enabled lowest signal bit rates, and such a difference is independent of both ADC/DAC sampling speed and transmission distance (up to 35km)[3].

Considering the fact that the above-mentioned statement may have huge potential for practical cost-effective OOFDM transceiver architecture design, and that IMDD SMF systems have simple system frequency response profiles, further verification of the validity of the statement in arbitrary transmission systems is of great importance. To achieve the objective, the employment of legacy multi-mode fibres (MMFs) with more complicated system frequency responses is essential. As different MMF systems reveal large variations in both the 3-dB bandwidths and the system frequency responses, any explorations of such a topic over a given MMF system are not adequate. Therefore, statistical investigations of the performance of these three algorithms are undertaken over 1000 statistically constructed worst-case MMF systems [4]. The use of the worst-case MMFs is because their frequency responses have more unpredictable peaks and nulls occurring within the signal spectral region. Statistical results agree very well with the experimental measurements. It is also shown [4] that, for MMF systems of less than 300m, in comparison with the sophisticated BPL algorithm, the simplest PL algorithm is an effective means of escalating the OOFDM MMF system performance to its maximum potential, and the effectiveness of the PL algorithm can be further improved when the number of subcarriers is increased. Whilst for relatively long MMF systems with 3-dB bandwidths much less than the transmitted OOFDM signal spectrum, the BPL algorithm has to be adopted.

3. Low-cost transceiver intensity modulators

Since typical directly modulated DFB lasers employed in the previously demonstrated real-time OOFDM transceivers take the majority of the transceiver cost [1-3], the utilization of intensity modulators of even lower cost is thus preferable. To further reduce the transceiver cost and improve the wavelength management functionality, use has been made of 1GHz RSOA intensity modulators. This leads to the experimental demonstrations of colorless OOFDM ONUs across the entire C-band [5]. In addition, un-cooled, low-cost, low modulation bandwidth VCSEL intensity modulators have also been experimentally proven to be feasible for supporting, with excellent performance stability and robustness, 64-QAM-encoded 11.25Gb/s real-time OOFDM signal transmission over 25km IMDD systems [6]. It should be pointed out that the major disadvantage associated with RSOA/VCSEL intensity modulators is their low modulation bandwidths, which can, however, be exploited through the spectral efficient and adaptive loading scheme via live parameter adaptation. Owing to the salient properties of VCSELs such as extremely low-cost, very low power consumption, high reliability and long lifetime, VCSEL intensity modulators may have great potential for significantly reducing the OOFDM transceiver cost for future mass production.

The maximum achievable transmission performance of the PON systems of interest in the present paper is predominantly limited by the following three physical factors including the low extinction ratio (ER) of an intensity modulated OOFDM signal, the intensity modulation-induced frequency chirp effect and the subcarrier intermixing effect associated with square-law photon detection in the receiver [7,8]. Simple and effective wavelength offset optical filtering has been proposed to considerably improve the OOFDM signal ER via converting unwanted chirp-induced frequency modulation into useful amplitude modulation [7]. In addition, a novel frequency chirp compensation technique has also been reported, which utilizes an analogue electrical circuit to produce an electrical signal (here referred to as a phase signal). The phase signal that mimics the phase of the optical signal emerging from the intensity modulator is used to drive a phase modulator, in which frequency chirp compensation is undertaken in the optical domain [9].

4. Synchronization

The realization of high-speed OOFDM system synchronization with acceptable accuracy using simple and cost-effective approaches is crucial and technically challenging. Generally speaking, there are two distinct methods:

an asynchronously clocked receiver with any clock offset between the transmitter and the receiver being automatically compensated in the receiver, and a synchronously clocked receiver with timing information being extracted from the received optical signal to generate a clocking signal in the receiver. For asynchronous clock recovery, we have proposed and experimentally demonstrated a simple technique without the need for any extra DSP, in end-to-end real-time DML-based 25km IMDD OOFDM systems for signal bit rates of up to 11.25Gb/s [10]. The proposed technique combines an OOFDM signal with a dedicated timing signal generated in the transmitter. The timing signal is simply a sine wave at a frequency outside the OOFDM signal band. After direct detection in the receiver, the timing signal and OOFDM signal are separated by electrical filtering. The received, jittered clock signal is pre-scaled to reduce its frequency before driving a phase locked loop (PLL), which generates the required receiver clocks. Detailed experimental results have shown [10] that, in comparison with the case where a common clock is employed, the high quality of the recovered clock does not directly degrade the system performance, and, more importantly, the system performance stability is significantly improved. In addition, the proposed technique also offers not only the opportunity of greatly simplifying the synchronization of OOFDM multiple access (OOFDMA) PONs, but also potential to perform accurate and stable synchronization allowing co-existence with conventional PONs.

For synchronous clocking, making use of relatively stable optical fiber channels, to extract embedded timing information, an OOFDM synchronization technique has been proposed based on parallel subtraction operations between a received analogue noise-like OFDM signal and its delayed copies, and subtraction profile averaging followed by Gaussian windowing [11]. The technique has also been experimentally demonstrated for signal bit rates of up to 11.25Gb/s in DML-based 25km IMDD systems [12]. Experimental results also show that the technique is capable of simultaneously compensating for arbitrary symbol timing offsets (STOs) and determining sampling clock offset (SCO) with an accuracy of <1ppm for an initial SCO as large as 4000ppm. In comparison with synchronous clocking techniques widely adopted in wireless systems, the demonstrated technique has low complexity, fast tracking speed, high accuracy and suitability for high-capacity optical transmission systems.

5. Network architecture simplification and network impairment reduction

Downstream wavelength reused bidirectional transmission IMDD colorless PONs are attractive for simplifying network architectures and improving their cost-effectiveness and wavelength control functionalities. Detailed investigations have been undertaken to explore the OOFDM transmission performance and physical limitations in the above-mentioned networks, where a fraction of the SOA intensity-modulated downstream OOFDM signal is directly fed, without passing through any extra data eraser and/or introducing feed-forward current injection, into a RSOA intensity modulator for upstream data re-modulation in the ONU [13]. Results have shown that the Rayleigh backscattering (RB) effect and residual downstream signal-induced crosstalk are dominant factors limiting the maximum achievable downstream and upstream transmission performance. Under optimum SOA and RSOA operating conditions as well as practical downstream and upstream optical launch powers, 10Gb/s downstream and 6Gb/s upstream over 40km SMF transmission of conventional double sideband OOFDM signals are feasible. In particular, the above-mentioned transmission performance can be improved to 23Gb/s downstream and 8Gb/s upstream over 40 km SMFs when single sideband subcarrier modulation is adopted in downstream. In addition, OOFDM is also effective in considerably reducing the filter concatenation effect in transparent IMDD Metro/Regional networks incorporating cascaded ROADMs based on different optical filters [14].

6. Conclusion

Based on the above discussions, it is concluded that OOFDM is feasible for mass deployment in cost-sensitive PON scenarios.

References

1. R.P. Giddings, et al, *Opt. Express*, **18**, pp.5541-5555, 2010.
2. R.P. Giddings, et al, *IEEE PTL,* **22**, 2010 (accepted for publication)
3. X.Q. Jin, et al., *OFC/NFOEC'2011* (submitted).
4. E.Giacoumidis, et al, *IEEE Photonics J.* **2**, pp.1051-1059, 2010.
5. R.P. Giddings, et al, *IEEE PTL,* **22**, pp. 745-747, 2010.
6. E. Hugues-Salas, et al., *OFC/NFOEC'2011* (submitted).
7. J L Wei, et al, *Opt. Express*, **18**, pp.20732-20745, 2010.
8. X. Zheng, et al., *IEEE Photonics J.* **2**, pp.532-542, 2010.
9. X. Zheng, et al., OFC/NFOEC'2011 (submitted).
10. R.P.Giddings, et al., OFC/NFOEC'2011 (submitted).
11. X.Q. Jin, et al, *Opt. Express*, **18**, pp.21100-21110, 2010.
12. X.Q. Jin, et al., *OFC/NFOEC'2011* (submitted).
13. J L Wei, et al, *Opt. Express*, **18**, pp.9791-9808, 2010.
14. E.Giacoumidis, et al, *Opt. Express*, 2010. (submitted).

Dependence of Upstream Power Budget on the Number of ONUs in IMDD Optical OFDMA PONs

X.Q. Jin[1,2], J. Groenewald[1], E. Hugues-Salas[1], R.P. Giddings[1] and J.M. Tang[1]
[1]School of Electronic Engineering, Bangor University, BANGOR, GWYNEDD LL57 1UT, UK
[2]Department of Engineering Science, University of Oxford, OXFORD, OX1 3PJ, UK
xianqing.jin@eng.ox.ac.uk, j.tang@bangor.ac.uk

Abstract: In optical OFDM multiple access PONs utilizing intensity-modulation/direct-detection, we show, for the first time, that doubling the number of ONUs gives an 1.9dB reduction in upstream power budget, mainly due to decreased signal-to-carrier power ratios.
OCIS codes: (060.2330) Fiber optic communications, (060.4080) Modulation, (060.2430) Fibres, single mode.

1. Introduction

Next generation passive optical networks (NG-PONs) should provide significantly improved bandwidths to end-users to support newly emerging bandwidth-intensive and multimedia-rich applications. In addition, NG-PONs should also have features such as flexible and efficient bandwidth management, smooth and cost-effective upgradability, as well as low capital/operation expenditure. Optical orthogonal frequency division multiple access (OOFDMA)-PONs are one of the most promising technologies satisfying all the aforementioned requirements [1, 2], because of their large signal transmission capacity, high spectral efficiency, excellent cost-effectiveness, and good compatibility with conventional TDM-PONs and WDM-PONs [3].

To further enhance the cost-effectiveness of OOFDMA-PONs, colorless ONUs and intensity modulation and direct detection (IMDD) are highly preferable. In IMDD PONs, optical beat interference (OBI) associated with direct detection of combined upstream signals of the same or similar wavelengths in the OLT receiver, produces unwanted frequency components, which considerably degrade the upstream PON performance when those frequency components fall into the useful signal spectrum region. The OBI effect can be reduced by the utilization of different wavelengths for upstream signals from different ONUs [1], coherent detection in the OLT [2] and visual-tree OOFDMA-PONs [4]. However, the last two approaches suffer from considerably increased system complexity. On the other hand, for simple IMDD PONs with colorless ONUs of interest of the present paper, to implement centrally-controlled wavelength management at the OLT, the use of reflective intensity modulators (IMs) in ONUs is greatly advantageous. These IMs include, for example, reflective semiconductor optical amplifiers (RSOAs) [1], reflective electro-absorption modulators (REAMs) [5] and reflective Fabry-Perot lasers [6].

Recently, based on our previously developed real-time OOFDM transceivers, we have experimentally demonstrated aggregated 11.25Gb/s end-to-end real-time IMDD OOFDMA PONs with adaptive dynamic bandwidth allocation (DBA) and RSOA-based colorless ONUs, and have experimentally identified the minimum wavelength spacing between ONUs for eliminating the OBI effect [1]. However, in [1] just 2 ONUs are considered, which are considerably smaller than the number of ONUs simultaneously accommodated by a single OLT in practice. From the practical IMDD OOFDMA PON design point of view, two important technical issues still remain unsolved, i.e., 1) Whether or not the number of simultaneously accommodated ONUs affect the upstream optical power budget; 2) Does the number of ONUs affect the minimum wavelength spacing between two adjacent ONUs? The provision of answers to these two questions is crucial for practical PON implementation, in this paper, detailed investigations are therefore undertaken, for the first time, to address the aforementioned two challenges.

2. System setup and fitting of experimental results

Fig. 1(a) shows the considered IMDD OOFDMA PONs with RSOA-based colorless ONUs. The diagram is very similar to that published in [1], except that the number of ONUs in Fig.1(a) is ≥2. In the *n-th* ONU transmitter, a digital electrical OFDM signal is generated following a DSP procedure listed below: M-QAM encoding, 32-point IFFT, cyclic prefix (CP) insertion and OFDM symbol serialization. With a 4GS/s @8-bit DAC, the digital OFDM signal is converted into an analog OFDM signal to directly modulate the RSOA IM operating at a specified wavelength. After combining all the upstream ONU signals of different wavelengths at a splitter/coupler, the combined OOFDM signal propagates along a 25km SSMF and is detected with a PIN in the OLT receiver. After passing through a LPF followed by a 4GS/s@8-bit ADC, transmitted data is finally recovered using an inverse procedure of the ONU transmitter. In addition, in the OLT receiver, additional DSP procedures are also implemented, which include synchronization [7], channel estimation and BER/EVM calculations.
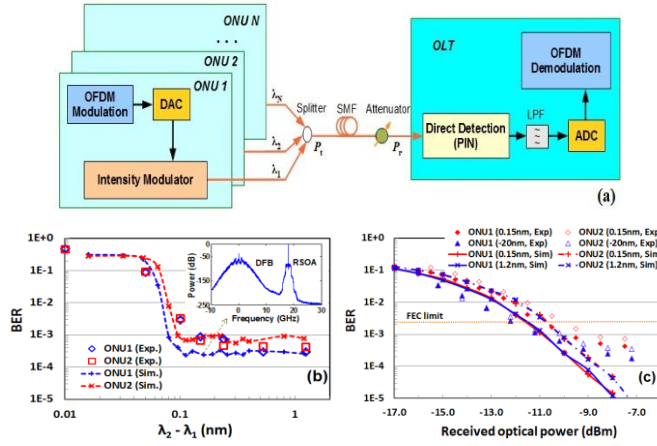
Fig. 1. (a) IMDD OOFDMA PONs with RSOA-based colorless ONUs. (b) Total channel BER against ONU wavelength spacing at a received optical power of -10dBm, inset is the received signal power spectra. (c) Total channel BER versus received optical power. A RSOA (DFB) intensity modulator is used in ONU 1 (ONU 2). Exp: experiments, Sim: simulations.

In numerical simulations, a RSOA-IM model [8] and a directly modulated DFB model [9] are adopted. To verify the validity of these numerical models and identify a set of parameters for each individual IM, fitting of experimental results with numerical simulations are first undertaken with all experimental measured parameters being fixed at those reported in [1]. The initial microscopic IM parameters are taken from [8,9], whose values are then finely adjusted within their acceptable ranges, until excellent agreements between numerical simulations and experimental results are achieved for both the wavelength spacing-dependent BER and the received optical power-dependent BER for each ONU, as shown in Fig. 1(b-c). For the RSOA-IM, the fitted confinement factor is 0.2 and the fitted differential gain is $1.5 \times 10^{-20} \text{m}^2$; whilst for the DFB laser, the fitted transparency carrier density is $3.98 \times 10^{24} \text{m}^{-3}$ and the fitted linewidth enhancement factor is 2.5. All other RSOA and DFB parameters not being mentioned explicitly above are identical to those reported in [8,9].

3. Results and discussions

Based on the verified RSOA-IM model, detailed numerical simulations are first made of the ONU wavelength spacing-dependent total channel EVM performance [shown in Fig.2(a)] and the received optical power-dependent total channel EVM performance [shown in Fig.2(b)]. To achieve an aggregated 11.25Gb/s upstream signal bit rate, 64-QAM is taken on all the 15 information-bearing OFDM subcarriers, which are evenly distributed among all the ONUs considered for different cases. In simulating Fig.2(a) [Fig.2(b)], the received optical power (ONU wavelength spacing) is fixed at 0.75dBm (18GHz). It can be seen in Fig.2(a) that, for different numbers of ONUs, almost identical EVM developing trends are observed, which become flat (at values below an EVM of -22dB corresponding to a FEC limit of 2.3×10^{-3} for 64-QAM) when the ONU wavelength spacing is larger than >8GHz. This indicates that the minimum ONU wavelength spacing is independent of the number of simultaneously accommodated ONUs, and that the OBI effect is significant only when wavelength spacing is <8GHz.

The total channel EVM performance as a function of received optical power is shown in Fig.2(b), from which it can be seen that the minimal received optical power required for achieving the FEC limit, P_{FEC}, increases with increasing the number of ONUs. To explicitly demonstrate such an important behavior, Fig. 2(c) is plotted to show the dependence of P_{FEC} on the number of ONUs for different wavelength spacing of 8, 18 and 50GHz. It is very interesting to note in Fig.2(c) that P_{FEC} in dBm increases with increasing the number of ONUs, and that P_{FEC} is increased by about 1.9dB when the number of ONUs is doubled. This implies that, for a specific PON system, doubling the number of ONUs gives rise to an 1.9dB reduction in upstream power budget.

The above-observed P_{FEC} characteristics can be explained as followings: For simplicity, an ideal IM in an optical BTB system is considered for each upstream transmission link. In the n-th ONU, the generated OOFDM signal can be written as $E_n = \sqrt{I_n} e^{j(\omega_n t + \phi_n)} = \sqrt{I_b + \sum_{m=1}^{M_n} (A/\sqrt{M_n}) \cos(2\pi f_{n,m} t)} \cdot e^{j(\omega_n t + \phi_n)}$, $\sum_{n=1}^{N_U} M_n = 15$. Here I_b is the bias current (assuming a threshold current of 0), ω_n is the optical carrier frequency, Φ_n is the optical phase introduced by the E-O conversion, $f_{n,m}$ and $A/\sqrt{M_n}$ are the frequency and amplitude of the m-th subcarrier, respectively, N_U is the total number of ONUs. In the OLT receiver, after square-law photon detection and low-pass filtering, the received electrical signal is

$$I_r = B^2 [N_U \cdot I_b + \sum_{n=1}^{N_U} \sum_{m=1}^{M_n} (A/\sqrt{M_n})/\cos(2\pi f_{n,m} t)] + W \qquad |\Delta\lambda| > |\Delta\lambda|_m \qquad (1)$$

where B is the constant coefficient, W is the noise introduced by the receiver, $\left|\Delta\lambda\right|_m$ is the minimum wavelength spacing. Making use of Eq.(1), the signal to carrier (average) power ratio (SCR) of the received electrical signal is thus given as

$$SCR = \sum_{n=1}^{N_U}\sum_{m=1}^{M_n} A^2/(2\sqrt{M_n})\Big/(N_U I_b)^2 = A^2/(2N_U I_b^{\ 2}) \qquad (2)$$

As seen in Eq. (2), for a fixed received optical power in the OLT receiver, the SCR of the corresponding electrical OFDM signal reduces with increasing N_U. This is also confirmed in Fig.3(a), where comparisons of the received electrical signal spectra are made between the cases of involving 2, 4 and 8 ONUs. As such, it is also expected that when various electrical ONU signals are directly combined in the electrical domain, and the combined signal is subsequently used to modulate the RSOA-IM and/or ideal IM, the total channel EVM performance is independent of the variation in N_U. The statement is verified in Fig.3(b), where almost perfectly overlapped EVM curves are present for different number of ONUs, regardless of the type of the IMs considered. Therefore, from the above discussions, it is concluded that the major physical mechanism underpinning the N_U dependent upstream power budget is a reduction in the SCR of the OFDM signal.

Here it is also worth mentioning that, theoretically speaking, when the number of ONUs is doubled, the effective OOFDM signal power from each ONU should be reduced by 1.5dB rather than the value of 1.9dB observed in Fig.2(c). Such a 0.4dB difference is mainly contributed by the multiple access interference (MAI) effect associated with the nonlinear E-O/O-E conversion, as a 0.7dB MAI-induced increase in received optical power for upstream transmission is measured experimentally in an IMDD OOFDMA PON [7].

In Fig.2(b), compared to the optical back-to-back (BTB) system, a negative power penalty of about -0.5dB is observed for different cases. This is due to the fact that the negative frequency chirp associated with the RSOA-based intensity modulation is compensated by the positive chromatic dispersion associated with the SSMFs. In the same figure, the observed EVM floor occurring at an EVM of -25dB for both 25km SSMFs and optical BTB is mainly due to the modulation nonlinearity of the RSOA-IM, as such a floor disappears when the RSOA-IM is replaced by an ideal IM, as shown in Fig.3(c).
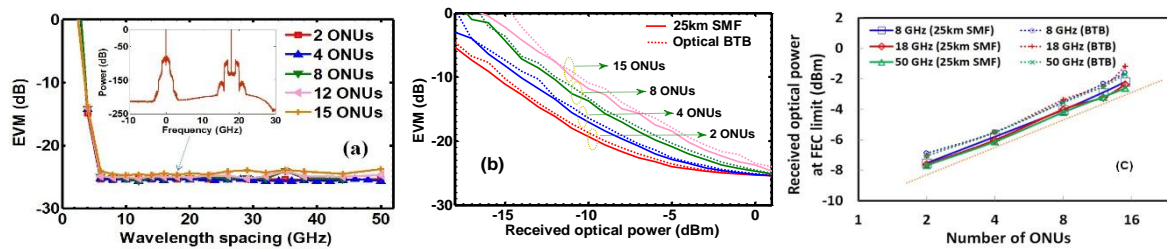
Fig. 2. EVM performance as a function of (a) ONU wavelength spacing, $|\Delta\lambda|$, and (b) received optical power at $|\Delta\lambda|$ of 18GHz. (c) Received optical power at the FEC limit versus the number of ONUs
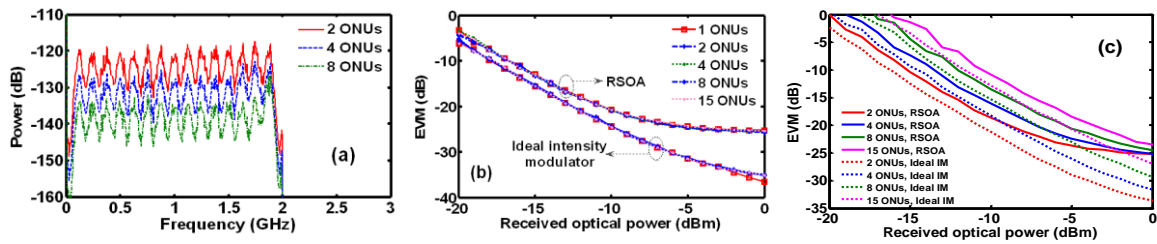
Fig. 3. (a) Electrical signal power spectra measured in the OLT for different number of ONUs, (b) EVM performance for electrically combined OFDM signals from each individual ONU incorporating different types of IMs; (c) Comparisons of the EVM performance of the RSOA-IM and ideal IM for optical BTB systems.

4. Conclusions

Numerical simulations have shown that, in IMDD OOFDMA PONs, doubling the number of ONUs gives an 1.9dB reduction in upstream power budget, and that the corresponding downstream power budget and the minimum ONU wavelength spacing required for eliminating the OBI effect are independent of the number of ONUs.

Acknowledgments

References

[1] X.Q. Jin, et al., J. Lightwave Technol., **30**, 2603 (2012).
[2] D. Qian, et al., Photon. Technol. Lett, **21**, 1265 (2009).
[3] N. Cvijetic, et al., J. Lightwave Technol., **30**, 493 (2012).
[4] M.C. Yuang, et al., J. Lightwave Technol., **30**, 1685 (2012).
[5] E. Hugues-Salas, et al., Opt. Exp., **20**, 21089 (2012).
[6]L.H. Spiekman, J. Lightwave Technol., **30**, to be published (2012)
[7] X.Q. Jin, et al., Opt. Exp., **19**, 20557-20570 (2011).
[8] J.L. Wei, et al., Opt. Exp. **18**, 8557 (2010).
[9] J.M. Tang, et al., J. Lightwave Technol., **24**, 2318 (2006).

Appendix J: Publications in Journals

Upstream Power Budgets of IMDD Optical OFDMA PONs Incorporating RSOA Intensity Modulator-based Colorless ONUs

X.Q. Jin, J. Groenewald, E. Hugues-Salas, R.P. Giddings and J.M. Tang

Abstract— In aggregated 11.25Gb/s over 25km SSMF intensity-modulation and direct-detection (IMDD) optical OFDM multiple access passive optical networks (OOFDMA PONs) incorporating colorless ONUs based on reflective semiconductor optical amplifier (RSOA) intensity modulators, excellent agreements are obtained between real-time upstream experimental measurements and numerical simulations for various system operating conditions. Making use of experimentally verified theoretical models and component/system parameters, extensive numerical explorations are undertaken, for the first time, of the impact of the number of ONUs on both upstream optical power budget and minimum ONU wavelength spacing required for eliminating the optical beat interference effect. It is shown that the minimum ONU wavelength spacing is independent of the number of ONUs, and that doubling the number of ONUs simultaneously accommodated in the aforementioned PON architectures gives a 1.9dB reduction in upstream power budget. Results also show that the utilization of an optimum frequency-offset super-Gaussian optical filter at an order of 5 immediately after the RSOA intensity modulator in each ONU can significantly improve the upstream power budget by >5.3dB, and simultaneously enhance the upstream power budget robustness to variations in the number of ONUs.

Index Terms—**Passive optical networks, optical modulation, optical orthogonal frequency division multiplexing.**

INTRODUCTION

AS the last-mile optical access to the Internet, next generation passive optical networks (NG-PONs) are required to provide significantly improved transmission bandwidths to end-users to support various newly emerging bandwidth-intensive and multimedia-rich applications [1]. In addition, since PONs are very cost-sensitive compared to core networks, NG-PONs should also have the features such as low capital/operation expenditure, dynamic, flexible and efficient bandwidth management, as well as smooth and cost-effective upgradability. Optical orthogonal frequency division multiple access (OOFDMA) PONs are one of the most promising and "future-proof" technical strategies capable of simultaneously satisfying all the aforementioned NG-PON requirements [2-6], because of their high signal transmission capacity, large spectral efficiency, excellent cost-effectiveness, inherent adaptability to system impairments, and good compatibility with both conventional time division multiplexing (TDM) PONs and wavelength division multiplexing (WDM) PONs [5]. Furthermore, use can also be made of digital signal processing (DSP) to maximize the signal transmission capacity of an arbitrary OOFDMA PON system and to dynamically assign different subcarriers to different end-users to offer adaptive dynamic bandwidth allocation (DBA) at sub-wavelength granularity.

To effectively enhance the cost-effectiveness of OOFDMA PONs, intensity modulation and direct detection (IMDD) system architectures are highly preferable. However, in IMDD upstream PON systems, optical beat interference (OBI) associated with direct detection of combined upstream signals of the same or similar

Fig. 1. Upstream IMDD OOFDMA PON systems with multiple RSOA-IM-based colourless ONUs.

wavelengths in the optical line terminal (OLT) receiver, produces unwanted frequency components, which considerably degrade the upstream PON performance when those new frequency components fall into the useful signal spectrum region [3]. The OBI effect can be reduced by the utilization of different wavelengths for upstream OOFDM signals from different optical network units (ONUs) [3], coherent upstream detection in the OLT [4] and virtual-tree OOFDMA PON architectures [6]. The last two approaches, however, bring about considerably increased transceiver/system complexity, as sophisticated and expensive coherent receivers in the OLT are required for the coherent detection approach [4], whilst for the virtual-tree approach [6], it is essential to replace existing installed PON architectures and develop new medium access control (MAC) schemes

Moreover, colorless ONUs greatly benefit the practical mass implementation of the IMDD OOFDMA PONs. To achieve colorless ONUs and simultaneously introduce centrally-controlled wavelength management in the OLT, the use of reflective intensity modulators (IMs) in ONUs is extremely advantageous. These IMs may include, for example, reflective semiconductor optical amplifiers (RSOAs) [3], reflective electro-absorption modulators (REAMs) [7] and reflective Fabry-Perot lasers [8].

Recently, based on our previously developed real-time OOFDM transceivers [9, 10], we have experimentally demonstrated aggregated 11.25Gb/s over 25km standard single-mode fibre (SSMF) end-to-end real-time IMDD OOFDMA PONs with adaptive DBA at sub-wavelength granularity [11]. More recently, RSOA-IM-based colorless ONUs have also been achieved experimentally in the above-mentioned real-time PON system, and the minimum wavelength spacing between adjacent ONUs has also been identified for eliminating the OBI effect [3].

To further improve optical power budgets of IMDD OOFDMA PONs, use can be made of frequency-offset optical super-Gaussian filters[12,13], which have potential of achieving a 7dB downstream power budget improvement in a directly modulated distributed feedback (DFB) laser (DML)-based 11.25Gb/s over 25km SSMF IMDD OOFDM PONs [12]. Apart from downstream transmission, it is envisaged that optical filtering is also applicable for improving optical power budgets of upstream PON systems utilizing RSOA-IM-based colorless ONUs.

In all the previously published real-time IMDD OOFDMA PONs [3, 11], the number of ONUs employed is just 2, which is considerably smaller than the number of ONUs simultaneously accommodated by a single OLT in practice. From the number of ONU point of view, three crucial technical challenges still remain unsolved, i.e., 1) Whether or not the number of simultaneously accommodated colorless ONUs affect the achievable upstream optical power budget; 2) Does the number of colorless ONUs affect the minimum wavelength spacing between adjacent ONUs, and 3) if the answer is "yes" to any of these two questions, whether or not the abovementioned simple optical filtering technique can be employed to improve the upstream performance. As the provision of answers to these questions is considerably beneficial to practical PON system design and implementation, in this paper, detailed explorations are therefore undertaken, for the first time, to address these challenges.

Colorless IMDD OOFDMA PON Systems and Experimental Result Fitting

System description

Fig. 1 illustrates the considered upstream IMDD OOFDMA PONs with multiple RSOA-IM-based colorless ONUs. The system setup and operating parameters are very similar to those reported in [3], except that the number of colorless ONUs in Fig.1 is larger than 2. As shown in Fig.1, the upstream signal transmission process can be briefly described as followings: In the *n-th* ONU transmitter, an electrical digital OFDM signal is generated using key DSP procedures outlined below: adaptive bit/power loading-enabled incoming binary bit encoding, 32-point inverse fast Fourier transform (IFFT), insertion of 8-sample cyclic prefix (CP) to each symbol and OFDM symbol
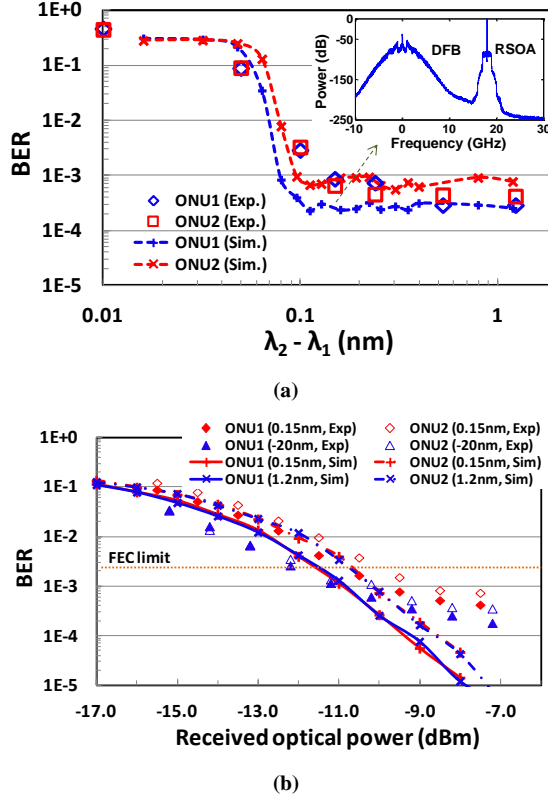
Fig. 2. (a) Upstream BER against ONU wavelength spacing at a received optical power of -10dBm, inset is a received optical signal power spectra. (b) Upstream BER versus received optical power. A RSOA-IM (DML-IM) is used in ONU1 (ONU2). Exp: experiments, Sim: simulations.

serialization. It should be noted, in particular, that for the entire upstream PON system, the maximum number of information-carrying subcarriers, M, is taken to be 15. The n-th ONU conveys data by its pre-assigned subcarriers only, while the ONU sets the amplitudes (powers) of all the remaining subcarriers to be zero. After passing through a 4GS/s, 8-bit digital-to-analogue converter (DAC), the digital OFDM signal is converted into an analog OFDM signal, which is combined with an optimum bias current. The combined electrical signal is employed to directly modulate a RSOA-IM operating at a specified wavelength. The optical power from the RSOA-IM is fixed at P_T /N with P_T being the total optical power launched into the fiber and N being the total number of accommodated ONUs. Throughout the present paper, P_T is taken to be 6dBm. After passively combining all the upstream optical signals of different wavelengths at an optical coupler, the combined OOFDM signal propagates along a 25km SSMF to the OLT.

At the OLT receiver, an optical attenuator is used to vary the received optical power. The received optical signal is detected using a PIN of a bandwidth of 12.4GHz and a sensitivity of -19dBm [corresponding to 10Gb/s non-return-to-zero data at a bit error rate (BER) of 10^{-9}]. Having being low-pass filtered, the electrical analogue signal is converted into the digital domain using a 4GS/s, 8-bit analogue-to-digital converter (ADC). The received data is finally recovered using an inverse DSP procedure compared to its counterpart in the ONU transmitter. In addition, some additional receiver DSP procedures are also implemented, which include the compensation of chromatic dispersion-induced time delay between different ONUs [11], automatic symbol synchronization [11], channel estimation/equalization and BER/error vector magnitude (EVM) calculations.

Theoretical models, experimental result fitting and numerical simulation parameters

To rigorously verify the validity of employed theoretical models and simultaneously identify a set of accurate numerical simulation parameters, in this subsection, fittings of experimental results measured in [3] with numerical simulations are first undertaken with all experimentally measured component/system parameters being adopted. Some of key component/system parameters can also be found in Section II.A. Here it is also worth mentioning that two ONUs are employed in [3]: which are an 1.125GHz RSOA-IM-based ONU and a 10GHz DML-IM-based ONU operating at 1551.18nm. In numerical simulations, use is made of a theoretical RSOA-IM

model developed in [14] and a DML-IM model reported in [15]. To simulate optical fiber transmission, a standard theoretical SMF model successfully verified in [14-15] is adopted, in which the effects of loss, chromatic dispersion and optical power dependence of refractive index are taken into account. In addition, similar to [14,15], a square-law photon detector model is also employed to simulate the OLT PIN, which detects the combined upstream optical signals emerging from the transmission systems. In photon detection, both shot noise and thermal noise are considered, which are numerically simulated following the procedures similar to those presented in [16].

In fitting the experimental results, as detailed in [3], the total number of information-bearing OFDM subcarriers is fixed at 15, and owing to the narrow modulation bandwidth of the RSOA-IM, the low frequency subcarriers (1st – 7th) encoded using 32-QAM are assigned to ONU1 incorporating the RSOA-IM, whilst the high frequency subcarriers (8th – 15th) encoded using 64-QAM are assigned to ONU2 incorporating the DML-IM. The variation in the upstream optical signal wavelength spacing between ONU1 and ONU2, λ_1–λ_2, is achieved by adjusting the wavelength of a 6.5dBm CW optical beam injected into the RSOA-IM, and the wavelength of the DML-IM is fixed at 1551.18 nm.

In simulating the intensity modulation performance of the RSOA-IM and DML-IM, in addition to the above-mentioned parameters, their experimentally measured operating parameters are also adopted, which include bias currents of 70mA and 36mA, and root mean square (RMS) driving currents of 4.9mA and 1.1mA for the RSOA-IM and DML-IM, respectively. Moreover, based on the approach reported in [17], the linewidth enhancement factor associated with the DML-IM is measured to be 2.5 and the κ parameter associated with nonlinear optical gain is measured to be 20GHz/mW. The initial values of all unknown microscopic RSOA-IM/DML-IM parameters are taken from [14, 15], those parameter values are then finely adjusted within their acceptable ranges until excellent agreements between numerical simulations and experimental measurements are achieved for the ONU wavelength spacing-dependent BER for each ONU, as well as the received optical power-dependent BER for different ONU wavelength spacing and different numbers of ONUs, as shown in Fig. 2(a-b).

For the RSOA-IM, the fitted confinement factor is 0.2 and the fitted differential gain is 1.5×10^{-20}m^2; whilst for the DML-IM, the fitted transparency carrier density is 3.98×10^{24}m^{-3}. The adopted SSMF parameters are listed as followings: an effective area of $80\mu m^2$, a dispersion parameter of 18.0ps/nm/km, a dispersion slope of 0.07ps/nm^2/km, a loss of 0.21dB/km and a Kerr coefficient of 2.35×10^{-20} m^2/W. All other RSOA-IM, DML-IM and PIN parameters that are not mentioned explicitly above are identical to those reported in [14, 15].

Simulation Results

The excellent agreements between the numerically simulated results and experimental measurements in Section II.B for various system operation conditions strongly confirm not only the validity of the adopted theoretical models but also the accuracy of the simulation parameter sets. In this Section, making use of these theoretical models and corresponding simulation parameters, detailed numerical investigations are undertaken to address these three technical challenges raised in Section I. To ensure fair performance comparisons between different cases where worst upstream performances are expected, only RSOA-IM-based ONUs are considered in this section.

It should be noted that different DBA schemes applied may slightly differ the upstream BER performance of a specific ONU [11]. For simplicity but without loosing any generality, the following simple DBA scheme is employed: the total 15 information-bearing subcarriers are evenly distributed among all the ONUs accommodated simultaneously. When 15/N is not an integer number, one extra subcarrier is assigned to (one subcarrier is removed from) the ONU in the vicinity of the optical carrier. For example, for a 4 ONU PON architecture, the subcarriers assigned to ONU1, ONU2, ONU3 and ONU4 are (1st-4th), (5th-8th), (9th-12th) and (13th-15th), respectively. In addition, 64-QAM is taken on all these subcarriers, this gives rise to an aggregated upstream signal bit rate of 11.25Gb/s. Finally, to speed up the computing execution process, EVM is used to evaluate the upstream transmission performance for various cases.

Impacts of number of ONUs on minimum ONU wavelength spacing and upstream optical power budget

For various numbers of colorless ONUs simultaneously accommodated in 25km SSMF IMDD OOFDMA PON systems, the ONU wavelength spacing-dependent total upstream EVM performance is shown in Fig. 3(a),
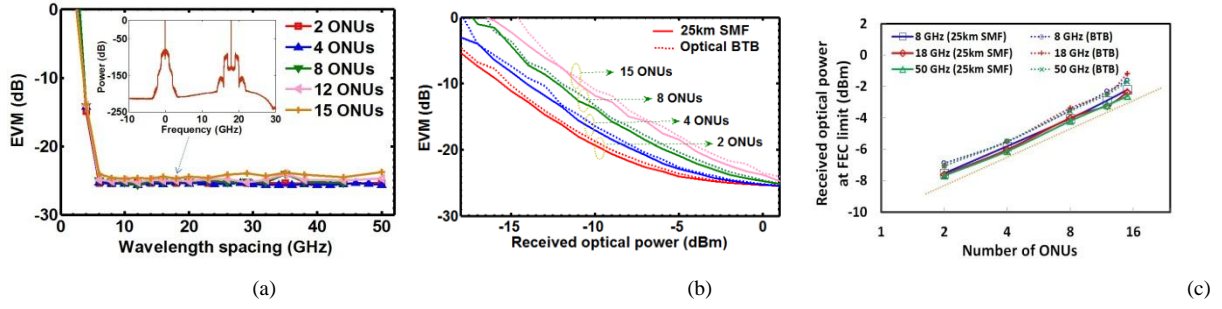
Fig. 3. EVM performance as a function of (a) ONU wavelength spacing, |Δλ|, and (b) received optical power at |Δλ| of 18GHz. (c) Received optical power at the FEC limit versus the number of ONUs for different ONU wavelength spacing

and the received optical power-dependent total upstream EVM performance is shown in Fig. 3(b). In simulating Fig. 3(a) [Fig. 3(b)], the received optical power (ONU wavelength spacing) is fixed at 0.75dBm (18GHz). It can be seen in Fig. 3(a) that, for different numbers of ONUs, almost identical EVM developing trends are observed, which become flat (at values below an EVM of -22dB corresponding to a forward error correction (FEC) limit of 2.3×10^{-3} for 64-QAM) when the ONU wavelength spacing is larger than >8GHz. This indicates that the minimum ONU wavelength spacing is independent of the number of simultaneously accommodated ONUs, and that the OBI effect is significant only when the ONU wavelength spacing is <8GHz.

For different number of ONUs, the total upstream EVM performance as a function of received optical power is shown in Fig. 3(b) for a fixed wavelength spacing of 18GHz. It can be seen in Fig.3(b) that, for the cases of both the 25km SSMF upstream transmission and optical back-to-back (BTB), the minimal received optical power required for achieving the FEC limit, P_{FEC}, increases with increasing the number of ONUs. To clearly demonstrate such an important behavior, Fig. 3(c) is plotted to explicitly show the dependence of P_{FEC} upon the number of ONUs for various ONU wavelength spacing of 8, 18 and 50GHz. It is very interesting to note in Fig. 3(c) that P_{FEC} in dBm increases almost linearly with increasing the number of ONUs, and that P_{FEC} is increased by approximately 1.9dB when the number of ONUs is doubled. This implies that, for a specific PON system, doubling the number of ONUs gives rise to a 1.9dB reduction in upstream power budget.

   The above-observed P_{FEC} developing characteristics can be explained as followings: for simplicity, an ideal IM is considered for each upstream transmission system in an optical BTB configuration. In the *n-th* ONU, the generated OOFDM signal can be written as

$$E_n = \sqrt{I_n}e^{j(\omega_n t+\phi_n)} = \sqrt{I_b + \sum_{m=1}^{M_n}(A/\sqrt{M_n})\cos(2\pi f_{n,m}t)} \cdot e^{j(\omega_n t+\phi_n)} \quad (1)$$

where $\sum_{n=1}^{N}M_n = 15$. I_b is the bias current (assuming a zero threshold current), ω_n is the optical carrier frequency, Φ_n is the optical phase introduced by electrical-to-optical (E-O) conversion, $f_{n,m}$ and $A/\sqrt{M_n}$ are the frequency and amplitude of the *m-th* subcarrier, respectively. In the OLT receiver, after square-law photon detection and low-pass filtering, the received electrical signal is given by

$$I_r = B^2[N \cdot I_b + \sum_{n=1}^{N}\sum_{m=1}^{M_n}(A/\sqrt{M_n})\cos(2\pi f_{n,m}t)] + W \quad (2)$$
$$|\Delta\lambda| > |\Delta\lambda|_m$$

where B is a constant coefficient representing an attenuated/amplified optical power of the combined upstream ONU signals, W is the noise introduced by the receiver, $|\Delta\lambda|_m$ is the minimum ONU wavelength spacing.

Making use of Eq.(2), the average signal to carrier power ratio, SCR, of the received electrical signal is thus expressed as

$$SCR = \sum_{n=1}^{N}\sum_{m=1}^{M_n}A^2/(2\sqrt{M_n})/(NI_b)^2 = A^2/(2NI_b^2) \quad (3)$$

As seen in Eq. (3), for a fixed RMS driving current and bias current in each ONU transmitter, the SCR of the received electrical OFDM signal reduces with increasing *N*. The statement is also confirmed in Fig. 4(a), where comparisons of the received electrical signal spectra are made between the cases of involving 2, 4 and 8 ONUs for a fixed received optical power in the OLT receiver.
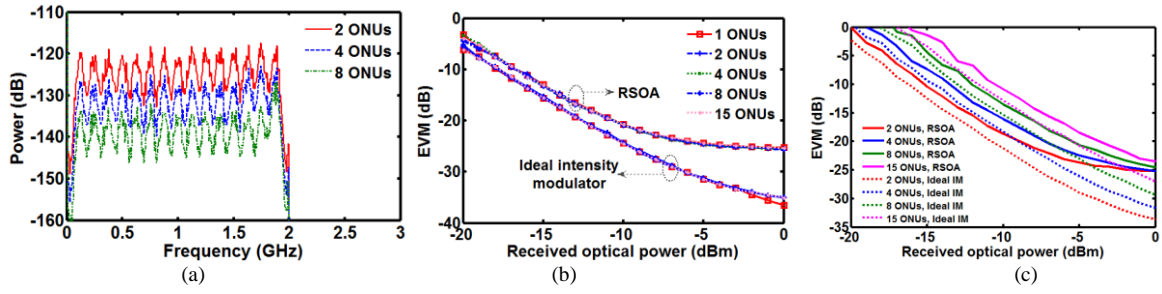
Fig. 4. (a) Electrical signal power spectra measured in the OLT for different number of ONUs, (b) EVM performance for electrically combined OFDM signals from each individual ONU incorporating different types of IMs in optical BTB systems, (c) Comparisons of the EVM performance of the RSOA-IM and ideal IM for optical BTB systems.

Eq.(3) suggests that a SCR reduction occurs only when individual E-O conversion takes place in each ONU. When all electrical ONU signals are combined directly in the electrical domain and the combined electrical signal is subsequently used to modulate the RSOA-IM or ideal IM, the total upstream EVM performance is independent of the variation in the number of ONUs, N. This statement is verified in Fig. 4(b), where almost perfectly overlapped EVM curves are present for different number of ONUs, regardless of the type of the IMs considered. From the above discussions, it is concluded that the major physical mechanism underpinning the N dependent upstream power budget is the multiple independent E-O conversion-induced reduction in SCR of OOFDM signals, rather than any impairments caused by electrical/optical components.

Here it is also worth mentioning that, theoretically speaking, when the number of ONUs is doubled, the effective OOFDM signal power from each ONU should be decreased by 1.5dB (half of 3dB in the electrical domain) rather than the value of 1.9dB, as observed in Fig. 3(c). Such a 0.4dB difference is mainly contributed by the multiple access interference (MAI) effect associated with the nonlinear E-O/O-E conversion, as a 0.7dB MAI-induced increase in received optical power for upstream transmission is measured experimentally in an 11.25Gb/s over 25km SSMF IMDD OOFDMA PON [11].

In Fig. 3(b), compared to the optical BTB systems, a negative power penalty of about -0.5dB is observed for different cases. This is due to the fact that the negative frequency chirp associated with the RSOA-IM is compensated by the positive chromatic dispersion associated with SSMFs [18]. Finally, in the same figure, the observed EVM floor occurring at an EVM of -25dB for both 25km SSMFs and optical BTB is mainly due to the modulation nonlinearity of the RSOA-IM, as such a floor disappears when the RSOA-IM is replaced by an ideal IM, as shown in Fig. 4(c).

Improved upstream power budget utilizing frequency-offset optical filtering
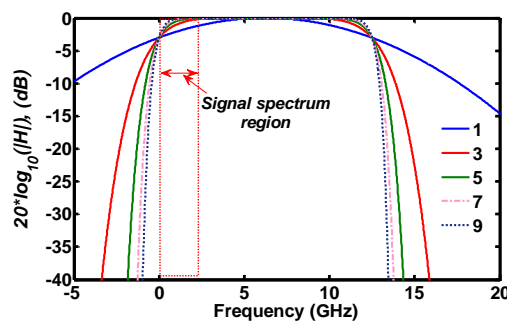
Fig. 5. Power transfer functions of optical Gaussian filters at different orders.
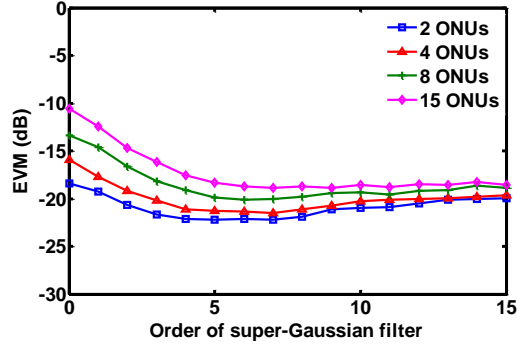
Fig. 6. EVM performances as a function of Gaussian filter order. The filter bandwidth is 12.5GHz and the frequency offsets is 6.25GHz. Received optical power: -10dBm. ONU wavelength spacing: 18GHz.

From [12] it is envisaged that the upstream optical power budget of an IMDD OOFDMA PON can be considerably improved by introducing an optimized frequency-offset optical super-Gaussian filter immediately after the RSOA-IM in each ONU transmitter. As the filter's group delay effect is compensable [12], only filter power transfer functions are therefore considered here, which can be written as

$$|H(f)|^2 = \exp[\ln(\frac{1}{2}) \cdot (\frac{f - f_0}{f_{BW}/2})^{2k}] \qquad (4)$$

where f_0 is the frequency-offset between the centre frequency of the optical filter and the optical carrier, f_{BW} is the 3dB bandwidth of the optical filter, and k is the order of the optical filter . When k = 1 Eq. (4) represents a normal Gaussian optical filter. As an example, Fig. 5 shows representative power transfer functions of various frequency-offset optical Gaussian filters at orders of 1, 3, 5, 7, and 9, as well as a corresponding OOFDM signal spectrum. Because the edge of the power transfer function becomes steep for a large k, the use of a super-Gaussian optical filter having an appropriate order and an optimized frequency-offset with respect to the optical carrier can effectively suppress the optical carrier power and one OOFDM signal sideband, whilst simultaneously preserve the other OOFDM signal sideband to a maximum, thus leading to an increased SCR, the reduced subcarrier-intermixing effect associated with single sideband detection, and subsequently an improved upstream power budget.
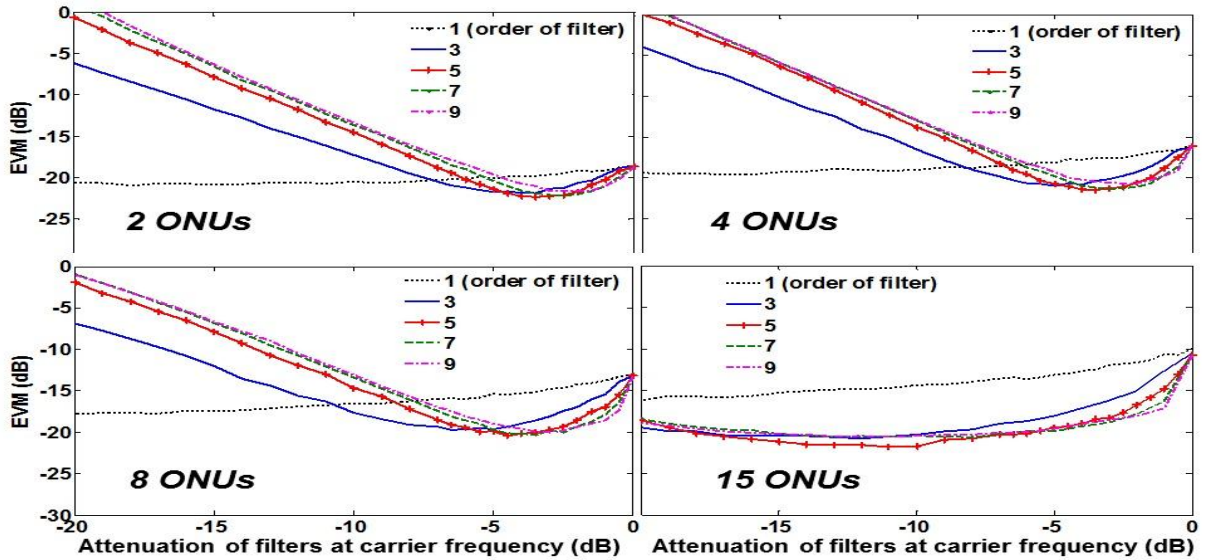
Fig. 7. EVM as a function of optical carrier attenuation for different numbers of ONUs utilising optical filters of different orders. Received optical power: -10dBm. ONU wavelength spacing: 18GHz.
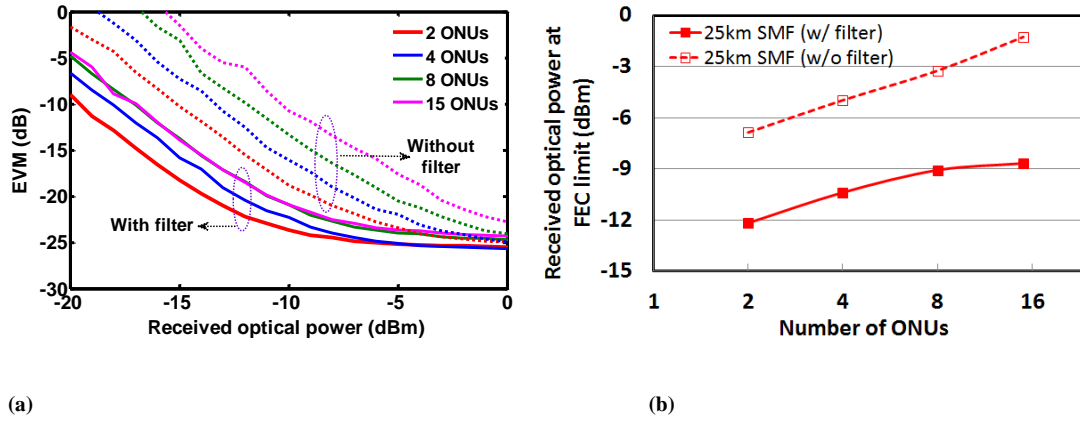
Fig. 8. (a) EVM performance versus received optical power for different number of ONUs utilising super-Gaussian optical filters with optimised orders and frequency-offset. (b) Minimum received optical power at the FEC limit versus the number of ONUs.

For different numbers of ONUs, the impact of the optical filter order on the upstream power budget is explored in Fig.6, in obtaining which the bandwidth and frequency-offset of the optical super-Gaussian filters are fixed at 12.5GHz (0.1nm at a wavelength of 1550nm) and 6.25GHz, respectively. Fig.6 shows that, to achieve the best EVM performance, there exists an optimum filter order of approximately 5, which is independent of the number of ONUs.

To further explore the filter frequency-offset effect on the upstream EVM performance, Fig. 7 is plotted, where a 12.5GHz-bandwidth filter attenuation at the optical carrier frequency, α_0, is used to represent the frequency-offset. For such a filer, a frequency-offset of 6.25GHz corresponds to $\alpha_0 = 3$dB. For gaining an in-depth understanding of the overall EVM performance, various EVM versus α_0 curves for different k values and different number of ONUs are also presented in Fig.7. It can be seen in Fig.7 that, for a given number of ONUs, an optimum α_0 is observed, above which an increase in EVM is due to a SCR reduction because of the existence of a relatively large optical carrier power, on the other hand, for α_0 below the optimum value an increase in EVM is mainly caused by the large carrier power attenuation-induced OOFDM signal clipping effect. From the above analysis, it is easy to understand that a large number of ONUs lowers the SCR, thus requires a high optical carrier power attenuation for achieving the best EVM performance. This results in a reduction in optimum α_0 with increasing the number of ONU, as shown in Fig.7.

Making use of optimum k and α_0 values of the 12.5GHz bandwidth super-Gaussian optical filters for different number of ONUs, the simulated EVM performance as a function of received optical power is presented in Fig.8 (a) in 25km SSMF IMDD OOFDMA PONs. As seen in Fig.8(a), in comparison with the optical filter-free cases, the utilization of optimum super-Gaussian optical filters not only improves considerably the EVM and decreases the minimum received optical power required for achieving the FEC limit for each PON architecture, but also minimizes the EVM performance differences between different PON architectures.

To explicitly demonstrate the optimum optical filter-induced improvement in upstream optical power budget, the number of ONU-dependent minimum received optical power corresponding to the FEC limit is given in Fig. 8(b) for the cases of including and excluding the optical filters. It is interesting to note in Fig.8(b) that, compared with the optical filtering-free cases, the utilization of optimum super-Gaussian optical filters can enhance the upstream optical power budget by at least 5.3dB for any number of ONUs. In addition, the upstream optical power budget robustness to variations in the number of ONU is also improved by at least 0.4dB.

Conclusions

In aggregated 11.25Gb/s over 25km SSMF IMDD OOFDMA PONs incorporating RSOA-IM-based colorless ONUs, excellent agreements have been obtained between real-time upstream experimental measurements and numerical simulations in terms of BER performances as functions of both ONU wavelength spacing and received optical power. Making use of experimentally verified theoretical models and component/system parameters, extensive numerical explorations have been undertaken, for the first time, of the impact of the number of ONUs on both upstream optical power budget and minimum ONU wavelength spacing. It has been shown that the minimum ONU wavelength spacing is independent of the number of ONUs, and that doubling the number of ONUs simultaneously accommodated gives a 1.9dB reduction in upstream power budget. In addition, numerical simulations have also shown that the utilization of an optimum frequency-offset super-Gaussian optical filter at an order of 5 immediately after the RSOA-IM in each ONU can significantly improve the upstream power budget

by >5.3dB, and simultaneously enhance the upstream power budget robustness to variations in the number of ONUs.

References

[1]   E. Wong, "Next-Generation Broadband Access Networks and Technologies", J. Lightwave Technol., vol. 30, no.4, pp. 597–608, Feb. 2012.

[2]   K, Kanonakis, I. Tomkos, H. Krimmel, F. Schaich, C. Lange, E. Weis, J. Leuthold, M. Winter, S. Romero, P. Kourtessis, M. Milosavljevic, I.N. Cano, J. Prat, "An OFDMA-based optical access network architecture exhibiting ultra-high capacity and wireline-wireless convergence," IEEE Commun. Magazine, vol. 50, no. 8, pp. 71–78, Aug. 2012.

[3]   X.Q. Jin and J.M. Tang, "Experimental Investigations of Wavelength Spacing and Colorlessness of RSOA-Based ONUs in Real-Time Optical OFDMA PONs," J. Lightwave Technol. vol. 30, no. 16, pp. 2603–2609, Aug. 2012.

[4]   D. Qian, N. Cvijetic, J. Hu, and T. Wang, "A novel OFDMA-PON architecture with source-free ONUs for next-generation optical access networks", IEEE Photon. Technol. Lett., vol. 21, no. 17, pp. 1265-1267, Sep. 2009

[5]   N. Cvijetic, M. Cvijetic, M.-F. Huang, E. Ip, Y.-K. Huang, and T. Wang, "Terabit Optical Access Networks Based on WDM-OFDMA-PON," J. Lightwave Technol. vol. 30, no. 4, pp. 493–503, Feb. 2012.

[6]   M.C. Yuang, P.-L. Tien, D.-Z. Hsu, S.-Y. Chen, C.-C. Wei, J.-L. Shih, and J. Chen, "A High-Performance OFDMA PON System Architecture and Medium Access Control," J. Lightwave Technol. vol. 30, no. 11, pp. 1685–1693, Jun. 2012.

[7]   E. Hugues-Salas, R.P. Giddings, X.Q. Jin, Y. Hong, T. Quinlan, S. Walker, and J.M. Tang, "REAM intensity modulator-enabled 10Gb/s colorless upstream transmission of real-time optical OFDM signals in a single-fiber-based bidirectional PON architecture," Optics Express, vol.20, no. 19, pp.21089-21100, Sep. 2012

[8]   L.H. Spiekman, "Active Devices in Passive Optical Networks," J. Lightwave Technol. vol. 31, no. 4, pp. 488–497, Feb. 2013.

[9]   X. Q. Jin, J. L. Wei, R. P. Giddings, T. Quinlan, S. Walker, and J. M. Tang, "Experimental demonstrations and extensive comparisons of end-to-end real-time optical OFDM transceivers with adaptive bit and/or power loading", IEEE Photonics Journal. vol. 3, no. 3, pp. 500-511 Jun. 2011.

[10] R.P. Giddings, X.Q. Jin, E. Hugues-Salas, E. Giacoumidis, J.L. Wei and J. M. Tang, "Experimental demonstration of a record high 11.25Gb/s real-time optical OFDM transceiver supporting 25km SMF end-to-end transmission in simple IMDD systems" Opt. Express, vol. 18, no. 6, pp.5541-5555, Mar. 2010

[11] X.Q. Jin, R.P. Giddings, E. Hugues-Salas, J.L. Wei, J. Groenewald, and J. M. Tang, "First real-time experimental demonstrations of 11.25Gb/s optical OFDMA PONs with adaptive dynamic bandwidth allocation," Optics Express, vol. 19, no. 21, pp. 20557-20570, Oct. 2011

[12] J. L. Wei, C. Sánchez, E. Hugues-Salas, P. S. Spencer, and J. M. Tang, "Wavelength-Offset Filtering in Optical OFDM IMDD Systems Using Directly Modulated DFB Lasers," J. Lightwave Technol. vol. 29, no. 18, pp. 2861–2870, Sep. 2011.

[13] D. Qian, S.-H. Fan, N. Cvijetic, J. Hu, T. Wang, "64/32/16QAM-OFDM using direct-detection for 40G-OFDMA-PON downstream", Optical Fiber Communication/National Fiber Optic Engineers Conference (OFC/NFOEC), (USA, 2011), Paper OMG4

[14] J.L. Wei, A. Hamie, R.P. Giddings, E. Hugues-Salas, X. Zheng, S. Mansoor and J.M. Tang, "Adaptively modulated optical OFDM modems utilizing RSOAs as intensity modulators in IMDD SMF transmission systems," Optics Express, vol.18, no.8, pp. 8556-8573, April 2010.

[15] J. M. Tang, and K. A. Shore, "30 Gb/s signal transmission over 40-km directly modulated DFB-laser-based single-mode-fibre links without optical amplification and dispersion compensation," J. Lightwave Technol. vol. 24, no. 6, pp. 2318–2327, Jun. 2006.

[16]   G. P. Agrawal, Fibre-Optic Communication Systems, 2nd ed., (Hoboken, NJ: Wiley, 1997)

[17] A. Villafranca, J. Lasobras, I. Garces, "Precise characterization of the frequency chirp in directly modulated DFB lasers," Spanish Conf. on Electronic Devices, pp. 173-176, Feb. 2007

[18] X. Zheng, X. Q. Jin, R. P. Giddings, J. L. Wei, E. Hugues-Salas, Y. H. Hong, and J. M. Tang, "Negative power penalties of optical OFDM signal transmissions in directly modulated DFB laser-based IMDD systems incorporating negative dispersion fibres," IEEE Photonics J., vol. 2, no. 4, pp. 532–542, Aug. 2010.

First real-time experimental demonstrations of 11.25Gb/s optical OFDMA PONs with adaptive dynamic bandwidth allocation

X.Q. Jin[*], E. Hugues-Salas, R.P. Giddings, J.L. Wei, J. Groenewald and J.M. Tang

School of Electronic Engineering, Bangor University, Dean Street, Bangor, LL57 1UT, UK
[*]x.jin@bangor.ac.uk

Abstract: End-to-end real-time experimental demonstrations are reported, for the first time, of aggregated 11.25Gb/s over 26.4km standard SMF, optical orthogonal frequency division multiple access (OOFDMA) PONs with adaptive dynamic bandwidth allocation (DBA). The demonstrated intensity-modulation and direct-detection (IMDD) OOFDMA PON system consists of two optical network units (ONUs), each of which employs a DFB-based directly modulated laser (DML) or a VCSEL-based DML for modulating upstream signals. Extensive experimental explorations of dynamic OOFDMA PON system properties are undertaken utilizing identified optimum DML operating conditions. It is shown that, for simultaneously achieving acceptable BERs for all upstream signals, the OOFDMA PON system has a >3dB dynamic ONU launch power variation range, and the BER performance of the system is insusceptible to any upstream symbol offsets slightly smaller than the adopted cyclic prefix. In addition, experimental results also indicate that, in addition to maximizing the aggregated system transmission capacity, adaptive DBA can also effectively reduce imperfections in transmission channel properties without affecting signal bit rates offered to individual ONUs.

OCIS codes: (060.0060) Fiber optics and optical communications; (060.4080) Modulation; (060.3510) Laser, fibre.

References and links

1. E. Wong, "Current and next-generation broadband access technologies", Optical Fiber Communication/National Fiber Optic Engineers Conference (OFC/NFOEC), (USA, 2011), Paper NMD1
2. L. G. Kazovsky, W.-T. Shaw, D. Gutierrez, N. Cheng, and S.-W. Wong, "Next-Generation Optical Access Networks", J. Lightwave Technology, **25**(11), 3428- 3442 (2007)
3. N. Suzuki, K. Nakura, T. Suehiro, M. Nogami, S. Kosaki and J. Nakagawa, "Over-Sampling based Burst-mode CDR Technology for High-speed TDM-PON Systems", Optical Fiber Communication/National Fiber Optic Engineers Conference (OFC/NFOEC), (USA, 2011), Paper OThT3
4. J. Kani, "Enabling technologies for future scalable and flexible WDM-POJN and WDM/TDM-PON systems," IEEE J. Sel. Top. Quantum Electron. **16** (5), 1290-1297 (2010).
5. D. Qian, J. Hu, J. Yu, P. N. Ji, L. Xu, T. Wang, M. Cvijetic, T. Kusano, "Experimental demonstration of a novel OFDM-A based 10 Gb/s PON architecture," European Conference on Optical Communication (ECOC), (Berlin, 2007), Paper Mo 5.4.1.
6. D. Qian, N. Cvijetic, J. Hu, and T. Wang, "A novel OFDMA-PON architecture with source-free ONUs for next-generation optical access networks", IEEE Photon. Technol. Lett., **21** (17), 1265-1267 (2009).
7. Y.-M. Lin, and P.-L. Tien, "Next-generation OFDMA-based passive optical network architecture supporting radio-over-fiber", J. on Selected Areas in Communications, **28** (6), 791-799 (2010).
8. X. Q. Jin, J. L. Wei, R. P. Giddings, T. Quinlan, S. Walker, and J. M. Tang, "Experimental demonstrations and extensive comparisons of end-to-end real-time optical OFDM transceivers with adaptive bit and/or power loading", IEEE Photonics Journal. **3** (3), 500-511 (2011)
9. N. Cvijetic, D. Qian, and J. Hu, "100 Gb/s optical access based on optical orthogonal frequency-division multiplexing," IEEE Commun. Mag. 48(7), 70–77 (2010).
10. R.P. Giddings and J.M. Tang, "Experimental demonstration and optimisation of a synchronous clock recovery technique for real-time end-to-end optical OFDM transmission at 11.25Gb/s over 25km SSMF," Opt. Express. **19** (3), 2831-2845 (2011).
11. R. P. Giddings, X. Q. Jin, E. Hugues-Salas, E. Giacoumidis, J. L. Wei, and J. M. Tang, "Experimental demonstration of a record high 11.25Gb/s real-time optical OFDM transceiver supporting 25km SMF end-to-end transmission in simple IMDD systems," Opt. Express. **18** (3), 5541-5555 (2010).
12. E. Hugues-Salas, R.P. Giddings, X.Q. Jin, J. L. Wei, X. Zheng, Y. Hong, C. Shu, and J.M. Tang, "Real-time experimental demonstration of low-cost VCSEL intensity-modulated 11.25Gb/s optical OFDM signal transmission over 25km PON systems", Opt. Express. **19** (4), 2979-2988 (2011)
13. X. Q. Jin, and J. M. Tang, "Optical OFDM synchronization with symbol timing offset and sampling clock offset compensation in real-time IMDD systems", IEEE Photonics Journal. **3** (2), 187 - 196 (2011)
14. X. Q. Jin, R. P. Giddings, and J. M. Tang, "Real-time transmission of 3 Gb/s 16-QAM encoded optical OFDM signals over 75 km SMFs with negative power penalties," Opt. Express 17(17), 14574–14585 (2009).
15. M. Morelli, C.-C. Jay Kuo, and M.-O. Pun, "Synchronization Techniques for Orthogonal Frequency Division Multiple Access (OFDMA): A Tutorial Review," Proceedings of the IEEE. **95** (7), 1394 - 1427 (2007).
16. M. Nölle, L. Molle, D.-D. Gross, R. Freund, "Transmission of 5x62 Gbit/s DWDM coherent OFDM with a spectral efficiency of 7.2 bit/s/Hz using joint 64-QAM and 16-QAM modulation", Optical Fiber Communication/National Fiber Optic Engineers Conference (OFC/NFOEC), (USA, 2010), Paper OMR4

17. J. L. Wei, C. Sánchez, R. P. Giddings, E. Hugues-Salas, and J. M. Tang, "Significant improvements in optical power budgets of real-time optical OFDM PON systems," Opt. Express 18(20), 20732-20745 (2010).
18. X. Zheng, X. Q. Jin, R. P. Giddings, J. L. Wei, E. Hugues-Salas, Y. H. Hong and J. M. Tang, "Negative power penalties of optical OFDM signal transmissions in directly modulated DFB laser-based IMDD systems incorporating negative dispersion fibres," IEEE Photonics Journal, 2 (4), 532-542(2010).

1. Introduction

Driven by the exponentially growing demand for bandwidth-intensive multimedia services such as video on demand, video conferencing, high-definition TV (HDTV) and interactive games, recent years have seen a significant increase in transmission capacity of access networks [1, 2]. The number of internet users worldwide has increased by ~445% from 2000 to 2010 [1]. It is also forecasted [1] that advanced internet video (3D and HDTV) demand will increase ~23-fold between 2009 and 2014, and that video-centric traffic will account for >91% of total global consumer traffic by 2014. Clearly, the current dominant copper-wire- and wireless-based access techniques namely very-high-speed digital subscriber line (VDSL) and WiMax [2] cannot satisfy the ever-increasing bandwidth requirement in such cost-sensitive application scenarios, passive optical networks (PONs) are, therefore, being widely adopted and practically implemented as a promising cost-effective and "future-proof" high-speed technical strategy for broadband access.

Generally speaking, PONs have been evolving from traditional time division multiplexing (TDM) PONs [3], wavelength division multiplexing (WDM) PONs [4], hybrid TDM/WDM PONs [4], and the most recently emerging optical orthogonal frequency division multiple access (OOFDMA) PONs [5-7]. A TDM PON provides a point-to-multipoint access between one optical line terminal (OLT) and a number of optical network units (ONUs) through the use of TDM to convey downstream signals from the OLT to the ONUs, and employs time division multiple access (TDMA) to multiplex upstream signals of a separate wavelength from the ONUs to the OLT. As a direct result, future high-speed TDM PONs impose serious constrains on transceiver designs in terms of ultra-fast burst mode operation function, complex scheduling algorithms and framing technologies, as well as pronounced sensitivity to packet latency. In WDM PONs, data information is transmitted over a pair of dedicated wavelengths assigned to a particular ONU for both downstream and upstream transmission directions. For widespread massive global deployment of WDM PONs, the most critical challenges are cost-effectiveness and flexibility [4]. The first challenging issue arises due to the achievements of some daunting tasks including, for example, colorless network operation and the fundamental alteration to legacy PON optical distribution networks. Whilst the restricted flexibility of WDM PONs is mainly due to the fact that dynamic bandwidth allocation (DBA) cannot be statistically performed at a sub-wavelength granularity. In hybrid TDM/WDM PONs, a number of wavelengths are utilized in each direction to link the OLT to several ONUs, and each individual wavelength is shared among a number of ONUs rather than being dedicated to a single ONU, therefore, it is envisaged that hybrid TDM/WDM PONs inherit, to some extent, the majority of the abovementioned technical challenges associated with TDM PONs and WDM PONs, despite the fact that future TDM/WDM PONs will gradually evolve from a fixed wavelength configuration into a tunable wavelength configuration.

In OOFDMA PONs, for both downstream and upstream transmission directions, an overall channel bandwidth can be divided into a large number of orthogonal subcarriers of different frequencies, one or more of which can be assigned statistically to a specific ONU, and a subcarrier can also be further shared among different applications via TDM. Therefore, DBA can be easily achieved using the following three means: 1) assigning a certain number of information-bearing subcarriers to a single high-speed ONU; 2) allocating a single subcarrier to several low-speed ONUs at different time slots previously assigned, and 3) varying independently signal modulation formats and/or powers taken on subcarriers to perform, in an extra dimension, DBA with an extremely fine granularity [8]. Throughout this paper, DBA with the extra dimension is referred to as adaptive DBA, which can not only maximize the aggregated system transmission capacity, but also effectively reduce imperfections in transmission channel properties without affecting signal bit rates offered to individual ONUs. In addition, owing to the nature of "noise-like" time-domain OOFDM waveforms, OOFDMA PONs are also free from burst mode operation.

In comparison with other PONs mentioned above, OOFDMA PONs have demonstrated a number of salient advantages capable of satisfying the network carriers' major targets for future high-speed PONs. The advantages are summarized below:

- Capability of providing an increased number of subscribers with high signal bit rates over extended reach [9];
- Considerably improved cost-effectiveness. This is because of the full exploitation of rapid advances in modern digital signal processing (DSP) technology, and the considerable reduction in PON system complexity owing to OOFDM's unique adaptability, excellent resistance to linear component/system impairments and efficient utilization of channel spectral characteristics [5-13];

- Full-scale DSP-based adaptive DBA with a fine bandwidth granularity. As mentioned above, the available channel bandwidth is shared statistically between various ONUs using dimensions of frequency, time and signal modulation format. This feature can use limited channel spectral bandwidths to provide end-users with required services.
- Backward compatibility. OOFDMA PONs can potentially support multiple TDM PON standards. This coexistence with different standards offers a seamlessly upgrading of installed legacy PONs [10];
- Excellent flexibility. OOFDM transceivers with adaptive bit and/or power loading [8] offer the PON systems great adaptability. This feature may not only facilitate the convergence of various access networks but also enable the accommodation of traditional heterogeneous services and newly emerging services over a common platform.

For practical deployment of cost-effective OOFDMA PONs, intensity-modulation and direct-detection (IMDD) using directly modulated lasers (DMLs) is greatly advantageous, which, however, causes the strong optical beat interference (OBI) effect upon direct detection of different ONU upstream signals of similar wavelengths [7]. OBI produces unwanted frequency products that fall into the useful signal spectral region. To mitigate the OBI effect, use can be made of two technical solutions including, 1) the utilization of DMLs operating at different wavelengths for upstream transmission in different ONUs [5], and 2) the use of coherent detection instead of direct detection to convert upstream signals to the electrical domain in OLTs [6]. As the second solution considerably increases the complexity of transceiver/PON system architectures including DSP algorithms, thus the overall PON system cost, only is the first solution considered in the present paper.

Over recent years, experimental investigations have been reported of OOFDMA PONs using off-line DSP approaches in the transmitters and/or receivers [5-7,9], which, however, do not consider either the limitations imposed by the precision and speed of practical DSP hardware, or the implementation of adaptive DBA. Experimental demonstrations of end-to-end real-time OOFDMA PONs with adaptive DBA are extremely vital for exploring the feasibility of the OOFDM technique for practical deployment in cost-sensitive and high-speed future PON systems. Unfortunately, as far as we are aware, such works have not been reported.

By making use of electrical baseband OFDM signals to modulate various commercially available, low-cost DMLs such as DFB lasers [11] and vertical cavity surface-emitting lasers (VCSELs) [12], we have successfully demonstrated experimentally end-to-end real-time 11.25Gb/s OOFDM transmission over 25km standard single-mode fibre (SSMF)-based point-to-point PON systems employing IMDD. In those real-time OOFDM systems, real product-like functions namely on-line performance monitoring and live parameter optimization have also been included. More recently, further improvements in the transceiver design have also been made by incorporating other crucial functionalities including adaptive bit and/or power loading [8], as well as asynchronous and synchronous symbol synchronization [10,13].

Based on modified real-time OOFDM transceivers, the thrust of the present paper is to experimentally demonstrate, for the first time, end-to-end real-time IMDD OOFDMA PONs with adaptive DBA at 11.25Gb/s over 26.4km SSMFs. The demonstrated OOFDMA PON system consists of two ONUs, each of which uses a DFB-based DML and a VCSEL-based DML. As the physical layer transmission performance is the main focus of the paper and the downstream transmission performance of the PON system is very similar to that published previously in point-to-point systems [8, 10-13], in this paper, special attention is, therefore, given to upstream transmission performances and adaptive DBA, which are the key factors for characterizing the PON system perfromance. In addition, extensive experimental investigations are also undertaken of the influence of practically encountered major ONU differences upon the performances of all upstream signals. These ONU differences include relative symbol offset, optical launch power and DML modulation characteristics. In addition, detailed discussions are also made of how to fully exploit the adaptability feature in DBA for a given OOFDMA PON system.
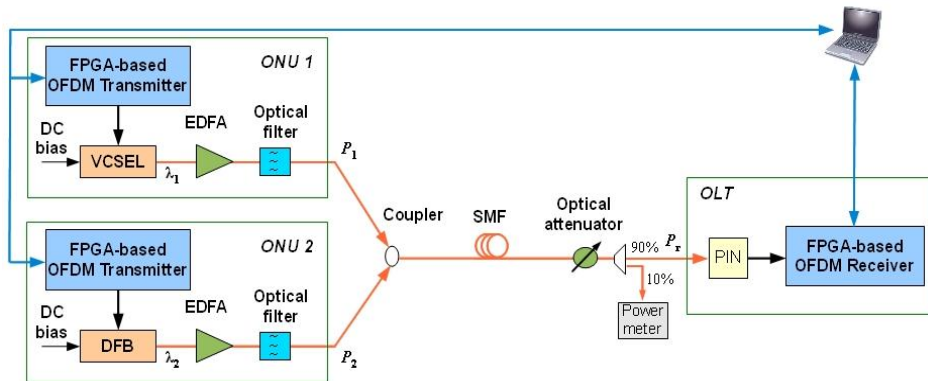

Fig. 1. OOFDMA PON system setup. λ_1 (λ_2): wavelength of the VCSEL- (DFB-) based DML. P_1 (P_2): optical launch power of ONU1 (ONU2). P_r: optical power received by the PIN in the OLT.

2. OOFDMA PON systems

2.1 OOFDMA PON system setup

Fig.1 illustrates schematically the experimental OOFDMA PON system considered here, which consists of two ONUs, a single OLT and a 26.4km SSMF linking a 3-dB optical coupler and a PIN in the OLT. The simple IMDD system is free from both chromatic dispersion compensation and in-line optical amplification. As our numerical simulations indicate that the incorporation of two ONUs in the OOFDMA PON system is sufficiently accurate for evaluating all the dynamic system characteristics of interest of the present paper, for simplicity but without losing generality, two ONUs are, therefore, considered in Fig.1.

In Fig.1, each individual ONU is composed of a field programmable gate array (FPGA)-based real-time OFDM transmitter having various DSP processes described in Section 2.2, a DML, an optical filter and an erbium doped fibre amplifier (EDFA) for fixing the optical launch power from each ONU at a required value. In the electrical OFDM transmitter, prior to performing the inverse fast Fourier transform (IFFT), encoded and adaptive power loaded user data is taken on preselected OFDM subcarriers with all the remaining subcarrier powers being set to zero. Combined with an appropriate bias current, the generated real-valued OFDM signal directly drives the DML to convert the upstream electrical signal to the optical domain. After the DML, an EDFA followed by a 0.8nm optical filter is used to set the optical launch power from each ONU at a fixed power level of 6dBm. These two upstream OOFDM signals from different ONUs are combined using a 3-dB optical coupler, and the combined optical signal propagates through the 26.4km SSMF link.

In the OLT, an optical attenuator is utilized to vary the combined optical signal power before injecting into a 12.4GHz linear PIN with a sensitivity of -19dBm (corresponding to a bit error rate (BER) of 10^{-10}, PRBS 2^{31}-1, NRZ @10Gb/s). To precisely monitor the received optical power, a 90:10 optical splitter is inserted between the optical attenuator and the PIN. Finally, the received combined upstream optical signal is converted to an electrical signal by the PIN detector. The converted electrical signal is then fed into the real-time OFDM receiver in the OLT for data recovery.

The above-mentioned two DMLs included in the ONUs operate at different wavelengths at a wavelength spacing of 4nm. According to our numerical simulations, such a wavelength spacing is sufficiently large to completely eliminate the OBI effect associated with direct detection of the combined upstream signals in the OLT. Furthermore, to rigorously evaluate the system flexibility, performance robustness and adaptive DBA of the OOFDMA PON system, a 3.6GHz, 1547nm un-cooled VCSEL (a threshold current of 2mA) and a 10GHz, 1551nm DFB laser (a threshold current of 29mA) are used in ONU1 and ONU2, respectively, to perform E/O conversion, as seen in Fig.1. The operating conditions of these DMLs are presented in Section 3.

2.2 Real-time OFDM transceivers

The real-time OFDM transmitter adopted in each individual ONU and the corresponding real-time OFDM receiver implemented in the OLT are shown in Fig.2, whose configurations are similar to those reported previously in [8, 10-13]. In the transceivers, real-time DSPs are employed to perform key transceiver functionalities including, for example, IFFT/FFT, pilot tone-based channel estimation/equalization, adaptive power loading, automatic asynchronous synchronization [13], live parameter optimization, as well as online monitoring of system performance of subcarrier/total channel BER and system frequency response. It should be pointed out, in particular, that, in the transmitter FPGA shown in Fig.2, a newly developed symbol timing offset (STO) compensation block is added prior to the 'Signed to Unsigned' function block. For a given upstream OOFDMA PON system, use can be made of the STO compensation block to adjust the signal time delay at a granularity of a sample time duration to synchronize different upstream signals in the OLT, as detailed in Section 2.4.

As the aforementioned transceiver functionalities and the implementation of real-time OFDM signal generation/detection have been presented in detail in [8, 10-13], thus an outline of the transceiver design together with corresponding parameters are briefed below:

In each transmitter FPGA clocked at 100MHz, pseudo random data sequences generate a stream of 84-bit (70 bits for 32-QAM) parallel words representing the data payload. Based on the approach detailed in [14], each of these parallel words is combined with a fixed 6-bit (5 bits for 32-QAM) pilot word for channel estimation/equalization. The combined 90-bit (75 bits for 32-QAM) words are mapped onto 15 parallel 64-QAM encoders. As discussed in Section 2.3, if N_i, i=1, 2, represents the total number of information-bearing subcarriers assigned to the ONU, the N_i encoded parallel complex numbers are arranged appropriately, together with 15-N_i zero values, to distribute among these 15 subcarriers, according to a specific adaptive DBA requirement. Adaptive power loading is then performed to the information-bearing subcarriers to compensate the effect of the system frequency response roll-off associated with the entire transmission system from the transmitter IFFT input to the receiver FFT output [11]. These 15 subcarriers and one zero-frequency subcarrier with a zero power are input, with their Hermitian-symmetry counterparts, to the transmitter 32-point IFFT to produce 32 real-valued samples. It should be noted that, in practice, a buffer can be used prior to pilot insertion to produce the required number of parallel words loaded on the information-bearing subcarriers.

160
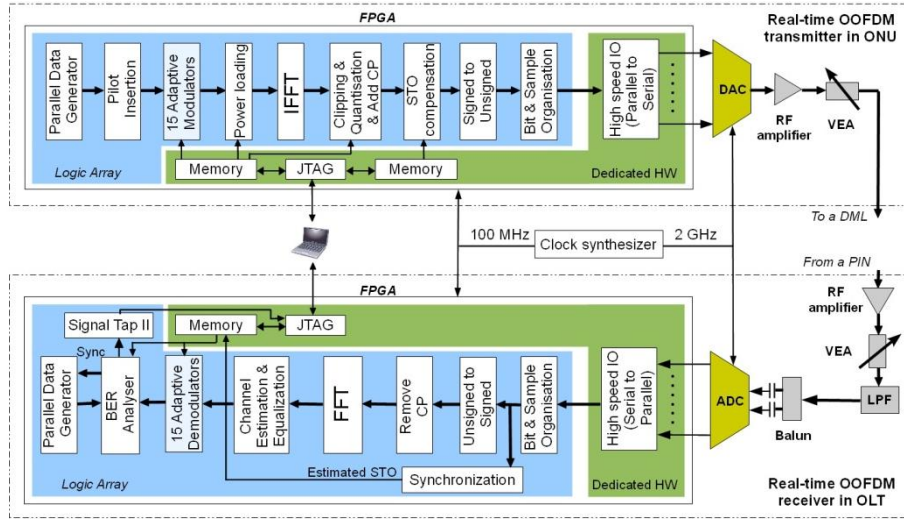
Fig. 2. Real-time OFDM transmitter/receiver in the ONU/OLT.

Having completed the above-mentioned DSP procedures, a cyclic prefix of 8 samples is added to each OFDM symbol. After performing signal clipping at an optimum clipping ratio of 12.0dB [8] and 8-bit quantization, the digital OFDM samples generated by the real-time DSP in the transmitter are transferred as 4 parallel samples by a 32-bit wide bus running at 1GHz to an 8-bit, 4GS/s digital-to-analogue converter (DAC) for conversion to an analogue electrical OFDM signal. In combination with a suitable bias current, the real-valued, unsigned electrical OFDM signal emerging from the DAC output port is then adjusted by a variable electrical attenuator/amplifier to have a desired amplitude to directly drive the DML mentioned in Section 2.1. The above transceiver design gives the ONU a raw signal bit rate of $0.75 \times N_i$ Gb/s ($0.625 \times N_i$ Gb/s for 32-QAM). The aggregated upstream raw signal bit rate is 11.25Gb/s (9.375Gb/s for 32-QAM).

In the OLT receiver, to minimize quantization noise and clipping-induced signal distortions in an 8-bit, 4GS/s analogue-to-digital converter (ADC), the baseband electrical signal converted by the PIN is amplified to an optimum level to provide a suitable amplitude prior to digitization by the ADC. All real-time DSP procedures in the receiver FPGA are identical to those reported in [8,10-13]. With the adaptive DBA-initiated data-bearing subcarrier distribution information for different ONUs, data for each individual ONU is finally recovered. In addition, BER measurements of both individual subcarriers and total transmission channel follow the procedures reported in [11].

Here it is worthy addressing the following two points:

- To effectively optimize the transmission performance of each upstream signal and simultaneously improve the DBA capability and the system insusceptibility to variations in transceiver components, adaptive power loading is used independently for each ONU transmitter. In comparison with the most sophisticated bit-and-power loading technique, the simplest adaptive power loading technique has been experimentally confirmed to be sufficiently effective in escalating the OOFDM system performance to its maximum potential [8].
- To prevent symbol alignment drift and ensure subcarrier orthogonality for data recovery in the OLT, the whole OOFDMA PON system should be synchronized to a common clock source. Therefore, in Fig. 2 a clock synthesizer with an internal common reference clock generates 2GHz clock signals for the 4GS/s, 8-bit DAC/ADC and 100MHz clock signals for all the transmitter/receiver FPGAs (100MHz is the OFDM symbol rate).

2.3 Adaptive DBA

Given the unique OOFDM features of subcarrier orthogonality and adaptive bit and/or power loading, adaptive DBA can be easily implemented in practice using the three approaches mentioned in Section 1. It should be noted that, based on online performance monitoring and live parameter optimization, the present OOFDM transceivers are capable of performing real-time adaptive DBA, according to both the channel quality and users' bandwidth requirement.

As an example of experimentally demonstrating adaptive DBA in the OOFDMA PON system, here 1st – 7th subcarriers are assigned to ONU1 using the VCSEL-based DML, whilst 8th-15th subcarriers are assigned to ONU2 using the DFB-based DML, as shown in Fig. 3, where the profiles of both data-encoding bit and adaptively loaded subcarrier amplitude are also presented for two ONUs. Because the modulation bandwidth of the VCSEL is much lower than that corresponding to the DFB laser, the allocation of low (high) frequency subcarriers to VCSEL-

based ONU1 (DFB-based ONU2) not only improves the transmission performance of the entire OOFDMA PON system, but also allows a better utilization of the available channel characteristics. Throughout the paper unless mentioned explicitly in the text when necessary, this DBA example is considered for exploring in detail OOFDAM PON performance characteristics presented in Section 3.
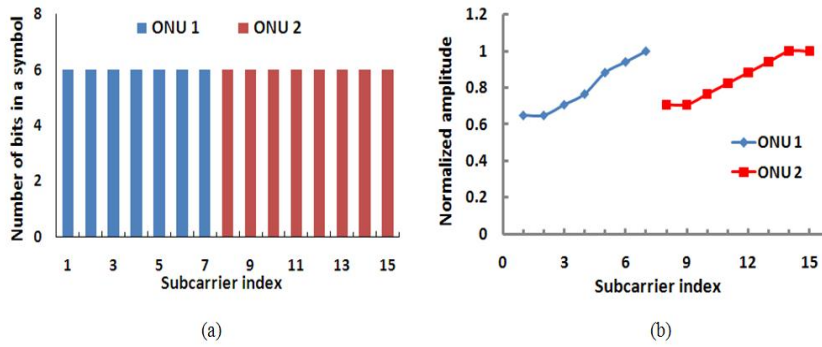
Fig.3. Data-encoding bit and adaptively loaded subcarrier amplitude distributions over different subcarriers assigned to different ONUs: (a) Data-encoding bit distribution and (b) normalized subcarrier amplitude prior to the IFFT in the transmitter of each ONU.

Considering the transceiver design parameters mentioned in Section 2.2, for the aforementioned adaptive DBA scheme, the raw signal bit rates for ONU1 and ONU2 are 5.25Gb/s and 6Gb/s, respectively. It is also easy to understand that, for the present 64-QAM-encoded OOFDMA PON system, the bandwidth provided to each ONU can vary from 750Mb/s to 11.25Gb/s with a granularity of 750Mb/s. Of course, the DBA granularity can be further improved if use is made of adaptive bit-and-power loading in OOFDM transceivers [8].

2.4 OOFDMA PON synchronization

It is well known that accurate synchronization of all downstream and upstream signals in OOFDMA PONs is vital for the practical realization of the systems with desired transmission performances. Given the fact that an effective asynchronous synchronization technique has been proposed and experimentally demonstrated in point-to-point real-time OOFDM systems [13], and that the technique can also be employed for downstream transmission in the present OOFDMA PON system, here special attention is, therefore, given to further extending the asynchronous synchronization technique for applications in OOFDMA PONs to enable accurate synchronization of different upstream signals.

A highly precise estimation of the STO associated with a upstream signal in the receiver plays a dominant role in achieving high-quality signal synchronization in multiple access networks. In conventional wireless OFDMA networks, an electrical filter is often used in the receiver to extract a wanted upstream signal from the mixed signals received. Based on the extracted signal and the synchronization technique adopted for downstream transmission, an estimated STO value is obtained, which is then sent back to the corresponding transmitter for conducting STO compensation [15]. For an access network shared by M users, M different filters are required to simultaneously synchronize all upstream signals. Clearly, the filter-based synchronization technique is not suitable for the present OOFDMA PON systems, as an extremely large number of end-users possibly supported by the OOFDMA PONs require a huge bank of filters to be implemented. Undoubtedly, the traditional approach significantly increases the transceiver complexity and the system cost.

Making use of the previously published asynchronous synchronization technique [13], and considering the fact that the STO of a signal in PONs does not vary significantly over time, the following "one-by-one" approach that is experimentally approved to be very effective, is thus adopted, throughout the paper, for use in the OOFDMA PON system. The procedures of implementing the approach are listed as following:

- In the initial phase of establishing an OOFDMA PON system, only one ONU is switched on and all other ONUs are switched off. In the OLT, use is first made of the asynchronous synchronization technique to estimate the STO of the upstream signal from the active ONU. The optimum position of the FFT window measured in the OLT is also recorded and regarded as a fixed reference for synchronizing all other ONUs;
- The estimated STO is fed to the active ONU via the joint test action group (JTAG) interface, as illustrated in Fig. 2;
- Upon receiving the STO information, the active ONU undertakes STO compensation in the STO compensation block by adjusting symbol offset at a resolution of a sample time duration. This leads to the accurate synchronization of the active ONU with the OLT;
- Having synchronized the first ONU, the second ONU is switched on. Taking the recorded FFT window position in the OLT as a reference, a repetition of the aforementioned steps results in the synchronization of

two upstream signals from both ONUs with the OLT. Such procedures continue until the upstream signals from all the ONUs are simultaneously synchronized successfully.

It should be addressed that, apart from synchronizing the OOFDMA PON system, the above-mentioned synchronization approach can also automatically compensate the chromatic dispersion-induced time delay between different ONUs operating at different wavelengths.

3. Experimental results

Having described the experimental OOFDMA PON system setup and the modified real-time OOFDM transceiver design in Section 2, this section is dedicated to extensive experimental explorations of dynamic OOFDMA PON system properties including, impact of DML operating conditions, ONU launch power variation range, performance susceptibility to symbol offset between different upstream signals, as well as impact of adaptive DBA on OOFDMA PON performance. These issues are of great importance for practical system design.

3.1 Impact of DML operating conditions

To gain an in-depth understanding of the influence of DML operating conditions on the OOFDMA PON performance and, more importantly, to identify optimum operating conditions for various DMLs adopted in the system, experimental measurements are first undertaken of the BER performance as a function of bias current for different DMLs in the OOFDMA PON system subject to a fixed received optical power of -8dBm in the OLT and with only one ONU being activated at a time. The measured results are shown in Fig.4, where bias current dependent optimum root mean square (RMS) driving currents are also presented for different DMLs.
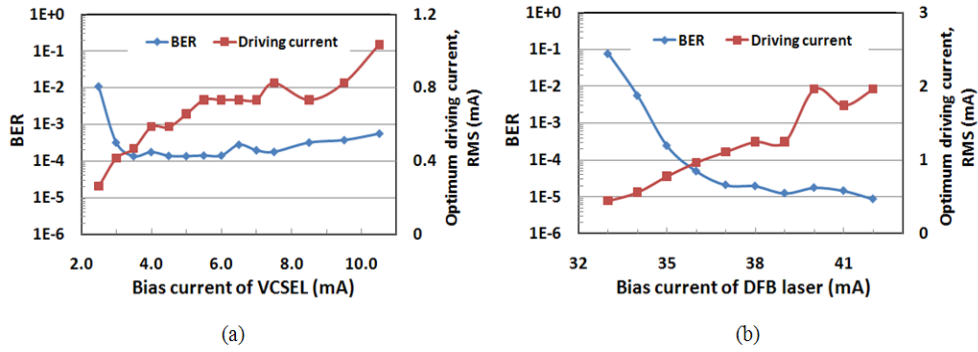
Fig. 4. Bias current dependent BER and optimum RMS driving current for different DMLs. (a) VCSEL-based DML and (b) DFB-based DML. In the OOFDMA PON system, only one ONU is switched on at a time and the received optical power is fixed at -8dBm in the OLT. Threshold currents: 2mA for the VCSEL and 29mA for the DFB laser.

As seen in Fig.4, the observed BER and RMS driving current developing trends are similar between different DMLs, and the dynamic bias current ranges, over which the measured BERs less than the forward error correction (FEC) limit of 2.3×10^{-3} [16] are obtainable, are from 2.5mA to 10.5mA for the VCSEL-based DML and from 34.5mA to 42mA for the DFB-based DML. For bias currents in the vicinity of a DML threshold, the BER increases sharply with decreasing bias current because of small bias current-induced strong effects of intensity modulation nonlinearity and signal clipping [17]. On the other hand, as shown in Fig.4(a), for excessively high bias currents, the BER performance degrades slightly due to a large bias current-induced reduction in OOFDM signal extinction ratio [17]. In addition, considering a typical L-I curve associated with a DML, it is easy to understand that the optimum RMS driving currents roughly linearly grow with bias current, as observed in Fig.4.

In the OOFDMA PON system with two ONUs simultaneously sending their upstream signals to the OLT, the BER of each ONU versus bias current is plotted in Fig.5 for the VCSEL-based DML and the DFB-based DML operating at fixed RMS driving currents of 0.72mA and 1.2mA, respectively. In measuring the figure, a constant DFB bias current of 37mA and a constant VCSEL bias current of 4.5mA are adopted in Fig.5(a) and Fig.5(b), respectively, and for all the cases the received optical launch powers in the OLT are fixed at -5dBm.

As expected, Fig.5 shows that a variation in DML bias current in an ONU (referred to as varied ONU) affects not only the ONU's own BER performance but also the performance of the other ONU having a fixed DML bias current (referred to as fixed ONU). In particular, BER degradations suffered by the fixed ONUs become severe when the varied ONUs operate at bias currents close to their DML thresholds, as seen in Fig.5. This is mainly due to the fact that, over such a region, the output optical power of the DML in the varied ONU is very low, which causes strong EDFA-generated ASE noise to be imposed onto the upstream signal from the fixed ONU. Furthermore, a DML bias current well above the threshold in the varied ONU produces a high optical signal power, which weakens the ASE noise effect, thus flattens the BER curves for the fixed ONU, as presented in Fig.5.

From Fig.5 it is also clear that, for the varied ONU, there exists an optimum DML bias current, corresponding to which a minimum BER is observed. The physical mechanisms underpinning the occurrence of the optimum bias current are very similar to those discussed in Fig.4, except that, for bias currents larger than the optimum value, an extra DC component associated with the fixed ONU leads to a further reduction in signal extinction ratio of the upstream signal from the varied ONU. As a direct result, in comparison with Fig.4, a much steep BER curve occurs for the varied ONU in Fig.5.

(a)

(b)
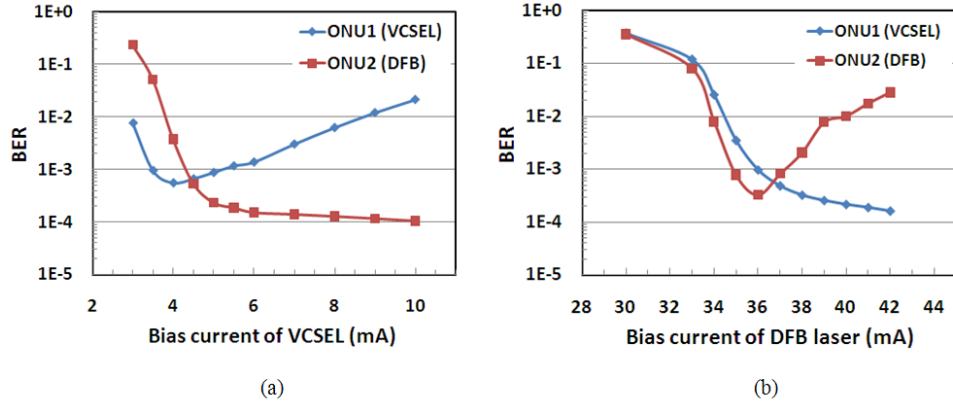
Fig. 5. BER of each ONU versus bias current in the OOFDMA PON system with two ONUs simultaneously sending their upstream signals to the OLT. (a) VCSEL-based DML and (b) DFB-based DML. The received optical power in the OLT is fixed at -5dBm.

From Fig.5, the optimum DML bias currents can be identified easily, which are 4.5mA for the VCSEL-based ONU (ONU1) and 37mA for the DFB-based ONU (ONU2). Also taking into account Fig.4, these two optimum bias currents correspond to the optimum RMS driving currents of 0.72mA for the VCSEL-based DML and 1.2mA for the DFB-based DML. These optimum DML operating conditions are adopted in all the experimental measurements presented below. It is worth addressing that the optimum RMS driving currents hold well for the present experimental system, as a variation in DML driving current does not considerably affect the system performance when the DML operates above its threshold [18].

3.2 ONU launch power variation range

In the OOFDMA PON system, the ONU launch power variation range is defined as, for a fixed optical power received in the OLT, the maximum allowable variation range of the optical launch power of a specific ONU, over which the BER of any individual upstream signal simultaneously transmitting in the system is still less than the FEC limit of 2.3×10^{-3}. Clearly, a large ONU launch power variation range improves not only the performance robustness but also the system flexibility because of the pronounced ability of accommodating a large diversity of low-cost optical components.

To examine the ONU launch power variation range for the present OOFDMA PON system with all the DMLs operating at their optimum conditions identified in Section 3.1, Fig. 6 is presented, where BER performances of all upstream signals against the optical launch power from an individual ONU are plotted for different received optical powers in the OLT. In obtaining Fig.6, the output power of the EDFA is adjusted to provide various required optical launch powers from the varied ONU, whilst the optical launch power from the fixed ONU is kept at a constant value of 6dBm. The optical attenuator allocated in the front of the PIN shown in Fig.1 sets the received optical powers at different values such as -5dBm and -7dBm.

(a)

(b)

It is observed in Fig. 6 that, for a given received optical power in the OLT, an increase in optical launch power from the varied ONU improves its own BER performance and simultaneously degrades the BER performance of the fixed ONU, mainly resulting from the changes in effective optical signal to noise ratio (OSNR) of the corresponding upstream optical signals. It is very interesting to note that the ONU launch power variation ranges as large as >3dB are practically feasible, which can be further extended if a relatively high received optical power is taken in the OLT. For example, for a received optical power of -5dBm in the OLT, the observed ONU launch power variation range are approximately 3.6dB for ONU1 and 3.2dB for ONU2. The upper limit of the dynamic power variation range is determined by the minimum OSNR allowed by the fixed ONU, whilst the lower limit of the dynamic power variation range is determined by the minimum OSNR allowed by the varied ONU. This implies that an increase in extinction ratio of DML-modulated signals from both ONUs enhances the ONU launch power variation range.

3.3 Performance susceptibility to symbol offset between different upstream signals

In the OOFDMA PON system, to maintain the orthogonality among subcarriers of the combined upstream OOFDM signals for data recovery in the OLT, it is envisaged that all upstream signals from different ONUs should arrive at the OLT at the same time so that OFDM symbols associated with different ONUs are aligned with each other. However, in real network deployments, symbol offsets between various synchronized ONUs sharing a single OLT may still be encountered from time to time due to a number of unexpected practical factors such as component perturbations, laser wavelength drift and extreme environmental conditions. Therefore, from a system designer's point of view, it is also of great importance to explore the performance sensitivity of the OOFDMA PON system to symbol offset between different upstream signals.

To examine the abovementioned issue, ONU BERs versus symbol offset between upstream signals of different ONUs are plotted in Fig.7, based on a fixed ONU launch powers of 6dBm and the DMLs at their optimum operating conditions. In measuring Fig.7, perfect synchronisation between all the upstream signals is first achieved to ensure that the FFT window in the OLT locates at the optimum position for the entire system. Then various symbol offsets are introduced to the upstream signal of a particular ONU via adjusting the 'STO compensation' function block in its transmitter. For each sample offset introduced, BER measurements are conducted simultaneously for both ONUs.
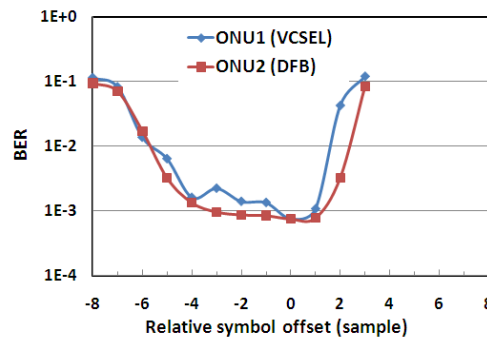
Fig. 7. BER performance sensitivity to symbol offset between upstream signals of different ONUs. The received optical power in the OLT is fixed at -7dBm.

It can be seen in Fig.7 that the OOFDMA PON system is tolerant to any symbol offsets within a dynamic range of approximate 6 samples, which is slightly less than the adopted cyclic prefix length of 8 samples. Within the optimum symbol offset range, relatively flat BER curves of less than the FEC limit are obtainable for all ONUs. Whilst outside the optimum range, perfect subcarrier orthogonality in the OLT cannot be maintained, this causes the BERs of all the involved ONUs to increase sharply and simultaneously, as shown in Fig.7. The duration of the optimum symbol offset range can be further prolonged when long cyclic prefix lengths are adopted in the OOFDM transceiver design [13].

3.4 Impact of adaptive DBA

The considered OOFDMA PON system utilizes the DMLs having significantly large differences in modulation characteristics, and the adopted real-time OOFDM transceivers exhibit system frequency response roll-offs as large as 12dB within the 2-GHz signal spectral region [11]. Inevitably, these system/transceiver design aspects

cause considerable variations in achievable SNRs experienced by individual subcarriers. Therefore, the BER performance of a specific ONU is expected to vary with the adopted adaptive DBA scheme due to alterations in assigning subcarriers of different frequencies to the ONU. Detailed explorations of such an effect and, more importantly, examinations of the feasibility of utilizing adaptive DBA to reduce the effect without affecting the signal bit rate offered to each ONU form the main objectives of this section.

Making use of the adaptive DBA scheme presented in Section 2.3, BERs versus received optical power for two ONUs involved are shown in Fig.8(a) for two cases: Case I, represented by solid lines, where both ONUs are activated, and Case II, represented by dash lines, where one ONU is activated and the other ONU is deactivated. In the deactivated states, the DML driving currents are turned off and their optimum bias currents are still turned on. The supply of the bias currents in the deactivated states is to distinguish the power penalty caused by multiple access interference (MAI) between upstream signals, as discussed below.

It can be seen in Fig.8(a) that, for each of the aforementioned two cases, almost identical BER developing curves are obtained. Considering the significant differences in DML modulation characteristics between different ONUs, and the 12dB system frequency response roll-offs, the identical BER developing curves indicate that the adopted adaptive DBA scheme is very effective in adaptively exploiting the available channel characteristics without affecting the BER performances of any ONUs. This statement is confirmed by Fig.8(b), where even numbers of subcarriers, i.e., 2nd, 4th, ... 14th, are assigned to ONU1 and odd numbers of subcarriers, i.e., 1st, 3rd, … 15th, are allocated to ONU2, and the definition of two cases are identical to those in Fig.8(a). Fig.8(b) shows that, although the subcarrier-interleaved DBA scheme is capable of providing each ONU with the same signal bit rate compared to that offered by the scheme used in Fig.8(a), ONU1, however, suffers a 2dB increase in received optical power at the FEC limit BER, compared to ONU2.

(a) (b)
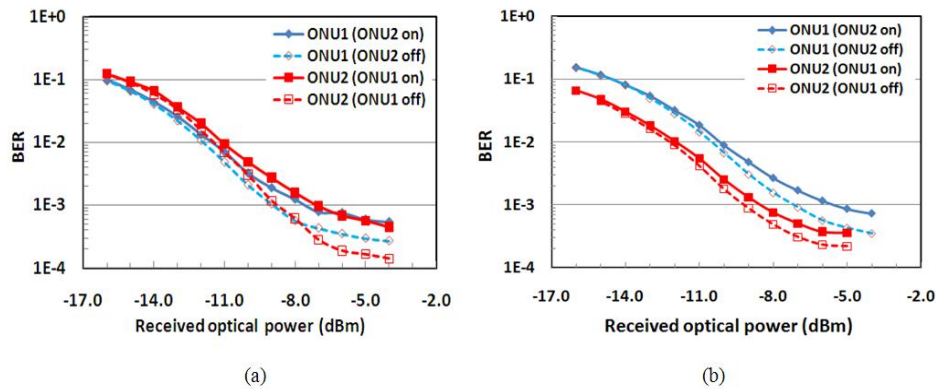
Fig. 8. BERs versus received optical power for two ONUs using 64-QAM. Case I, represented by solid lines, where both ONUs are activated; Case II, represented by dash lines, where one ONU is activated and the other ONU is deactivated. (a) The adaptive DBA scheme presented in Section 2.3, and (b) The adaptive DBA scheme based on interleaved subcarriers.
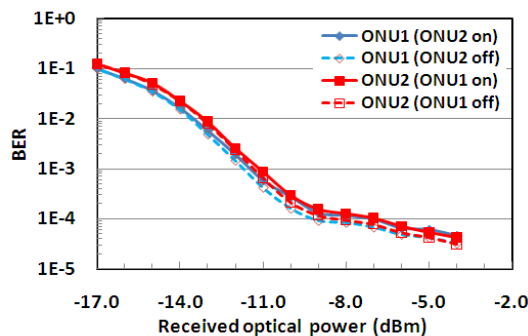
Fig. 9. BERs versus received optical power for two ONUs using 32-QAM. Case I, represented by solid lines, where both ONUs are activated; Case II, represented by dash lines, where one ONU is activated and the other ONU is deactivated. The adaptive DBA scheme and all other system parameters are identical to those utilized in Fig.8(a).

In addition, Fig.8(a) also shows that the minimum received optical powers required for achieving the FEC limit BER are -8.6dBm for Case I and -9.3dBm for Case II. The existence of a 0.7dB difference in the minimum received optical power between these two cases is mainly contributed by the MAI effect, which arises due to the imperfection in subcarrier orthogonalily. As such imperfection is free from the adopted adaptive DBA scheme, a

very similar minimum received optical power difference between Case I and Case II is thus observed in Fig.8(b) for each ONU.

It is well known that taking low signal modulation formats on OFDM subcarriers can considerably enhance the system BER performance tolerance to the effects of DML modulation nonlinearity, MAI and system frequency response roll off. From the discussions in Fig.8, it is, therefore, expected that a reduction in signal modulation format decreases the dependence of system BER performance on variations in adaptive DBA schemes but at a price of lowering aggregated signal bit rates. Such an expectation is experimentally confirmed in Fig.9, where almost identical BER curves for all these cases are observed when 32-QAM is considered. In Fig.9, all other system parameter values and the adaptive DBA scheme are identical to those adopted in Fig.8(a). This gives an aggregated upstream signal bit rate of 9.375Gb/s, of which 4.375Gb/s and 5Gb/s are occupied by ONU1 and ONU2, respectively.

4. Conclusions

Based on modified real-time OOFDM transceiver architectures, end-to-end real-time experimental demonstrations have been reported, for the first time, of aggregated 11.25Gb/s over 26.4km SSMF, IMDD OOFDMA PONs with adaptive DBA. The demonstrated OOFDMA PON system consists of two ONUs, each of which utilizes a DFB-based DML or a VCSEL-based DML. Extensive experimental explorations of dynamic OOFDMA PON system properties have been undertaken in terms of several crucial system design aspects, which include impact of DML operating conditions, ONU launch power variation range, performance susceptibility to symbol offset between different upstream signals, as well as impact of adaptive DBA on the BER performance of each individual ONU. Optimum DML operating conditions have been identified. It has been shown that, for achieving acceptable BERs for all ONUs simultaneously transmitting upstream signals to the OLT, the OOFDMA PON system has a >3dB dynamic ONU launch power variation range, and the BER performance of the system is insusceptible to any upstream symbol offsets slightly smaller than the adopted cyclic prefix. In addition, experimental results have also indicated that, in addition to maximizing the aggregated system transmission capacity, adaptive DBA can also effectively reduce imperfections in transmission channel properties without affecting signal bit rates offered to individual ONUs.

Acknowledgements

Appendix K

Electrical OFDM Modem

Generating bits and line rate calculation

```
N=sum(Form);%Number of subcarriers
M=dlmread('M', ' '); %at least 400 symbols for accuracy
randn('state',0); % same seed
b11=randn(M,N)>0;
dlmwrite('randomdataamoofonu2',b11, ' ');
b=dlmread('randomdataamoofonu2', ' ');
%Linerate
numberofsamplespersymbol=(totalnumbersubs*(1+prefixparm));
%Symbolrate=samplerate/munberofsamplespersymbol
Symbolrate=Fs_samp/numberofsamplespersymbol;
%Signalbitratepersub=*Symbolrate*N;
for countofsubs=1:1:numberofsubs
  Signalbitratepersub(1,countofsubs)=Symbolrate*Form(1,countofsubs);
end
```

```matlab
Signalbitratepersubmean=sum(Signalbitratepersub.*Ponsub22);
%Signalbitrate=N/(totalnumbersubs*(1+prefixparm)/Fs_samp);%signal bitrate
with symbol rate 100Mhz,for 50 MHz multiply totalnumbersubs wtih 2.
% Calculating signal line rate
Signal_Line_Rate=Signalbitratepersubmean/1e9;%(N*Fs_samp)/(2*(totalnumbersu
bs/2-1)*1.25)/1e9;
%Signal_Line_Rate=length(Form)*0.75; %RAW RATE =NUMBEROFSUBS*0.75 (FOR
64qam)
%Displays the signal line rate
disp(['The Signal Line Rate is(NET Bit rate): ' num2str(Signal_Line_Rate) '
Gb/s'])
RAWSignal_Line_Rate=Signal_Line_Rate+Signal_Line_Rate*25/100;%(N*Fs_samp)/(
2*(totalnumbersubs/2-1)*1.25)/1e9;
%Signal_Line_Rate=length(Form)*0.75; %RAW RATE =NUMBEROFSUBS*0.75 (FOR
64qam)
%Displays the signal line rate
disp(['The with Cyclic prefix Signal Line Rate is(RAW (with CP)): '
num2str(RAWSignal_Line_Rate) ' Gb/s'])
dlmwrite('Signal_Line_Rate2',Signal_Line_Rate, ' ');
dlmwrite('RAWSignal_Line_Rate2',RAWSignal_Line_Rate, ' ');
sum(Form.*Ponsub22)/(numberofsamplespersymbol*(1/Fs_samp))


%%%%%%%%%%%%%%%%%%%%%%%%%%%%%%%%%%%%%%%%%%
% Generate complex conjugates and perform serial to parallel
% conversion
%%%%%%%%%%%%%%%%%%%%%%%%%%%%%%%%%%%%%%%%%%%%


for z=(1:1:M)
    c_tx5(z,:)=c_tx(z,:).*Ponsub22;
    c_tx4(z,:)=c_tx(z,:).*Ponsub22;
    y(z,numberofsubs:-1:1) = [conj(c_tx5(z,1:numberofsubs))];  %
Generating complex conjugates
    s(z,1:totalnumbersubs) =
[0,c_tx5(z,1:numberofsubs),0,y(z,1:numberofsubs)]; %S/P conversion
end
M=dlmread('M2', ' ');
s=[zeros(2,totalnumbersubs);s;zeros(2,totalnumbersubs)];%Training sequence
dlmwrite('pon2pilot', c_tx4, ' ');
%%%%%%%%%%%%%%%%%%%%%%%%%%%%%%%%%%%%%%%%%%
% Perform IFFT and add Cyclic pre and post fix%
%%%%%%%%%%%%%%%%%%%%%%%%%%%%%%%%%%%%%%%%%%%%

[s_tx]=PrefixandSP(dlmread('M2', ' '),dlmread('prefixamount', '
'),dlmread('totalnumbersubs', ' '),dlmread('prefix1', '
'),IFFT_Out_Signal,dlmread('prefixstart', ' '));


function
[outputofPrefixandSP]=PrefixandSP(M,prefixamount,totalnumbersubs,prefix1,IF
FT_Out_Signal,prefixstart)

justprefix=dlmread('justprefix', ' ');
 if justprefix==1
   prefixamount= prefixamount*2;
   prefixstart=totalnumbersubs-prefixamount+1;
   prefix1=totalnumbersubs+prefixamount;%80

 else
 end
k_1=1;
```

```matlab
l=1;

for z=(1:1:M)

 if justprefix==1

  cyclic_prefix(z,1:prefixamount) =
IFFT_Out_Signal(z,prefixstart:totalnumbersubs);%Cyclic prefix
symbol(z,1:prefix1)=[cyclic_prefix(z,1:prefixamount),IFFT_Out_Signal(z,1:to
talnumbersubs)];
s_tx(k_1:(prefix1*l))=symbol(z,1:prefix1);    %Perform parallel to serial
conversion
    k_1=k_1+prefix1;
    l=l+1;

 else
 cyclic_prefix(z,1:prefixamount) =
IFFT_Out_Signal(z,prefixstart:totalnumbersubs);%Cyclic prefix
cyclic_postfix(z,1:prefixamount)= IFFT_Out_Signal(z,1:prefixamount);
%Cyclic postfix
symbol(z,1:prefix1)=[cyclic_prefix(z,1:prefixamount),IFFT_Out_Signal(z,1:to
talnumbersubs),cyclic_postfix(z,1:prefixamount)];
s_tx(k_1:(prefix1*l))=symbol(z,1:prefix1);    %Perform parallel to serial
conversion
    k_1=k_1+prefix1;
    l=l+1;
 end
end


outputofPrefixandSP=s_tx;
```

Digital to Analogue Converter

```matlab
%%%%%%%%%%%%%%%%%%%%%%%%%%%%%%%%%%%%%%%%%%
            %Digital to analogue converter%
%%%%%%%%%%%%%%%%%%%%%%%%%%%%%%%%%%%%%%%%%%
input=s_tx;
%input = input- mean(input);
Pm_input = mean(input.^2);              % the average power of the OFDM
symbols with Cyclic Prefix before clipping.
Max_amp = sqrt(10^(Clip_ratio/10)*Pm_input);
for k_s=1:length(input)
    if abs(input(k_s)) > Max_amp
        input(k_s) = sign(input(1,k_s))*Max_amp;
    end
end
%Doing quantization
Quan_peak = Max_amp;        %should be a constant in future but not
necessarily be max(input)
Quan_step = 2*Quan_peak/2^Quan_bit;
for kk_b = 1:length(input)
    input(kk_b) = round(input(kk_b)/Quan_step)*Quan_step;
  % index = floor(input(kk_b)/Quan_step);
    %input(kk_b) = (index+1/2)*Quan_step;
end
output1=input;
```

DFB laser

```matlab
function [OpticField_I, OpticField_Q, t_out, f_chirp_adiab,
f_chirp_adiab_vec] = ...
        dfbode1(I_modu, I_bias, fs, flag_dfb_type, I_PTP, angle_PolarAndX)
%
%dfbode  Solve the coupled differential equations (rate equation) of a
% directly modulated DFB(distributed feedback) laser.
% [OpticField_I, OpticField_Q, t_out, f_chirp_adiab, f_chirp_total] =
% dfbode(I_modu,I_bias,fs,flag_dfb_type,angle_PolarAndX), where the input
% and out parameters are illuminated as below.
%
%input parameters
% I_modu(vector,1*N): the modulated current. (unit: A)
% I_bias(scalar): represents bias current. (unit: A)
% fs(scalar): sampling frequency corresponding to the period between two
%       adjacent points. (unit: Hz)
% flag_dfb_type: '1' represent Bookham LC25 laser with 300um long
cavity(default),
%       '0' represent Bookham LC25 laser with 200um long cavity,
% I_PTP: Peak-to-peak of modulation current, used to normalise the input
%       signal I_modu. It is constrainedly changed if required.
%       Default set: input signal I_modu won't be changed. (unit: A)
% angle_PolarAndX: the angle between the signal polarisation and the x
%       direction. (unit: Degree)
%
%output parameters
% OpticField_I(raw vector): real part of optical field.
% OpticField_Q(raw vector): imaginary part of optical field.
% t_out(raw vector): the time sequency corresponding to output data
sequency.
%       (unit: s)
% f_chirp_adiab(scalar): abiabatic frequency chirp. (unit: Hz)
% f_chirp_adiab_vec(raw vector): total frequency chirp including adiabatic
chirp
%       and transient chirp. (unit: Hz)
%
%Attention
% 1) the units for all above variable are international standard unit.
% 2) modulated current defined here is a positive variable.
% 3) sampling period, 1/fs, is better to be defined smaller than 20 ps for
accuracy.

% Related equations corresponding to DFB laser
% 1) the coupled differential equations:
% d_N_CD/d_t =  I_drive/(ElectCharge*d_cavity*w_cavity*l_cavity) - N_CD/t_c
...
%     - B_BCR*N_CD^2 - C_ACRC*(N_CD^3) - G_LGC*(N_CD - N_t)*PD/(1+NGC*PD);
% d_PD/d_t =  MCF*G_LGC*(N_CD-N_t)*PD/(1+NGC*PD) + FSE*B_BCR*(N_CD^2) -
PD/t_p;
% d_OptPhase/d_t = -2*pi*v_OptFreq*MCF*dnri_dnc*(N_CD - N_t)/n_phase;
%
% 2) output optical power:
% P_optic = w_v*w_h*h_PlancCons*v_OptFreq*PD*c_LightVelo/(2*n_g);
%
% 3) optical frequency of output optical signal
% f = v_OptFreq*(1 - MCF*dnri_dnc*(N_CD - N_t)/n_phase;
%
```

```matlab
% N_CD -- the carrier density
% PD -- the photon density
% I_drive -- the current drive into the active region of the laser
%


%
% ------------------------ Initialization ------------------------------
%
% check inputs
if nargin <= 5
    angle_PolarAndX = 0;        % the angle between the signal polarisation
...
                                % and the x direction.
    if nargin <= 4
        if nargin <= 3
            flag_dfb_type = 1;
            if nargin <= 2
                error('MATLAB:odedfb:NotEnoughInputs',...
                'Not enough input arguments.  See ODEDFB.');
            end
        end
    else                        % Normalise input modulation current signal.
        I_modu = I_modu - min(I_modu);
        I_modu = I_modu*I_PTP/max(I_modu);
    end
end


%
% ----- Parameters for directly modulated DFB laser ( Light Sourse ) ------
%
if flag_dfb_type == 1
    % 300um Bookham LC25 laser.
    l_cavity = 300e-6;          % the cavity length  ( m )
    t_p = 3.6e-12;              % the photon lifetime  ( s )
    NGC = 7.4e-23;              % the nonlinear gain coefficient  ( m-3)
    dnri_dnc = -1.381e-26;      % Rate of refractive index change with ...
                                % carrier density
else
    % 200um Bookham LC25 laser,
    l_cavity = 200e-6;          % the cavity length  ( m )
    t_p = 2.65e-12;             % the photon lifetime  ( s )
    NGC = 6.8e-23;              % the nonlinear gain coefficient  ( m-3 )
    dnri_dnc = -1.473e-26;      % Rate of refractive index change with ...
                                % carrier density
end
ElectCharge = 1.60217646e-19;   % the electronic charge  ( C )
WaveLen = 1550e-9;              % the Wavelength ( unit:m )
h_PlancCons = 6.626068e-34;     % the Planck's constant  ( J s )
c_Light = 2.99792458e8;         % the velocity of light in vacuum  ( ms-1 )
v_OptFreq = c_Light/WaveLen;    % the optical frequency  ( Hz )

N_t = 1.5e24;                   % the transparency carrier density  ( m-3 )
d_cavity = 0.033e-6;            % the cavity thickness  ( m )
w_cavity = 2e-6;                % the cavity width  ( m )
LGC = 7.5e-20;                  % the differential gain coefficient  ( m2 )
B_BCR = 1e-16;                  % the bimolecular carrier recombination  (
m3s-1 )
C_ACRC = 6.5e-41;               % the Auger carrier recombination
coefficient  ( m6s-1 )
FSE = 1e-5;                     % describe the fraction of spontanous
emission  ( no )
```

```matlab
MCF = 0.07;                         % the mode confinement factor  ( no )
t_c = 10e-9;                        % the carrier linear recombination lifetime
( s )
w_v = 0.47e-6;                      % the vertical widths of the guided mode
...
                                    % power distributions  ( m)
w_h = 1.80e-6;                      % the horizontal widths of the guided mode
...
                                    % power distributions  ( m )
n_g = 3.7;                          % the group index  ( no )
n_phase = 3.2203;                   % Phase refractive index

G_LGC = LGC*(c_Light/n_g);      % the linear gain coefficient  ( m3s-1 )
CoupEff = 0.38;                     % the coupling efficiency from the laser
chip to SMF.
alfa = 120;                         % the addition of a rear facet phase shift
T_unstable = 10e-9;                 % a period of warm-up sequence at the
                                    % beginning of unstable state
val_AbsTol = 1e-50;                 % absolute error tolerance for ODE solver
% val_RelTol = 1e-6;                       % relative error tolerance for ODE
solver

% parameters shared with the nested function.
Coeff_dfb = [1/(ElectCharge*d_cavity*w_cavity*l_cavity) 1/t_c B_BCR C_ACRC
G_LGC; ...
          MCF FSE*B_BCR 1/t_p 0 N_t; ...
          N_t  NGC dnri_dnc n_phase v_OptFreq];   % Coefficient matrix of
the ...
                                        % coupled differential equations
N = length(I_modu);
N_AddFront = floor(T_unstable/(1/fs));      % the number of points in ...
                                        % the unstable state
tmp = I_bias + I_modu;
if N > N_AddFront        % check whether the number of input signal is
enough
   I_drive = [tmp(end - N_AddFront + 1: end) tmp];
else
   I_drive = [(I_bias*ones(1,N_AddFront-N)) tmp tmp];
end
if 1/fs > 20e-12
   disp(['Warn: Input sampling period of ' num2str(1e12/fs) 'ps is too
long!!!'])
   disp(['     It is suggested to be smaller than 20ps for accuracy.'])
end

if min(I_modu) < 0          % check the modulated current defined here
should be positive
      error('MATLAB:odedfb:lowmodulatedcurrent',...
      'The modulated current defined here should be positive!');
end
if sum(I_drive < 0) >= 1        % check the input current which should be
positive
      error('MATLAB:odedfb:lowinputcurrent',...
      'The input current is negative!');
end

I_drive_DC = I_bias*ones(1, 2*N_AddFront);      % input direct current
tt_Id = 0: 1/fs: (length(I_drive) - 1)/fs;
tt_Id_1 = 0: 1/fs: (length(I_drive_DC) - 1)/fs;
```

```matlab
%
% --------- Solve the differential equations with ode~ subroutine ---------
%
tspan = tt_Id;
tspan_1 = tt_Id_1;
y0 = [(t_c*I_bias/(ElectCharge*d_cavity*w_cavity*l_cavity)); 0; 0];  %
Initial value
J_Pattern = [1 1 0; 1 1 0; 1 0 0];
options = odeset('absTol', val_AbsTol, 'Jpattern', J_Pattern);
                % include: 'RelTol',val_RelTol,'absTol', val_AbsTol,...
                % 'Jacobian',@Jaco,'Jpattern',
J_Pattern,'Vectorized','on','stats','on';
[t_tmp,y_DC_tmp] = ode45(@f,tspan_1,y0, options, Coeff_dfb, tt_Id_1,
I_drive_DC, fs);
N_CD_bias = mean(y_DC_tmp(end - ceil(N_AddFront/10):end,1));
                % carrier density under the condition of input direct
                % current of bias current.
[t_tmp,y_DC_tmp] = ode45(@f,tspan_1,y0, options, Coeff_dfb, tt_Id_1,...
                (I_drive_DC + max(I_modu)), fs);
N_CD_biasPTP = mean(y_DC_tmp(end - ceil(N_AddFront/10):end,1));
                % carrier density under the condition of input direct
current
[t,y] = ode45(@f,tspan,y0, options, Coeff_dfb, tt_Id, I_drive, fs);

% Calculate the output variable
t_out = t(1:N)';
y_out = y(N_AddFront + 1: end,:);         % remove the warm-up sequence
P_dfb_out =
CoupEff*w_v*w_h*h_PlancCons*v_OptFreq*c_Light*(y_out(:,2)')/(2*n_g);
                                % output optical power
tmp_1 = y(N_AddFront: end,3)';            % remove the warm-up sequence
                                          % but keep the last point of the
                                          % warm-up sequence to calculate
slope
tmp_2 = 0:length(tmp_1) - 1;
slop_ph = (tmp_1(end) - tmp_1(1))/(length(tmp_1) - 1);
OpticPhase = tmp_1 - tmp_1(1) - slop_ph*tmp_2; % optical phase without DC
part of frequency chirp
OpticPhase = OpticPhase(2: end);          % remove the last point of the
warm-up sequence

f_chirp_total = -1*v_OptFreq*MCF*dnri_dnc*((y_out(:,1)') - N_t)/n_phase;
                                % frequency chirp
f_chirp_adiab_vec = -1*v_OptFreq*MCF*dnri_dnc*((y_out(:,1)') -
N_CD_bias)/n_phase;
                                % adiabatic Frequency chirp
f_chirp_adiab = -1*v_OptFreq*MCF*dnri_dnc*(N_CD_biasPTP -
N_CD_bias)/n_phase;
                                % adiabatic Frequency chirp
OpticPolar_x = cos(angle_PolarAndX)*sqrt(P_dfb_out).*exp(j.*OpticPhase +...
            j*(2*pi)*alfa/360);
                                % the x polarisation optical field
OpticPolar_y = sin(angle_PolarAndX)*sqrt(P_dfb_out).*exp(j.*OpticPhase);
                                % the y polarisation optical field
OpticField = OpticPolar_x + OpticPolar_y;    % total optical fields
OpticField_I = real(OpticField);          % real part
OpticField_Q = imag(OpticField);          % imaginary part


%
% ---------------------- nested function ----------------------------------
%
```

```matlab
    % Nested function
    function dydt = f(t, y, Coeff_dfb, tt_Id, I_drive, fs)
        dydt= zeros(3,1);
        tmp = floor(t*fs) + 1;
        tmp = (tmp > length(I_drive))*length(I_drive) + (tmp <= 0)*1 + ...
            (tmp > 0 & tmp <=length(I_drive))*tmp;
        if tmp >= 2 & (tmp <= length(I_drive) - 2)   % cubic interplolation
            mu = fs*(t - (tmp-1)/fs);
            mu2 = mu^2;
            a0 = I_drive(tmp + 2) - I_drive(tmp + 1) - I_drive(tmp - 1) +
I_drive(tmp);
            a1 = I_drive(tmp - 1) - I_drive(tmp) - a0;
            a2 = I_drive(tmp + 1) - I_drive(tmp - 1);
            a3 = I_drive(tmp);
            I_d_t = (a0*mu*mu2 + a1*mu2 + a2*mu + a3);

        elseif (tmp == length(I_drive) - 1)
            tmp_1 = abs(t - (tmp-1)/fs);
            I_d_t = I_drive(end - 1) + (I_drive(end) - I_drive(end -
1))*tmp_1;
        else
            I_d_t = I_drive(tmp);
        end
        dydt(1) = I_d_t*Coeff_dfb(1,1) - Coeff_dfb(1,2)*y(1) - ...
            Coeff_dfb(1,3)*y(1).^2 - Coeff_dfb(1,4)*y(1).^3 -
Coeff_dfb(1,5)...
            *(y(1) - Coeff_dfb(3,1))*y(2)/(1 + Coeff_dfb(3,2)*y(2));
        dydt(2) = Coeff_dfb(2,1)*Coeff_dfb(1,5)*(y(1) - Coeff_dfb(3,1))...
                *y(2)/(1 + Coeff_dfb(3,2)*y(2)) + Coeff_dfb(2,2)*y(1).^2 ...
                - Coeff_dfb(2,3)*y(2);
        dydt(3) = -2*pi*Coeff_dfb(3,5)*Coeff_dfb(2,1)*Coeff_dfb(3,3)*(y(1) -
...
                Coeff_dfb(2,5))/Coeff_dfb(3,4);
    end
    % Generate Jacobian Matrix
        function dfdy = Jaco(t, y, Coeff_dfb, tt_Id, I_drive, fs)
        dfdy = [(-1*Coeff_dfb(1,2) - 2*Coeff_dfb(1,3).*y(1) - ...
            3*Coeff_dfb(1,4)*(y(1).^2) - Coeff_dfb(1,5).*y(2)./(1 + ...
            Coeff_dfb(3,2).*y(2))), (-1.*Coeff_dfb(1,5).*(y(1) - ...
            Coeff_dfb(3,1))./((1 + Coeff_dfb(3,2).*y(2)).^2)), 0; ...
            (Coeff_dfb(2,1).*Coeff_dfb(1,5).*(y(1) - Coeff_dfb(3,1))./((1
...
            + Coeff_dfb(3,2).*y(2)).^2) - Coeff_dfb(2,3))
(Coeff_dfb(2,1).*...
            Coeff_dfb(1,5).*y(2)./(1 + Coeff_dfb(3,2).*y(2)) +...
            2*Coeff_dfb(2,2).*y(1)), 0; ...
            -1*Coeff_dfb(2,1)*Coeff_dfb(3,3)/Coeff_dfb(3,4), 0, 0 ];
    end



% % % display carrier density and photon density
% u = y(:,1);
% v = y(:,2);
% w = y(:, 3);
% % figure(111)
% % [Ay, H1, H2] = plotyy(t*1e9, u,t*1e9, v,'semilogy'); hold on;
% % set(H1, 'Linestyle', '--')
% % set(H2, 'Linestyle', '-.')
% % set(get(Ay(1),'ylabel'), 'String', 'Carrier density')
% % set(get(Ay(2),'ylabel'), 'String', 'Photon density')
% % title(['DFB laser']);
```

```matlab
% % xlabel('time (ns)');
%
% figure(112)
% semilogy(t*1e9, u,'-b'); hold on; grid on;
% xlabel('time (ns)');
% ylabel('Carrier density');
% figure(113)
% semilogy(t*1e9, v,'-b'); hold on; grid on;
% xlabel('time (ns)');
% ylabel('Photon density');
% figure(114)
% P_dfb_out_tmp =
CoupEff*w_v*w_h*h_PlancCons*v_OptFreq*c_Light*(y(:,2)')/(2*n_g);
% semilogy(t*1e9, P_dfb_out_tmp,'-b'); hold on; grid on;
% xlabel('time (ns)');
% ylabel('Output optical power (W)');
% figure(115)
% plot(t*1e9, P_dfb_out_tmp,'-b'); hold on; grid on;
% xlabel('time (ns)');
% ylabel('Output optical power (W)');
% figure(116)
% plot(t*1e9, w,'-b'); hold on; grid on;
% xlabel('time (ns)');
% ylabel('Phase');
%
% plot(t_out*1e9, OpticPhase)
% xlabel('Time (ns)')
% ylabel('Phase')


end  % function dfbode
% end of function file odedfb


%%------------------------------Old_version------------------------------
%%----%%BAD VERSION REALLY !!!
% function [OpticField_I, OpticField_Q, t_out, f_chirp_adiab,
f_chirp_total] = ...
%         dfbode(I_modu,I_bias,fs,flag_dfb_type,angle_PolarAndX)
% %
% %dfbode  Solve the coupled differential equations (rate equation) of a
% % directly modulated DFB(distributed feedback) laser.
% % [OpticField_I, OpticField_Q, t_out, f_chirp_adiab, f_chirp_total] =
% % dfbode(I_modu,I_bias,fs,flag_dfb_type,angle_PolarAndX), where the input
% % and out parameters are illuminated as below.
% %
% %input parameters
% % I_modu(vector): the modulated current.
% % I_bias(scalar): represents bias current.
% % fs(scalar): sampling frequency corresponding to the period between two
adjacent points.
% % flag_dfb_type: '1' represent Bookham LC25 laser with 300um long
cavity(default),
% %        '0' represent Bookham LC25 laser with 200um long cavity,
% % angle_PolarAndX: the angle between the signal polarisation and the x
% %        direction.
% %
% %output parameters
% % OpticField_I(raw vector): real part of optical field.
% % OpticField_Q(raw vector): imaginary part of optical field.
% % f_chirp_total(raw vector): frequency chirp.
% % t_out(raw vector): the time sequency corresponding to output data
sequency.
```

175

```matlab
% % f_chirp_adiab(raw vector): abiabatic frequency chirp.
% % f_chirp_total(raw vector): total frequency chirp.
%
% % Related equations corresponding to DFB laser
% % 1) the coupled differential equations:
% % d_N_CD/d_t =  I_drive/(ElectCharge*d_cavity*w_cavity*l_cavity) -
N_CD/t_c ...
% %     - B_BCR*N_CD^2 - C_ACRC*(N_CD^3) - G_LGC*(N_CD - N_t)*PD/(1+NGC*PD);
% % d_PD/d_t =  MCF*G_LGC*(N_CD-N_t)*PD/(1+NGC*PD) + FSE*B_BCR*(N_CD^2) -
PD/t_p;
% % d_OptPhase/d_t = -2*pi*v_OptFreq*MCF*dnri_dnc*(N_CD - N_t)/n_phase;
% %
% % 2) output optical power:
% % P_optic = w_v*w_h*h_PlancCons*v_OptFreq*PD*c_LightVelo/(2*n_g);
% %
% % 3) optical frequency of output optical signal
% % f = v_OptFreq*(1 - MCF*dnri_dnc*(N_CD - N_t)/n_phase;
% %
% % N_CD   -- the carrier density
% % PD -- the photon density
% % I_drive -- the current drive into the active region of the laser
% %
%
% %
% % ----------------------- Initialization ---------------------------
--
% %
% % check inputs
% if nargin <= 4
%     angle_PolarAndX = 0;        % the angle between the signal
polarisation ...
%                                 % and the x direction
%     if nargin <= 3
%         flag_dfb_type = 1;
%         if nargin <= 2
%             error('MATLAB:odedfb:NotEnoughInputs',...
%                 'Not enough input arguments.  See ODEDFB.');
%         end
%     end
% end
%
% %
% % ----- Parameters for directly modulated DFB laser ( Light Sourse ) ----
--
% %
% if flag_dfb_type == 1
%     % 300um Bookham LC25 laser.
%     l_cavity = 300e-6;                % the cavity length  ( m )
%     t_p = 3.6e-12;                    % the photon lifetime  ( s )
%     NGC = 7.4e-23;                    % the nonlinear gain coefficient  (
m-3)
%     dnri_dnc = -1.381e-26;            % Rate of refractive index change
with ...
%                                       % carrier density
% else
%     % 200um Bookham LC25 laser,
%     l_cavity = 200e-6;                % the cavity length  ( m )
%     t_p = 2.65e-12;            % the photon lifetime  ( s )
%     NGC = 6.8e-23;                    % the nonlinear gain coefficient  (
m-3 )
%     dnri_dnc = -1.473e-26;     % Rate of refractive index change with ...
```

176

```matlab
%                                      % carrier density
% end
% ElectCharge = 1.60217646e-19;        % the electronic charge  ( C )
% WaveLen = 1550e-9;                    % the Wavelength ( unit:m )
% h_PlancCons = 6.626068e-34;           % the Planck's constant  ( J s )
% c_Light = 2.99792458e8;         % the velocity of light in vacuum  ( ms-1
% )
% v_OptFreq = c_Light/WaveLen;    % the optical frequency  ( Hz )
%
% N_t = 1.5e24;                         % the transparency carrier density  ( m-3
% )
% d_cavity = 0.033e-6;                  % the cavity thickness  ( m )
% w_cavity = 2e-6;                      % the cavity width  ( m )
% LGC = 7.5e-20;                        % the differential gain coefficient
% ( m2 )
% B_BCR = 1e-16;                        % the bimolecular carrier
% recombination  ( m3s-1 )
% C_ACRC = 6.5e-41;                     % the Auger carrier recombination
% coefficient  ( m6s-1 )
% FSE = 1e-5;                  % describe the fraction of spontanous
% emission  ( no )
% MCF = 0.07;                  % the mode confinement factor  ( no )
% t_c = 10e-9;                 % the carrier linear recombination lifetime
% ( s )
% w_v = 0.47e-6;                        % the vertical widths of the guided
% mode ...
%                                      % power distributions  ( m)
% w_h = 1.80e-6;                        % the horizontal widths of the
% guided mode ...
%                                      % power distributions  ( m )
% n_g = 3.7;                            % the group index  ( no )
% n_phase = 3.2203;                     % Phase refractive index
%
% G_LGC = LGC*(c_Light/n_g);      % the linear gain coefficient  ( m3s-1 )
% CoupEff = 0.38;                       % the coupling efficiency from the
% laser chip to SMF.
% val_AbsTol = 1e-6;                    % absolute error tolerance for ODE
% solver
% val_RelTol = 1e-3;                    % relative error tolerance for ODE
% solver
%
% % parameters shared with the nested function.
% Coeff_dfb = [1/(ElectCharge*d_cavity*w_cavity*l_cavity) 1/t_c B_BCR
% C_ACRC G_LGC; ...
%             MCF FSE*B_BCR 1/t_p 0 0; ...
%             N_t  NGC dnri_dnc n_phase v_OptFreq];   % Coefficient matrix
% of the ...
%                                      % coupled differential
% equations
% N = length(I_modu);
% T_unstable = 1e-9;                    % unstable period in the
% beginning
% N_AddFront = floor(T_unstable/(1/fs));    % the number of points in ...
%                                      % the unstable state
% I_drive = I_bias + I_modu;
% if sum(I_drive < 0) >= 1       % check the input current which should be
% positive
%       error('MATLAB:odedfb:lowinputcurrent',...
%               'The input current is negative!');
% end
% I_drive_DC = I_bias*ones(1, 64*N_AddFront);   % input direct current
```

```matlab
% tt_Id = 0: 1/fs: (N - 1)/fs;
% tt_Id_1 = 0: 1/fs: (length(I_drive_DC) - 1)/fs;
%
% %
% % --------- Solve the differential equations with ode~ subroutine -------
--
% %
% tspan = tt_Id;
% y0 = [(t_c*I_bias/(ElectCharge*d_cavity*w_cavity*l_cavity)); 0; 0];  %
Initial value
% J_Pattern = [1 1 0; 1 1 0; 1 0 0];
% options = odeset('absTol', val_AbsTol,'Jpattern', J_Pattern);
%           % include: 'RelTol',val_RelTol,'absTol', val_AbsTol,...
%           % 'Jacobian',@Jaco,'Jpattern',
J_Pattern,'Vectorized','on','stats','on';
% [t,y] = ode45(@f,tspan,y0, options, Coeff_dfb, tt_Id, I_drive, fs);
% [t_tmp,y_DC] = ode45(@f,tspan,y0, options, Coeff_dfb, tt_Id_1,
I_drive_DC, fs);
%
% % Calculate the output variable
% t_out = t';
% y_out = [y(end - N_AddFront + 1: end,:); y(N_AddFront + 1: end,:)];
%           % replace the first part which is in unstable state with
the ...
%           % the copy the last part
% N_CD_bias = y_DC(end,1);        % carrier density under the condition of
...
%                                % input direct current of bias current.
% P_dfb_out = CoupEff*w_v*w_h*h_PlancCons*v_OptFreq*c_Light*...
%           (y_out(:,2)')/(2*n_g);       % output optical power
% slop_tmp = (y_DC(end,3) - y_DC(4*N_AddFront, 3))/(length(y_DC(:,3)) -
4*N_AddFront);
% Phase_tmp = y_out(:,3)';         % absoluted phase obtained by solving the
equations set
% OpticPhase(N_AddFront + 1: length(Phase_tmp)) = Phase_tmp(N_AddFront + 1:
...
%           length(Phase_tmp)) - slop_tmp*(1:length(Phase_tmp) - ...
%           N_AddFront) - Phase_tmp(N_AddFront);
% OpticPhase(1: N_AddFront) = Phase_tmp(1: N_AddFront) - slop_tmp*...
%           (1: N_AddFront) - Phase_tmp(1);
%                                % output optical phase
%
% f_chirp_total = -1*v_OptFreq*MCF*dnri_dnc*((y_out(:,1)') - N_t)/n_phase;
%                                % frequency chirp
% f_chirp_adiab = -1*v_OptFreq*MCF*dnri_dnc*((y_out(:,1)') -
N_CD_bias)/n_phase;
%                                % adiabatic Frequency chirp
%
% alfa = 120/360*2*pi;                    % the addition of a rear facet
...
%                                % phase shift of 120/360
% OpticPolar_x = cos(angle_PolarAndX)*sqrt(P_dfb_out).*exp(j.*OpticPhase);
%                                % the x polarisation optical
field
% OpticPolar_y = sin(angle_PolarAndX)*sqrt(P_dfb_out).*exp(j.*OpticPhase +
j*alfa);
%                                % the y polarisation optical
field
% OpticField = OpticPolar_x + OpticPolar_y;     % total optical fields
% OpticField_I = real(OpticField);        % real part
% OpticField_Q = imag(OpticField);        % imaginary part
```

```matlab
%
% %
% % ------------------- nested function -----------------------------
--
% %
%       % Nested function
%       function dydt = f(t, y, Coeff_dfb,tt_Id, I_drive, fs)
%           dydt= zeros(3,1);
%           tmp = floor(t*fs) + 1;
%           tmp = (tmp > length(I_drive))*length(I_drive) + (tmp <= 0)*1 +
...
%               (tmp > 0 & tmp <=length(I_drive))*tmp;
%           if tmp >= 1 & tmp < length(I_drive)
%               I_d_t = I_drive(tmp) + abs(t - (tmp - 1)/fs)/(1/fs)*...
%                   (I_drive(tmp + 1) - I_drive(tmp));   % in order to
estimate ...
%                       % the value of time t: I(t1 + dt) = I(t1) +
(|dt|/Ts)*(I(t2) - I(t1))
%           else
%               I_d_t = I_drive(tmp);
%           end
% % % %         I_d_t = interp1(tt_Id, I_drive, t);
%                   % 'v5cubic', 'extrap';'v5cubic' 'spline' and 'pchip'
%           dydt(1) = I_d_t*Coeff_dfb(1,1) - Coeff_dfb(1,2)*y(1) - ...
%               Coeff_dfb(1,3)*y(1).^2 - Coeff_dfb(1,4)*y(1).^3 -
Coeff_dfb(1,5)...
%               *(y(1) - Coeff_dfb(3,1))*y(2)/(1 + Coeff_dfb(3,2)*y(2));
%           dydt(2) = Coeff_dfb(2,1)*Coeff_dfb(1,5)*(y(1) -
Coeff_dfb(3,1))...
%                   *y(2)/(1 + Coeff_dfb(3,2)*y(2)) + Coeff_dfb(2,2)*y(1).^2
...
%                   - Coeff_dfb(2,3)*y(2);
%               dydt(3) = -
2*pi*Coeff_dfb(3,5)*Coeff_dfb(2,1)*Coeff_dfb(3,3)*(y(1) - ...
%                   Coeff_dfb(3,1))/Coeff_dfb(3,4);
%       end
%       % Generate Jacobian Matrix
%         function dfdy = Jaco(t, y, Coeff_dfb, tt_Id, I_drive, fs)
%           dfdy = [(-1*Coeff_dfb(1,2) - 2*Coeff_dfb(1,3).*y(1) - ...
%               3*Coeff_dfb(1,4)*(y(1).^2) - Coeff_dfb(1,5).*y(2)./(1 + ...
%               Coeff_dfb(3,2).*y(2))), (-1.*Coeff_dfb(1,5).*(y(1) - ...
%               Coeff_dfb(3,1))./((1 + Coeff_dfb(3,2).*y(2)).^2)), 0; ...
%               (Coeff_dfb(2,1).*Coeff_dfb(1,5).*(y(1) - Coeff_dfb(3,1))./((1
...
%               + Coeff_dfb(3,2).*y(2)).^2) - Coeff_dfb(2,3))
(Coeff_dfb(2,1).*...
%               Coeff_dfb(1,5).*y(2)./(1 + Coeff_dfb(3,2).*y(2)) +...
%               2*Coeff_dfb(2,2).*y(1)), 0; ...
%               -1*Coeff_dfb(2,1)*Coeff_dfb(3,3)/Coeff_dfb(3,4), 0, 0 ];
%       end
%
% % % % display carrier density and photon density
% % u = y(:,1);
% % v = y(:,2);
% % w = y(:, 3);
% % % figure(111)
% % % [Ay, H1, H2] = plotyy(t*1e9, u,t*1e9, v,'semilogy'); hold on;
% % % set(H1, 'Linestyle', '--')
% % % set(H2, 'Linestyle', '-.')
% % % set(get(Ay(1),'ylabel'), 'String', 'Carrier density')
% % % set(get(Ay(2),'ylabel'), 'String', 'Photon density')
```

```matlab
% % % title(['DFB laser']);
% % % xlabel('time (ns)');
% %
% % figure(112)
% % semilogy(t*1e9, u,'-b'); hold on; grid on;
% % xlabel('time (ns)');
% % ylabel('Carrier density');
% % figure(113)
% % semilogy(t*1e9, v,'-b'); hold on; grid on;
% % xlabel('time (ns)');
% % ylabel('Photon density');
% % figure(114)
% % P_dfb_out_tmp =
CoupEff*w_v*w_h*h_PlancCons*v_OptFreq*c_Light*(y(:,2)')/(2*n_g);
% % semilogy(t*1e9, P_dfb_out_tmp,'-b'); hold on; grid on;
% % xlabel('time (ns)');
% % ylabel('Output optical power (W)');
% % figure(115)
% % plot(t*1e9, P_dfb_out_tmp,'-b'); hold on; grid on;
% % xlabel('time (ns)');
% % ylabel('Output optical power (W)');
% % figure(116)
% % plot(t*1e9, w,'-b'); hold on; grid on;
% % xlabel('time (ns)');
% % ylabel('Phase');
%
% end  % function dfbode
% % end of function file odedfb
```

Square-law Photon Detector

```matlab
function E_array = APD(Opt_signal, Inter_gain, Ionisation_k, Noise_band, Wavelength, Noise_switch)
%E_array = APD(Opt_signal, Inter_gain, Ionisation_k, Noise_cut_dens, Noise_band, Wavelength)
%E_array = APD(Opt_signal, Inter_gain, Ionisation_k, Noise_cut_dens, Noise_band, Wavelength)
% Opt_signal: input optical signal
% Inter_gain : APD internal gain. InGaAs(10<=M<=40). usually M=10 for APD.
% when it is set to M=1, it is a PIN detector
% Ionisation_k: Ionisation constant k.Suppose InGaAs(0.5<=k<=0.7) APD is applied...
% usually used value is 0.5
% Noise_cut_dens: pA/sqrt(Hz) equivalent input noise current density
% (0--100). 8 is a proper value for 10GHz
% Noise_band = Fs_samp/2*0.75;
% Wavelength = 1550e-9;           %wavelength of light in m.
% Noise_switch: 1 with shot and thermal noise in the output signal. 0
% without noise in the output signal
Ratio1=dlmread('Ratio1', ' ');
Ratio2=dlmread('Ratio2', ' ');
Noise_band=Noise_band*Ratio1*Ratio2;
Quan_eff = 0.8;
C_light = 2.997924580e8;
E_charge = 1.602176487e-19;
H_planck = 6.626068e-34;
%Noise_cut_dens = Noise_cut_dens*1e-12;     %convert pA/sqrt(Hz) to A/sqrt(Hz)
ExNoise_factor = Inter_gain*(1-(1-Ionisation_k)*(1-1/Inter_gain)^2);
%F(M) = M [ 1 ï¿½ (1-k)(1-1/M)2 ] , where k is the ionisation constant,
```

```matlab
                                                                    %ie. ratio
of the ionisation coefficients of holes and electrons;
Apd_freqency = C_light/Wavelength;
R_resp = Quan_eff*E_charge/(H_planck*Apd_freqency)


%phaseofsignalintofibre=dlmread('phaseofsignalintofibre', ' ');
%phaseofreceivedsignal=angle(Opt_signal);
% dlmwrite('phaseofreceivedsignal',phaseofreceivedsignal', ' ');


% phaseofreceivedsignal=dlmread('phaseofreceivedsignal', ' ');
%anglecomp=phaseofreceivedsignal-phaseofsignalintofibre;
%dlmwrite('anglecomp',anglecomp', ' ');
%anglecomp=dlmread('anglecomp', ' ');
%E_array = Inter_gain*2*(Opt_signal).*conj(exp(sqrt(-1).*anglecomp'));
%I = M*R*P  electrical current. and also 0.3dB optical connetor loss
E_array =R_resp* Inter_gain*(abs(Opt_signal)).^2;
disp('APD Opt_signal power is:');
10*log10(mean(abs(Opt_signal).^2)*1e3)



%Add shot noise
%Shot_noise = sqrt(2*E_charge*gain*ExNoise_factor*Fs_samp.*E_array);
Delta_shot =
sqrt(2*E_charge*Inter_gain*ExNoise_factor*(Noise_band/2*0.75).*E_array);
%Delta_shot is a sequence
Shot_noise = Delta_shot.*randn(1,length(Opt_signal));
Shot_variance = var(Shot_noise)



%Add themal noise
PrecindBm=dlmread('PrecindBm', ' ');
Qfactor=dlmread('Qfactor', ' ');
BWofpin=dlmread('BWofpin', ' ');




Prec=10^((PrecindBm-30)/10);
niosecurrentdensity=(Prec*R_resp/Qfactor)^2/(BWofpin);
stdthermalnoise=sqrt(niosecurrentdensity*(Noise_band/2*0.75));
%if Noise_cut_dens >= 0
    %Delta_them = Noise_cut_dens*sqrt(Noise_band)
    Themal_noise = stdthermalnoise*randn(1,length(Opt_signal));
    Themal_variance = var(Themal_noise)
%end

% disp('output SNR of APD is:');
% 10*log10(mean(abs(E_array).^2)/(var(Shot_noise+Themal_noise)))
% disp('output AC SNR of APD is:');
% 10*log10(mean(abs(E_array).^2-
min(abs(E_array).^2))/(var(Shot_noise+Themal_noise)))
% disp('output TURE AC SNR of APD is:');
% 10*log10(mean(abs(E_array-
mean(E_array)).^2)/(var(Shot_noise+Themal_noise)))


E_array = E_array + Noise_switch*(Shot_noise + Themal_noise);
```

Electrical Low-pass Filter

```matlab
% Electrical filter
ss_in_tmp2 = dlmread('outputofPIN', ' ')';
    tmp_1 = fft(ss_in_tmp2);
    % Electrical DSB
    tmp_4 = Fs_samp/2;
    singlesideband=dlmread('singlesideband', ' ');
    if singlesideband==1
        startoflowerlimitforfilter=F_RF-tmp_4;
    elseif singlesideband==0
        startoflowerlimitforfilter=F_RF-tmp_4;

    end;
    tmp_2 = floor((startoflowerlimitforfilter)/(Fs_OS_Ch/length(tmp_1))) -
0;      % lower limit
    tmp_3 = ceil((F_RF+tmp_4)/(Fs_OS_Ch/length(tmp_1))) + 0;    % upper
limit
    tmp_1(2: tmp_2) = 0;          % lower limit
    tmp_1(end - tmp_2 + 1 + 1: end) = 0;    % lower limit
    tmp_1(tmp_3 + 1 + 1: end/2) = 0;    % upper limit
    tmp_1(end/2 + 2: end - tmp_3 - 1) = 0;  % upper limit
outputofPIN2222 =(ifft((tmp_1)));
```

Analogue to Digital Converter

```matlab
function [outputofADC]=ADC(Quan_bit,Clip_ratio,input1)

input1 = input1 - mean(input1);            %make the average amplitude be
zero.
Pm_input = mean(input1.^2);            % the average power of the OFDM
symbols with Cyclic Prefixes before clipping.
Max_amp = sqrt(10^(Clip_ratio/10)*Pm_input);
for k_s=1:length(input1)
    if abs(input1(k_s)) > Max_amp
        input1(k_s) = sign(input1(1,k_s))*Max_amp;
    end
end

%Doing quantization
Quan_peak = Max_amp;          %should be a constant in future but not
necessarily be max(input)
Quan_step = 2*Quan_peak/2^Quan_bit;
for kk_b = 1:length(input1)
   %  index = floor(input1(kk_b)/Quan_step);
   %  input1(kk_b) = (index+1/2)*Quan_step;
    input1(kk_b) = round(input1(kk_b)/Quan_step)*Quan_step;
end
outputofADC=input1;
```

SMF Data File

```matlab
%Fibre_Para_Store.m
%This M-file is used to store parameters of fibre feature . These data
%will be kept in a MAT-file named "Fibre_Paras_Data.txt"

%       mon_detail    int         level of detail reported to monitor file
%       algorithm                 linear  nonlinear  or nonlinearx
%       length        km          fibre length
```

```matlab
%        split_len     km           Split step length
%        attenuation   dB/km        loss of the fibre at the attenuation
wavelength
%        att_slope     dB/nm/km     slope of the loss at the attenuation
wavelength
%        att_slp_chng  dB/nm/nm/km rate of change of att_slope with
wavelength
%        att_wlength   nm           wavelength at which atten. parameters
are valid
%        dispersion    ps/nm/km     dispersion of the fibre at the
dispersion
%                                    wavelength
%        disp_slope    ps/nm/nm/km slope of the dispersion at the
dispersion
%                                    wavelength
%        disp_wlength  nm           wavelength at which disp. parameters are
valid
%        kerr_coef     m^2/W        Kerr coefficient
%        area          um^2         Effective Area
%        birf_delay    ps/km        Mean birefringence delay
%        birf_sd       ps/km        Standard deviation of delay
%        ang_dist                   Coupling angle distribution Uniform or
Gaussian
%        min_ang       degrees      Min|mean mode coupling angle
%        max_ang       degrees      Max|standard deviation of angle
%        step_method                Step size calculation method Fixed or
Auto
%        MAX_DELTA_BOUND
%        MAX_FLOOR_BOUND


%The following paras are for non-dispersion shifted fibre(NDSF)
mon_detail = 5;
fib_length=25;
algorithm = 'Nonlinear';

split_length = 0.5;
attenuation = 0.20;         %0.21
att_slope = 0;
att_slp_chng = 0;
att_wlength = 1550;
dispersion = 17;%   %17.0
dlmwrite('dispersionparameter',dispersion, ' ');
disp_slope = 0.07;%0.07;          %0.07
disp_wlength = 1550;
kerr_coef = 2.35e-20;        %2.35e-20 for all types SMF
area = 80;
birf_delay = 0;
birf_sd = 0;
ang_dist = 'Uniform';
min_ang = 0;
max_ang = 0;
step_method = 'Fixed';
MAX_DELTA_BOUND = 0;
MAX_FLOOR_BOUND = 0;
%fib_length =0;
fid = fopen('Fibre_Paras_Data.txt','wt');
fprintf(fid,'%s\n','mon_detail');
fprintf(fid,'%d\n',mon_detail);
fprintf(fid,'%s\n','algorithm');
fprintf(fid,'%s\n','Nolinear');
fprintf(fid,'%s\n','fib_length');
```

```
fprintf(fid,'%g\n',fib_length);
fprintf(fid,'%s\n','split_length');
fprintf(fid,'%g\n',split_length);
fprintf(fid,'%s\n','attenuation');
fprintf(fid,'%g\n',attenuation);
fprintf(fid,'%s\n','att_slope');
fprintf(fid,'%g\n',att_slope);
fprintf(fid,'%s\n','att_slp_chng');
fprintf(fid,'%g\n',att_slp_chng);
fprintf(fid,'%s\n','att_wlength');
fprintf(fid,'%g\n',att_wlength);
fprintf(fid,'%s\n','dispersion');
fprintf(fid,'%g\n',dispersion);
fprintf(fid,'%s\n','disp_slope');
fprintf(fid,'%g\n',disp_slope);
fprintf(fid,'%s\n','disp_wlength');
fprintf(fid,'%g\n',disp_wlength);
fprintf(fid,'%s\n','kerr_coef');
fprintf(fid,'%g\n',kerr_coef);
fprintf(fid,'%s\n','area');
fprintf(fid,'%g\n',area);
fprintf(fid,'%s\n','birf_delay');
fprintf(fid,'%g\n',birf_delay);
fprintf(fid,'%s\n','birf_sd');
fprintf(fid,'%g\n',birf_sd);
fprintf(fid,'%s\n','ang_dist');
fprintf(fid,'%s\n',ang_dist);
fprintf(fid,'%s\n','min_ang');
fprintf(fid,'%g\n',min_ang);
fprintf(fid,'%s\n','max_ang');
fprintf(fid,'%g\n',max_ang);
fprintf(fid,'%s\n','step_method');
fprintf(fid,'%s\n',step_method);
fprintf(fid,'%s\n','MAX_DELTA_BOUND');
fprintf(fid,'%g\n',MAX_DELTA_BOUND);
fprintf(fid,'%s\n','MAX_FLOOR_BOUND');
fprintf(fid,'%g\n',MAX_FLOOR_BOUND);
fclose(fid);

clear mon_detail algorithm fib_length split_length attenuation att_slope
att_slp_chng att_wlength dispersion disp_slope ...
    disp_wlength kerr_coef area birf_delay birf_sd ang_dist min_ang max_ang
step_method MAX_DELTA_BOUND MAX_FLOOR_BOUND fid
```

References

[1]   M. Seimetz, "Higer-Order Modulation for Optical Fibre Transmission", Springer.

[2]   Jean-Benoit Larouche, "Understanding PAPR in OFDM systems", http://nutaq.com/en/blog/understanding-papr-ofdm-systems, Jan. 2014.